Development of vapour-based multistage solar still desalination system

by

MFANAFUTHI MTHANDENI MKHIZE

Thesis is submitted in fulfilment for the degree

Doctor of Engineering: Mechanical Engineering

in Mechanical and Mechatronic Engineering Department

in the Faculty of Engineering and the Built Environment

At the Cape Peninsula University of Technology

Supervisor: Dr V. Msomi

Co-supervisor: Dr O. Nemraoui

Bellville

March 2022

DECLARATION

I, Mfanafuthi Mthandeni Mkhize, declare that the contents of this thesis represent my own unaided work, and that the thesis has not previously been submitted for academic examination towards any qualification. Furthermore, it represents my own opinions and not necessarily those of the Cape Peninsula University of Technology.

15 MARCH 2022

Date

ABSTRACT

The current study conceived, constructed, and experimentally tested the vapour-based multistage solar still with stacked stages (MSS-SS). The construction of the system was done at Cape Peninsula University of Technology (CPUT), Bellville campus. The experimental tests were conducted for a period of 10 months which covered the four seasons of the year, starting from Sept. 2020 to the end of June 2021. Moreover, there were key difference that can be noted from the waterbed-based MSS-SS and the current vapour-based MSS-SS. The vapour-based MSS-SS did not have waterbed in the stages, it employed a direct vapour input through the vapour make-up tubes to the stages, adopted a dynamic mode (impulse circulation) of waterbed in the entry stage (evaporator), it was a standalone system, brine solution was recirculated to aid in saline water (SW) pre-heating, direct SW heating in the evacuated tube solar collectors (ETSCs), vapour cooling SW in a zigzagged SW tube, minimal SW quantity in the entry stage to mention few. The vapour-based MSS-SS was integrated with a passive basin solar still (BSS) situated at the top of the stacked stages.

The distillation unit operated at SW temperatures ranging from 90°C to 100°C which indicated increased vapour production in the evaporator. However, the experimental tests indicated the collector to basin area (CBA) ratio was larger and the distillation unit required a thermal energy storage (TES) as the system reached thermal damage conditions under increased thermal energy input.

For a typical day, the thermal efficiency of the distillation unit was found to be 18.23%. The MSS-SS daily cumulative distillate yield ranged from non-measurable (NM) quantities to a maximum of 7790 ml (7.8 litres) under low to high average solar irradiance, respectively. Furthermore, the quality of the distillate suggested that food grade material should be used for construction to minimize contaminants. At its most productive days, the cost per litre (CPL) was R4.69 and R4.05 (R=South African Rands) for the MSS-SS stacked stages and the MSS-SS stages plus the BSS, respectively. For the thermally insulated condensing tower, the thermal efficiency was 18.23%. Under insulated conditions, the thermal efficiency decreased further.

The experimental tests showed that the performance of the MSS-SS can be enhanced by an improved SW pre-heating and heat recovery processes. Therefore, it was concluded that the developed standalone MSS-SS with circulation waterbed, improved SW pre-heating and heat recovery processes, had a potential to be an alternative and supplement to the existing distillation.

Publications

Intellectual of property:

Inventors: MM Mkhize and V Msomi

Title: Multistage solar desalination system

Patent number: 2021/05366

Papers:

Mkhize, M.M. and Msomi, V., 2021. Challenges and progress made toward the improvement of a multistage solar still desalination system. *Desalination and Water Treatment*, *222*, pp.23-35.

M. M. Mkhize and V. Msomi, "Feasibility of a Multistage Solar Still in Southern Africa," *2020 9th International Conference on Renewable Energy Research and Application (ICRERA)*, 2020, pp. 48-54.

M.M. Mkhize, V. Msomi, A Comparative study of the Multistage Solar Stills with Stacked Stages (MSS-SS), *Journal of Engineering, 2021*, pp. 1-13.

AKNOWLEDGEMENTS

I wish to acknowledge and thank all the Mechanical Engineering workshop staff at Cape Peninsula University of Technology (CPUT), Bellville campus for their assistance in the construction of the system.

I further acknowledge Dr Ncediwe Ndube-Tsolekile from the Department of Chemistry for assisting in testing the pH in the water.

I also would like to thank my supervisor Dr Velaphi Msomi for his invaluable technical guidance and mentoring. This work was made possible by his in-depth knowledge which he shared with me.

Furthermore, the support and patience my wife Sikelelwa Innocentia Mkhize gave me was unparalleled. It was the most critical aspect in ensuring that I continued to work even under stressful times.

Last but not least,

The financial assistance of the National Research Foundation towards this research is acknowledged. Opinions expressed in this thesis and the conclusions arrived at, are those of the author, and are not necessarily to be attributed to the National Research Foundation.

DEDICATION

Lo msebenzi ube yimpumelelo ngeDlozi lakithi noMveli'kqala wesizwe sakithi. Ngibonga ukusekwa yibo ngokomoya nobuchule abangiphe bona.

Ngiqhubeke ngibonge uNkosikazi wami uSikelelwa Innocentia Mkhize ngegalelo abenalo neqhaza alibambile nokuba nethemba nokukholelwa kimi ukuze lomsebenzi ube yimpumelelo.

Siyabonga.

TABLE OF CONTENT

LIST OF FIGURES

LIST OF TABLES

NOMENCLATURE

Terms/Acronyms	Explanation
BSS	Basin solar still
CBA	Collector to basin area ratio
CPC	Compound parabolic concentrator
CPC-TSS	Compound parabolic concentrator – tubular
CPL	Cost per litre
CPUT	Cape Peninsula University of Technology
CrSS	Corrugated solar still
CrWSS	Corrugated wick solar still
CSS	Conventional solar still
DC	Direct current (electricity)
DME	Department of Mineral and Energy
DoE	Department of Energy
DS	Double slope
DSS	Developed solar still
DWA	Department of water affairs
DWAF	Department of Water and Forestry
DWS	Department of Water and Sanitation
ED	Electrodialysis
ETSC	Evacuated tube solar collector
FPCB	Flat plate collector basin still
FPSC	Flat plates solar collector
FSS	Four solar stills
GW	Ground water
HDH	Humidification-dehumidification
HTF	Heat transfer fluid
ISPB	Inclined solar panel basin
MED	Multi-effect distillation
MENA	Middle East and North Africa
MSF	Multistage flash
MSS-SS	Multistage solar still with stacked stages
MSW	Mediterranean seawater
OSS	Ordinary solar still
PCM	Phase change material
PTC	Parabolic trough collector
PV	Photovoltaic
PV/T	Photovoltaic-thermal
RDP	Reconstruction and Development Programme
RE	Renewable Energy
RO	Reverse osmosis
RSW	Red seawater
SA	South Africa
SADC	Southern African Development countries
SS	Single slope
SSS	Single solar still
Stats SA	Statistics South Africa
SW	Saline water (seawater)

SWRO	Seawater reverse osmosis
TES	Thermal energy storage
UV	Ultraviolet
VRW	Vertical rotating wick
VSDC	Vertical single distillation cell
WHO	World Health Organisation
WTW	Water treatment works
WWTW	Wastewater treatment works

Equation Symbols

Symbol	Description
AC	Annual cost
A_{cc}	BSS condensing cover surface area (m^2)
AMC	Annual maintenance cost
ASV	Annual salvage vale
cp	Specific heat capacity (J/kg.K)
CRF	Capital recovery factor
E_o	Eccentricity correction factor
FAC	Fixed annual cost
f_{Hay}	Hay's anisotropic index
H_b	Daily beam radiation on horizontal surface (W/m^2)
H_d	Daily diffuse radiation on horizontal surface (W/m^2)
$H_{d\beta}$	Daily diffuse radiation on an inclined surface (W/m^2)
hfg_{BSS}	Latent heat of evaporation in the BSS (kJ/kg)
hfg_{evap}	Latent heat of evaporation in the evaporator (kJ/kg)
H_H	Daily total solar radiation on horizontal surface (W/m^2)
H_o	Daily extra-terrestrial radiation (W/m^2)
H_r	Daily reflected radiation (W/m^2)
I_b	Hourly beam radiation on a horizontal surface (W/m^2)
$I_{b\beta}$	Hourly beam radiation on an inclined surface (W/m^2)
I_d	Hourly diffuse radiation on a horizontal surface (W/m^2)
$I_{d\beta}$	Hourly diffuse radiation on an inclined surface (W/m^2)
I_H	Hourly total solar radiation on a horizontal surface (W/m^2)
I_o	Hourly extra-terrestrial radiation (W/m^2)
I_{sc}	Solar constant (1367 W/m^2)
I_r	Hourly reflected radiation (W/m^2)
I_T	Hourly total solar irradiance on a titled surface (W/m^2)
I_β	Hourly total solar radiation on an inclined surface (W/m^2)
K_t	Daily clearness index
L_L	Longitude of the local location (degrees)
L_s	Standard meridian for local zone
LT	Local standard time
$\dot{m}_{dist}$	Distillate mass flow rate (kg/s)

$\dot{m}_e$	Vapour mass flow rate (kg/s)
$\dot{m}_{sw}$	SW mass flow rate (kg/s)
M_t	Hourly clearness index
n	Number of the day in a year
P	Present capital cost
P_d	Daily cumulative distillate productivity (litres/m^2)
Q_{ETSC}	Total thermal energy collected by the ETSC (W)
$\dot{Q}_{loss}$	Heat losses from the stage walls (W)
$\dot{Q}_{TOTAL}$	Total heat transmitted through the glass (W)
S	Salvage value
SFF	Sinking fund factor
ST	Local solar time
T_a	Ambient or surrounding temperature (°C)
T_b	BSS basin temperature (°C)
T_m	SW mean temperature in the ETSC (°C)
T_{sw}	SW temperature of SW in the BSS basin (°C)
T_v	Vapour temperature in the BSS (°C)
V_t	Daily cumulative distillate yield in litres

Greek symbols and subscripts

Symbols	**Description**
β	Angle of inclined surface (degrees)
θ	Angle of incident of solar radiation (degrees)
i	Annual interest rate (%)
δ	Declination angle (degrees)
η	ETSC collecting efficiency (%)
ρ_g	Ground reflectance
ω	Hour angle (degrees)
φ	Latitude of the local location (degrees)
R_b	Tilt factor or conversion factor
θ_z	Zenith angle, angle of incident on horizontal
1	Stage 1
2	Stage 2
3	Stage 3
4	Stage 4
5	Stage 5

CHAPTER ONE
INTRODUCTION

1.1 Historical water shortages and methods to eradicate water shortages

This chapter discusses the causes of water scarcity, with the focus in South Africa (SA) and Southern Africa, encompassing both structural and physical water scarcity. It further looks at the modern-day provision of fresh water and the cost and processes involved. It then discusses an alternative to fossil fuels in the form of renewable energy (RE). It also discusses the historical developments of a small-scale desalination system. Finally, the problem statement which presents the problem this current study aims to address is laid out.

1.1.1 Structural water scarcity

Structural water scarcity refers to political economy of resource allocation and other related factors (Tapela, 2012). Domestic structural water challenges in SA started many years back. Based on the historical background of water development in SA, the structural water scarcity was by design in the early 20th century. At the end of the 19th and early 20th century, white agricultural, mining and other sectors were prioritised. Water for irrigation and other industries was diverted from the rivers to supply white farmers for irrigation and other uses. Legislations were passed to protect the water rights of farmers since few dams were constructed at the time. These historical water structures influenced the South African socio-economic structure which lasted for many years. Evidently, at the start of the democratic dispensation, this was no difference, as shown in Figure 1.1. The figure shows a South African population without piped water distribution at the beginning of a democratic dispensation in 1994.

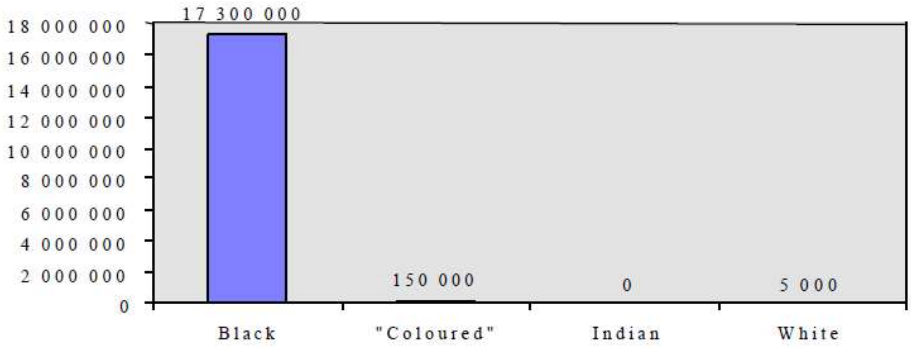

Figure 1.1: Population without piped water

(DWAF, 1994)

At the introduction of the apartheid regime in the middle of the 20th century, a large portion of water infrastructure was benefiting the white minority, while 75% of the country was left with little to benefit from. In fact, the lack of decent piped water distribution left 75% of the

population with no clean water supply. The political-economy policies enacted at the time had a devastating impact on the health of a large portion of the population as well as the environment (DWAF, 1994). As a result, 75% of the population resorted to alternative means of obtaining water free from biological contamination. One of the means was through pasteurization, which refers to boiling of water (Gadgil, 1998). Lack of clean water, poor sanitation and inadequate hygiene contributes to a large proportion of disease burden, including water borne diseases (WHO, 2019). Large scale water treatment was limited to a conventional municipal method which required piped water supply systems. Thus, 75% of the population could not access the municipal water infrastructure. Figure 1.2 shows piped water distribution in terms of the population percentage in SA at the beginning of a democratic dispensation.

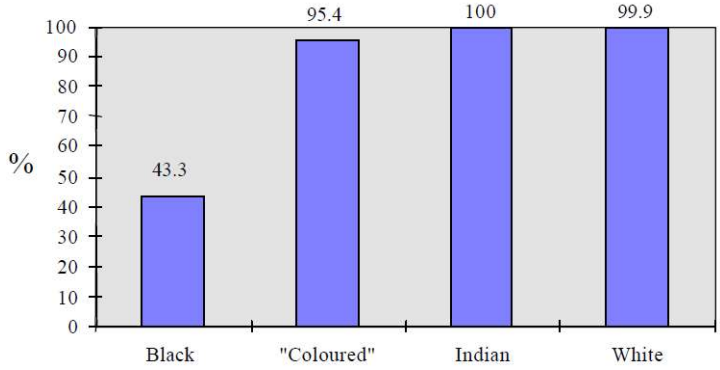

Figure 1.2: Piped water distribution

(DWAF, 1994)

In a new SA, post-1994, the country became a democratic state. However, the domestic water challenges emanate from the ineffectiveness in remedying water shortages and consultation from policy makers when water management policies are made (Kanjere et al., 2014). DWS (2018) reported that 14.1 million people are still exposed to sanitation facilities below the Reconstruction and Development Programme standard (RDP), and only 10.3 million households have access to a reliable water supply. In addition, an estimated 56% of wastewater treatment works (WWTW) and 44% of water treatment works (WTW) are in poor condition. Furthermore, the overall 11% of the WWTW and WTW are completely dysfunctional.

The democratic setting abolished and eliminated the segregation policies; 100% of the citizens were to be included in the water infrastructures. While this brought the promise of a better life to SA citizens, the government was faced with the monumental task of developing water infrastructure to cater to all its citizens. Putting such water infrastructure in place to eradicate the structural water scarcity is evidently a tedious process and has taken many years. By

2017, Black farmers had access to only 5% of water used in the agricultural sector (DWS, 2018). The challenges due to structural water scarcity have dragged on for many years and still exist in 21st century SA.

The national water supply is further compounded by a growing demand for water in the cities, farms and towns (Binns et al., 2001). For instance, Stats SA (2014) reported a total estimated population of about 54 million. Four years later, Stats SA (2018) reported a total estimated population of about 58 million. Despite a growing population, South Africa remains a water-stressed country. The growing population demands economic growth and increased water provision. Yet there will all be an increase in pollution of water resources (Mukheibir & Sparks, 2003).

Over and above the domestic water dilemmas in SA mentioned above, there are international challenges such as the Southern African Development Countries (SADC) region transboundary of water basins. SADC countries are grappling with their sovereignty as well as lack of cooperation concerning water resources as a strategic commodity (Redelinghuys & Pelser, 2013). SA shares four of its river systems with six neighbouring countries: Botswana, Mozambique, Swaziland, Zimbabwe, Lesotho and Namibia (DWA, 2012). Water resources cause conflicts in the SADC region if not managed well due to the nature of the transboundary of water basins. Some of the water sources amongst the Southern African countries originate from outside their borders (Matchaya et al., 2019). Water scarcity is evident as one looks at the few factors constituting the fact. At some point, Southern African countries must engage with their neighbours for cooperation in the matter of water sources. Figure 1.3, a Southern African map with annual rainfall in different regions, shows that a large portion of SA receives the least amount of rainfall relative to other SADC countries.

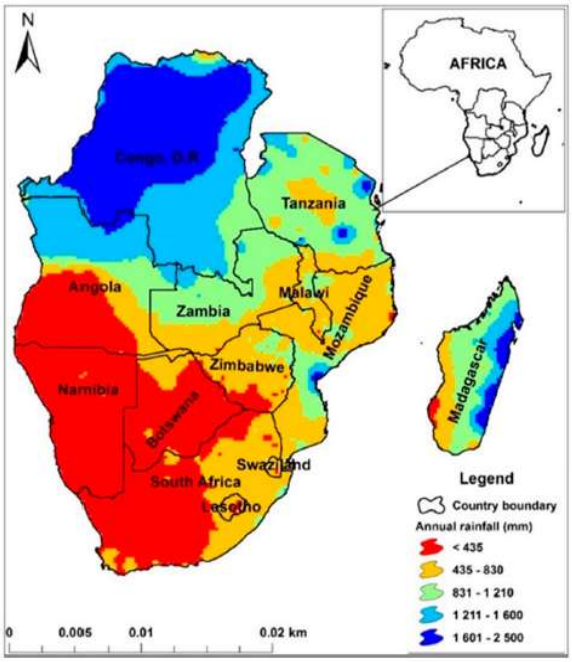

Figure 1.3: Southern African regional map with annual rainfall

(Matchaya et al., 2019)

1.1.2 Physical water scarcity

Physical water scarcity refers to the natural unavailability of water which depends on climatic conditions (Tapela, 2012). The problematic shortage of water in Southern African dams is explained as due largely to a climatic change (Lumsden et al., 2009). Rief and Alhabahi (2015) report that available fresh water constitutes about only 3 to 5% of world's water. The brackish water constitutes about 23% of world's water with the salinity range of approximately 5000 to 35000 ppm. The saline water is at 58% of world's water, with the salinity range of approximately 35000 to 45000 ppm. Wastewater and river constitute about 5 and 7% of the world's water.

Binns et al. (2001) report that SA is a semiarid country, with 70% of the country receiving less than 600 mm of rainfall per year. In summer, evaporation can be 2750 mm in west and northwest coasts and less than 1250 mm in the south and southeast coast. DWAF (1994) further reports that SA receives an average rainfall of 500 mm, 60% of the world's average. In summer, the evaporation is about 1100 mm in the east and 3000 mm which is above the annual rainfall. According to Bwapwa (2018), rainfall received by SA per annum is 450 mm while the global average per annum is at 860 mm. This low rainfall is apparent in figure 1.3. The low annual rainfall in the country could have devastating effects with respect to water shortages. However, SA is regarded as adhering to a high standard when it comes to managing water resources as compared to other countries. There may be some shortfalls but

as a developing country, it is rated well amongst the world's developed countries (Seago, 2016).

There is a current and projected water scarcity up to 2050 in the Eastern and Southern African regions. Water scarcity is projected to increase because of climate change, population growth and improved living standards (Meigh et al., 1999). Climate change as a natural phenomenon is projected to impact already vulnerable livestock and crop production, causing negative repercussions for food security, human health, water resources, forested areas, and tourism (Coetzee, 2011). The South African government regards climate change as a viable threat which, if not mitigated, will usher in unprecedented damage in the future (Department of Environmental Affairs, 2010; DWS, 2018). Figure 1.4 presents a low-level dam due to shortage of rainfall in the region. Low levels of water in dams lead to water restrictions on citizens by municipalities and cities (City of Cape Town, 2017).

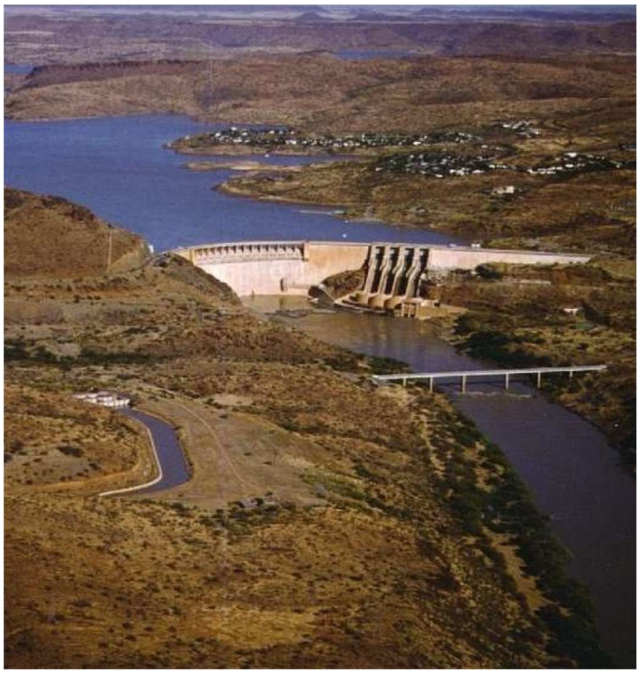

Figure 1.4: Low dam levels

(DWS, 2015)

In recent years, one of South Africa's provinces was severely devastated by water shortages due to drought. Baatjies (2014) explains that the drought, occurring from 2009 to 2011, forced SA's national government to intervene with efforts to remedy the water shortage situation. According to Schreiner et al. (2018), drought severely impacts both water quality and the economy. However, as the impact on water quality and the economy in the South African context is under-researched, definitive conclusions cannot be drawn. In addition to climate

change and the fact that South Africa is a semiarid country, there are other causes of water scarcity. According to Binns et al. (2001), alien plants which consume more water than indigenous plants cover 8% of South Africa's land and continue to invade the land to date. These alien plants cause a loss of about 3300 million m^3 of surface water per annum. And droughts and water scarcity are not only occurring in the southern African region, but regions such as the Middle East and North Africa (MENA) as well (Kamal, 2017).

1.1.3 Modern day freshwater provision

Every government has a responsibility to provide fresh water to its citizens where local municipalities are involved. Access to fresh water is a human right; everyone is entitled to water in SA and around the world (Bos et al., 2016). In a study by Swartz et al. (2006), a desalination guide for municipalities was provided. The guide discusses various aspects such as raw water sources, location of the municipality treatment plants relative to raw water sources, pre-treatment and post-treatment of water, the cost of using a particular technology and other related useful information. Consumers are supplied by their respective municipality which charges a tariff on water consumption (DWAF, 1999; DWAF, 2004), described a pricing strategy for individuals, households and industrial usage of water. The provision of fresh water requires, at the least, a monetary injection into the production of fresh water for direct and indirect costs. A detailed breakdown of water charges at municipal level was reported by (DWS, 2015). The costs of freshwater production are absorbed by households or the end user through water charges and tariffs.

Traditionally, desalination plants are powered by fossil-based fuels such as petrol, diesel or gas. The costs of running fossil-based fuel systems are adversely affected by increasing prizes. The prices of fuels can increase rapidly within a short space of time. For instance, the DoE (2019a; 2019b) announced the fuel price hike twice: the first hike was on 3 April and the second was on 1 May 2019. These fossil fuels also have adverse impact on the climate due to CO_2 emissions as well as global conflicts surrounding fossil energy sources. In addition, the desalination of water through fossil fuel is not sustainable nor economically feasible (Trieb & Müller-Steinhagen, 2008). In addition, building of water infrastructure, day-to-day operations and maintenance of the equipment is very expensive (Alkhadra et al., 2020). The study by Chinyama et al. (2016) determined that even pollution on the rivers and dams increases the cost of treating water due to the taste and odour present in the water. The day-to-day operations, the costs of fuels, chemicals, electricity, and other expenses are subsidised by national government through its annual budget allocation (Smith & Green, 2005). Thus, an individual or a household that cannot afford to pay water tariffs faces a structural water scarcity. However, the tariff system was not only implemented for financial incentives to the national government but also to curb wastage of potable water by the users (Malan, 1987).

People who reside in remote and rural areas suffer far worse due to the same structural water scarcity brought about the political-economy processes or lack thereof. Unfortunately, people are forced to look for alternative water sources as water infrastructure is not readily available. There are various sources of water such as bore holes, wells, ponds, rivers and oceans. However, the water in these sources is not fit for human consumption. Drinking water must be free from pathogenic organisms, be clear and not salty, taste and smell good and be absent of any harmful foreign material (Crouse,1986). There are several guidelines which govern the quality of water for domestic use in South African (DWAF, 1996).

1.1.4 Desalination methods

There are two basic technologies used in desalting saline water: thermal and membrane desalination (Eltawil et al., 2009). Thermal desalination involves a phase change process where liquid changes to vapour (evaporation) and back to liquid (condensation). The membrane method is a single-phase process, and the liquid does not change phases (Panchal & Patel, 2017). Historically, SA has not had large-scale thermal desalination plants. However, thermal desalination plants such as MSF and MED are widely used in other parts of the world (Goldie & Sanderson, 2004; Alkaisi et al., 2017). The desalination plants used by municipalities in SA are all reverse osmosis (RO), a membrane desalination method (Swartz et al., 2006). In fact, RO is a widely used desalination method globally compared to other method in the desalination of water (see Figure 1.5).

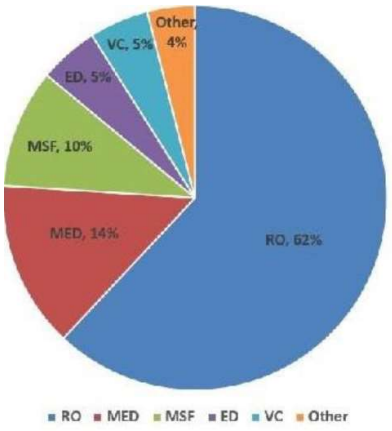

Figure 1.5: Various desalination technologies in use

(Alkaisi et al., 2017)

Rief and Alhalabi (2015) and Buros (2000) describe how the reverse osmosis system operates in desalinating contaminated water to produce the end-product of pure clean water. In addition, since desalination methods are energy intensive, there is a need to reduce energy consumption (Li, 2011). Figure 1.6 shows a schematic diagram of the RO system with its main components.

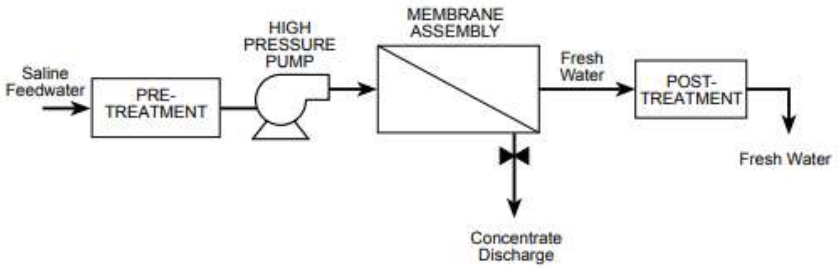

Figure 1.6: Reverse osmosis

(Buros, 2000)

There are several membrane desalination methods either being used or developed in conjunction with renewable energy. The electrodialysis (ED) method falls under membrane desalination. Figure 1.7 show the make-up of the electrodialysis system with its main components.

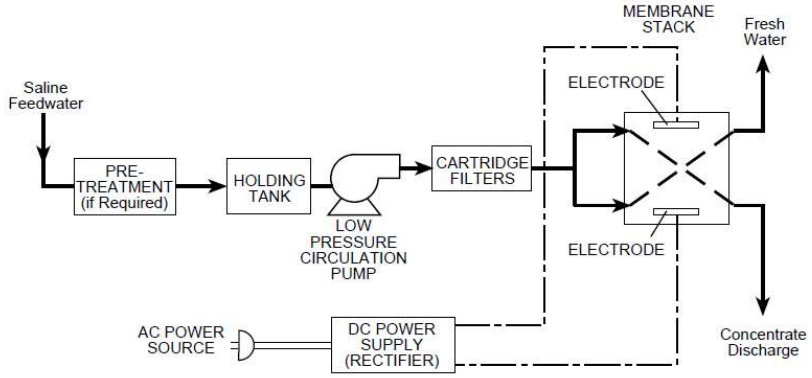

Figure 1.7: Electrodialysis plant

(Buros, 2000)

The distillation processes are MED and MSF which involve evaporation and condensation. Rief and Alhalabi (2015) describe how the MED desalinates brackish and saline water to produce the end-product of pure clean water which falls under thermal desalination. Pugsley et al. (2016) discuss desalination methods already mentioned in this study and others. Figure 1.8 presents a schematic diagram of the MED and its main components.

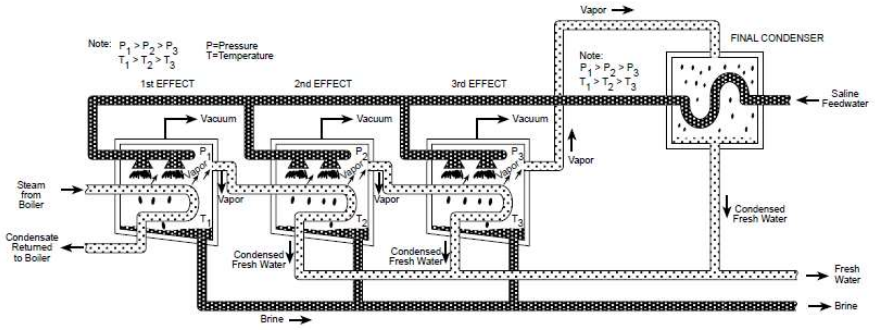

Figure 1.8: Multi-effect desalination plant

(Buros, 2000)

The MSF diagram, presented in Figure 1.9, is a phase changing process of desalination. The product water is also used to feed water for high pressure boilers (Khoshrou et al., 2017). The RO is the most used desalination method around the world, followed by the MSF (Shemer & Semiat, 2017). However, as seen in Figure 1.5, MED is the second most used after the RO.

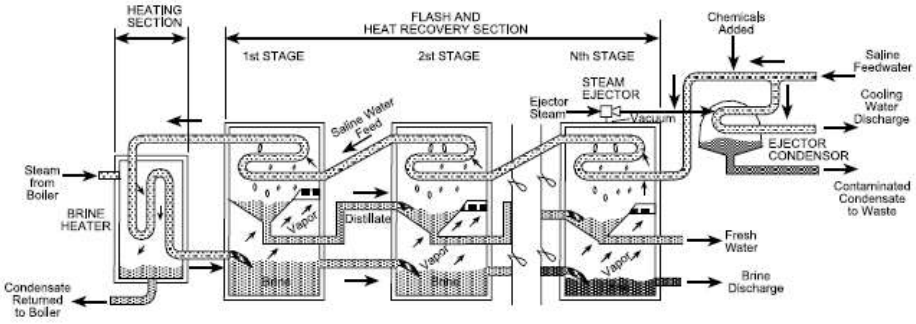

Figure 1.9: Multistage flash plant

(Buros, 2000)

The desalination plants, whether thermal or membrane based, used for the treatment of contaminated water discharge a highly salt-concentrated substance called “brine”; the brine is rejected by the surrounding environment. Research has been carried out to study the impact of brine, especially in the marine environment. The discharge of brine could cause changes in temperature, salinity levels and other non-organic materials in the marine environment (Roberts et al., 2010). However, the study by Shemer and Semiat (2017) refutes the assertion that brine discharged into the ocean has major impact on the environment. It was reported that the temperature and salinity variations were within a natural range despite the discharge.

The fossil-based fuel systems are inadequate, impractical in remote areas, expensive, unsustainable and have adverse effects to the environment. Accordingly, Bundschuh and Hoinkis (2012) contend that these economically exploited fossil-based fuels have become

increasingly limited because of natural limitations. Their use is questioned by large population groups, especially in industrialized countries, because of their adverse impact and their contribution to global climate change. It is, therefore, logical to consider an alternative technology for water provision to the general population. An alternative should be better than the fossil fuel systems. One alternative source that has increasingly been researched is RE sources.

1.1.5 Renewable energy (RE): an alternative to fossil fuels

Recent years have seen a surge in research studies seeking to complement and/or replace traditional fossil fuels with RE. SA has established RE focused institutions and incorporated RE into already existing institutions of higher learning (Osuri et al., 2015). Historically, SA had little contribution from renewable energy sources. The Department of Mineral and Energy (DME) (1998) reports that about 10% of primary energy in SA has been provided by renewable energy sources. The country had not invested in renewable energy at the time, however as the renewable energy policy was only drafted in 2003. This policy was designed to fast track the implementation of renewable energy (Aliyu et al., 2018). It was at the Johannesburg World Summit on Sustainable Development in 2002 when the declaration to promote renewable energy was made. Before then, SA's vast renewable energy sources remained largely untapped (DoE, 2003). SA, as with most other countries in the world, has taken a step towards implementing renewable energy technologies. This implementation comes as the country is attempting to reduce its carbon footprint and explore greener and cleaner energy options.

However, SA is still largely dependent on fossil fuels. Joubert et al. (2016) report on different types of fuels used for heating purposes in SA. Figure 1.10 shows the overall usage of different fuels in percentage terms in SA. Coal is largely used for industrial and commercial purposes: these sectors are energy intensive and thus, the demand is high. Based on this, the coal and renewable energy usage was at 65.7% and 7.6%, respectively, in 2010 (DoE, 2010). Years later, the coal and renewable energy usage shifted to 59% and 20%, respectively, in 2018 (DoE, 2018a). There has been a clear decline in coal usage and concomitant increase in RE usage. Despite the large use of coal and other fossil based-fuels, SA is leading SADC countries in terms of renewable energy technological advancements (Jadhav et al., 2017).

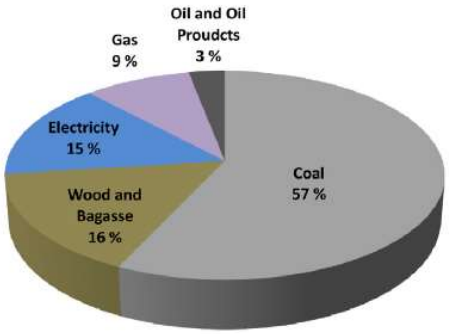

Figure 1.10: Energy used for heating in South Africa

(Joubert et al., 2016)

There has been a growing interest in recent years in utilising RE technologies on a range of systems. The DoE (2018b) reports that the world's renewable energy capacity has increased from 989 GW in 2007 to 2006 GW by 2016. Asia alone has increased its RE capacity to 812 GW by 2016 which accounts for approximately 41% of the world's total RE capacity. On the other hand, Africa installed only about 38 GW of RE capacity by the same year. The progress of the implementation of RE in African countries is very slow compared to Asia. Nevertheless, there are various RE sources available that can be used to drive desalination and other plants. These RE sources are geothermal, solar, wind, biomass and ocean energy (Garcia-Rodriguez, 2002; Abdelkareem et al., 2018).

The use of RE has become an attractive option to desalination systems, an attractiveness partly due to the availability of solar energy, wind and other energy sources in the regions that are grappling with water scarcity, typically arid areas. Coupling desalination technologies with RE has low operating and maintenance costs (Eltawil et al., 2009; Alkaisi et al., 2017).

A study by Fant et al. (2016) investigating the estimated future impact of the climate change on the renewable energy technologies in the SADC region determined that renewable energy technologies are largely influenced by variation of the surrounding climate and thus wind and solar energies would be greatly affected by a shifting climate.

The desalination systems discussed under 1.1.3 and many others have been studied with the aim of coupling these with RE sources. Some of these systems show a promising future, while some are still in a developmental phase. For example, ED is one of the plants that could be coupled with a photovoltaic (PV) panel as an energy source given its flexibility (Campione et al., 2018). Penate and Garcia-Rodriguez (2012), in a detailed review on the saline water reverse osmosis (SWRO), focused on RE as an energy source to power the system. The SWRO is usually based on coastal regions and wind energy is considered the most suitable as it is cost effective compared to the solar energy. Moreover, a small-to-medium scale system

is rapidly being developed using alternatives to fossil fuels. Studies partnering with RE-assisted technologies have been undertaken by various researchers (Chafidz et al., 2016; Alsehli et al., 2017; Al-Othman et al., 2019; Al-Karaghouli et al., 2009; Chandrashekara & Yadav, 2017; Ghaffour et al., 2014; Ghaffour et al., 2015; Hou et al., 2018; Yilmaz & Söylemez, 2012; Khayet, 2013).

But, for the purpose of this study, the focus is narrowed to an investigation of solar energy only as an energy source. Figure 1.11 shows an average annual horizontal global solar insolation (H) with the SI units of kWh/m^2. The typical annual global insolation shown is in the horizontal plane. It is evident from Figure 1.11 that the primarily arid areas which are reported to experience water shortages receive a much higher concentration of insolation. However, there are factors which should be considered such as relative humidity, wind speed, ambient temperature and height above sea level to estimate solar radiation that reaches the surface (Adeala et al., 2015).

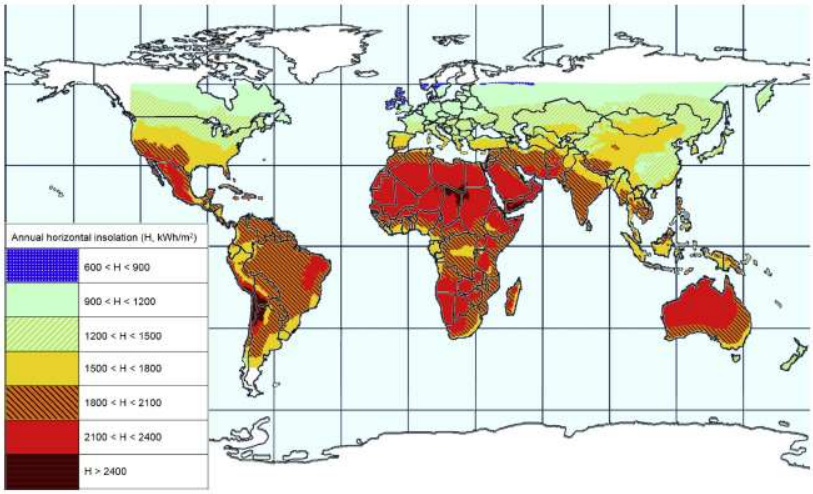

Figure 1.11: Annual cumulative global solar insolation on a horizontal plane

(Pugsley, 2016)

The Department of Mineral and Energy (2004) reported that SA receives 4.5-6.5 kWh/m^2 daily average of solar radiation compared to other countries such as United States of America which receives only 3.6 kWh/m^2. Furthermore, the annual solar irradiation in SA is around 2000 kWh/m^2 while that of central Europe is about 1200 kWh/m^2 (Joubert et al., 2016). Solar radiation differs depending on geographical location, as shown in Figure 1.12. Within the nine provinces of SA, for example, there is varying intensity of solar radiation (Adeala et al., 2015).

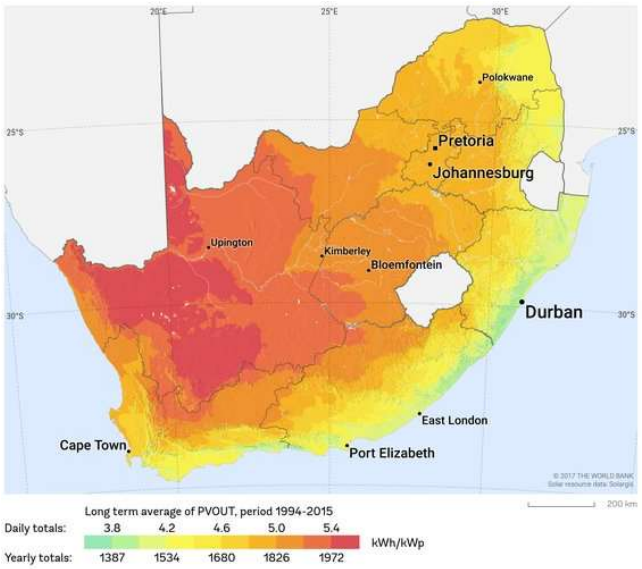

Figure 1.12: Daily and annual solar insolation in South Africa

(Solargis, 2015)

1.1.6 Solar stills

The focus is further narrowed to deal with small-scale solar stills with special attention on thermal desalination. Mkhize and Msomi (2020) conducted a feasibility study of a multistage and other solar stills in Southern Africa in terms on solar energy availability, finding that based on the solar radiation shown in Figure 1.12, the Southern African region could be an ideal location to study solar stills. Furthermore, Rajamanickam and Ragupathy (2012) explain that a solar still (water distiller) uses the process of evaporation and condensation to produce distilled water through solar thermal energy. During this process, impurities such as inorganic materials and chemicals are left behind in the pool of contaminated water in the basin. The study further suggests that distillation is one of the earliest forms of water purification for mankind. Solar thermal energy is used in many developed and developing technologies such as solar stills, solar drier, solar cookers, solar drier, solar conditioning, solar ponds, solar chimneys, solar architecture and solar power plants (Thirugnanasambandam et al., 2010). The use of solar energy on solar stills was recorded as far back as medieval periods to concentrate diluted alcohol solutions and the extraction of medical properties from herbs. The recorded desalination description dates back as far as 1500 BC. However, the first water desalination system was reported by Della Porta between 1535 and 1615 (Delyannis, 2003). A passive single-basin single-slope type is the most common design: it is simple and inexpensive to construct (Rajan & Kaushik, 2013). Solar stills, as an alternative means to produce fresh drinking water on a small scale, has been a welcome option for many decades. Besides the fact that solar stills do not require any fossil fuels to produce water, some are even transportable or can be erected anywhere (Arunkumar et al., 2012).

Furter (2004) explains that solar distilled water is chemically very pure as no chemical additives are present in the distilled water. It contains less than 10 mg/litre of the total dissolved solids (TDS). There have been many modifications made to improve the performance of solar still over the years. These include linking the desalination process with the solar energy collectors, incorporating several effects to recover the latent heat of condensation, improving the configurations and flow patterns to increase the heat transfer rate, and using low-cost material in construction to reduce costs (Bundschuh & Hoinkis, 2012). However, renewable technologies as discussed earlier are strongly dependent on the surrounding climate. The fluctuation and seasonal variation of the weather patterns result in intermittent energy and freshwater output from renewable energy sources (Asmus, 2005; Fant et al., 2016). The development and improvements of solar stills are discussed in detail in Chapter 2.

1.2 Problem statement

The shortage of potable water remains the growing concern worldwide. This then suggests that the long-lasting solution needs to be determined before all the current resources become completely dry. There are various systems that have been developed that are looking at purifying seawater since this kind of water is available in abundance. The majorly reviewed systems are pressure-based and thermal-based desalination systems. However, thermal-based desalination systems are known to have high capital costs while the pressure based are known with high maintenance costs. The current study is looking at developing low-cost multistage solar desalination system that will be fully dependable to solar for its operation. The configuration of the system is derived from the existing systems, but the working principle will be completely new. The system will be tested under Cape Town (South Africa) environmental conditions.

1.3 Background to the research problem

Multistage solar still desalination systems have been in existence for a while. However, the existing systems experience various challenges for them to operate optimally. The different kinds of challenges that the systems are facing are discussed below.

1.3.1 Stage dependencies

Figure 1.13 shows a cut-away view of a typical multistage solar still. Schwarzer et al. (2001) reports that thermal energy is supplied to a multistage solar still through the first stage of the condensing tower. When the saline water in the first stage is heated, it exchanges its heat with the second stage through evaporation, convection, and radiation. The exchange of heat with the upper stages (stage 3, stage 4, etc.) occurs as described above. The stages in the setting

described above are dependent in the sense that the heat is first transferred to stage 1 (the entry stage of the system) only. When the saline water is sufficiently heated, it gives off the vapour (vapour generated in stage 1). The vapour rises and condenses at the bottom of the condensing tray and thus gives off its latent heat to stage 2. The saline water in stage 2 is gradually heated until it vaporises (vapour generated in stage 2) as well, giving off its latent heat of evaporation to stage 3. Heat transfer continues to the rest of the upper stages in the system. In other words, stage 2 cannot produce the distillate without stage 1; stage 3 cannot produce any distillate without stage 1 and 2, and so on.

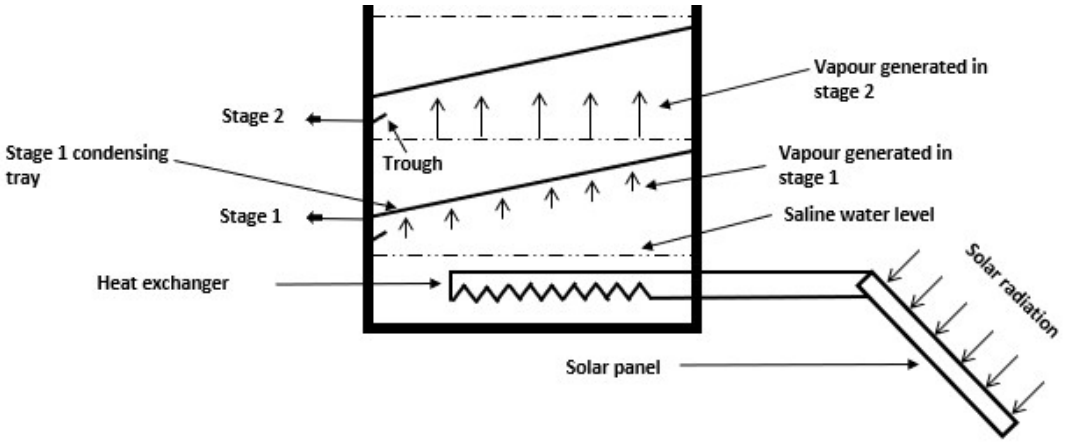

Figure 1.13: Stages of a multistage system with waterbed

1.3.2 Lack/loss of production in the upper stages

The problem in the setting discussed above (stage dependencies) is that a loss of thermal energy (i.e., vapour leaks) in any of the lower or intermediate stages (stage 1, stage 2, stage 3 or stage 4) will deem the upper stages unproductive. The loss/insufficient supply of thermal energy to the upper stages may also occur due to salt deposits accumulating on any of the stage trays, especially lower and intermediate stages. Since the stages are dependent, they are likely to follow the distillate production pattern of the lower stages. In essence, the productivity of the stages above is most likely to remain lower than that of the lower stages at all times.

1.3.3 Occasional cleaning of the stage and the stage trays

Soni et al. (2017), Schwarzer et al. (2009) and Chen et al. (2017) contend that the stage trays of a multistage solar still system must be cleaned regularly over a period of time due to salt deposits left on the tray surface. The stage trays continuously come into contact with the saline water during operation. The cleaning process involves removing, cleaning and replacing the stage trays. The air and vapour tightness in a solar still are of utmost importance for the enhanced productivity of the still (Ibrahim & Elshamarka, 2015; Rajamanickam & Ragupathy,

2012; Sharshir et al., 2016a). The cleaning process may have some effect on the vapour tightness and the structural integrity of the system. During the cleaning process, the stages must be opened, cleaned and re-sealed to ensure vapour tightness. In addition, salt deposit accumulating on the surface (fouling) of a stage tray may affect the heat transfer ability of a stage material over time. A multistage solar still system with saline water in contact with the majority of the system's components increases the maintenance work on the whole system.

1.3.4 Electrically assisted multistage solar still systems

To maximise the distillate yield from a multistage solar still, researchers have coupled a multistage solar still with vacuum pumps and water circulating pumps. These pumps require electricity to operate efficiently. The disadvantage of these systems, however, is that they require more equipment to operate compared to a standalone solar still (Schwarzer et al., 2009). Due to additional equipment, its weight and floor space requirements may be increased. Additional equipment would make the whole system expensive, unattractive and cumbersome to operate; service will require skilled personnel to conduct it (El-Baily et al., 2016). Furthermore, since solar stills came as an alternative to traditional desalination, they are most likely to operate as decentralised and in a rural and isolated environment when commercialized. The end users in a rural setting may be technically unskilled people with regards to such machinery. A multistage solar still coupled with additional equipment were reported by Reddy et al. (2012), Feilizadeh et al. (2015), Shatat and Mahkamov (2010) and Estahbanati et al. (2015).

1.3.5 Remote feeding of saline water and pre-heating the saline water in the system

In a solar still, the saline waterbed diminishes as the evaporation takes place in the basin (Taghvaei et al., 2015). The saline water must therefore be replenished in a controlled manner to maintain the level required in the still's basin. Rajaseenivasan et al. (2014) explain that the process of evaporation-condensation diminishes the saline water level in the basin. The pre-heated saline water is supplied to the basin by manually operating valves connected to the storage tank. The reduction in saline water depth causes a dry spot in the basin and these dry spots impact negatively on the performance of a solar still as no evaporation takes place. The refilling of saline water, therefore, requires constant human intervention to maintain the saline water level. However, there is an alternative method that can be used to remotely regulate the saline water in the basin (Badran & Al-Tahaineh, 2005). Furthermore, saline water in the basin level can also be maintained by through a float mechanism (Kabeel et al., 2019). Since multistage solar stills (MSS-SS) are more complex than simple solar stills, an equally complexed but compact refilling system is required.

1.3.6 Disposal of brine solution

According to the studies by Franco and Saravia (1994) and Reddy et al. (2012), the brine is disposed of into the brine tank. In some of the solar stills reported, the brine is reused so that the thermal energy is extracted from it. The extracted thermal energy is then used to pre-heat the incoming saline water. The brine is a hot liquid left after evaporation has taken place. The pre-heated saline water (not at room temperature) requires less energy to heat and vaporise it.

1.3.7 Minimal saline water in the entry stage

It is agreed by various researchers that a solar still is more productive when the saline water in the stage, or basin, is at its lowest (El-Sebaii, 2011; Morad et al., 2015; Prakash & Velmurugan, 2015; Kabeel et al., 2018). This assertion supports the fact that it requires more thermal energy to heat a large body of water and less thermal energy to heat a smaller amount of water. Multistage solar stills such as discovered in the literature (Feilizadeh, et al., 2015; Soni et al., 2017; Adhikari et al., 1995; Schwarzer et al., 2009) demonstrate that the entry stage of the system consists of a stagnant pool of saline water. It has been experimentally shown that lower levels of saline water contribute to enhanced distillate production. Therefore, rapid evaporation can be achieved by heating small quantities of saline water compared to larger amounts. However, lower levels of saline water have low thermal storage capacities while higher depths have higher storage capacities (Abujazar et al., 2016; Morad et al., 2015).

1.3.8 Saline water circulation in the entry stage

In addition to the amount of saline water in the entry stage, the circulation instead of stagnant saline water could be beneficial in an entry stage. Çengel (2003) suggests that under the convective mode of heat transfer, the faster the fluid motion, the greater the heat transfer. In addition, the convective heat transfer is proportional to the temperature difference. Therefore, a thin layer of a fluid dissipates heat much rapidly than a pool of stagnant water. Several researchers (Soni et al., 2017; Manokar et al. 2018; Reddy et al., 2012) have reported the flowing waterbed in the stages or basin. However, no researcher has reported a flowing waterbed in the entry stage of a multistage solar still.

1.3.9 Direct heating of the saline water in the solar collector

Various researchers have determined the use of heat transfer fluid (HTF) or desalinated water to supply heat to the entry stage through a heat exchanger of a multistage solar still (Soni et al., 2017; Feilizadeh, et al., 2015; Schwarzer et al., 2009; Adhikari et al., 1995). Schwarzer et al. (2009) contends that desalinated water is used in the heat exchanger to avoid corrosion in the collector. Fouling is caused by a direct contact with saline water in a solar still. Therefore, when the HTF is used in a heat exchanger, fouling will occur in the entry stage on the heat

exchanger. However, when direct heating is used, fouling will occur in the solar collector manifold outside the condensing tower.

1.4 Aims and objectives

The focus of the present study intends to develop the design of a vapour-based multistage solar still desalination system. This aim will be achieved through the following objectives:

- Develop an alternative vapour-based multistage solar still with independent stages
- Study the effect of independent stages in a vapour-based multistage solar still
- Observation for any signs of contamination as a result of fouling on the inner surfaces of the condensing tower
- Minimise human intervention for feeding the saline water to the solar still through self-regulating principle
- Re-circulate brine solution in the condensing tower instead of disposing of it
- Minimise the quantity of saline water heated by the solar collector at any time during operation of the solar still.
- Maximise heat exchanging process between solar collector and saline water by direct heating.

1.5 Design overview

The current study consisted of three main components: the design, construction and experimental tests components. The three components constituted a quantitative based study on a vapour-based multistage solar still desalination system. The multistage system consisted of six stacked stages of which the topmost stage was passive type solar still. Five of the six stages were supplied by the evaporator with the vapour. The passive basin still was not supplied by the evaporator with the vapour. The passive basin still had two main functions in the system. It was producing its own distillate independently and acting as a primary storage tank for saline water. While storing the saline water, the direct solar radiation was pre-heating it. The multistage was a standalone system with only solar radiation as its pre-requisite for operation. The thermal energy was generated and supplied by two series connected evacuated tube solar collectors (ETSCs). The circulation of saline water in the system was made possible by a non-return valve which created an ‘impulse flow’. The construction of the multistage was undertaken in a Mechanical Engineering workshop at Cape Peninsula University of Technology, Bellville campus. The experimental tests were conducted on the rooftop of the same campus. During experimental tests, distillate yield from the stages was

collected and measured separately. The system was made primarily from aluminium sheet metal and copper tubes of different diameters, each for a specific purpose.

1.6 Thesis overview

Chapter 1 – Introduction

This chapter presents the problem statement, background, objectives, design overview and thesis overview in the sequence listed.

Chapter 2 – Literature Review

This chapter acknowledges all related literature consulted, and proceeds to lay out the findings on a basin type solar still and a multistage unit. Factors which contribute to the system's efficiency and productivity are discussed. Furthermore, the final section of the chapter presents the adverse factors which affect the solar stills.

Chapter 3 – Design and Construction

This chapter describes the major components of the system, defining them in terms of their designs, construction, and functions. Lastly, it demonstrates how numerical results obtained through mathematical procedures were arrived at.

Chapter 4 – Experimental Performances

This chapter explains the instruments used in testing the system during operations. It also details how the tests were performed under given conditions by means of providing test data related to its performance.

Chapter 5 – Results and Discussions

This chapter presents the experimental results, followed by a discussion based on the results obtained during the tests.

Chapter 6 – Conclusions and Recommendations

This chapter offers conclusions from the results obtained in the study. It then recommends some improvements and approaches to enhance the yield of the distillate.

CHAPTER TWO

LITERATURE REVIEW

This chapter discusses different meteorological conditions which largely influence the performance of a solar still. It then addresses various types of solar stills in existence and discusses some of these solar stills in detail. Moreover, it thereafter details several of the major components and parameters under which solar stills are generally operating. It also presents some additional techniques to enhance the performance of the solar still. Subsequently, it discusses different types of solar collector with the main focus on the flat plate solar collector (FPSC) and the evacuated tube solar collector (ETSC). Multistage solar stills are discussed in detail with a focus on their mode of operation, their challenges and the trends reported in surveyed literature. Few useful methods or technique reported to ease the operation of a solar still are also briefly discussed. A brief explanation of some cost analysis parameters as well as the tabulated cost per litre (CPL) data of distillate produce is provided. Finally, the entire contents of the chapter are summarised.

2.1 Meteorological influence on the performance of a solar still

There are various factors that must be considered for optimum performance of a solar still. These various factors affect the performance of a solar still and are categorically described as climatic, design and operating conditions (Muftah et al., 2014; Lal et al., 2017; Selvaraj & Natarajan, 2018; Abujazar et al., 2016; Sivakumar & Sundaram, 2013). However, Jamil and Akhtar (2017) and Sampathkumar et al. (2010) insist that **m**eteorological conditions cannot be controlled, therefore, the performance of a solar still can be enhanced by the optimisation of the other two conditions, namely, design and operating conditions. Climatic, design and operating conditions include parameters such as saline water depth in the basin, level of salinity in the feed water, feed water inlet temperature, condensing cover angle, its thickness and the material from which it is made, thickness and type of insulating material, wind velocity, solar radiation intensity, location of experimental tests, orientation of the still and painted basin walls (Kabeel & El-Agouz, 2011). Climatic conditions are discussed below. Design and operating conditions are discussed later in the chapter.

2.1.1 Solar radiation

Solar radiation intensity depends on the latitude of the local area from which the still is operated (Sivakumar & Sundaram, 2013). Furthermore, Muftah et al. (2018) define solar radiation by geography, meaning that in addition to latitude, geographical location is also an important factor. The amount of solar radiation received by the solar still falls in the category of ambient conditions, with solar radiation among other factors playing an important role in the

production of the distillate in a solar still. Nafey et al. (2000) report that solar radiation has a pivotal role in the productivity of a solar still. Empirical results show that the effect of the solar radiation on the solar still can greatly improve or adversely affect its efficiency and productivity. Due to weather patterns, solar radiation received by a solar still is intermittent and varies based on time of day, time of year and latitude of the location of the solar still (Mowla & Karimi, 1995). Solar intensity differs, either between the daytime (sunshine hours) and night-time (off-sunshine hours) or from one area to the other, or even in different seasons (Sivakumar & Sundaram, 2013). Solar radiation intermittency leads to an instantaneous distillate yield fluctuation from a solar still (Kamal,1988). Distillate production is dependent on seasonal changes and thus the distillate yield varies according to prevailing time of the day or season of the year. Ambient temperature, solar irradiation, sunshine hours, solar declination, angle of incidence and wind velocity are all responsible for the fluctuation of the distillate output (Kumar & Dwivedi, 2015). The behaviour of solar radiation on a solar still is such that not all radiation received by the solar still is absorbed and utilised entirely. Part of it is absorbed by the condensing cover, with only a fraction transmitted through the condensing cover. Furthermore, only some of the fraction of solar irradiance transmitted reaches the saline water in the basin while the remainder is absorbed, transmitted or reflected by the basin walls. The solar radiation transmitted through the condensing cover is less than that intercepted by the condensing cover. The magnitude of the transmitted radiation depends on the surface orientation, surface inclination and latitude angle (Altarawneh et al., 2017). According to Iqbal (1983), the solar altitude angle is the angular height of the sun above the observer's celestial horizon. The solar altitude angle ranges from 0 to 90°. In simple terms, the angle of the sun relative to the horizon decreases in winter months. Hence, the optimum condensing glass tilt angle is greater in winter and smaller in summer (Tiwari & Tiwari, 2007).

2.1.2 Air and wind velocity

Controlled air at room temperature blowing over the surface of heated water increases evaporation rate of water. The air increases humidity as it picks up the airborne water-vapour particles at saline water interface in the basin (Al-Shammiri, 2002). The wind blowing over a heated surface of saline water has some effect on the evaporation rate of saline water even if not in direct contact with the hot saline water. Sharshir et al. (2016a) have determined that higher wind velocity causes high convective heat transfer from the glass to the atmosphere. High wind velocities reduce the condensing glass temperature which further increases the temperature difference between the condensing cover and the saline water in the basin. This increases the evaporation rate which in turn increases distillate production in the solar still. The temperature difference of the evaporating saline water surface and the condensing surface is a driving force in the production of the distillate. Lal et al. (2017) further contend that

the blowing wind or increased wind velocity carries away heat from the hot outer surface of the condensing cover, thereby cooling the cover rapidly. However, according to the study by El-Sebaii (2011), where the determination of the effect of wind speed on a passive type solar still was conducted, there is a contradiction about the effect of the wind. Others suggest that the upper surface of the glass cover should be used to determine the effect of wind speed. Furthermore, there is a critical saline water depth where the daily productivity and evaporation increases with an increase in wind velocity. The increase in daily productivity and evaporation with the increase in wind velocity occurs when the temperature of the inner surface is equal to the outer surface. When saline water depth in the basin is lower than a critical saline water depth, daily productivity decreases with increase in wind velocity. Zurigat and Abu-Arabi (2004), in a study on modelling and performance analysis of a regenerative desalination unit, found that wind speed has a huge impact on the productivity of the still. A 50% increase in productivity with an increase in wind velocity from 0-10 m/s was discovered. Nafey et al. (2000) report that for a wind speed variation from 1-9 m/s, the productivity of a solar still decreases by 13%. Al-Hinai et al. (2002a) report that increasing the ambient temperature and the wind speed increases the distillate yield of a solar still. Moreover, increasing the wind velocity has a significant effect on the distillate compared to increasing the ambient temperature. Increasing the ambient temperature by 10°C enhances distillate yield by 8.2% but increasing the wind velocity slightly from 1-3 m/s, increases the distillate yield by 8%. However, studies by Zurigat and Abu-Arabi (2004), Nafey et al. (2000) and Al-Hinai et al. (2002b) did not specifically report any details pertaining to the critical saline water depth in the basin of a solar still.

2.1.3 Salinity level in saline water

The salinity level in the saline or brackish water has a similar effect on both the passive and active solar still. Morad et al. (2017) reported results from testing three different feed waters with different salinities: ground water (GW) had the least amount of salt content; Mediterranean saline water (MSW) had a fair amount of salt content; and red saline water (RSW) had the highest salt content. Table 2.1 shows the distillate yield as a result of an experimental study on three different feed waters with varying salt contents.

Table 2.1. Distillate yield from three different feed waters

Description	DYGW (L/day)	DYMS (L/day)	DYRS (L/day)	Author(s)
DSS	10.94	10.16	9.04	Morad et al. (2017)
OSS	5.54	5.07	4.45	

DSS-developed solar still, OSS-ordinary solar still, DYGW-distillate yield from ground water, DYMS-distillate yield from Mediterranean Sea water, DYRS-distillate yield from Red Sea water

Abdenacer and Nafila (2007) acknowledge that the salt content in the saline water is about 35 grams per litre (g/l) while that of the brackish water with high concentration is 10 g/l and beyond. The saltier the water, the more thermal energy required to heat and evaporate that water. Salt content influences the changing of the boiling point of water: high salt content increases the boiling point of water. According to Al-Shammiri (2002), increasing the salinity in the saline water increases the boiling point of water. In addition, the evaporation rate of water with salinity level of 26 ppm varies from 2000 to 6000 g/h m^2, while that of water with a salinity level of 68 720 ppm varies from 500 to 1700 g/h m^2. In both conditions above, a constant air velocity, directly in contact with the saline water, was maintained blowing over the water surfaces.

2.2 **Different types of solar stills**

The basic operating principle of a solar is as follows: the sun rays in the form of solar radiation are transmitted through the condensing cover of the solar still. Some of the solar irradiance fraction is absorbed by glass cover, saline water in the basin and basin liner and some is reflected to the basin walls. The thermal energy from the saline water in the basin is transmitted to the glass cover by convection, radiation and evaporation. This heat is then transferred through the glass cover thickness and is carried away by convection to the atmosphere. The water-vapour droplets form on the underside of the condensing cover and are collected as fresh water (Kabeel et al., 2019; Hamadou & Abdellatif, 2014). However, Sampathkumar et al. (2010) explains that as the above basic operation principle applies to passive solar stills, this operating process is a drawback for passive solar stills. An improved method involving the integration of an external heat source is introduced to a passive still which then activates it. The external source (solar collector) provides extra thermal energy in addition to direct saline water heating by solar radiation in the basin.

Desalination through solar stills have generally and largely remained experimental globally. There is no large-scale solar desalination plant in use; they are typically used as small-scale distillation plants for households in few countries around the world (Goldie & Sanderson, 2004). Solar stills, whether active or passive, are completely dependent on the availability of solar radiation and thus their output fluctuates based on the weather conditions prevailing on a particular region (Al-Tabbakhand & Mohammed, 2017). There are many different types of small-scale solar stills in existence today: cone, CPC-TSS pyramid, pit, double-basin double-sloped basin type, portable single basin, demo, regenerative active solar still, corrugated, wick, inclined basin solar still, vertical solar still and triangular solar still. While they have differing designs, shapes and appearances, they have a singular purpose of producing fresh water from saline water, brackish water or wastewater through solar energy. Solar stills are classified

into two categories: passive and active solar stills (Reddy et al., 2012). In a passive solar still, also known as a conventional still (CSS), saline water in the basin is heated directly by sun rays. But passive solar stills have been proven to be less productive than active stills. For instance, a passive pyramid solar still is less productive than a similar solar still which has been modified into an active solar (Kabeel et al., 2017c).

Fath (1998) finds that the efficiency and productivity of a single effect solar still can be increased using passive and/or active methods. Heat transfer processes on solar stills are modelled as transient due to the intermittent nature of solar radiation. The heat flux and temperature of the solar irradiance fluctuate throughout the day. The transient heat transfer processes are difficult to analyse as the heat flux and temperature changes with time. However, transient heat transfer processes are modelled with a presumption of some steady conditions. To the contrary, the steady state heat transfer process assumes that the heat flux and temperature do not change with time. The steady heat transfer process is much easier to model compared to the transient heat transfer process. Furthermore, there are internal and external heat transfer processes in a solar still. The internal heat transfer consists of three modes of heat transfer: convection, radiation, and evaporative processes. The external heat transfer process consists of three heat transfer processes as well: convection, conduction and radiation heat transfer processes. The evaporative heat transfer occurs at the saline water interface where the vapour pressure is lower than the saturation pressure of water (Elango et al., 2015).

An elaborate discussion on the general convection, radiation and conduction heat transfer processes is reported by Çengel (2003). The internal heat transfer is the evaporation that occurs at the interface of saline water which causes the vapour to rise to the condensing cover inner surface. The pure water-vapour leaves the impurities in the pool of saline water. The external heat transfer occurs at the condensing cover due to the temperature difference between the cover and the atmosphere. These phenomena cause the vapour to condense and thus, pure water is formed in droplets (Kumar & Dwivedi, 2015).

Thermal efficiency and productivity of a solar still are dependent on its ability to capture and retain the heat to produce distilled water. There is an effective surface area in the basin of a solar still which contributes to the distillate yield of the solar still. This effective surface area is defined as the area that receives direct solar radiation. The side walls of the still, depending on the position of the sun in the sky, cast a shadow on the base of a solar still, thereby diminishing the effective surface area. The effects of the shadow are more significant at low solar altitudes during winter. However, these effects become insignificant at solar noon,

especially during summer periods. The effective surface area is dynamic and changes with the change in time as the sun moves daily from sunrise to sunset (Altarawneh et al., 2017).

In an active solar still, the saline water is heated both directly by the sun and indirectly by the solar collector (Kumar & Tiwari, 2009). The use of solar heater, solar concentrator or a waste heat recovery system and other means to supply electrical or thermal energy, qualifies the still as an active solar still (Fath, 1998). Solar stills, coupled with solar collectors (active), are further classified into two categories: natural mode and forced mode (Singh et al., 2013; Kumar et al., 2014). Moreover, solar stills are either operating under static or dynamic mode depending on the nature of saline water in the basin or stage (Salem, 2013). Figure 2.1 shows a passive and active solar still hierarchy diagram. Generally, active solar stills are more complex than passive solar stills.

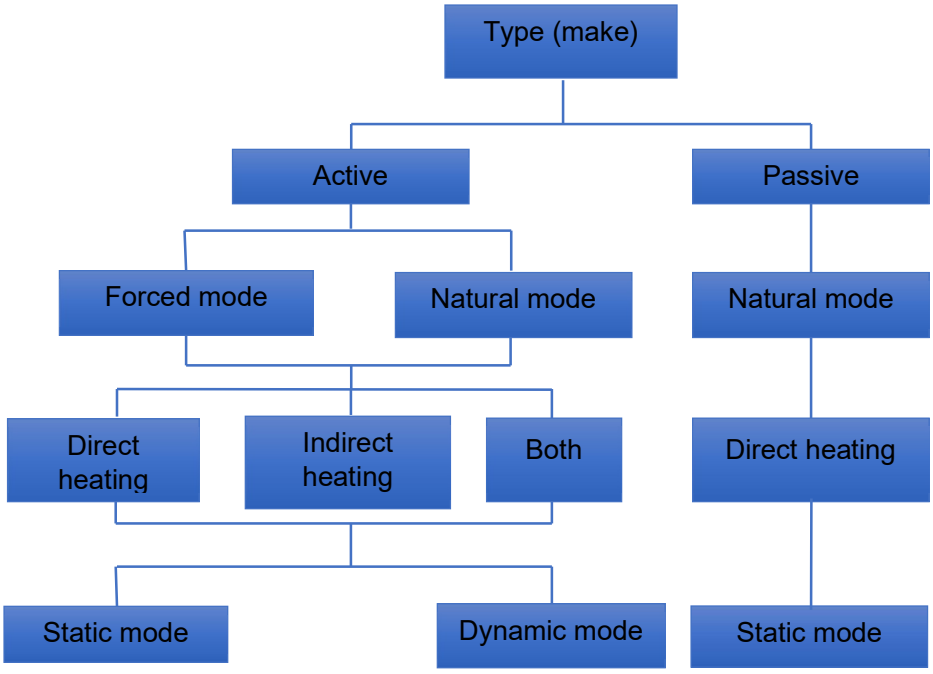

Figure 2.1: Passive and active solar stills

(Reddy et al., 2021; Badenhorst, 2018; Hartwig, 2013)

Solar stills, whether passive or active, are driven and guided by certain surrounding climatic conditions of the local area. Under actual weather conditions, a solar still follow the wind, radiation intensity, relative humidity and ambient temperature patterns of the local conditions (Hamadou & Abdellatif, 2014). These climatic conditions determine the daily productivity and how soon or later the steady state is reached. The daily productivity and efficiency of a solar still is dependent on the sun intensity, orientation of the still, wind, ambient temperature, condensing cover material and its thickness, temperature difference between saline water and

condensing cover, saline water temperature, saline water depth, insulation on the still, internal lining of the basin and sealing efficiency of the still (Van Steenderen, 1977). No one variable such as wind, solar radiation or ambient air temperature can correct the operation of the still. In other words, to optimise the operation of the solar still, various pertinent parameters must be considered. Solar still operation is further complicated by the fact that external factors largely influence its performance, or simply put, it is not independent from external influences. Therefore, in a bid to resolve the issue of low efficiency and productivity on solar stills, various researchers have sought ways to improve the distillate yield from solar stills by designing many different shapes, sizes, effects, configurations and flow patterns.

Fath et al. (2003), in a comparative analytical study on a pyramid and single slope single basin solar still, simulated the meteorological conditions of Aswan City, Egypt. Both stills had an effective basin surface area of 1.5274 m^2. The daily average solar incident absorption of the pyramid shape still was reported as higher than that of the single basin still. However, its daily average solar radiation losses were 1% higher than the single basin still. The ratio of solar radiation losses to the incident ration were the same for both stills. The daily yield of the single slope still was reported as higher both in winter and summer by 30% and 3%, respectively. In addition, the distillate yield trend followed that of the solar radiation which is higher in summer and lower in winter. Both stills' annual average daily distillate yields were similar at 2.6 litre/m^2/day.

The are many types of configurations applied to small-scale desalination systems. In addition to those discussed above, the highlights and some important discoveries of the configurations are presented below. Sharshir et al. (2016b) conducted a study on the hybrid desalination system using humidification-dehumidification and solar stills integrated with evacuated solar water heater. Four different solar still systems were studied, namely single solar still (SSS), four solar stills (FSS), humidification-dehumidification (HDH) and a hybrid (HDH-FSS). A cumulative daily yield from the four systems was reported at 10.5, 42, 24.3 and 66.3 kg/day for SSS, FSS, HDH and HDH-FSS, respectively. Liu et al. (2014a) conducted a novel integrated solar desalination system with multistage evaporation/heat recovery processes, finding that the system was able to recover almost all the latent heat of the vapour (steam) and reuse it to evaporate saline water in the system. Furthermore, a compound parabolic concentrator (CPC) used to collect solar irradiance was able to collect solar irradiance for a longer period during the day without tracking the sun (stationary collector). It was also reported that due to the heat recovery process, the system was able to reach an efficiency of 80% and 90% on cloudy and sunny days, respectively.

Monowe et al. (2011), conducting a study of a portable single-basin solar still with an external reflecting booster and an outside condenser, determined that the size of the external condenser should be at least 20 times larger than the daily productivity. This size was as a result of uncondensed vapour as it travelled through the saline water in a downward direction in the condenser (vertical condenser). The saline water temperature at the top of the condenser increased drastically such that the evaporative surface (saline water in the basin) and condenser temperature were 60°C and 54°C, respectively, at around 2 pm. However, the saline water at the bottom of the condenser was reported at 18.2°C around the same time. Furthermore, when the system was experimentally tested without a fan and a booster, the cumulative daily distillate yield was 3.5 litres with a solar still efficiency of 30%. The system was reported to produce up to 8 litres/day of freshwater when the fan and booster were turned on and working. The efficiency was reported at 68% when the fan and booster were operational. Lastly, the system was able to produce an additional 1 litre of saline water when operating after off-sunshine hours.

Ahsan et al. (2014), in a study on a triangular solar still using cheap and locally available and eco-friendly materials, found that the productivity of the solar still was highest at minimum saline water depth. The solar still productivity was almost proportional to the solar intensity on the day. Hence, it was recommended that an ideal period for saline water desalination using the triangular solar still was in summer. The highest distillate reported was 1.6 kg/m^2/day at 1.5 cm of saline water depth. Muftah et al. (2018) reported the results of an unmodified and modified stepped solar still. Internal and external reflectors, external condenser and fins enhanced the performance of the modified solar still; determining that daily yield of the modified and unmodified solar stills was 8.9 and 6.9 kg/m^2/day, respectively. The modified solar still was 29% higher than the unmodified stepped solar still. The cumulative daily efficiency of the modified and unmodified solar stills was reported to be 60.2 and 52.3%, respectively. Prakash and Velmurugan (2015) conducted a review study of different parameter influencing the productivity of solar stills. Various solar stills were discussed, including some covered in the above discussion. There are additional types of solar still, methods used and energy sources for the enhancement of solar still productivity (Sampathkumar et al., 2010; Yadav & Sudhakar, 2015).

2.3 Solar still make-up

2.1.1 Condensing cover

Solar stills, like any other equipment, are designed to be highly efficient and productive. One factor that contributes to their high productivity is the condensing glass cover (Sivakumar &

Sundaram, 2013). The condensing glass cover should meet certain criteria before being used on a solar still. Raj and Manokar (2017) explain that the criteria or specifications of the condensing glass cover are minimum heat absorbing abilities, minimum reflectivity of solar radiation, maximum transmittance of solar radiation, and high thermal resistance for heat loss from the basin to the ambient air. According to Mahian et al. (2017), for maximum solar radiation flux, the condensing cover tilt angle must be equal to that of the local area. In addition, Jamil and Akhtar (2017) suggest that the cover material influences the heat transfer rate inside a solar still. Moreover, Gnanaraj et al. (2017) report that the larger temperature difference between saline water in the basin and the glass temperature is primarily responsible for distillate yield in the solar still. The saline water in the basin and the inner glass temperature gradually increases from the morning, reaching a peak in late afternoon. The difference in temperature gap widens from morning and reaches its maximum later in the day. The gap then narrows as the solar radiation intensity fades away into the night. These behavioural patterns are not limited to a conventional solar still as a modified solar still behaves similarly. A condensing cover of a solar still condenses the vapour to produce the distillate. Sharshir et al. (2016a) and Sampathkumar et al. (2010) concur that a larger temperature difference between the glass cover and the saline water in the basin increases the natural circulation of air mass inside the solar still. The temperature difference is a driving force for the condensation process as it increases the evaporative and convective heat transfer. To the contrary, Aburideh et al. (2012), in an experimental study on a single basin double slope solar still, found that the decrease in temperature difference between the condensing cover and the saline water in the basin enhanced the distillate production. However, no further details were provided as to what influenced this behaviour, since other studies reported otherwise.

Arunkumar et al. (2012) conducted a study on a hemispherical shaped solar still with its basin painted black to increase solar absorptivity. The still, made from mild steel material, had a 0.95 m diameter and 0.10 m height. The saline water depth was maintained at 50 mm and a 3 mm thick condenser cover. The still was insulated with glass wool material to minimise heat loses from the still. Water was used to cool the condenser cover to increase the temperature difference between the saline water surface and the condenser cover. The distillate yield for an average solar intensity of 732 W/m^2 was 4.2 and 3.66 litre/m^2/day with and without cover cooling, respectively

Many approaches to improve the distillate yield of a basin type solar still have been attempted. Some approaches are simple, and others complex. One pertinent consideration is the type of material from which the cover is made. Sharshir et al. (2016a) express that the cover can be made from plastic or glass. However, a glass material is preferable as it has greater solar

transmittance for different angles of incidence and can be used for a prolonged time. Alternatively, plastic lasts for a shorter period of time than glass. According to Bosman's (1983) study on the spectral difference of glass and Perspex shields and the effect of solar radiation, that there was an optical difference in transmission of light between the glass and Perspex shield. The glass had the ability to transmit the light at a shorter wavelength. It also has consistently better transmission ability in the spectral range of 250 – 4600 nm. The Perspex material caused a sharp drop in the transmission of light beyond 1000 nm. In addition to the type of material, another vital consideration is the angle of inclination of the condenser cover.

Kabeel and EL-Agouz (2011), in a review study, report that a solar still with a condensing cover inclination equal to the latitude angle of the location receives sun rays close to normal to it surface. The radiation remains almost normal throughout the year and therefore increases the evaporation rate in the solar still. However, the evaporation in a solar still is a function of solar irradiance which implies that the higher the solar irradiance, the higher the evaporation rate. In a study by Tiwari et al. (1994), an optimisation of glass cover angle of inclination on a passive single-slope single-basin still was carried out, finding that the increase in cover inclination increases the surface area of the condensing cover exposed to the solar radiation. The inclination also increases the temperature difference between the cover and the evaporative surface of the saline water in the still. The increase in cover inclination enhances the distillate production during sunshine hours but decreases during off-sunshine hours with a similar inclination. The effects of the inclination of the cover apply both in summer and winter for the area of Delhi. It was concluded, however, a maximum of 10° angle in summer and for winter, the angle can be as large as possible. According to Tiwari and Tiwari's study (2007) on different inclinations of the condensing cover on a passive single-basin single slope solar still, the optimum angle of 15° was best in summer and rainy seasons for a single sloped solar still, while the 45° angle was much better in winter. The studies above agree in that the orientation and inclination of the cover for different seasons significantly affect the yield of the solar still.

According to the results of Altarawneh et al. (2017) from an experimental and analysis study to optimise the passive single slope, double slope and the pyramid shaped solar still, the productivity of a double slope (DS) and a single slope (SS) both with a condensing cover at 45° improved by 92% and 38%, respectively, in summer compared to the same condensing cover angles in winter. The increases were attributed to the long sun exposure and the sun position in the sky. It was further determined that the condensing cover tilt angle has a significant effect on the productivity of a solar still. In addition, changing the tilt angle affects some parameters of the solar still such as cover surface area for heat transfer and the space

volume between the saline water and the condensing cover. Due to sun position in the sky, larger condensing cover angles are desirable for winter and smaller angles for summer. While the suggested variation of condensing cover angles agrees with Tiwari and Tiwari (2007), the reported results of Altarawneh et al. (2017) reveal some contradiction. The 92% and 38% improvement reported above contradict the reported results from other studies that smaller angles are preferred for summer. This contradiction is valid, though, if only the effects of the cover angle are attributed to the improved productivity. However, Altarawneh et al. (2017) also reported that the productivity of the SS with 45° was 70% higher than the SS with 15° condensing cover angle in winter, which agrees with other researchers.

Al-Hinai et al. (2002b) explain that increasing the tilt angle of the condensing cover of a single-basin double slope solar still in winter increases the distillate yield. However, the same condensing cover tilt angle used in winter reduces the distillate yield under summer conditions. An optimum condensing cover tilt angle is obtained by taking an average distillate yield on different tilt angles experimented on for the duration of the year. In addition to the angle of a condensing glass cover, the condensing cover thickness has some effect on the production of the distillate, as alluded to earlier. Van Steenderen (1977) suggests that the thicker the glass cover, the less distillate produced from a solar still. Lower distillate yield can be attributed to the lower light transmission through the thick condensing glass cover, as reported in the literature. Maximum production of the distillate was achieved at the smallest thickness of approximately 2 mm thickness.

According to Morad et al.'s (2015) study to improve the performance of a single-basin double-slope solar still coupled with a flat plate solar collector (FPSC) and condensing cover cooling, increasing the thickness of a condensing cover from 3 mm to 5 mm decreases the instantaneous and internal efficiencies of both the passive and active solar still. The decrease in the efficiencies is attributed to the decrease in the solar radiation transmission through the condensing cover. In addition, this decrease in transmission negatively affects solar still to accumulate and retain thermal energy inside it. Furthermore, the cooling effect of the condensing cover by a thin film of cool water enhances the instantaneous and internal efficiencies. The thin film of cool water reduces the temperature of the condensing cover and thus increases the evaporation rate.

The larger temperature difference between the saline water and the condensing cover increased the evaporation rate. Moreover, as reported, the highest distillate yield was achieved at 0.01m saline water depth and 3 mm condensing cover thickness. The information displayed in the figure was recorded at 3 mm thickness: an active and passive solar still saline

water (water temperature) was the highest at 75°C and 54.5°C. The elevated temperatures of an active solar still were attributed to the pre-heating of saline water by the FPSC. For the same solar stills with a 4 mm thick condensing cover, the maximum temperature reached decreased. Likewise, a 5 mm condensing cover thickness further decreased the temperature values inside the solar still. Saeedi et al. (2015) report that increasing the ambient temperature from 27 to 47°C increases the temperature of a condensing glass cover. Increasing the temperature of glass cover decreased the thermal efficiency from 21.56% to approximately 20%. Moreover, the increase in glass cover temperature causes the desalination process to be reduced, which in turn produces less distillate.

Al-Hinai et al. (2002b), in a comparative parametric investigation study of a double-effect and single effect solar stills, found that in winter months, greater condensing cover tilt angles tend to increase the distillate yield of the solar still while the same angles in summer tend to decrease the solar still's productivity. The distillate yield fluctuation based on the tilt of the condensing cover may be due to the negative declination angle in winter and positive values in summer. Furthermore, positive declination angles tend to show an increase in solar radiation reflectivity of the cover as the cover angle decreases. The optimum tilt angle of the condensing cover should be based on the average distillate yield when various cover angles are used. The effects of a condensing cover on a solar still have been reported by numerous researchers (Al-Nimr & Dohdolan, 2015; Hassan & Abo-Elfadl, 2017; Rabhi et al., 2017; Lal et al., 2017).

2.1.2 Painted walls

In addition to the orientation of the condenser cover, a black dye or paint is used to enhance the absorption rate of the solar irradiance in the basin of the still. Hamadou and Abdellatif (2014), Raj and Manokar (2017) and Tiwari and Sahota (2017) contend that the interior basin walls of a solar still are blackened to maximise solar absorption of solar irradiance. The side walls and bottom wall of a basin are painted with such paint or dye to minimise reflection ability of the walls. The blackbody absorbs maximum amount of solar radiation and increases the amount of heat in the basin. Elevated temperatures in a solar still increase the evaporation rate which then enhances the distillate yield (Lal et al., 2017). The black painted basin also reduces reflective behaviour of the basin of the solar still. Therefore, the internal sides and bottom walls of a solar still are painted black to maximise solar radiation absorption (Singh et al., 2011; Singh et al., 2016; Rabhi et al., 2017; Hassan & Abo-Elfadl, 2017).

2.1.3 Saline water depth

According to Sivakumar and Sundaram (2013), saline water depth is inversely proportional to the productivity of a solar still. Therefore, solar stills – whether passive, active, forced mode, natural mode, static mode or dynamic mode – have several common challenges concerning saline water depth. For instance, Prakash and Velmurugan (2015) report that productivity of the still is maximum when saline water depth is minimal in the basin of the still. Likewise, different distillate production rates occur at different saline water depths. Low saline water depths prove to yield more distillate under similar operating conditions. However, relatively high saline water depths may have lower distillate production rates during the daytime, but they have larger thermal energy storage capacities. The storing capacity enables the still to continue producing distilled water until late at night when there is less or no solar radiation. The combination of the thermal energy storage capacity of saline water and a well-insulated solar still translate to prolonged distillate production into the night. However, a very low water depth of less than 25 mm leads to dry spots in the basin which affect the productivity of a solar still (Van Steenderen, 1977). Dry spots occur as evaporation diminishes the saline water level in the basin.

Kabeel et al. (2019) studied the effect of water depth in a pyramid solar still with its basin painted with TiO_2 nano black paint. The saline water temperature at a depth of 10 mm was reported to decrease with decreasing solar intensity while a higher water depth (up to 35 mm) increased under the same conditions. Upper and lower temperature values of saline water with the TiO_2 coating were 63 and 55°C for water depth of 10 and 35 mm, respectively. The temperature values of saline water without the coating were 61 and 48°C for corresponding depths. The coating improved the saline water temperature with higher water depth 1.5-2.2°C and increased the distillate yield by 6.25%. However, the accumulation of vapour in the basin reportedly increased the condensing cover temperature. Elevated cover temperature reduces and even halts the condensation process, primarily because the evaporative saline water surface and glass cover temperature difference are driving forces for condensation. The cumulative daily yields with and without coating were 6.6 and 6.2 kg/m^2 at 10 mm water depth. The productivity of the still with TiO_2 reportedly increased during sunshine hours while decreasing during off-sunshine hours for different depths.

Bouzaid et al. (2019) conducted a numerical analysis on a novel cascaded inclined solar still with vertical baffles. The still was inclined at a latitude equal to Rabat-Morocco with its basin painted black and designed such that minimal saline water is contained for quick and efficient evaporation. The temperature in the novel (modified) cascade solar increased by 9°C

compared to a conventional cascade solar still. The hourly yield was numerically estimated to be as high as 1.6 kg/m^2/hr for solar intensity of 900 W/m^2.

According to Saeedi et al. (2015), the effect of water mass inside a solar still is relative to the effect of a number of PV/T collectors. The thermal efficiency of the solar still decreased with an increase in saline water depth (mass). However, it was reported that the decrease in thermal efficiency was insignificant when a number of PV/T collectors were less than 7. Furthermore, decreasing the saline water from 50 to 1 kg decreased the saline water depth and as a result, increased the evaporative heat transfer and thermal energy efficiency. Therefore, energy efficiency was higher at lower saline water depth.

Researchers have also determined that the productivity of the still is dependent on the depth of the saline water in the basin. However, the saline water depth must be at an optimum depth for better distillate yield (Lal et al., 2017). The depth of saline water differs from one study to another, and in fact, some studies experiment on numerous saline water depths. Such variation from 2, 4, 6, 8,10 and 12 cm saline water depths was studied by Phadatare and Verma (2007), who concluded that a maximum distillate yield was achieved at a depth of 2 cm with the thermal efficiency ranging from 10% to 34%. Maximum efficiency was found to be 34% at a saline water depth of 12 cm. An increase in saline water depth reduces the distillate production in a solar still (Srivastava & Agrawal, 2013). However, as reported, higher saline water depth has higher thermal energy storage capacity and can prolong the desalination process well into the night. In a study by Tarawneh (2007), four different saline water depths (namely 0.5, 2, 3 and 4 cm) were experimented on. The increase in distillate yield due to different saline water depths was reported as follows: yield at 0.5 cm was 8% higher than that of 2 cm; yield at 2 cm was 12% higher than that of 3 cm; and yield at 3 cm was 14% higher than that of 4 cm. There is consensus in that the lower the saline water depth the higher the productivity in studies by Phadatare and Verma (2007) and Tarawneh (2007). Khalifa and Hamood (2009a), as verification of the effect of water depth in the basin study, reported the effect of different saline water depths: 1, 4, 6, 8 and 10 cm. Lower saline water depth reportedly maintains higher temperature and distillate yield during sunshine hours. Higher saline water depths maintain higher temperatures late in the day and thus a continuous distillate yield is possible during the off-sunshine hours. Kumar and Dwivedi (2015) acknowledge that lower saline water depths enhance the distillate of the still. Out of three saline water depths – 0.01 m, 0.02 m and 0.03 m – the 0.01 m saline water depth achieved the highest distillate yield from the solar still. According to Sharshir et al. (2016a), the distillate yield is inversely proportional to the saline water depth. That is, the deeper the saline water the lesser the distillate production from a solar still.

Al-Hinai et al. (2002a) report that lower saline water depth decreases the saline water heat capacity. This allows higher saline water temperatures in the basin which in turn increases the evaporation rate of water. Additionally, decreasing the saline water depth from 0.29 m to 0.1 m only enhanced the productivity by a mere 6.3%. However, decreasing the saline water depth from 0.1 m to 0.005 m enhanced the productivity by 19.6%. In addition, Morad et al. (2015) in a study to improve the performance of a double slope solar still coupled with FPSC and condensing glass cooling, investigated the influence of saline water depth. Findings suggest that increasing the saline water depth from 0.01 m to 0.03 m has a severe effect on the instantaneous and internal efficiencies of both passive and active solar stills. The decrease in efficiency was attributed to the high specific heat capacity and thermal energy storage ability of the saline water. As apparent, the studies corroborate findings by various other researchers on the effects of saline water depth.

In a study by Taghvaei et al. (2014b), long-term effects of saline water depth were investigated on an active solar still. The short-term (i.e., within 24 hours) effects of the saline water depth in the basin corroborates the findings of the studies discussed above, that the lower the saline water depth, the higher the efficiency and productivity of a solar still. Moreover, higher saline water depth has larger thermal storage capacity which in turn produces more distillate at night. However, the long-term (i.e., up to 10 days) effects are completely different from those of the short-term effects. Experimental tests conducted over a period of 10 days with an initial basin water depth of 95 mm which diminished over time to 40 mm on the last day (10^{th} day), experienced a decline in both solar still efficiency and productivity of 18.5% and 23.8%, respectively. There is a contradiction or difference in settings as the efficiency and productivity patterns of a study by Taghvaei et al. (2014b) decrease with decreasing saline water depths. The behaviour of the higher productivity with lower saline water depth was consistent on both passive and active solar stills reported above, except for the long-term effect as reported by Taghvaei et al. (2014b) which suggested otherwise. The long-term results reported by Taghvaei et al. (2014b) may have been the cause of an increase in salinity levels over time. As reported earlier in the chapter, the literature surveyed suggest that higher salinity levels increase the boiling point and decrease the temperature of saline water, with other researchers also reporting on the effect of saline water depth in a solar still (Garg & Mann, 1976; Al-Abbasi et al., 1992; Aves, 2011; Santos, 2011; Elango & Murugavel, 2014; Rajamanickam & Ragupathy, 2012).

2.1.4 Solar still integrated with a condenser

Solar stills are coupled with different equipment to increase their efficiency and productivity. The roles of a vacuum fan, external condenser or a nanofluid in a basin-type solar still are explained below. In an evacuated solar still with external condenser operated at vacuum pressure, the fan removes non-condensable gases and directs them to the condenser. The fan also enables an effective separation of the evaporated gases and the saline water at the saline water interface, thereby enhancing evaporation in the basin. Moreover, a solar still operated with the nanofluids (nanoparticles), absent the vacuum fan and an external condenser, has certain effects when compared with a conventional solar still (CSS). The distillate yield from a solar still with nanofluid is higher than that of a CSS, due to enhanced heat transfer rate as a result of elevated temperatures because of incorporated nanofluids in the solar still (Kabeel et al., 2014).

Morad et al. (2017) studied a developed solar powered desalination system for freshwater production, comparing two identical basin-type solar still systems, an ordinary solar still (OSS) and a developed solar still (DSS). The difference was that one system was equipped with a vacuum pump while the other was not. Both systems were coupled with an external condenser to cool and condense the vapour. The distillate yield from the OSS and the DSS were found to be 5.54 and 10.94 l/day, respectively. The distillate yield shows a huge improvement of about 97.5%. The condenser efficiency of a developed solar powered system was higher than that of an ordinary solar still. It was reported that the presence of a vacuum enabled evaporation at a lower temperature as it reduced pressure in a flat plate solar collector (FPSC). The enhancement of evaporation also improved the distillate production. Table 2.2 shows condenser efficiencies from various saline water flow rates. The efficiency is at its highest with the lowest flow rate. Moreover, the condenser efficiency of a DSS is constantly higher than that of an OSS.

Table 2.2. Condenser efficiency of two systems

Description	Parameters			Author(s)
Saline water flow rates (L/h)	0.4	0.6	0.8	Morad et al. (2017)
Maximum condenser efficiency for OSS (%)	62.5	53.8	50	
Maximum condenser efficiency for DSS (%)	66.7	57.1	54.5	

Ibrahim and Elshamarka (2015), in an experimental study on a modified basin type solar still with air cooled external condenser and a vacuum pump, concluded that the use of an external condenser in conjunction with a vacuum pump increased the efficiency of the solar still by 30% while its productivity increased by 16.2% as compared to a conventional solar still. However,

the cost of this modified solar still was about 17% higher than that of a conventional solar still. Faegh and Shaffi (2017) conducted a study with a single slope basin solar still coupled to an ETSC and an external condenser with the phase change material (PCM) for heat storage. In general, the PCM is used to store thermal energy during the daytime and supply that energy to saline water during off-sunshine hours. Four different tests were conducted on a solar still: test 1) solar still coupled with ETSC only; test 2) heat storage (PCM) added to test 1; test 3) the condensing glass cover is insulated and no PCM material used; and test 4) PCM is added to test 3. The distillate yield for test 1 is 0.68 kg/m^2 hr; the yield of tests 2 was reported to be very close to that of test 1. This slight increase was attributed to heat loss through the condensing glass cover of a solar still. Test 3 reached a maximum distillate yield of 1.025 kg/m^2 hr and test 4 achieved the highest yield of 1.05 kg/m^2 hr. Despite insulating the condensing glass cover during test 3, the distillate yield continued to increase. In addition, test 4 was able to store the thermal energy effectively as compared to test 2 since test 2 was losing heat through the condensing cover glass. Test 4 achieved 86% increase in distillate production compared to a conventional solar still. The heat stored in the PCM during test 4 was used to continue the desalination process up until 21h00 at night. Sharshir et al. (2016a) explains that the basic principle of storing the latent heat of condensation depends on the fact that the PCM changes its phase (solid to liquid or liquid to vapour) when exposed to the heat.

The condenser in a solar still creates an additional room for the vapour to condense. According to EL-Bahi and Inan's (1999) study to improve the basin type solar still by coupling it with an external condenser, the still's efficiency was 75% with the condenser and 70% without the condenser. Daily distillate yield of the solar still with condenser was reported at 6.52 L/m^2/day. Rahmani and Boutriaa (2017) found a distillate yield improvement of 4.73 kg/m^2/day from 2.71 kg/m^2/day due to an integration of a condenser to a solar still. Furthermore, increasing the condenser area also increased the distillate yield as wind velocity influences its performance. However, there is a critical area (maximum area) to which any further increase in area has insignificant impact on the distillate yield. Hassan and Abo-Elfadl (2017) conducted an experimental study on a single basin single slope solar still with different condensers and saline water modifications. The condensers were the glass cover, aluminium heat sink, aluminium plate and the aluminium plate covered with an umbrella. The saline water modifications in the basin were the ordinary saline water, saline water with layers of black steel fibre, saturated sand with saline water and lastly, a mixture of sand and black steel fibre saturated with saline water. Various results were reported from the study, but those with a focus of the productivity of the still are discussed here. It was concluded, for example, that using glass condenser and black steel fibres increased the productivity to 35%, while using the heat sink condenser increased the daily productivity by 31%. However, not all

modifications resulted in increased daily productivity as using the aluminium plate condenser decreased the daily productivity by 13%. The use of aluminium condenser in conjunction with an umbrella decreased daily productivity by 21%. According to Rabhi et al. (2017), integrating a solar still with an external condenser achieves lower basin and condensing glass temperatures compared to a conventional solar still (CSS). Solar stills operating at low temperatures attain high overall system efficiency. Maximum efficiencies of 40.6% and 31% were achieved for a solar still with a condenser and CSS, respectively. However, due to the fluctuations, the daily efficiency was averaged. A typical daily efficiency of a solar still with a condenser and a CSS is 29.54% and 21.9%, respectively, with a daily productivity of 2.38 l/m^2 and 3.146 l/m^2 for a solar still with a CSS and a condenser, respectively.

Kabeel et al. (2017b), in a numerical investigation of a modified solar still using nanofluids and external condenser, determined that the distillate yield from a modified solar still (integrated with an external condenser) was higher than that of a conventional solar still. The fan reportedly created a turbulence inside the solar still which extracted the vapour from the saline water surface. In addition, the fan sucked the incondensable gases away from the saline water surface and into the condenser. Theoretically, a solar still with external condenser enhanced the distillate productivity by 56% compared to the conventional solar still.

2.1.5 Effect of the insulation on a solar still

Nagarajan et al. (2016) contend that the heat loss from the solar still to the surrounding is predominantly in the form of convection and radiation modes. The heat is generally lost through the sidewalls, bottom wall and the glass surface of the solar still. This heat loss can be minimised by applying insulation material to all identified heat loss areas. But heat loss from the condensing glass cover is advantageous as it reduces the cover temperature and increases the evaporation-condensation driving force inside the solar still.

While the common purpose of the insulation on a solar still is to prevent the loss of thermal energy through the walls of a solar still, there are various types of insulation materials (Lal et al., 2017). The prevention is mostly helpful during low solar intensity periods such as late in the day, at night or in winter months when there is little or no solar radiation available. Elango and Murugavel (2014) studied the effect of water depth on the productivity for single and double basin slope glass solar stills, focusing on the insulation of the still. Some improvements were reported based on the application of the insulation. The distillate yield from the uninsulated and insulated basin type solar stills were compared. The type of the solar stills investigated were single basin double slope and double basin double slope solar stills. Both a single basin double slope and double basin double slope insulated solar still achieved higher

cumulative distillate yield during the heating period (during sunshine hours) compared to the uninsulated ones. It was also reported that during the cooling period (off-sunshine hours), the uninsulated still lost thermal energy at a higher rate than the insulated one. Therefore, production of distilled water continued until 11pm for the uninsulated and 1am for the insulated stills.

Khalifa and Hamood (2009b) studied the effect of the insulation thickness on the productivity of a solar still using different insulation thicknesses ranging from 30, 60 and 100 mm. It was found that the thicker the insulation, the more productive the solar still. This implies that the solar still was least productive with 30 mm thickness and more productive with a 100 mm thickness. Manokar et al. (2018) reported on an inclined solar panel basin (ISPB) integrated with a thermal photovoltaic panel (PV/T). Three different settings were experimented on: i) no insulation on the walls of a solar still; ii) only side walls insulated; and iii) the side and bottom walls insulated. The setting with the side and bottom wall insulation increased the temperature of a still by 33% compared to a still with no insulation. In addition, a solar still with insulation on side and bottom walls produced the highest distillate compared to the other two settings.

According to Taghvaei et al.'s (2014a) investigation into the effects of water depths on the performance of a single-basin single-slope active solar still, the thermal conductivity of an insulation is important for storing thermal energy used for distillate production after sunset. When comparing the productivity of two identical and insulated solar stills with different saline water depths operated at night, the one with lower depth is more productive. However, if both solar stills are well insulated, the difference in their productivity during this time is insignificant.

Al-Hinai et al. (2002a), in a study on the effect of climatic, design and operational parameters on the yield of a simple solar still, found a limiting thickness value with regards to the enhancement of the distillate yield. Insulation thickness above the limiting thickness value is unjustified as the distillate yield does not proportionally increase accordingly. In addition, the insulation thickness above the limiting thickness can cause the system to reach a condition referred to as "thermal damage" (Shatat & Mahkamov, 2010). Thermal damage refers to the over-insulated system where the condensing surfaces reach temperatures equal to that of vapour. When this happens, the desalination process halts altogether due to high temperatures. In other words, the condensing surfaces and the vapour have reached thermal equilibrium, and therefore, no heat transfer takes place.

Altarawneh et al. (2017) report that an increased productivity of 28% was observed when 1 cm insulation material was used on a 45° double slope (DS) as compared to other similar

systems. However, insulation material beyond 2 cm thickness has minimal effects on the productivity of the solar still, owing to its limiting thickness. It is evident that there is a limiting value, experimentally determined, depending on the location and ambient temperature of the solar still. Sharshir et al. (2016b) studied a hybrid desalination system using humidification-dehumidification and solar stills integrated with evacuated solar water heater, reporting on the effect of the glass-wool insulations material on a single solar still (SSS). The combination of the perfect insulation and heated water reportedly increased the yield up to 10kg/day and the efficiency up to 90%. The insulation material had a thermal conductivity of 0.047 kW/m K. It was reported that the optimum or required insulation thickness was about 0.02 m during sunshine hours. Due to the lower or no-existent solar incident later in the day or at night, a 0.03 m thick insulation was required to minimise the losses. In addition, insulation material thicker than 0.03 m was undesirable as it had little effect on the performance of the still.

According to Kaushal et al.'s (2016) experimental study of an improved basin type vertical single distillation cell (VSDC), solar stills are able to be productive even during off-sunshine hours due to the energy stored both in saline water and the insulation material. It was reported that the 10 mm air gap between the partitioning plates of double glass covers reduced the surrounding heat loss. The daily cumulative efficiency of the VSDC was reported higher than conventional basin solar still.

2.1.6 Additional techniques to enhance solar stills

Additional techniques used to enhance solar stills productivity are briefly discussed below. Some of these techniques are relatively simple while others are complex. For instance, Haddad et al. (2017) conducted a study on improving the performance of a single slope simple solar still by integrating it with a vertical rotating wick (VRW) and a static wick. The modified solar still was compared with simple solar still on various parameters. It was determined that a simple solar still produced about 6.25 kg/m^2/day and 3.33 kg/m^2/day of distillate in summer and winter, respectively. Moreover, a modified solar still with the VRW produced about 7.17 kg/m^2/day and 5.03 kg/m^2/day of distillate in summer and winter, respectively. The efficiency increase for the modified solar still was determined as 14.72% and 51.1% for summer and winter, respectively. The solar still daily efficiency was determined for a solar still with VRW, static wick and without a wick as 64%, 54% and 41% respectively, in winter; whereas, for summer conditions, the daily efficiency was determined to be 66%, 49% and 51% for a solar still with VRW, static wick and without a wick, respectively. In addition, the solar still experimented on was equipped with a trough (distillate collector) on four vertical walls of the solar still to improve the collecting rate. The trough is generally at the lower end of the incline condensing cover. Adding troughs on all four walls of a solar still enhances the rate of distillate

collection. It was then concluded that the average thermal efficiency of the modified and simple solar still solar still were 65% and 46%, respectively.

Kumar and Dwivedi (2015) conducted a comparative study on a modified active single slope solar still; the modification was an enlarged condensing surface area by 57.4%. The surface area was enlarged by adding a secondary condensing cover; thus, the solar still had a main and secondary condensing cover. The saline water in the modified solar still and the CSS achieved a maximum temperature of 70.3°C and 66.4°C, respectively, for the same saline water depth. The higher temperatures on the modified solar still were attributed to larger solar thermal energy received due to the modification of the condensing cover. The distillate production of a modified solar still was reported to be 25.4% higher than that of the CSS for the same saline water depth. The secondary cover was replaced with an aluminium 1 mm sheet which rendered a distillate yield increase by 14.5%.

According to Kwatra's (1996) study to determine the effects of enhancing the evaporation area and the evaporation temperature, increasing the surface area of evaporating body up to four times the initial area enhances the distillate yield by 19.6%. However, the enhanced distillation was limited to around 30.2% for further increments of the evaporation areas above 32 m^2 to infinity. Increasing the surface area of evaporation also reduced surface temperature as well as the temperature difference between the evaporating surface and the condensing glass cover. The distillate yield increased despite the temperature reduction of saline water in the basin.

Rajaseenivasan et al. (2017) conducted an experimental and mathematical study on the influence of height variation between the saline water and the condensing cover. Four electric motors with 2-Watt capacities driven by a photovoltaic panel were used for stirring the saline water in the basin. In addition, thermal energy storing materials such as paraffin and charcoal were used in the basin of the solar still. It was determined that distillate production increases with a decrease in height between the saline water and the condensing cover. Kumar et al. (2000), analysing the annual performance of an active solar still, found that the distillate yield was maximum during days with clear skies and sunny days. Meanwhile, the glass condensing cover was tested under varying inclinations of 15° and 45°. The variation of the glass reportedly had only a marginal effect on the distillate yield. An angle of 15° inclination was chosen as an optimum angle for maximum yield of the solar still. Since evaporation in a solar still is a function of solar radiation, it is evident from the studies that during the seasons with higher solar radiation, the condensing cover angle can be moderate, while in colder seasons, it can be larger.

A modified passive solar still was reported by Rabhi et al. (2017) from a study with a pin fin absorber and a condenser. The pin fins were augmented vertically on the floor of the basin to increase the surface area in the basin. The study compared the modified solar still with a conventional solar still (CSS), noting that the condensing glass temperature of a solar still with pin fin absorber and the CSS were 52.4°C and 48.1°C, respectively. In addition, a basin temperature for a solar still with pin fin absorber and a CSS were reported as 77.7°C and 63.9°C, respectively. A condensing glass temperature of a solar still with pin fin absorber and a condenser compared with a CSS was 50.8°C and 49.3°C, respectively. The basin temperature of both a solar still with pin fin absorber and a condenser compared with a CSS were 76.1°C and 64.7°C, respectively. Even though the experimental tests were conducted two days apart, it is apparent that the addition of a condenser reduces both the glass and absorber temperatures for the modified solar still. The productivity of a solar still with pin fin absorber and the CSS were 2.83 l/m^2 and 2.471 l/m^2, respectively. However, adding a condenser to the set up gave distillate yield for a solar still with pin fin absorber and a condenser compared with a CSS 3.146 l/m^2 and 2.38 l/m^2, respectively. Once again it can be observed that as the basin and glass temperatures change as a result of adding a condenser, so does the modified solar still productivity.

A modelling and performance analysis of a regenerative solar still was studied by Zurigat and Abu-Arabi (2004), wherein a regenerative still was compared to a single effect solar still. It was concluded, based on the results, that the distillate yield from a regenerative unit is more than 20% higher than a single effect solar still. Sharshir et al. (2017) conducted an experimental study to enhance the performance of a solar still using nanofluids and glass cover cooling. When using copper oxide and graphite micro-flakes, the productivity was reported to improve by 44.91% and 53.95%, respectively. When the glass cover cooling was added, productivity increased by 47.80% and 57.60% for copper oxide and graphite micro-flakes, respectively. The daily efficiency of the conventional still was 30% while that of a solar still with copper oxide and graphite micro-flakes without glass cooling were 38% and 40%, respectively. Daily efficiency with glass cover cooling was 46% and 49%, respectively. It can, therefore, be seen that the use of copper oxide and graphite micro-flakes increases both the productivity and the efficiency of the solar still. Moreover, Ayoub and Malaeb (2014) introduced a rotating cylinder in a single basin double slope conventional solar still. A new modified solar still performance was compared with a similar solar still but without a rotating cylinder. It was noted that the average improved distillate yield ranged between 160-260%, depending on the time of experimental tests for the month of May. The overall distillate production improvement for other months ranged from 200-300% compared to a passive solar still.

A conclusion emanating from a study of Samuel et al. (2016) is that different modifications on a conventional solar still enhance its performance differently. Three setting were experimented on: a conventional solar still alone, a conventional solar still with sponges for capillary effect and a conventional solar still with spherical balls for sensible heat storage. Distillate yield of a solar still with spherical balls, sponges and a conventional solar still alone was 3.7 kg/m^2,2.7 kg/m^2 and 2.2 kg/m^2, respectively. Omara et al. (2015a) conducted a comparative study on a conventional solar still (CSS) and corrugated wick solar still (CrWSS) with internal reflectors operating at vacuum pressure. The saline water temperature in the CrWSS basin was reported as 3.5°C higher than that of the CSS. Moreover, since the CrWSS was operated at vacuum pressure, the glass temperature of the condensing cover was reportedly in the range of 0.3 to 1.7°C lower than that of the CSS. The low inner glass temperature means there is a larger temperature difference between the evaporation surface of saline water and the glass temperature. In addition, the internal reflectors were reported to aid in deflecting the solar radiation onto the saline water in the basin which elevated the saline water temperature. Applying additional modifications renders different but consistent saline water and inner glass temperature results. For instance, it was reported that by adding the cuprous oxide nanoparticles, basin water was 0.5 to 5.7°C higher than that of the CSS. Furthermore, the glass temperature was 0.2 to 1°C lower than that of the CSS. Moreover, different modifications enhanced the productivity of the solar still differently. For instance, CrWSS with internal reflectors and an external condenser reached 180% higher than a CSS; adding cuprous oxide nanofluid and a vacuum pressure to the CrWSS elevated its productivity to 285.1% higher than the CSS; and finally, the CrWSS with internal reflectors, vacuum pressure and using aluminium nanofluid enhanced the productivity to 254.88% higher than the CSS. The study confirmed that indeed the modifications on the solar still enhance the productivity of the CrWSS in comparison with the CSS under similar saline water depth.

Gnanaraj et al. (2017) explain that a distillate yield of a modified solar still is higher than that of a conventional solar still. Four distillate productivity settings were recorded: a conventional single basin; a conventional double basin; a conventional double basin coupled with external reflectors; and a double basin solar still coupled with external reflectors, flat plate collector and a mini solar pond. The conventional double basin solar still was 57.83% higher than conventional single basin solar still; the conventional double basin solar still with external reflectors was 105.8% higher than a conventional double basin solar still; and a conventional solar still with external reflectors, flat plate collector and mini solar pond was 127.65% higher than a conventional double basin with external reflectors.

According to Omara et al.'s (2015b) comparative experimental investigation of a corrugated solar still (CrSS) with a wick and reflectors and a CSS, the surface area of the corrugated basin was larger than that of a flat sheet. The areas were 1.34 m^2 and 1m^2, respectively. This study was similar to a study by Omara et al. (2015a), CrWSS, except there were several features not included such as that the system was not operated at vacuum pressure (evacuated) and no external condenser amongst other features. One of the main differences noted between the two studies was the condensing glass temperatures. The condensing glass temperature of the CrWSS was lower than the CSS. However, Omara et al. (2015b) reported that the CrSS glass cover was 1°C higher than the CSS. Lower glass temperatures in the CrWSS could be attributed to the vacuum pressure a solar still was subjected to. The modifications on the CrSS were reported to have improved the temperature levels of saline water in the basin and the productivity of the still compared to the CSS. In addition, the CrSS has a smaller amount of saline water in the basin compared to the CSS, enabling higher productivity of the CrSS. It was further noted that different modifications enhance the productivity differently. For instance, the productivity of a CrSS alone reached a maximum of 55.36% higher than the CSS; a CrSS with a wick was 90% higher than the CSS; and CrSS with a wick and reflectors was 145.5% higher than the CSS. Tanaka's (2011) theoretical analysis of a single basin single slope solar still with flat plate external bottom reflectors determined that when the flat plate external bottom reflector was installed and set into an optimum angle, an increase in distillate output was estimated. A maximum increase was predicted that under three different periods – spring equinox, summer and winter solstice – the distillate production would improve by 42%, 25% and 62% above the CSS.

Mahian et al. (2017) conducted a study on nanofluids effect on the evaporation rate in a solar still equipped with a heat exchanger. The nanofluid effects were separated into three categories, namely concentration, type and size on the nanofluids. It was determined that at a concentrated volumetric fraction of 4% and inlet temperature of 70°C, the exergy efficiency and thermal efficiency increased by 1% and 0.66%, respectively, despite the increase in convective heat transfer coefficient by 15.4%. At 50°C inlet temperature, however, the solar still thermal efficiency, exergy efficiency and distillate yield (performance indices) increased marginally. With regards to the type of nanofluids, SiO_2/water and Cu/water were experimentally tested, finding that when SiO_2/water was used, the performance indices increased at maximum concentration of 4%. To the contrary, when Cu/water was used, performance indices increased at 1% concentration. With regards to the size of the nanoparticles, it was reported that increasing the size of the nanofluids decreases the performance indices insignificantly. This was associated with the observation that the heat transfer coefficient of nanofluids with smaller size is larger. An elaborate discussion on these

summarised results, covering the different flow rates, temperature variation and depth of saline water for example, was given in the study. Verma and Tiwari (2015) contend that the thermal conductivity of nanoparticles plays an important role as one of the parameters governing heat transfer capabilities of nanofluids. The heat transfer capabilities depend on various aspects such as volume fraction of concentration, aspect ratio and shape of the nanoparticles. It was reported that the thermal conductivity of nanoparticles is proportional to the percentage volume concentration of nanoparticles in base fluid. This means the thermal conductivity increases linearly with increase in percentage volume concentration of nanoparticles.

Sivakumar and Sundaram (2013), in a review study, found that the baffle suspended absorber plates in a solar still increase a free surface area. Moreover, a phase changing material used to store thermal energy in one form (liquid to solid or vapour to liquid) changes its phase when heat is extracted from it. In addition, a black rubber with 10 mm thickness was reported to enhance the distillate yield 20% more due to the thermal storage properties of the material. Black gravel with sizes ranging from 20 – 30 mm enhanced the distillate yield by 19%; the enhanced productivity was the ability of the gravel to absorb increased solar incidence. It was also determined that the vacuum technique helps in increasing the evaporation rate inside a solar still; water can be evaporated at lower temperature and thus less energy is required. It was further reported that reflectors are made from highly reflective materials. Further modifications reported in the study were the charcoal particles, spherical glass packed layer with high thermal properties, hot water tank integrated with a solar still, black rubber mat, black dye, and black ink, jute cloth, wick material and sun tracking systems. Various conclusions stemming from different materials and their effects on the solar still were discussed. Muftah et al. (2017) studied the performance of basin type stepped solar still enhanced with superior design concept, finding that reflectors reflect portions of solar irradiance onto the water surface which increases saline water and condenses glass cover temperatures. The reflected solar irradiance is thus increased as a result of high temperatures in the solar still. Further details on the different aspects of reflectors integrated with solar still are presented in a review study of Omara et al. (2016).

According to Kabeel et al. (2017b), in a numerical study investigating the performance of a modified solar still using nanofluids and external condenser, the saline water temperature of a modified solar still was higher than that of a conventional solar still. Compared to the conventional solar still, the cuprous oxide nanoparticles with a weight fraction of 0.2% concentration increased the saline water temperature of a modified solar still by 0.5 – 4.5°C with the use of a fan. Furthermore, without the use of the fan, saline water temperature of a modified solar still increased by 1.35–5.5°C above that of a conventional solar still. The fan

was reported to operate at 1350 rpm from 9h00 am to 17h00 pm. Moreover, it was reported that when using aluminium oxide nanoparticles with the same concentration as cuprous oxide nanoparticles, the saline water temperature of a modified solar still increased by 0.5–2.7 °C and 1.35 – 3.55 °C, with and without the use of the fan, respectively. The fan was operated for the same duration and at the same speed at reported above. The temperature of the condensing glass cover was reported to fluctuate with and without the fan under the application of the two different nanoparticles. It was concluded that using the cuprous oxide and aluminium oxide nanoparticles enhanced the thermal efficiency of the modified solar still to 84.16 and 73.85%, respectively, when using the fan. The thermal efficiency of the conventional solar still was reported at 33%.

Jamil and Akhtar (2017) conducted an experimental study on the effect of specific height on the performance of a single slope solar still. Five cases of different specific heights of solar stills were presented. Solar still 1 (case 1) had the highest specific height and the specific heights were gradually reduced from case 1 to case 5. Solar still 5 had the lowest specific height amongst the five tested solar stills. Observation showed that the distillate yield increased as the specific height of the solar still decreased, attributable to the reduced volume (space) inside the solar still. In addition, it was determined that larger specific height meant that the vapour travel higher (long distance) to get condensed when the specific height was larger. On the contrary, the vapour travelled a shorter distance when the specific height of the still was reduced. Accordingly, by reducing the specific height, more thermal energy was available per unit volume. A solar still productivity increase was observed between case 1 and case 5 of the tested cases. The increase in daily productivity of 212% was reported between case 1 and case 5 as well.

Saeedi et al. (2015) studied the optimisation of a PV/T (photovoltaic/thermal) active solar still, finding that the daily productivity of the solar increases as does the number of PV/T collectors. Likewise, increasing the number of PV/Ts was reported to proportionally increase the temperature of saline water in the basin. A limit of the effect of the number of PV/T collectors was reported at 30; more than 30 PV/T collectors had an insignificant effect on the productivity of the solar still. Furthermore, Kabeel et al. (2017a) and Prakash and Velmurugan (2015) conducted review studies wherein different parameters influencing the productivity of solar stills were discussed.

2.4 Solar collectors integrated with a solar still

2.1.7 Types of solar collectors

There are various types of solar collectors, but for the purpose of this study, only two types, namely flat plat solar collector (FPSC) and the evacuated tube solar collector (ETSC), will be discussed further. Garcia-Rodriguez (2002) reports that the solar collectors mainly used for saline water desalination are FPSC, ETSC, compound parabolic collectors (CPC) and parabolic trough collector (PTC). In a study by Zambolin and Del Col (2010), a comparative analysis in steady-state and quasi-dynamic test methods of the FPSC and ETSC was carried out, concluding that the optical efficiency of the FPSC suffers reflection losses in the morning and late in the afternoon due to its geometry. Similar losses occurring in the ETSC are reduced due to the shape of the evacuated tubes. The cylindrical shape of the ETSC is advantageous because that sun's rays remain normal for longer periods of time throughout the day. Sampathkumar et al. (2010) conducted a detailed review on active solar distillation, investigating the advantages of the ETSC over the FPSC. It was determined that in the FPSC, the sun's rays are perpendicular only at noon. Some fraction of the solar radiation was reported to be likely reflected; however, this was not the case in the ETSC. El-Bialy et al. (2016) reported that solar still with evaporation area between 0.5-1m^2 and integrated with the FPSC produced about 3-6 litre/day of distillate. However, similar solar stills with evaporating area between 0.5-1m^2 integrated with ETSC produced about 3-12.2 litre/day of distillate. It can, therefore, be concluded that the ETSC is more efficient than the FPSC in terms of capturing the intermittent solar radiation.

The ETSC efficiency is higher for a larger range of operating conditions compared to the FPSC. Garcia-Rodriguez (2002) reported that the losses in the ETSC are minimised by the cover receiver which is glass and tubular. Sun rays remain normal to the surface of the ETSC throughout the day, thereby maximising the thermal energy collected. The study reiterates the fact that ETSCs are more efficient and lose less heat during operation as they are evacuated, resulting in higher collector efficiency. There are two types of ETSC: dewar tubes (two coaxial tubes made of glass) and ETSC (made of metallic receiver). Al-Tabbakhand and Mohammed (2017), in an experimental investigation of an evacuated tube solar air collector, found that the pattern of collector exit temperature follows that of an irradiance. That is, the intermittency and fluctuation of solar radiation have a direct impact on a collected solar energy. However, the patterns of the collector efficiency were attributed to the air flowing in the evacuated tube cavities. Studies which coupled a single-basin single-slope solar stills are discussed below.

2.1.8 Effect of solar stills integrated with solar collectors

Supplying thermal energy to the solar still through a solar collector in known as indirect heating (Adhikari et al., 1995). Tiwari and Sahota (2017) noted both conventional (electricity grid) and non-conventional (photovoltaic, PV) external energy used on a solar still. Using a PV to operate pumps under forced modes and integrating the FPSC, ETSC and CPC make the solar still an electrical-thermal system (PV/T). The PV/T systems are also known as hybrid desalination systems. The effect of integrating the solar collector with a solar still can be noted in various studied. For instance, Rajaseenivasan et al. (2014) conducted an experimental investigation on a solar still with an integrated flat plate collector, finding that the distillate output and the hourly efficiency of the flat plate collector basin still (FPCB) were constantly higher than those of a CSS. This was associated with the flat plate solar collector used in the active solar still. Sampathkumar et al. (2010) conducted a detailed review on active solar distillation, finding that active solar stills are classified into three categories, namely, high temperature active solar distillation, pre-heated water application and nocturnal production. In the high temperature active solar distillation system, the temperature of saline water increased from 20°C to 80°C. In essence, high temperature active solar distillation operates at high temperatures. In the pre-heated water application, pre-heated water is used to increase the temperature in the basin. The pre-heated water was reported to be available from various sources such as paper and chemical industries, thermal power plants as well as food processing. Nocturnal production refers to the operation of the still in the absence of solar radiation. The operation of the still during off-sunshine hours can be achieved by the stored energy during sunshine hours.

Mahian et al. (2017) studied the effect on nanofluids on the evaporation rate in a solar still equipped with a heat exchanger. The study reported that in an active single effect solar still, the saline water evaporates due to both the direct solar irradiation received from the sun as well as the thermal energy collected by the solar collectors. It was reported that at 70°C, an active still (integrated with solar collectors) productivity, energy efficiency and energy exergy were more than 2.5 times higher that of the CSS. However, at temperatures less than 50°C, the active solar still productivity was 81% lower than the CSS. Therefore, at lower temperatures (less than 50°C), integrating a solar still with a solar collector is unjustified and reduces the performance indices. Further information on the effect of coupling a solar collector to a single-basin single-slope solar still was reported by Badran and Al-Tahaineh (2005); for example, enhanced distillate production as a result of coupling a passive solar still to a solar collector. The daily productivity of a passive solar still alone was found to be 2240 ml while that of an active was 3510 ml. In percentage terms, an active solar still was 36% more productive than a passive solar still. Firozuddin and Ahmad (2014) conducted a study of a

single basin slope coupled with an evacuated tube solar collector. Several conclusions were drawn from the study: first, daily productivity improved to its maximum by 50.2% when a solar still was coupled with an ETSC; second, an ETSC can operate at higher temperatures than an FPSC; and third, ETSC was efficient even in winter.

Raju and Narayana (2018) conducted a study with a different number of FPSCs connected to the single slope basin type solar still: three FPSCs and two FPSCs connected in series as well as a single FPSC connected to a single slope basin type solar still. It was noted that a solar still obtained maximum temperatures when coupled with three FPSCs, a direct result of an increase in collector area. The series connection increases the temperature of saline water each time it passes through a collector. Furthermore, the maximum yield for the three FPSCs, two FPSCs and single FPSC connected to a solar still was 5.04 kg, 3.76kg and 2.67kg, respectively. However, the efficiency of the still behaves differently from the distillate yield which is positively influenced by larger collector area. There is a limiting value in the advantage the larger collector area has. It was noted that an efficiency of a two FPSC connection was 0.47% higher than a single FPSC connection. However, the efficiency of the three FPSC connection was 0.48% lower than the single FPSC connection. The three FPSC connection has reached the limiting value the series connection of the FPSC has on the solar still. The advantages of integrating a solar still with a solar collector appear limited, as confirmed in the studies above. Yadav and Yadav (2004), in a parametric study on the transient performance of the high temperature desalination system with a basin type solar still integrated with absorber asymmetric line-axis solar CPC, found that the absorber asymmetric line-axis solar compound parabolic concentrator can achieve the high temperature effect that is usually achieved by a number of collectors connected to a solar still.

Taghvaei et al. (2014b) studied the long-term effects of the collector area and saline water depth in the basin. Four similar solar stills with different collector areas were used for the experimental study conducted over five days, with the brine depth diminishing over the course of time, unlike in the passive solar still where the lower depths of saline water in the basin have been reported to enhance the productivity and efficiency. Diminishing brine depths reduces both the productivity and efficiency in the active solar still. It was noted that for a collector-to-basin area (CBA) ratio of 3.52, with initial saline water depth of 100 mm which diminishes to 40 mm by the fifth day, the productivity and efficiency of a solar still is reduced by 7.6% and 14.1%, respectively. In addition, the study reported that the effects of saline water depth on the solar still are insignificant when solar collectors have larger collector areas. The insignificance of the brine depth is due to larger collector areas supplying enough thermal energy to heat and evaporate deeper saline water. However, larger collector areas are

dependent on the CBA: for a CBA of 0.88, the saline water depth has up to 5% influence on the productivity, but for a CBA of 3.52, the effect is reduced to 1%. In addition, active solar stills cause elevated temperatures of saline water which increase the productivity but negatively affect the efficiency of the still. Larger solar collectors augmented with a solar still causes the brine to boil, which is undesirable as it reduces the productivity and efficiency. The study also addressed the variation and influence of temperature differences between the saline water and the condensing glass cover in the solar stills with different CBAs.

Kumar and Tiwari (2010) conducted a study comparing passive and active single-basin single slope performance. The study was carried out under New Delhi, India, weather conditions with a latitude of 28.34°. The condensing cover optimised at 30° and the basin walls were painted black. The effective basin areas of the solar stills were 1 m^2 each, with a condensing glass cover thickness of 4 mm. The hybrid photovoltaic/thermal (PV/T) active still was coupled with the series connected FPSC, each with 2 m^2 areas and a direct current (DC) pump. In the active still, the saline water was heated both directly by the sun and indirectly by the solar collector. Experimental tests were conducted under actual weather conditions with 50-, 100- and 150-mm saline water depths. In summer, the distillate yield of an active still compared to a passive was 7.22 and 2.26 kg/day, respectively, at 50 mm saline water depth. It was reported that the productivity is significantly reduced to 5 and 1.51 kg when saline water depth is increased 100 mm for an active and passive still, respectively. Furthermore, the thermal efficiency of a hybrid still was found than that of a passive still, but its overall efficiency was higher. This was caused by elevated operating temperatures which resulted in larger thermal losses. However, the overall efficiency was enhanced by the energy conversion of an active system.

Gaur and Tiwari (2010) conducted an optimisation of the number of collectors on a hybrid PV/T basin solar still. Again, this study, closely related to that conducted by Kumar and Tiwari (2010), was conducted under New Delhi, India, weather conditions. The study involved coupling a basin still with PV/T collector as reportedly increasing the evaporative heat transfer coefficient above that of radiative and convective heat transfer coefficients. In addition, the effect of collectors increases the daily yield while decreasing the still's efficiency due increased losses to the surroundings. Moreover, increasing the number of collectors from 2 to 10 showed a decrease of 40% in the still's daily efficiency. Increasing the saline water mass from 50 to 200 kg under this collector set-up, the efficiency decreased by 41%. When the number of collectors is fixed and saline water increased from 50 to 200 kg, both the daily yield and efficiency decrease by around 46%. The daily exergy and exergy efficiency were reported to increase with increase in collector number until two collectors. The exergy of the still varied

and maximised late in the day, thereafter decreasing. Increasing the number of collectors beyond two collectors decreases the exergy efficiency. The optimum number of collectors was reported to increase with an increase in saline water. However, the distillate yield hit a maximum at 50 kg of saline water depth coupled with four collectors.

Manokar et al.'s (2018) study on an inclined solar panel basin (ISPB) sola still involved comparing passive and active modes of the ISP. An active ISPB was achieved by coupling it with an FPSC for the enhancement of distillate productivity. For almost similar average solar intensities, the average temperatures of saline water flowing through the basin and the basin itself were 9.3% and 5.1%, respectively, higher than a passive still. In addition, the maximum evaporative heat transfer coefficient for an active mode was reported to be 25% higher than that of a passive still. Furthermore, the distillate production was found to be 7.91 kg/day and 4.38 kg/day for an active and passive mode, respectively. Lastly, the maximum thermal efficiencies of an active and passive mode were 66.49% and 50.94%, respectively. The distillate yield of an active mode was 44.63%, higher than the passive mode

Badran et al. (2005) studied enhanced distillate production due to solar still augmented with a flat plate solar collector compared to a passive solar still. The highest improvements were reported at 231% when tap water was used and 52% when saline water was used. The high production rate of an active solar still was attributed to higher temperatures in the basin compared to a passive solar still. However, the efficiency of an active solar still was reduced by 2.5% and 6% when freshwater and saline water were used, respectively. It is evident, when comparing the studies by Manokar et al. (2018) and Badran et al. (2005) above, there is a distinct difference in efficiencies. One study reported an increase in solar still efficiency in an active mode while the other reported the opposite. This inconsistency could be attributed to the fact that one system had a stagnant saline water pool which could eventually reach its boiling point. The boiling of saline water in the basin reduces the solar still efficiency (Chen et al., 2017). The other system had a thin film of flowing saline water over the basin surface area and thus heat dissipation occurred rapidly. It has been reported by various researchers that the downside of elevated temperatures in the solar still with a pool of saline water is that it affects the efficiency of the still negatively. Alternatively, a passive solar still has the advantage of producing vapour at lower temperatures and thus the efficiency is increased.

Morad et al. (2015) conducted a study to improve the performance of a double slope solar still coupled with FPSC using condensing glass cooling. The condensing cover and saline water temperature of a passive solar still reached a maximum of 48°C and 54.5°C in the afternoon, respectively. On the other hand, the condensing cover and the saline water of an active solar

still were maximised at 70°C and 75°C in the afternoon, respectively. Therefore, the effects on the temperature of a double slope solar still with and without a solar collector are evident. However, the question remains concerning solar still efficiency as higher saline water temperature is reached.

2.5 Multistage solar still with waterbed

In this section, a multistage solar still with stack stages (MSS-SS) is discussed in detail. The multistage solar stills in the literature are categorised based on the nature of waterbed in their stages. There are two categories of waterbed in the stages of typical multistage solar stills. One can be defined as a pool of stationary saline water in the stage, also known as stagnant waterbed. The other can be defined as saline water flowing over the surfaces of the trays in the system, also known as flowing waterbed. Waterbed in the stages of a multistage have a common purpose of transferring evaporative and convective heat to the immediate surroundings. Based on the description above, improvements such as different stage configurations, vapour flow patterns and stage tray angles occurring over time are discussed. The MSS-SS are discussed in chronological order, starting with the earliest MSS-SS as found in the literature.

2.1.9 Stagnant waterbed

A simulation study of MSS-SS reported by Adhikari et al. (1995) involved an experimental work and theoretical modelling of the MSS-SS. An indoor experimental work was conducted on a three-stage MSS-SS. An electrical immersion heater with parallel heating coils, one with 51.6 ohms resistance and the other with 46.7 ohms, were used instead of a solar collector. Thermal energy was supplied in the entry stage of the solar still. Stage 2 received its heat from the latent heat of condensation from stage 1. Stage 3 was heated-up by the vapour generated in stage 2. Heat recovery and the heating-up of saline water was achieved in the process. The feed water (saline water) was fed from the topmost tray of the system by gravitational influence. The theoretical modelling data of the steady state performance of the three-stage system was based on this experimental work. A rectangular shaped tray was used for the first stage with an area of 0.330 m^2 and depth of saline water at 80 mm and 100 mm in the middle and sides, respectively. An approximate averaged amount of saline water in the first tray was 29.7 litres (say 30 litres). The intermediate trays were made into V- shapes to allow distillate to collect on the underside of the tray where the trough was located. The Saline water depth on the V-shaped trays was maintained at 50 mm. Vapour tightness between the stages was achieved with rubber sealing. It was reported that the experimental distillate yields were 0.640 and 2 kg/h for an input power of 358 and 890 W, respectively. The theoretical values were

reported to be 0.646 and 2.207 kg/h for the same power input values. Furthermore, the distillate yield increased proportionally with an increase in the number of stages. However, there was a limit to the number of stages to which the distillate could increase linearly. The study concluded that the three-stage MSS-SS showed tremendous potential in terms of productivity compared to other solar stills developed at a time.

Jubran et al.'s (2000) study on a numerical modelling of a multistage solar still involved the development of a numerical model to analyse the performance of the multistage solar still. Thermal energy was supplied to the entry stage at the base of the system through a heat exchanger. Stage 2 received its thermal energy from the latent heat of condensation from stage 1. Stage 3 received its thermal energy from stage 2 through the latent heat of condensation as well. The heat recovery through heating-up of saline waterbed and the expansion nozzle was employed to enhance the productivity of the system. The three-stage MSS-SS was also evacuated to enhance the evaporation rate at relatively lower temperatures. The stage trays, except for stage 1, were inclined but not depressed in the middle to form a V-shape. Power input equivalent to 120 to 1200W/m^2 were used in the determination of the performance of the solar still where a 1.2 m^2 solar collector is used. These daily average solar intensities were estimated for the Middle East and Far East geographical locations. It was determined that as the number of stages increase, the distillate yield of the added stage decreases. In addition, at high solar insolation (equivalent) the distillate yield reduction is significant compared to low solar insolation. The maximum hourly distillate yield was reported at 0.56 kg at 1000W of input power. The cumulative daily distillate yield was reported at 4.5 kg at an evaporation area of 6.5 m^2. Moreover, increasing the evaporation area increases the efficiency and productivity of the solar still. The optimised operating conditions were predicted to produce 9 litres/m^2 and a feed water flow rate of 0.0028 kg/s based on the 87% thermal efficiency and the evaporation area of 6.5 m^2.

A standalone MSS-SS was reported by Schwarzer et al. (2009); this system was reported to fully function without any external energy source except for a solar collector. The experimental and simulated work was conducted in four different geographical location – Germany, India, Spain and Brazil – in a laboratory using an electric heater on single stage set-up. The field work consisted of four prototypes divided into two energy source type. One energy source type was the FPSC, the other was the ETSC. A distillate yield when potable water was used as feed water was 32-60 litre/day under solar intensity of 6-8 kWh/m^2 and collector areas of 5 m^2 and 2.2 m^2 for the FPSC and ETSC, respectively. There was a 20% reduction in productivity when the saline water was used as feed water. Distilled water was used as the

heat transfer fluid (HTF) to avoid corrosion in the collector. A feed water (saline water) supply mechanism that can be either mechanically or electronically controlled was used. The feed water was supplied as reported by Adhikari et al. (1995), and the heat recovery and saline water heating was achieved, as reported by Adhikari et al. (1995) and Jubran et al. (2000). The study reported the condensing tower had 5-7 condensing stages stacked on top of one another for heat recovery. The stages of MSS-SS can be removed, cleaned and replaced. Saline water in the entry stage of the system was heated-up to 95 to 100°C. Therefore, the system can be classified as high temperature active solar distillation (Sampathkumar et al., 2010). Due to the insulation and water thermal storage capacity, the saline water temperature in the system was reported at 80°C after sunset and 45°C the following morning. In addition, the night productivity was reported as higher due to the thermal storage capacity of feed water. The MSS-SS was considered suitable for remote and rural areas as its standalone ability made it suitable for such working environment. No electric equipment or complex electrical controlling units were required for the system to operate. The distillate produced was also tested for its quality: it was found that about 98% of incondensable, potentially harmful solids were removed.

Ahmed et al. (2009) conducted a study on the characteristics of an evacuated multistage solar still consisting of experimental work under actual weather conditions and simulated results. The three-stage MSS-SS was vapour tight and well insulated from outside conditions. The thermal energy supply, feed water supply, heat recovery process and heating of saline water in the intermediate stages was done the same way as reported by Adhikari et al. (1995), Jubran et al. (2000) and Schwarzer et al. (2009). However, unlike the standalone MSS-SS, a solar operated vacuum pump was employed to evacuate the stages of the system. Each stage was maintained at a pressure below atmospheric pressure. The pressure gradient P1 >P2 > P3 was maintained in the stages, that is, the pressure in stage 2 was lower than the pressure in stage 1. Decreasing the working pressure in the stages from 1 bar to 0.7 and 0.5 bar enhanced the distillate yield by 20 and 45%, respectively. Moreover, the maximum distillate yield was achieved at the lowest vacuum pressure of 0.5 bar. For simulated analysis, FLUENT computer software determined the varying heights of the solar still. The characteristic height of the stages varied from 26 to 36 cm at constant temperature differences and constant pressure. The height of the system has profound influence on the productivity of the solar still. Increasing the height reduces the still's productivity. In addition, as the lower waterbed was operating at a temperature of 70°C, the system can be classified as a high temperature active solar distillation (Sampathkumar et al., 2010).

Shatat and Mahkamov (2010) conducted a study to determine the rational design parameters of a multistage solar still using transient mathematical modelling. The four stage MSS-SS was tested in a laboratory with the heat source as heat pipe-in-evacuated tube collector with 20 tubes. The experiments were conducted under two setting, namely, when the system was partially insulated and when it was fully insulated. An array 110 halogen flood lights simulated solar intensity over the ETSC. The stage trays were made into rectangular shapes with length and width of 1200 and 400 mm, respectively. The stage trays were inclined at 8° to allow the distillate to trickle down for collection. The entry stage was reported to be the largest compartment with saline with a saline water depth of 40 mm. The synthetic saline water was 18.4, 4.2, 4.8 and 4.3 litres in the first, second, third and fourth stage, respectively. Saline water depth in the inclined intermediate stages was maximum at 25 mm. A closed loop thermosiphon circuit with external copper pipe diameter of 15 mm and total length of 7 m was used. The system was simulated using prepared synthetic brackish water. The thermal energy supply, feed water supply, heat recovery process and heating of saline water in the intermediate stages occurred in the same way as reported by Adhikari et al. (1995), Jubran et al. (2000), Schwarzer et al. (2009) and Ahmed et al. (2009). The heat transfer fluid (HTF) was circulated by an electric pump between the solar collector and the entry stage. At a certain aperture area of the solar collector and the dimensions of the still when the system is fully insulated, the system gradually reaches thermal damage. Thermal damage is an instance when the condensing surface temperature exceeds the evaporative surface temperature. When thermal damage is reached, the desalination process stops altogether. However, partially insulating the solar still prevented the instance when thermal damage was reached. The desalination process was reported to continue for a full 24-hour period after which, the saline water temperature was at 30 and 40°C. The continued desalination process can be attributed to the saline water thermal storage ability and insulation material on the body. In addition, after the simulated sunset (switching the flood lights off), the saline water temperature gradually decreased. The uninsulated top tray temperature was observed to decrease to 80°C while that of the lower stages (stage 1 and stage 2) was maximum at 99-100°C. The distillation efficiency of the solar still was 90% and the experimental distillate yield was 9 kg/day. The optimised number of stages was reported to be 4 or 5 for stage trays with 1 m^2 dimensions and an ETSC of 1.7 m^2.

Singh et al. (2012) conducted a performance evaluation of low inertia multistage solar still. The five-stage MSS-SS was experimentally studied under actual weather conditions. Corrugated (V-shaped and A-shaped) stage trays had a small 15° inclination on each corrugated part. In other words, instead of a normal flat tray, the surfaces of the trays were made from a series of small, inclined surfaces. It was reported that the V shape was to have

as minimal saline water on the tray's surface as possible, whereas the A shaped part of the tray is used to separate the saline water into small pools. Thermal energy was supplied through an FPSC of a fin and tube type. The mass of saline water in the entry stage was 14.7 kg and in the upper stage was 6.125 kg. The thermal energy supply, feed water supply, heat recovery process and heating of saline water in the intermediate stages occurred in the same way as reported by Adhikari et al. (1995), Jubran et al. (2000), Schwarzer et al. (2009), Ahmed et al. (2009) and Shatat and Mahkamov (2010). The highest distillate yield was reported to be at 1.5 $m^2$of evaporation area of the stage tray. Maximum distillate yield of 7.41 litres/m^2/day was reported as 2223 litre/m^2/year for a 300-day period. The theoretical distillate yield values were reported to be 10% higher than the experimental values.

Estahbanati et al. (2015) conducted an experimental investigation of the effect of the number of stages on a multistage solar still. The four-stage MSS-SS was experimentally studied as four separate units on continuous and non-continuous modes. Continuous mode is a non-stop operation of the system, while the non-continuous mode, the experimental work, is only conducted for a certain period of the day (i.e., daytime). Saline water was supplied from the top of the stacked stages, similar to the systems discussed above. Thermal energy was supplied to the entry stage in the similar manner as reported by Shatat and Mahkamov (2010). The MSS-SS entry stage was rectangular shaped with 20 kg of saline water. The rest of the stages were inclined at 8° and each had a 14 kg of saline water. Vapour tightness was achieved to prevent any vapour leaks from the system. The simulated solar intensity followed the actual solar variation throughout the day. It was reported that under non-continuous mode, the distillate production of the upper stages of the MSS-SS was delayed. In addition, the delay increases as the number of stages increases. The cause of the delay was that thermal energy is supplied from the bottom only (entry stage) while the rest of the stages wait for the entry stage to supply thermal energy. During the continuous mode experiments, the delay in the production of the upper stages was absent. Moreover, the upper stages were more productive during the night. The lower stages were reported to be more productive than the upper stages during sunshine hours. The low productivity of the upper stages was associated with the thermal energy supply at the bottom of the system. The upper stages depend entirely on the lower stages for thermal energy supply. Low heat transfer efficiency between the stages was reportedly a result of heat loss from the walls, vapour condensing on the walls and other parts/components where it cannot be collected, droplets dropping back into the pool of saline water, removal of some thermal energy with freshwater and unsteady device operation mode resulting in the storage of some energy at the end of the experiment. The current study can add that the disposal of brine also removes some thermal energy along with it. Furthermore, entry stage produced maximum distillate; the production reportedly decreased with an

increased number of stages, as reported by Jubran et al. (2000). Introducing one or more additional stages, the distillate yield increases more under a continuous mode compared to non-continuous mode. In a continuous mode, adding up to ten stages increases each stage output by 1 kg, which is contrary to the behaviour of a non-continuous mode: having more than six stages increases productivity by an insignificant value and thus only 23.8 kg can be produced a day. The overall distillate output of the still is increased by adding additional stages. Comparing the continuous and the non-continuous mode in terms of the distillate yield, the continuous mode shows that adding the 4th stage on a three-stage system, the distillate yield improves dramatically to 27.1 kg/day. However, the non-continuous mode shows only slight increase to 22.9 kg/day in the distillate produced when the fourth stage is added.

Feilizadeh et al. (2015) studied the effect of amount and mode of input energy on the performance of a multi-stage solar still. To do so, two MSS-SS were built, and experiments were conducted indoors. The construction of the MSS-SS was similar to those reported by Estahbanati et al. (2015). Furthermore, the indoors experiments were reported to expressly demonstrating the productivity capabilities of the evaporation chamber. The four-stage MSS-SS was constructed with stage trays sloped at a minimum angle of 8°. A 1200 W electric heater supplied thermal energy and 100 mm insulation material was used on the body of the still. The thermal energy supply apparatus was similar to that reported by Shatat and Mahkamov (2010). Different distillate yields were determined based on the CBA ratios. It was reported that the distillate production in the MSS-SS was a quadratic function of the CBA ratio. It was further reported that feeding the energy impulsive only enhances the distillate productivity by 5-10%. The distillate yield decreased as the number of stages increased, for instance, the fourth stage produced only half of what the entry stage produced. The decrease in distillate as the number of stages increase was also reported by Estahbanati et al. (2015), Shatat and Mahkamov (2010) and Jubran et al. (2000). The delay reported by Estahbanati et al. (2015) was due to the method of energy input into the system, the production in the upper stages starting later than the lower stages. The productivity of stages was reported to mimic the temperature variations of the stage, that is, the higher the saline water temperature in the stage, the higher the productivity. In addition, the upper stages were reported to surpass the productivity of the lower stages at night. Distillate production was high when the impulse thermal energy input was employed, compared to applying and following solar energy patterns. Only when the CBA is higher, that is, if the area of a collector is much larger than that of a basin and the system cannot operate at high temperatures, that thermal energy storage (TES) can be augmented.

Bait and SI-Ameur (2016) conducted a numerical investigation on a multistage solar still, investigating the effect of solar radiation term on mass and heat energy balance. The four-stage MSS-SS consisted of V-shaped trays made into a rectangular shape. The flat plate solar collector was inclined at an altitude equal to the local area. The stage set-up was similar to that reported by Estahbanati et al. (2015) with the entry stage tray being the largest. The trays of the system were inclined at an angle to allow produced distillate to collect at the bottom. A closed-loop thermosiphon cycle supplied the thermal energy to the system under natural mode. A maximum of 80.96°C saline water temperature in the first stage was reached during daytime operations. Therefore, the system can be categorised as a high temperature active solar distillation (Sampathkumar et al., 2010). The bottom trays of the first stage were varied to study the effect of different areas on evaporation. Enhanced evaporation was achieved on the largest area of (1.2 x 0.4) m^2. The distillate production pattern is the same as in other studies above. The entry stage produced more distillate than the rest of the stages above. The total daily cumulative distillate yield from the system was reported to be 8.88 kg.

Chen et al. (2017) studied a multistage solar still with stack stages with the intent to analyse the heat and mass transfer mechanism in a system. The three-stage MSS-SS had stacked stages and a CSS situated on top of the rest of the stages. The last stage had a transparent glass to receive solar radiation directly from the sun rays. For simulation purposes, an electric heater simulated solar intensity on the MSS-SS. While during tests under actual weather conditions, the MSS-SS was supplied with thermal energy through an evacuated tubes solar collector. The solar collector was inclined based on the latitude of the local area where the still was tested. The effective area of each stage tray was reported to be 0.4 x 0.55 m^2. The stage trays were made into shape similar to that reported by Singh et al. (2012). It was determined that since heat is transferred through evaporation and condensation between the stages, the system does not reach a steady state easily. The saline water temperature of the last tray (stage 3) was reportedly higher than of the second tray momentarily, attributable tto the direct heating by solar radiation as the third stage was a CSS. The distillate production delay in the intermediate stage of the solar still was similar to those reported by Estahbanati et al. (2015), Shatat and Mahkamov (2010), Feilizadeh et al. (2015) Jubran et al. (2000) and Chen et al. (2017). Due to the adverse effects of boiling of saline water, the temperature of the system was maintained below 100°C. Temperatures beyond boiling point reduce the production rate of the distillate. The daily maximum distillate yield of 8.1 kg/m^2 was reported at minimum saline water depth of 2 cm and a performance coefficient of 1.12.

Soni et al. (2017) studied a wind-solar hybrid system for wastewater treatment. The hybrid MSS-SS condensing tower consisted of four stages and wastewater was used as feed water.

The solar still was a self-sustaining system which can be installed in a household. The system, assisted by wind energy, raised wastewater from the ground up to the roof where desalination takes place. The system was evacuated as such that P1 >P2 > P3 > P4 was as described by Jubran et al. (2000). Sealing material prevented any vapour leaks to the surroundings or ambient air from entering the system since it was evacuated. The MSS-SS had a CSS at the top of the stacked stages, as reported by Chen et al. (2017) and Shatat and Mahkamov (2010). Thermal energy was supplied at the bottom of the stacked trays as reported by Shatat and Mahkamov (2010) and Bait and SI-Ameur (2016). Likewise, it was reported that the distillate increases linearly with the increase in the number of stages. However, there is a limit of the number of stages to which the distillate increases proportionally, also in agreement with earlier studies. The productivity of the hybrid MSS-SS was three times greater than that of a CSS. Moreover, the greater flow rate or larger body of water has more thermal storage and thus less evaporation takes place. A distillate yield of 17.4 kg/m^2/day was reported when the system was operated for 6 hours per day.

Abdessemed et al. (2019) conducted a study on the design of stage trays with trays of V and A shapes. The four-stage MSS-SS was experimentally studies using tap water. The saline water in the entry stage was 17 litres and the rest of the intermediate stages were 6 litres each. The experiments were first conducted on the V-shaped trays and then the A-shaped trays. The method of heat transfer through the latent heat of condensation, as reported by other studies above, was used in this system. The maximum temperature reached in the first stage was 53.7°C, that is, the highest temperature in the system. Daily distillate yield of 1370 ml was produced by the V-shaped trays which were reportedly more effective than the A-shaped trays. On the other hand, the daily distillate yield of 1020 ml was reported to have been produced by the A-shaped trays. In addition, the heat loss from saline water in the stages was reportedly lower on the V-shaped trays as the water was concentrated in the middle. However, the A-shaped trays lost more heat as saline water was against the walls of the condensing tower. The distillate productivity pattern in both the shapes of the trays was reported to follow that of the studies above, that is, the lower stages yield more freshwater than the upper stages. Table 2.3 shows the energy input type and the distillate yield from each MSS-SS. The MSS-SS has not been widely studied like the single effect solar stills and therefore, limited information is available in the literature.

Table 2.3. MSS-SS energy input type and distillate output

System type	Energy type	No. of stages	Distillate output	Author(s)
Multistage	Auxiliary immersion heater	3	2 kg/h	Adhikari et al. (1995)
Multistage	Solar panel	3	9 kg/m^2/day	Jubran et al. (2000)
Multistage	FPSC and ETSC	5-7	15 -18 l/day	Schwarzer et al. (2009)
Multistage	Solar collector	3	14.2 kg/m^2/day	Ahmed et al. (2009)
Multistage	ETSC	4-5	9 kg/day	Shatat and Mahkamov (2010)
Multistage	FPSC	5	7.41 kg/m^2/day	Singh et al. (2012)
Multistage	Solar collector	4	27.1 kg/day	Estahbanati et al. (2015)
Multistage	Solar collector	4	9.54 kg/day	Feilizadeh et al. (2015)
Multistage	FPSC	4	8.88 kg/day	Bait and SI-Ameur (2016)
Multistage	ETSC	4	7.29 kg/day	Chen et al. (2017)
Multistage	FPSC	4	17.4 kg/m^2/day	Soni et al. (2017)
Multistage	Electric heater	4	1370 ml	Abdessemed et al. (2019)

2.1.10 Flowing waterbed

Franco and Saravia (1994) introduced a new design of multistage solar still with stack stages. The four-stage MSS-SS was designed with inclined stage trays at 25° to allow saline water to flow over the surface of the tray. An electric heater was used for experimental tests of the system. The stage trays were covered with a fabric that enhances the saline water distribution over the trays as it flows over it. Saline water, supplied from the top of the system, flowed down through the trays under gravitational influence. Thermal energy was supplied in the entry stage as in the MSS-SS, discussed under the stagnant waterbed section. The saline water increases its temperature as it flows over the trays from top to bottom of the system. However, saline water that reaches the lowest tray without evaporating it is ejected from the system at the higher temperature. The study further reported that a distillate of 5 litres per hour was possible for 1 m^2 stage tray. In addition, the distillate yield was reportedly affected by the change in temperature of the stage tray. A minimum saline water level is recommended for increased productivity in the solar still. The distillate yield was inversely proportional to the stage numbers, such that the fewer the stages, the higher the distillate output from the system. Furthermore, changing the saline water flow rate and its temperature had minimal effect to the distillate productivity.

Schwarzer et al. (2001) conducted a study on solar thermal desalination with heat recovery. The six-stage MSS-SS was constructed with the last stage as a saline water supplier to the rest of the system. Thermal energy was supplied at the bottom of the system through natural

convection using HTF and at the entry stage of the condensing unit. Heat transfer to the upper stages (stage 2, stage 3, etc.) was achieved in the similar way discussed under the stagnant waterbed section. That is, latent heat of condensation from stage 1 is transferred to the saline water in stage 2, from stage 2 to stage 3, and so on. A single stage unit was constructed and experimentally tested to establish various parameters required for the construction of the main system. The upper plate of the unit was tilted at 14°. During the experimental tests, an electric heater simulated solar insolation. Each tray was constructed to dimensions of 0.8 x 0.8 m^2 and the amount of saline water in each stage was reported as 25 litres. The saline water was fed from the topmost tray of the system and flowed down under gravitational influence. The system reportedly has a potential distillate productivity of 25 litre/m^2/day.

Reddy et al. (2012) conducted an elaborate analysis on an evacuated multistage system with a series or parallel connections of the FPSCs. The modelling of the MSS-SS with stage trays inclined at 16° and had a total area of 1 m^2 each. Thermal energy was supplied at the entry stage as reported by all the above studies. Heat transfer to the upper stages originated from the entry stage by means of latent heat of condensation from the adjacent lower stage. Furthermore, the thermal energy external energy source was FPSC connected in either series or parallel. The gravitational influence was employed to circulate the saline water through the FPSC and the condensing tower. The stage tray surfaces were covered with porous silk cloth for the purpose described by Franco and Saravia (1994). The cloth aided in enhancing the distillate due to the minimum saline water depth over the tray surface. It was reported that, in addition of thermal energy contained by incoming saline water, the latent heat of condensation from the lower stages increased the evaporation in the upper stages. The increased evaporation also increased the distillate productivity in the upper stages. For this reason, upper stages produced more distillate than lower stages. It was reported that the series connected FPSC experiences higher thermal energy loses and thus the cumulative thermal energy collected is reduced. However, the parallel connected FPSCs were reported to collect more thermal energy than the series connection. The optimum daily distillate yield was reported at 21.77 and 24.13 kg/m^2 for series and parallel connected FPSC, respectively. The number of stages clearly impacted the daily distillate yield for the MSS-SS operating at atmospheric pressure. Increasing the number of stages beyond five stages had no significant impact on the distillate yield; therefore, an optimum number of stages was four under any climatic conditions. An optimum feed water flow rate and stage gap were reported at 55 kg/m^2/day and 100 mm, respectively. Decreasing the flow rate any further to 30 kg/day also decreases the distillate yield. The high salinity concentration in the saline water was reported to decrease the evaporation rate by as much as 20%. In turn, the reduced evaporation rate affects distillate output from the MSS-SS. An optimised system was reported to produce a

maximum daily distillate yield of 28.044 kg/m^2 in March. In the absence or reduced solar incidence, the cumulative distillate yield increased slightly due to the sustained stage temperature difference from the FPSC. Furthermore, the vacuum pressure in the stages can only be reduced to a certain pressure and not beyond that. This is because the temperature difference between the stages decreases, causing the vapour condensation to retard, thereby decreasing the distillate output. Distillate output and some important features of the systems with flowing waterbed are presented in Table 2.4.

Table 2.4. Distillate yield from MSS-SS with flowing waterbed

System type	Energy source type	No. of stages	Distillate output (kg/m^2/day)	Author(s)
Multistage	Electric heater	4	5	Franco and Saravia (1994)
Multistage	FPSC	5	25	Schwarzer et al. (2001)
Multistage	Solar panel	4	28.04	Reddy et al. (2012)

1 litre = 1kg

2.6 Identified hurdles in the operation of the MSS-SS

Some of the reported, observed challenges and hurdles in the operation of the MMS-SS are presented under the following sub-headings. Some of these hurdles apply to MSS-SS with stagnant waterbed only, some to MSS-SS with flowing waterbed and some apply to both types of waterbeds. While the hurdles also reportedly affect solar stills in general, attention is given to the MSS-SS in particular.

2.1.11 Salinity levels in the saline water and other related contaminants

There have been some reported adverse effects caused by salt content and other related contaminants in solar stills in general and MSS-SS specifically. Adhikari et al. (1995), Schwarzer et al. (2001) and Soni et al. (2017) concur that in a system with waterbed, feed water (saline water, wastewater, brackish water) comes into contact with the stage trays. The contaminants present in the feed water leave behind some sort of build-up (of contaminants) which contaminate the stage tray and the lining. Due to the presence of salt residue and other contaminants, the stage lining clogs over time from impurities left behind by the feed water. The build-up on the tray surface also causes fouling over time which then affects the heat transfer ability of the tray (Chen et al., 2017). Therefore, regular cleaning of the stage trays is required. However, depending on the methods used to clean the trays, the vapour tightness and structural integrity of the system may be affected. In addition, additional cost of cleaning the trays is added as the dissolved solids can be cleaned using citric acids or oxalic acid; these acids are not harmful (Salem, 2013). The two types of waterbeds, stagnant and flowing, are

representative of static and dynamic modes of operations, respectively. The static mode results in dissolved solids deposited onto the tray's surface during operation, deposits that harden on the tray's surface and require cleaning as the major maintenance work. The dissolved salt deposits or solids that accumulate on the surface of the tray under dynamic mode of operation are continuously washed away (Salem, 2013). Schwarzer et al. (2001) also reports that the circulation of feed water in a stage eliminates salt accumulation in the stage. Therefore, salt residue build-up in the MSS-SS with flowing waterbed is less as the feed water removes some salt as it flows over the tray surface. The MSS-SS with stagnant waterbed is most likely to experience exponential growth of such contaminants in the stage tray. Soni et al. (2017) also found that the larger body of water, the more thermal storage capacity it has and thus, less evaporation would occur. Furthermore, the higher the salinity concentration that accumulates over time and the bigger the pool of water, the lower the evaporation rate (Abdenacer & Nafila, 2007). Reddy et al. (2012) contend that high salinity concentration in the saline water decreases the evaporation rate by as much as 20%.

2.1.12 Dependency of stacked stages of the MS-SS system

In the studies discussed under section 2.5, all report that thermal energy was supplied to the entry stage at the bottom of the condensing tower. Thermal energy transfer to the upper stages was achieved through the latent heat of condensation from the lower stages. Therefore, there is a delay in starting the desalination process in the upper stages due to the way thermal energy is supplied (Estahbanati et al., 2015; Shatat & Mahkamov, 2010). This also means any thermal energy loss, vapour leaks or unproductiveness of any lower stage(s) of the MSS-SS; the upper stage will be affected too. In fact, the evaporation rate in the upper stage is directly proportional to the thermal energy received from latent heat of condensation in the lower adjacent stage. Estahbanati et al. (2015) reported that the lower stages tend to be more productive than the upper stages. The low productivity of the upper stages was associated with the thermal energy supply at the bottom of the system. The upper stages depends entirely on the lower stages for thermal energy supply. Low heat transfer efficiency between the stages was reported as a result of heat loss from the walls, vapour condensing on the walls and other parts/components where it cannot be collected, droplets dropping back into the pool of saline water, removal of some thermal energy with freshwater and device operation in unsteady mode resulting in the storage of some energy at the end of the experiment. This current study can add that the disposal of brine also removes some thermal energy along with it. However, in the set-up such as the one reported by Chen et al. (2017), the top stage in the MSS-SS is exposed for direct heating by solar incidence and therefore, evaporation in such a stage is also influenced by direct heating. Reddy et al. (2012) reported that in addition to hot incoming

feed water from the solar collector, the latent heat of condensation from the lower stages increases the temperature of saline water in the upper stages. The upper stages thus experienced a higher evaporation rate. This high evaporation leads to higher distillate output and therefore upper stages produce more distillate than the lower stages. Therefore, with the exception of the configuration reported by Chen et al. (2017) and Reddy et al. (2012), the distillate production pattern is that lower stages yield more freshwater than upper stages. The stage dependency is still common to all system with varying degrees of dependency.

2.1.13 Collected distillate by the trough

The distillate collecting trough position and orientation differs from one system to the other. The produced instantaneous distillate in the solar MSS-SS is collected by the trough and delivered to the distillate tank. The distillate is formed on the underside of the stage tray and is directed to the collecting trough for collection. Estahbanati et al. (2015) claimed that one of the causes related to low productivity was the vapour condensing on the walls and other parts/components where it cannot be collected as well as droplets dropping back into the pool of saline water. Furthermore, Abdessemed et al. (2019) explain that due to the design of the trough, some droplets trickle back into the pool of saline water in the stage. Distillate collecting troughs are designed and installed in different ways. Some are positioned along the inclined length of the tray on the underside (Bait & SI-Ameur, 2016) while others are installed at the bottom end of the inclined tray (Soni et al., 2017; Estahbanati et al., 2015). Soni et al. (2017) suggest that the condensing surface of a tray must be inclined at a certain angle to enable the condensate to trickle downwards and not fall back into the pool of saline water in the stage. In the MSS-SS studied by Singh et al. (2012) and Chen et al. (2017), corrugated stage trays were presented. Distillate collecting troughs were installed under each corrugated V-shape of the tray resulting in far superior collecting efficiency of these designs.

2.1.14 Stagnant waterbed with unequal saline water depth

It has been reported by Prakash and Velmurugan (2015) that a solar still's productivity is maximised when the saline water is at its minimum in the basin or stage. However, in the MSS-SS system with inclined stage trays, a minimum saline water depth cannot be maintained throughout the stages. Figure 2.2 shows a typical MSS-SS with inclined stage trays. The depth of saline water has a linear relationship with the angle of an inclined tray. This relationship means the greater the inclination angle, the deeper the saline water depth. Higher angles can lead to dry spots on the shallow end of the saline water in the stage tray (Van Steenderen, 1977). In an inclined stage tray, especially with greater angle of inclination, a 5 cm saline water depth as recommended Adhikari et al. (1995) cannot be maintained.

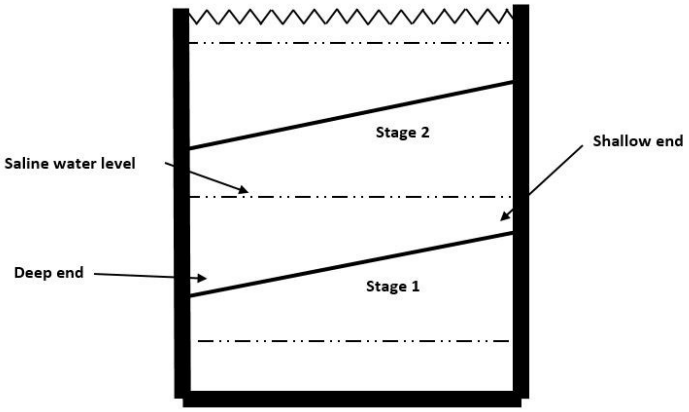

Figure 2.2: Stage trays with unequal saline water depth

2.7 Distillate yield pattern of individual stages of the MSS-SS with waterbed

A trend of distillate yield in the MSS-SS with waterbed in the stages was briefly alluded to under section 2.6.2. The MSS-SS under either static or dynamic mode of operation in the stages shows a certain pattern of freshwater output from individual stages. The lower stages of the MSS-SS tend to produce more distillate than the upper stages (Feilizadeh et al., 2015; Bait & SI-Ameur, 2016). It has already been discussed that there are systems reported to have more productive upper stages compared to the lower stages (Reddy et al., 2012; Chen et al., 2017). Table 2.5 presents one example of stage productivities of the MSS-SS with flowing waterbed. It is evident that the saline water temperature and the distillate yield in the entry stage are higher than the rest of the other individual stages

Table 2.5. Distillate yield of each individual tray of the MSS-SS with flowing waterbed

Description	Stage 1	Stage 2	Stage 3	Stage 4	Total	Author(s)
Distillate per stage (kg/h)	0.3	0.27	0.22	0.14	0.93	Franco and Saravia (1994)
Temperature per stage (°C)	82.2	70.5	53.2	27		

In Table 2.6, distillate yield of individual stages of the MSS-SS is presented. Once again, it is evident from the table that the entry stage has a higher distillate and saline water temperature compared to other individual stages. Productivity decreases as the number of stages increases.

Table 2.6. Distillate yield of each individual stage of the MSS-SS with stagnant waterbed

Description	Stage 1	Stage 2	Stage 3	Stage 4	Total	Author(s)
Distillate per stage (ml)	310	235	145	110	1120	Abdessemed et al. (2019)
Temperature per stage (°C)	53.7	50.9	45.3	43		

However, in the study reported by Reddy et al. (2012), the opposite of what is reported in Table 2.5 and Table 2.6 is revealed. Table 2.7 presents the distillate yield results of the individual stages of the evacuated MSS-SS. The results show that the uppermost tray produced more distillate than the rest of other individual stages. It should be noted, however, that thermal energy in the study by Reddy et al. (2012) was not supplied in the entry stage.

Table 2.7. Distillate yield of each tray of a multistage solar still with stacked trays and flowing waterbed at atmospheric pressure

Description	Stage 1	Stage 2	Stage 3	Stage 4	Total	Author(s)
Distillate per stage ($kg/m^2/d$)	0.85	4.17	9.45	13.58	28.04	Reddy et al. (2012)

Distillate yield as a result of different pressure and feed water is presented in Table 2.8. The table shows that varying the pressure below atmospheric pressure enhances the distillate yield of the system. In addition, when using feed water with different salinity levels, different distillate yields are achieved. For instance, at 0.03 bar when freshwater was used as feed water, about 97% distillate yield improvement was achieved compared to atmospheric conditions.

Table 2.8. Total distillate yield from different feed water and pressure below atmospheric pressure

Pressure (bar)	Feed water	Distillate per stage ($kg/m^2/d$)	Percentage increase (%)	Author(s)
0.03	Freshwater	53.21	96.75	Reddy et al. (2012)
0.02	Brackish water	42.04	76.44	
0.02	Saline water	40.26	73.13	
0.02	Brine solution	33.05	60.09	

2.8 Some reported methods used to ease the operation of solar stills in general

There are many ways that researchers have introduced to improve the operability of solar stills. For instance, Badran and Al-Tahaineh (2005) and Manokar et al. (2018) integrated an external saline water tank to constantly supply the basin type solar still with saline water

throughout the experimental tests. It was reported by Taghvaei et al. (2014b), under sub-section 2.3.3, that saline water diminished from 95 mm to 40 mm over time as evaporation takes place. In a system integrated with an external saline water tank, the saline water level is maintained throughout the operation of the system. In addition, there is no need for human intervention in terms of regularly refilling the diminished saline water. However, to maintain the level of saline water, a control mechanism such as a valve is required. Badran and Al-Tahaineh (2005) reported that a saline water tank was fitted with a float valve to control and regulate the saline water level at a pre-determined water depth. This type of valve is self-regulating and does not require any human intervention.

Many active solar stills are coupled with vacuum pumps and saline water circulation pumps. Solar still such as those studied by Morad et al. (2017), Reddy et al. (2012), Jubran et al. (2000) and others used such pumps. However, Schwarzer et al. (2009) reported a standalone multistage solar still with no pump integrated to the system. The study also reported that the multistage needs no electricity, pumps or control units to operate and consequently is suitable to operate in remote, isolated areas. The standalone feature of this present study has made a system unique from other systems using complex control units.

2.9 Cost implication of a solar still

Various authors have reported on costs related to the construction, operation and maintenance of different solar stills. The use of inexpensive, locally available materials reduces the costs associated with solar stills (Ahsan et al., 2013). Under this section, an economic analysis of solar stills in general is presented. There are many reported economic studies of solar still, however, for the purpose of this study, the economic analyses presented here are based on the studies by Fath et al. (2003), Adhikari et al. (2000) and El-Bialy et al. (2016). Parameters are applied to determine cost implications of operating a certain type of a solar still. When equipment has depreciated, there is still some value left in it; therefore, a salvage value (S) is one parameter. When the still is design constructed from start to end, there are costs involved; those costs are referred to as the present capital cost (P). The cost of ownership, operation and land rental are considered on an annual basis and hence are known as annual costs (AC). An estimated cost of producing 1 litre of water, known as cost per litre (CPL), considers all the operational costs involved. As the system tends to depreciate over time, the sinking fund factor (SFF) is used to estimate the future value of the equipment. The fixed annual cost (FAC) refers to the fixed cost of operating the equipment. The FAC does not change with the CPL. The capital recovery factor (CRF) is the ratio of constant return on the value of the equipment over the equipment's lifetime. Annual maintenance costs (AMC) is the cost of equipment upkeep and is generally estimated to be a fraction of the FAC. The

annual interest and number of productive years of the equipment are represented by i (%) and n, respectively. Annual salvage values and abbreviated as (ASV). Table 2.9 shows the summary of the CPL of various solar stills reported in the literature.

$$CRF = \frac{i(1+i)^n}{[(1+i)^n - 1]}$$

$$FAC = P \times CRF$$

$$SFF = \frac{i}{[(1+i)^n - 1]}$$

$$ASV = SFF \times S$$

$$AC = FAC + AMC - ASV$$

$$AMC = 0.15 \times FAC$$

$$S = 0.2P$$

$$CPL = \frac{AC}{M}$$

Table 2.9. Summarised cost per litre of distillate

Solar still type	CPL ($/litre)	Author(s)
Evacuated multistage solar still with expansion nozzles	0.00676	Jubran et al. (2000)
Evacuated multistage solar still	0.0672	Ahmed et al. (2009)
Multistage solar still	0.0281	Estahbanati et al. (2015)
Conventional basin-type solar still	0.0096	Rashidi et al. (2017)
Modified basin-type solar still	0.0104	
Multistage solar still	-	Adhikari et al. (1995)
Multistage solar still	-	Singh et al. (2012)
Multistage solar still	-	Shatat and Mahkamov (2010)
Standalone multistage solar still	0.0333	Schwarzer et al. (2009)
Multistage solar still	-	Feilizadeh et al. (2015)
Multistage solar still	0.0136	Bait and SI-Ameur (2016)
Multistage solar still	0.0959	Chen et al., (2017)

Conventional solar still	0.049	Sharshir et al. (2016b)
Hybrid solar desalination system (HSDS)	0.034	
Humidification-dehumidification (HDH)	0.0578	
Multistage solar still	0.0075-0.018	Soni et al. (2017)
Multistage solar still	0.000483-0.000704	Abdessemed et al. (2019)
Multistage solar still	-	Franco and Saravia (1994)
Multistage solar still	-	Schwarzer et al. (2001)
Evacuated multistage solar still	-	Reddy et al. (2012)
hemispherical shaped solar still	0.017	Arunkumar et al. (2011)
Pyramid and single slope single basin solar stills	0.026 and 0.03	Fath et al. (2003)
-Single slope single basin solar still integrated with the FPSC	0.0526	El-Bialy (2016)
-Other active single stage solar stills	0.0066-0.1103	
-Passive single slope single basin solar still	0.0124	
-Single slope single basin solar still integrated with sun tracking devices	0.1667	
-Passive single slope single basin solar still	0.009	Haddad et al. (2017)
-Modified single slope single basin solar still	0.011	
Modified single slope double basin solar still	0.006-0.06	Ayoub and Malaeb (2014)
Passive single basin double slope solar still	0.0163	Al-Hinai et al. (2002b)

1 litre = 1kg

Based on the literature surveyed, an active solar still system has a higher present capital cost as compared to a passive solar still. Passive solar stills are preferred as they have lower present capital costs while their daily productivity is relatively higher. However, the advantage of an active solar still is that it has low evaporation areas which result in low cost per litre. A single basin solar still is amongst those with the lowest cost per litre (CPL). Devices and equipment such as solar concentrating techniques contribute to the high present capital costs (El-Bialy, 2016). According to a study by Kabeel et al. (2010), the main parameters used in determining economic feasibility of a solar still are capital recovery factor (CRF), fixed annual cost (FAC), sinking fund factor (SFF), annual salvage value (ASV), average annual productivity (M) and annual cost (AC). There is also an annual maintenance cost (AMC), present capital cost (P) as well as cost per litre (CPL) which are not part of the main

parameters. However, for each specific desalination unit, the above main parameters are influenced by system size, site location, feed water properties, product water required quality and qualified staff availability.

Solar stills are subject to their design, construction and operational costs over their life span. The life cycle cost of a solar still depends on several key variables: initial investment, rate of interest, annual distillate yield, maintenance cost, lifetime of a solar still, production cost of distilled water, selling price of distilled water and salvage value of the system (Kumar & Tiwari, 2009). According to Ayoub and Malaeb (2014), the cost of distillate production is dependent on various factors such as the service lifetime, interest rate, productivity and initial capital costs. The payback period on the solar still, then, is dependent on all those factors as well. In essence, the payback period varies in each study as the authors consider different parameters and factors involved in a particular solar still.

2.10 Energy balance equation of a solar still

2.1.15 Energy balance equation of a single effect solar still

For the purpose of this study, special attention has been given to the single-effect and multistage solar stills. Solar stills, as with much other engineering equipment, have some form of energy input required for work to be done. The work in the system produces an end product (also known as system output) which can then be used or processed further. Energy balance equations are important to account for all the energies entering and leaving the system. Energy input is the sum of all energy interactions throughout the system, that is:

$$Energy\ input = \text{Useful enegry} + total\ losses$$

or

$$\text{Useful enegry} = Energy\ input - total\ losses$$

In a solar still, however, different components of the system receive instantaneous thermal energy from solar radiation throughout the day and thus each main component is determined separately. Taghvaei et al. (2014b) suggest an energy balance of a single effect active solar still as follows:

Energy balance of a condensing glass cover:

$$(m\ Cp)_g \frac{dT_g}{dt} = \left[Q_{sun,g} + U_{w-g} \times A_w \times \left(T_w - T_g\right)\right] - \left[U_{g-a} \times A_g \times \left(T_g - T_a\right)\right] \quad (1)$$

As previously demonstrated above, the term $(m\ Cp)_g \frac{dT_g}{dt}$ is the thermal energy retained by the condensing glass cover; $\left[Q_{sun,g} + U_{w-g} \times A_w \times \left(T_w - T_g\right)\right]$ is the thermal energy input to the glass cover; and $\left[U_{g-a} \times A_g \times \left(T_g - T_a\right)\right]$ is the thermal energy loss to the atmosphere. Thereafter, all other main components of a solar still follow the same approach in developing the energy balance. Energy balance for saline water, basin, and the heat transfer fluid (HTF), respectively, are as follows:

$$(m\ Cp)_w \frac{dT_w}{dt} = \left\{\left[Q_{sun,w} + U_{HTF-w} \times A_{ex} \times (T_{HTF} - T_w)\right] + [U_{b-w} \times A_w \times (T_b - T_w)]\right\} - \left[U_{w-g} \times A_w \times (T_w - g)\right] \quad (2)$$

$$(m\ Cp)_b \frac{dT_b}{dt} = \left[Q_{sun,b} + U_{b-w} \times A_w \times (T_b - T_w)\right] - [U_{b-a} \times A_w \times (T_b - T_a)] \quad (3)$$

$$(m\ Cp)_{HTF} \frac{dT_{HTF}}{dt} = Q_{col,HTF} - \{[U_{HTF-w} \times A_{ex} \times (T_{HTF} - T_w)] + [U_{HTF-a} \times A_{HTF-a} \times (T_{HTF} - T_a)]\} \quad (4)$$

Duffie and Beckman (2013) explain that the energy balance equation of a solar collector is represented by:

$$\dot{Q}_u = A_C\left[I_T(\tau\alpha) - U_L\left(T_{f,m} - T_a\right)\right] \quad (5)$$

Where $Q_{col} = A_C I_T(\tau\alpha)$, (6)

represents the solar irradiance capture by the solar collector.

The $I_T = I_b + I_d + I_r$, where I_T is the total irradiance on a tilted surface and the sum of the three components of solar irradiance, namely, beam, diffuse and reflected radiation are measured on a horizontal surface.

Where Equations (4) and (5) represent the same thermal energy balance for the solar collector in an active solar still.

2.1.16 Energy balance equation of the MSS-SS

An energy balance for the MSS-SS with waterbed was reported by Shatat and Mahkamov (2010) as follows:

In the entry stage of the MSS-SS:

$$\dot{Q}_H = M_{s1}C_P\frac{dT_{s1}}{dt} + \Delta\dot{Q}_{losses1} + m_{e1}\left(h_{fg1} + C_P T_{c1}\right) \quad (7)$$

Where $\dot{Q}_H = A_C I_T(\tau\alpha)$, energy collected by the solar collector; $M_{s1}C_P\frac{dT_{s1}}{dt}$, energy absorbed by saline water or useful energy; $\Delta\dot{Q}_{losses1}$, energy losses as reported Estahbanati et al. (2015); $m_{e1}\left(h_{fg1} + C_P T_{c1}\right)$, energy in the vapour and the condensate produced by the condensing vapour.

Stage 2

$$\dot{m}_{e1}h_{fg1} = M_{s2}C_P\frac{dT_{s2}}{dt} + \Delta\dot{Q}_{losses2} + m_{e2}\left(h_{fg2} + C_P T_{c2}\right) \quad (8)$$

The product $\dot{m}_{e1}h_{fg1}$ is the thermal input energy into stage by means of latent heat of condensation of the vapour from stage 1.

Stage 3

$$\dot{m}_{e2}h_{fg} = M_{s3}C_P\frac{dT_{s3}}{dt} + \Delta\dot{Q}_{losses3} + m_{e3}\left(h_{fg3} + C_P T_{c3}\right) \quad (9)$$

Stage 4

$$\dot{m}_{e3}h_{fg3} = M_{s4}C_P\frac{dT_{s4}}{dt} + \Delta\dot{Q}_{losses4} + m_{e4}\left(h_{fg4} + C_P T_{c4}\right) \quad (10)$$

2.11 **Summary**

This chapter has reported on a variety of aspects and parameters guiding the operation of a solar still. Special attention has been given to single-effect and multistage solar stills with stack stages. It has been discovered that even though solar stills have been studied for decades, there are remaining contradictions in the literature surveyed. Furthermore, solar stills have largely remained experimental systems as they are not widely used for commercialized desalination. There are also various configurations being introduced to ease the operation of the solar stills and enable them to be competitive in a commercial space. Solar stills, when fully developed, can be an ideal option for small-scale desalination in remote, isolated areas lacking an electricity grid or piped water infrastructure.

2.1.17 Single effect solar stills

The single effect solar still which can be identified as CSS was not the central focus of the current study. The CSS was integrated with the MSS-SS, similar to the set-up reported by Chen et al. (2017), for two purposes: 1) to act as a primary saline water tank where initial pre-heating of saline water and recovery of thermal energy was done; and 2) to produce part of the total freshwater which will be a fraction of the overall distillate output from the system. The literature survey was conducted on the single effect to gain valuable knowledge on the influence of meteorological, design and operational conditions.

2.1.18 Multistage solar still with stacked stages (MSS-SS)

As the MSS-SS was central to the current study, the literature was surveyed in detail to gain useful knowledge on the basic operation of the still. The current work has identified from the literature surveyed that a vapour-based MSS-SS has not yet been carefully studied. Therefore, the vapour-based solar still performance remains unknown. Furthermore, the vapour-based MSS-SS is yet to be optimised on all it its parameters. Alternative configurations of independent stages in the MSS-SS from those reported under section 2.6.2 have not been reported in the literature surveyed. Therefore, the current study presents a new configuration of independent stages. Estahbanati et al. (2015) and Shatat and Mahkamov (2010) report that the thermal energy supplied in the entry stage of the MSS-SS causes distillate production delay in the upper stages as they receive their thermal energy from latent heat of condensation from the lower stages. In addition, the current work has identified that a standalone multistage solar still has not been widely reported as only one standalone MSS-SS was reported by Schwarzer et al. (2009). The current work seeks to introduce another standalone MSS-SS. Furthermore, a feed water replenishment system which can operate remotely and without any electrically controlled instruments is presented. A method to maximise saline water pre-heating within the system to increase its temperature so that less energy is used in evaporating it is presented (Liu et al., 2014a). Furthermore, the MSS-SS reported under section 2.6 were reported to have waterbed in the stages which brings certain challenges such as maintenance. The current study presents a waterless stage MSS-SS which requires no stage maintenance since the trays cannot be contaminated by salt residue. Low saline water depth or a small body of saline water in a stage have reportedly enhanced the distillate yield in the system. The current work presents an MSS-SS with a small body of saline water in the evaporator (i.e., entry stage); in addition, the body of water is constantly circulated in a loop (dynamic mode). Even though pre-heating and heat recovery has been reported in other studies, the present work seeks to introduce a multistage pre-heating and heating recovery process in the MSS-SS. Minimum saline water in the entry stage is also introduced by the current study. Various researchers such as Schwarzer et al.

(2009), Estahbanati et al. (2015) and Chen et al. (2017) insist that the temperature of saline water in the MSS-SS increases linearly with an increase in solar intensity. The maximum temperature of saline water is reached somewhere in the afternoon. Generally, larger body of saline water has high thermal storage capacity and requires more energy to heat-up a large body of saline water compared to a small body of the same water (Soni et al., 2017). However, the current study presents a set-up with minimal saline water in the entry stage aimed at increasing the temperature of saline water rapidly to enable evaporation to being sooner. In addition to the minimum quantity of saline water in the entry stage, saline water will be circulated in the entry stage (dynamic mode).

CHAPTER THREE

MANUFACTURING, CONSTRUCTION AND ASSEMBLY

This chapter discusses the manufacturing and construction of the vapour-based multistage solar desalination system. It describes at length the processes used at arriving at the final assemblies and components of the system. The construction process is described from top to bottom. It concludes with the presentation of a complete system.

The body of the system was partially insulated by a 25 mm thick polystyrene material. Fully insulating the system causes the system to reach thermal damage during operation (Shatat & Mahkamov, 2010). The evaporator and the secondary saline water tank were insulated with an 80 mm thick glass fibre material. All copper tubes exposed to the outside weather elements were insulated using a thermaflex insulation with internal diameter of 15.8 mm and a thickness of 50 mm, made from a polyethylene material.

3.1 **Main frame**

The main frame shown in Figure 3.1 was the main support of the whole system including the external saline water tank. The frame was made from a galvanised steel of 40 mm x 40 mm square tubes, with all joints joined by means of arch welding. The frame was bolted onto the concrete floor by means of four M10 concrete bolts with a length of 40 mm. The frame consisted of two pieces, bottom and top. The frame was painted with two layers of corrosion resistant black paints.

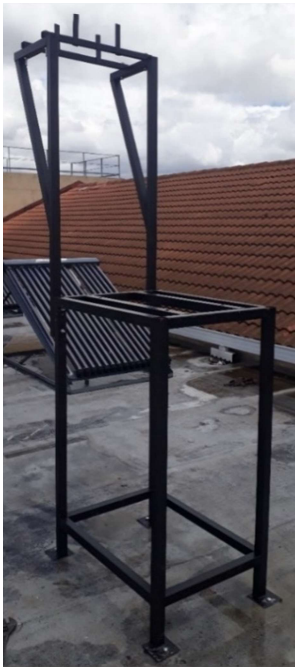

Figure 3.1: Main frame

3.1.1 Bottom piece

The bottom piece was used to mount the multistage tower by means of foursquare mounting holes drilled through the width of the parallel hollow tubes (see Figure 3.2). The hole dimensions are 16.5 mm x 16.5 mm and accommodated the four legs of the skeleton structure which will be discussed later in the chapter. The two parallel hollow tubes were made from a 40 x 40 mm galvanized hollow square tubes with 0.82 m lengths. This frame had a height, width and length of 1.4 m x 0.6 m x 0.9 m, respectively. Four 80 x 60 mm galvanized steel sheets were welded at the bottom of the bottom piece. The sheets were 3 mm thick and secured the piece into the ground. The required sizes of the bottom piece were achieved by marking off with a scraper, steel ruler and engineer's square and cutting by an angle grinder-cutting blade. Rough edges on the square tubes were filed with a flat file and welded together.

Figure 3.2: Bottom piece

Figure 3.3 shows the square holes for securing the skeleton structure onto the main frame. The holes enabled the skeleton structure to be easily removed by pulling it vertically upwards. The legs of the skeleton structure were a tight fit, restricting movements during heavy winds. The square holes were drilled with a 14 mm drill bit and hand drill. The square shape and size was achieved with a square file.

Figure 3.3: Square to secure the skeleton structure

3.1.2 Top piece

The top piece, shown in Figure 3.4, was mounted onto the bottom piece by means of four M10 bolts with a length of 70 mm. This piece's function was to elevate and support the external saline water tank so that the tank supplies the vapour-based multistage solar still with saline water under gravitational influence. The top piece had two identical sections made from 40 x 40 mm hollow square tubes.

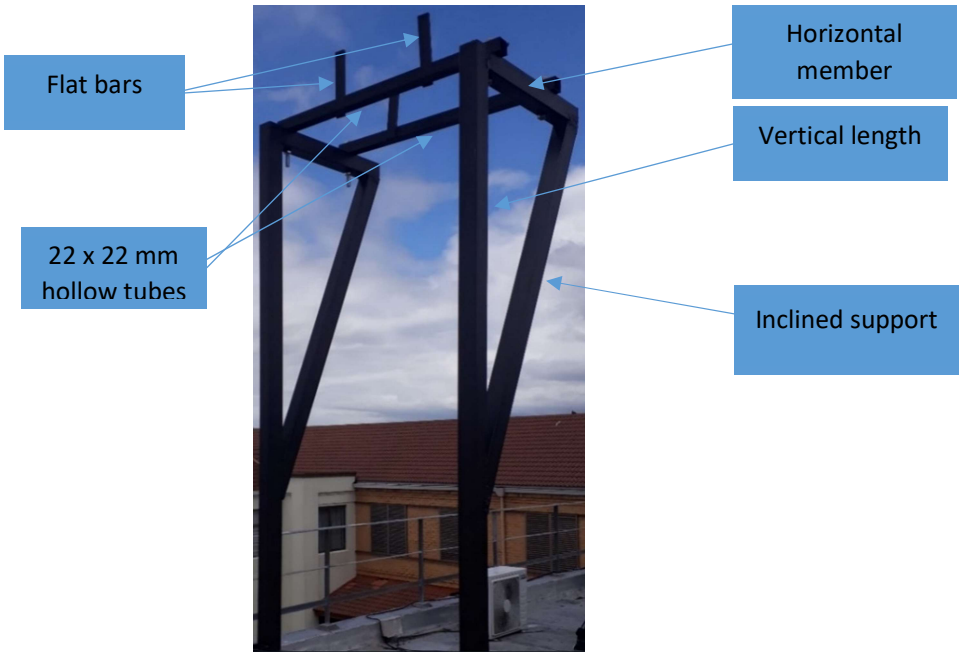

Figure 3.4: Top piece

Each section had a vertical length of 0.8 m and a support mounted at a 25° angle from the vertical. The length of the support was 0.35 m, a horizontal member with a length of 0.2 m connected the sections. Two hollow square tubes of 22mm x 22 mm with a length of 0.6 m were mounted across on top of the top piece. The two hollow tubes were secured with four M10 with a length of 70 mm. Two flat bars were welded on each hollow tube to secure the saline water external tank into place. The flat bars have dimensions of 80 mm x 16 mm x 6mm, length, width and thickness, respectively. The structure was achieved by marking off with a scraper, steel rule and engineer's square and cutting with an angle grinder cutting blade. Rough edges on the square tubes were filed by a flat file and welded together. Figure 3.5 shows the joining of the top and bottom pieces by means of four bolts and nuts.

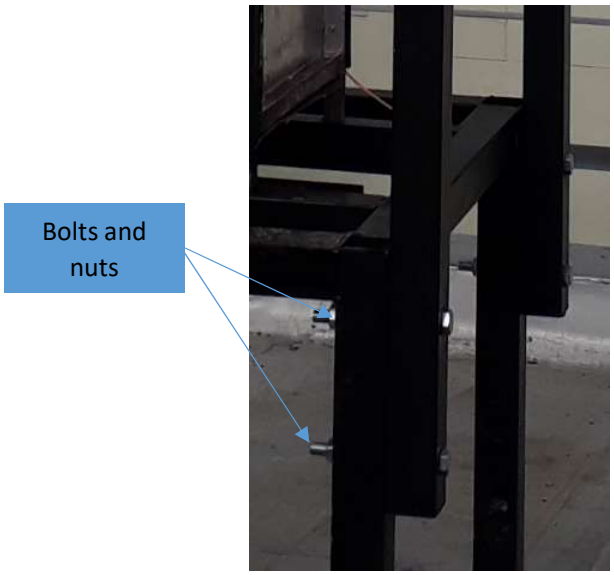

Figure 3.5: Joining of top and bottom pieces

3.2 Vapour and saline water sealing

All vapour and water-sealing work in the construction of the system occurred with a water-resistant adhesive (see Figure 3.6). The sealant can withstand temperatures from -40°C to 120°C, ideal for the working temperature of the system.

Figure 3.6: Water-resistant sealant

3.3 External saline water tank

The external saline water tank was a 20-litre cylindrical plastic bucket. Its base diameter was 300 mm and height 450 mm. The tank had a top cap which sealed the top end of the cylindrical tank. The cap had a filling hole which allows saline water to be refilled occasionally. The tank had a 15.5 mm hole drilled at its lower end, as shown in Figure 3.7, and a saline water transfer tube connected to this hole. The saline water transfer tube hole on the external saline water tank was drilled 145 mm from the base of the tank.

Figure 3.7: External saline water tank

This was done so that a large amount of ocean sand and other dense foreign particles would be prevented or at least minimised from entering the system through the float valve. The dense particles sank to the bottom of the tank and thus were prevented from entering the external saline water transfer tube. The dense particles blocked the float valve mechanism and in so doing, disrupted the flow of saline water. If the holes were drilled at any lower point, more foreign particles could enter the system through the saline water transfer tube. Each time the saline water was being refilled in the external saline water tank, a mixture of saline water and ocean sand was introduced.

This mixture gradually separated due to the difference in densities, as ocean sand is heavier than saline water. The sand settled at the bottom of the external saline water tank. The tank must be cleaned periodically to remove dense particles. When the saline water was transferred from the external tank to the basin solar still (primary tank), some of the ocean sand and other foreign particles interrupted the flow of saline water into the system. If the flow of saline water is interrupted, the distillate production is also disrupted. To minimise the blockages in the float valve, two things must be done. Firstly, saline water must be syphoned, or the sand removed from the saline water as far as possible prior to pouring saline water into the external saline water tank. This will ensure that a minimum amount of sand or foreign objects are present in the saline water and thus blockages are minimised. Secondly, the external saline water tank must be cleaned occasionally to prevent a build-up of saline water sand and other foreign particles. A different view is presented in Figure 3.8, showing the external saline water tank, the top piece of the main frame and the top section of the multistage tower.

Figure 3.8: External saline water tank connection

3.4 External saline water transfer tube

The external saline water transfer tube was made from a thin-walled transparent PVC material, with dimensions of 16 mm in diameter and 95 mm long. The tube was force fitted into a 15.5 mm hole at the lower end of the external saline water tank, discussed in 3.3, and sealed around the edges with an adhesive, discussed under 3.2. It was positioned in such a way that it protrudes through the body of the external saline water tank and secured onto the float valve that fed saline water into the basin type solar still by means of a hose clamp. The difference in pressure heads between the external saline water tank and the basin type solar still caused the flow of saline water from one point to the other. The tube, shown in Figure 3.9, was connected through the back cover of the basin type solar still.

Figure 3.9: External tank saline water transfer tube

3.5 **Basin type solar still (BSS)**

The basin solar still, also called the primary saline water tank or stage 6, was mounted on top of a series of identical stacked stages which forms a multistage tower. The basin still had additional functions in addition to producing the distillate. It was the primary saline water storage tank within the multistage tower. It also pre-heated the saline water as it entered the system from the external saline water tank. The basin type solar still had several components – back cover, front cover, two side covers, all round trough, float valve mechanism, distillate collecting tube and bottom plate – which collectively constitute a single-slope single-basin solar still. The edges of the covers were fixed onto each other by means of pop rivets and all sealing was done by applying a water-resistant adhesive. Figure 3.10 shows a complete basin type solar still with its float valve to regulate saline water inflow. The basin still was conceived and constructed based on the experimental findings of previous studies. The length-to-width ratio of the still was limited to at least 0.5 and its front cover height-to-back cover ratio was limited to 0.21 (Feilizadeh et al., 2017). The inner walls of the basin were then painted black to maximise solar absorption (Singh et al., 2011).

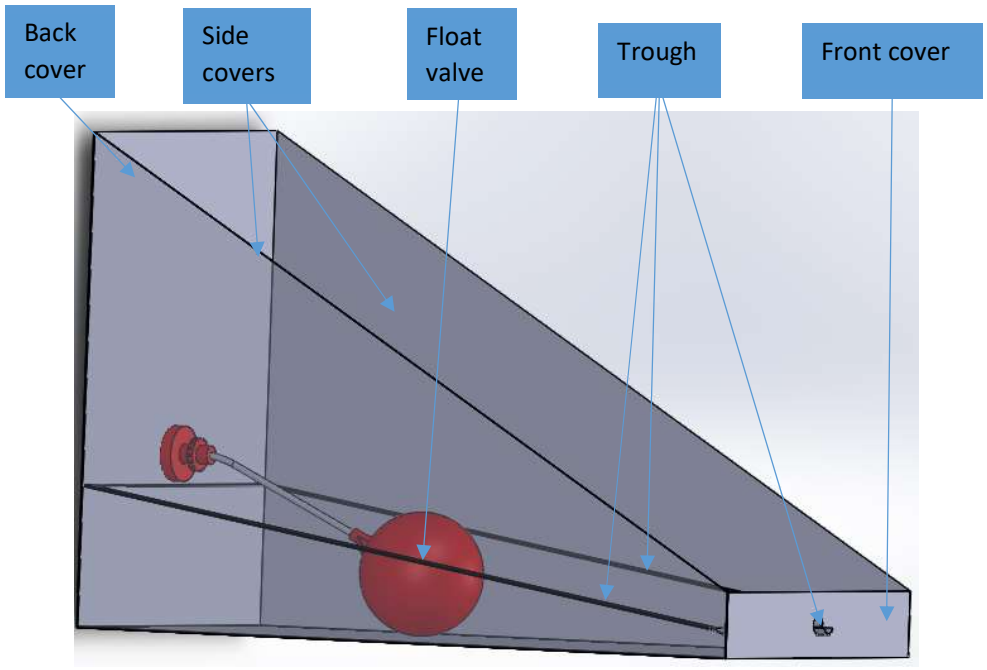

Figure 3.10: Basin type solar still in 3D

The basin type solar still was then insulated all around with 20 mm thick polystyrene insulation on the outside body. This was to minimise heat loss from the basin type solar still through the walls. In an insulated solar still, the daily distillate productivity is enhanced compared to an

uninsulated solar still (Mohamad et al., 1995; Abujazar et al., 2016). An insulated basin still is presented in Figure 3.11.

Figure 3.11: Basin type solar still insulation

3.5.1 Float valve

In a single basin still simulation study, Hamadou and Abdellatif (2014) reported that the saline water depth is the main factor that determines the distillate yield variation. Therefore, in the current study, the float valve controls and regulates the flow of saline water to maintain the required saline water level in the basin. The float valve prevents the saline water from diminishing during evaporation which causes dry spots in the solar still basin. The float valve was connected to the external saline water transfer tube, discussed under section 3.4. The valve (see Figure 3.12) had a ball float of 100 mm in diameter. A connecting rod of 8 mm in diameter and 121 mm long connected the valve mechanism and the ball float.

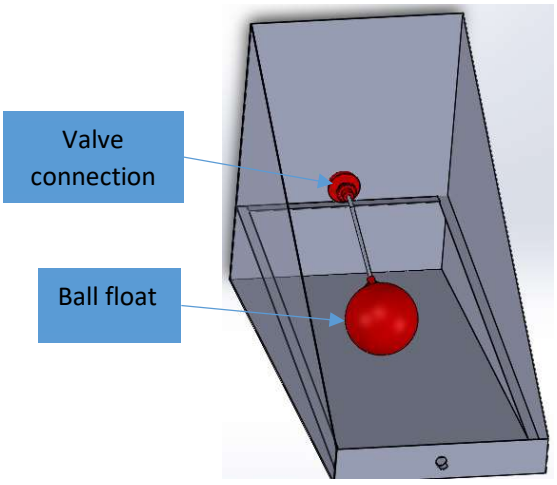

Figure 3.12: Float valve in 3D

The valve mechanism had an extremely narrow opening for saline water to flow through, as discussed under 3.3. In addition, the valve was adjusted and set to limit the depth of saline water at 20 mm in the basin solar still. It has been experimentally shown from previous studies that lower levels of saline water contribute to enhanced distillate production in a solar still. However, lower levels of saline water have low thermal storage capacity while higher depths have higher storage capacities. High storage capacity enabled the basin solar still to continue with the production of the distillate until late in the night and on cloudy days (Abujazar et al., 2016; Morad et al., 2015).

3.5.2 Condenser cover

The condenser cover (see Figure 3.13) was made from a clear, 3 mm thick Perspex sheet with the surface area of 300 mm x 620 mm. The cover was sloped at a 35° angle equal to the latitude of Cape Town, South Africa. The edges of the cover were sealed by 12 x 12 mm rubber sealant strip in conjunction with the water-resistant sealant, discussed under 3.2. The cover was held in place by clamps for approximately 12 hours to allow the adhesive to dry and hold. Additional sealant was applied to ensure vapour tightness. The front end was secured by means of three 4 x 4 mm rivets and the rear end was secured by three 4 x 8 mm screws. Since the screw are generally considered non-permanent fasteners and are easy to remove, they were chosen for accessibility of the basin of the solar still for cleaning and maintenance purposes.

Figure 3.13: Sloped condenser cover

3.5.3 Side covers

Identical side covers were made from a 0.9 mm thick aluminium material sheet. The covers were positioned vertically and cut into a triangle. The two side covers (see Figure 3.14) were

a hypotenuse: the longest sloped side was 717 mm in length; the vertical rear end was 360 mm; and the horizontal side was 620 mm in length. The front end of a triangular sloped side cover was 75 mm high and the cover was sloped 35° from the horizontal. The covers were bent at both front and rear ends using the bending machine to form the cover lips (lips not shown). The lips were bent 10 mm from each end to form a 90° angle with the body of each cover. These lips secured the cover onto the skeleton structure through the three holes drilled along their height. The water-resistant sealant then sealed the mating joints of the cover and skeleton structure.

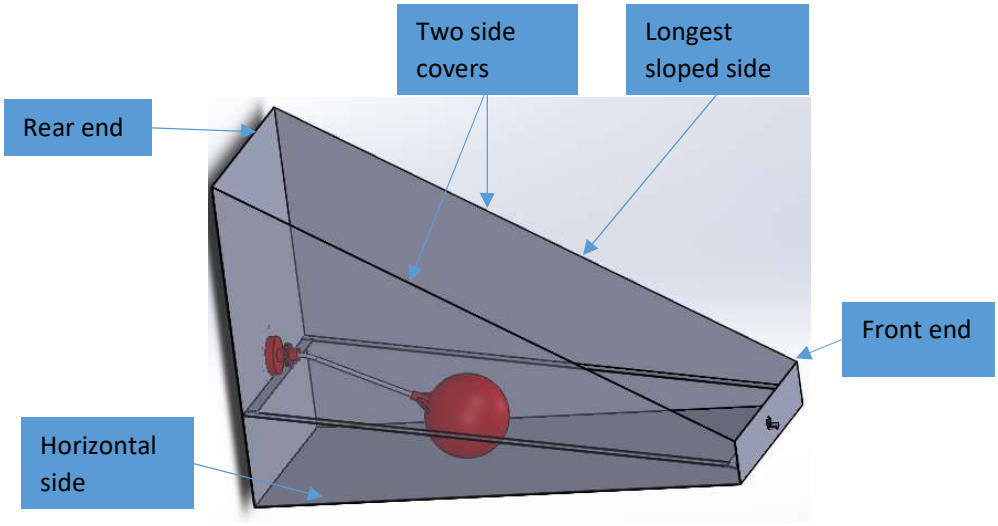

Figure 3.14: Sloped side cover from inside in 3D

The sloped side cover (see Figure 3.15) had five 4 mm holes along the horizontal sides that attached it onto the skeleton structure using 4 x 4 mm pop rivets. The covers were manufactured by marking them off with marking-off paint, a scraper, steel rule and engineer's square. They were then cut with a guillotine machine and the small, required shapes were obtained with tin snip pliers.

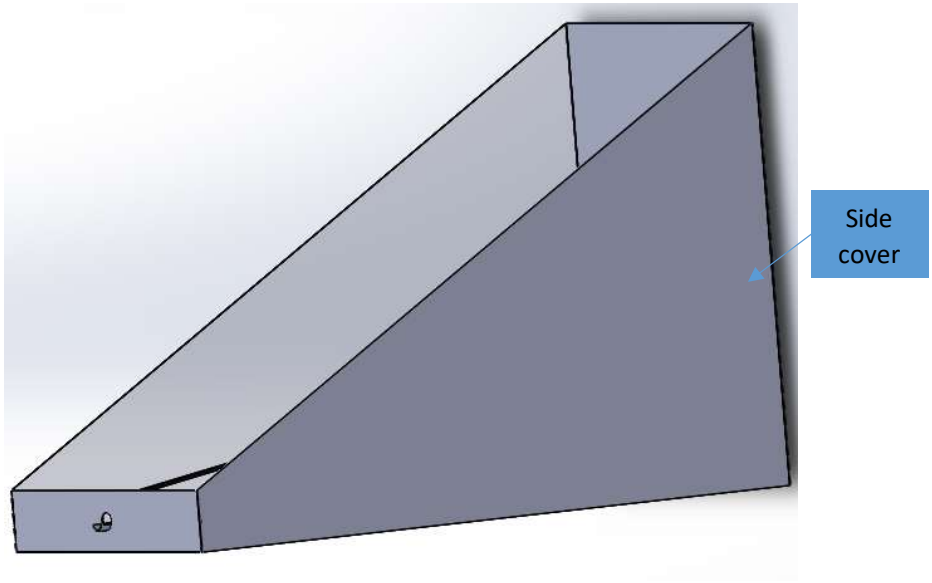

Figure 3.15: Sloped side cover from outside in 3D

The holes used to attach them were achieved by measuring and marking off. A 4 mm drill bit and a hand drill were used to drill holes which were then used to secure the cover onto the skeleton structure. The sealant was placed in between the cover and the skeleton structure to seal the joints. Four 4 mm trough attachment holes (not shown) were drilled to secure the trough onto the side cover.

3.5.4 Back cover

The cover shown (see Figure 3.16) was made from 0.9 mm thick aluminium cover, with a surface area of 360 mm x 306 mm, height and width, respectively. The cover had 17 mm lips that bent at 90° to attach the cover onto the skeleton structure, as well as sloped side covers. The back cover was manufactured by marking off with a scraper, marking-off paint, a steel rule and engineer's square. The cutting was by guillotine machine; the small, desired sizes were achieved with a tin snip; and the back cover lips were formed by a bending machine. The height of the back cover determined the total height between the condenser cover and the evaporating surface of saline water. When basin height is reduced, the distillate yield increases. The height of the basin still was therefore minimised as much as possible to enhance production rate (Rajaseenivasan et al., 2017).

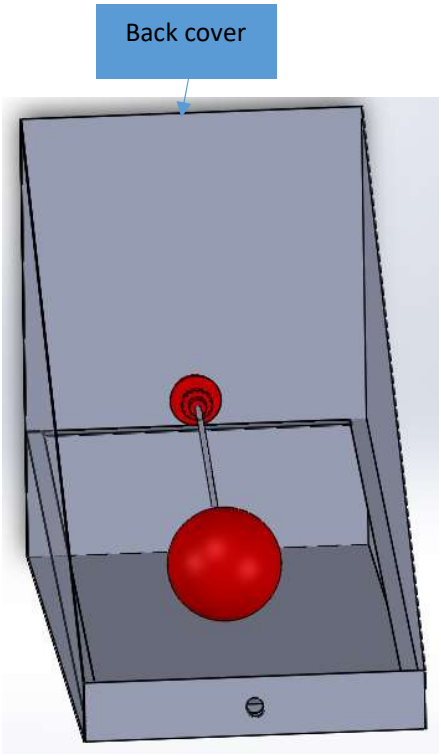

Figure 3.16: Back cover in 3D

The saline water transfer tube was connected to the basin type solar still through the back cover. A 16 mm hole was marked off and drilled 116 mm from the bottom and 150 mm from one side of the cover. Figure 3.17 shows the float valve connection for saline water supply. The back cover also had three pop rivets holes on each lip to secure the cover onto the side covers. A water-resistant sealant was applied between the joining surfaces of the back cover and the side covers. Furthermore, the cover had additional three pop rivet holes along its bottom end to secure the cover onto the skeleton structure by means of pop rivets. A water-resistant sealant sealed the mating surfaces between the back cover and skeleton structure. An additional two 4 mm holes were drilled to attach the trough onto the back cover. The trough and the back cover were attached using 4 x 4 mm pop rivets. A water-resistant sealant was applied between the mating surfaces of the covers to prevent the distillate produced from trickling back into the pool of saline water.

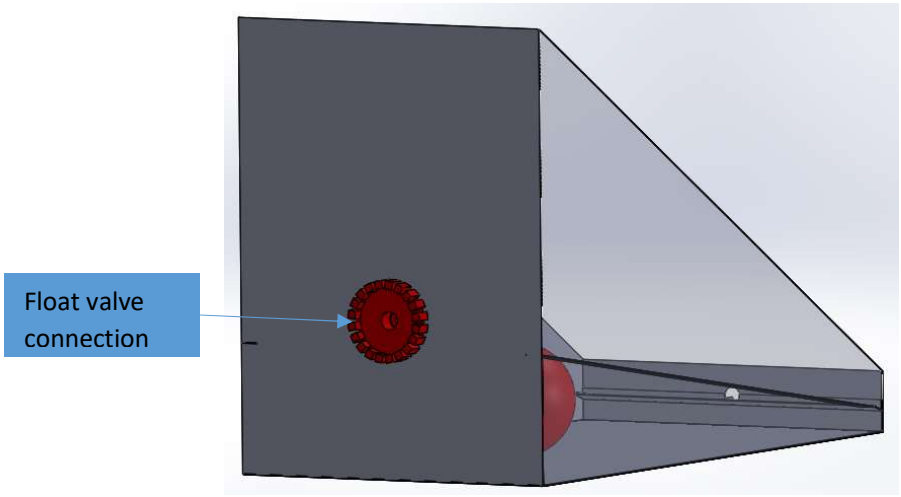

Figure 3.17: Float valve connection in 3D

3.5.5 Front cover

The front cover and its lips (see Figure 3.18) were made from a 0.9 mm thick aluminium cover with a surface area of 320 mm x 75 mm, width and height, respectively. The cover was measured and marked off using the scraper, marking-off paint, steel rule and engineer's square. The cutting was accomplished with a guillotine machine and required sizes obtained by using a tin snip pliers. The 4 mm holes were achieved by marking them off and drilled using a 4 mm drill bit and hand drill.

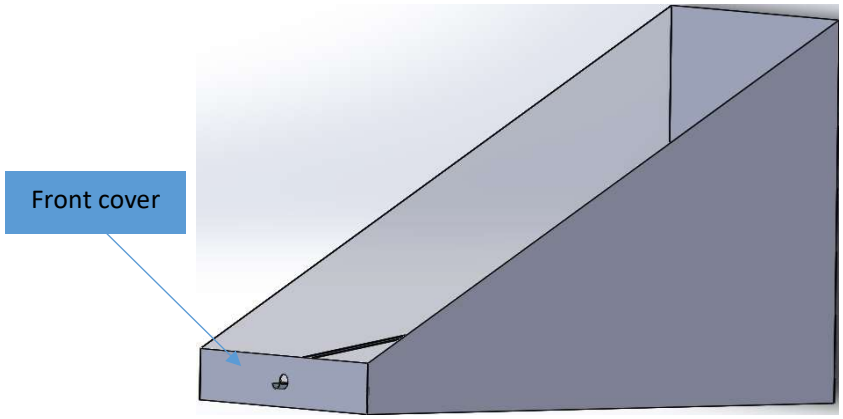

Figure 3.18: Front cover in 3D

The front cover also had lips which fixed the cover onto the side covers and skeleton structure. The lips of the cover were bent at 10 mm from each end to a 90° angle from the body of the cover. The front cover (see Figure 3.19) has a 15 mm diameter hole, drilled in the middle of the cover, to accommodate the cross over or the U-shaped tube which collected the distillate from the trough. A hole was marked off and drilled using a 4 mm and 14 mm drill bit and a hand drill. A round file was then used to obtain smooth edges and to enlarge the hole to a 15

mm diameter. The U-shaped tube was tight fitted since the hole was smaller, preventing the tube from falling off. Water-resistant sealant was applied to seal off the water and vapour from leaking from the solar still.

Figure 3.19: U-shaped tube

3.5.6 All round trough

The trough (see Figure 3.20) was manufactured by marking off using the marking-off paint, scraper, steel rule and engineer's square. The initial cutting was achieved with guillotine machine. Thereafter, an angle grinder with a cutting blade was used to remove the inner section of the sheet. The bending along the edges was done by a bending machine and pliers were used to achieve accurate shapes. The trough was made from a 0.9 mm thick aluminium sheet installed on all four vertical walls of the solar still. The length of the trough along its inclined length was 656 mm and 342 mm wide. The all-round trough was anticipated to be more effective than the normal trough which is usually installed on the front cover. The anticipation was that, in addition of collecting the distillate from the condensing cover, it would also collect the distillate dripping from the other three walls of the solar still.

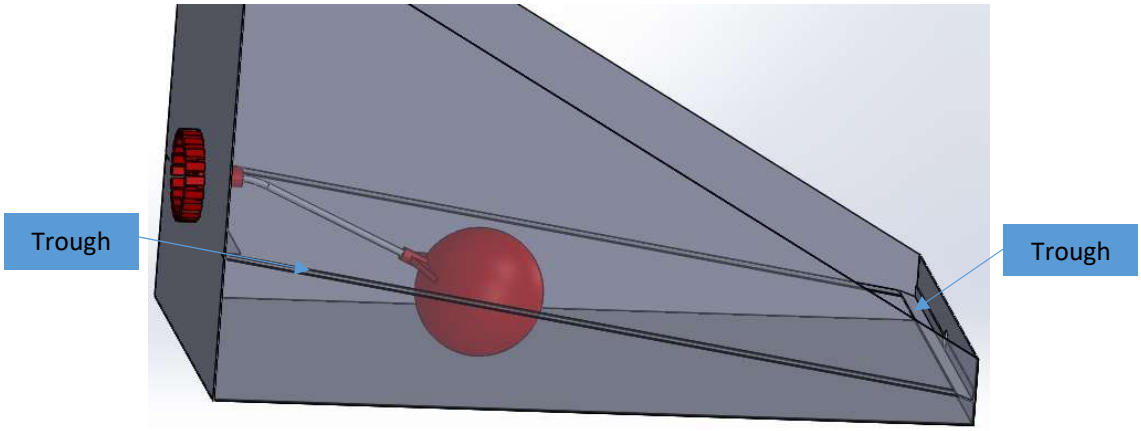

Figure 3.20: All round trough in 3D

The trough is one continuous piece that formed a watertight border between itself and the rest of the vertical covers. At the lower end of the solar still, a U-shape tube connecting piece protrudes through the front cover (see Figure 3.21) which connects to the distillate collecting tube (U-shape tube). The connecting piece dimensions were 20 mm x 15 mm, length and diameter, respectively. The trough, attached to all four vertical walls of the solar still as discussed previously, was elevated and inclined in such a way that the distillate collecting point was its lowest point. Its inclination angle was determined as approximately 26° from the horizontal. The space between the trough and the walls was sealed by the water-resistant sealant.

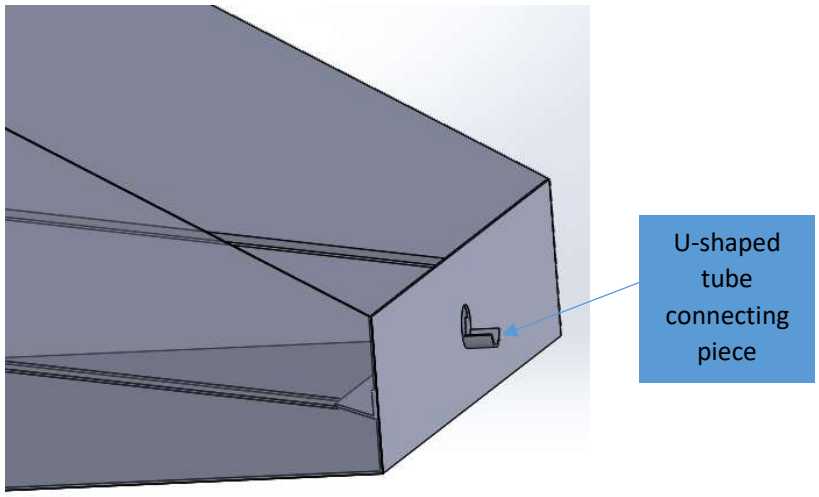

Figure 3.21: U-shaped tube connecting piece in 3D

3.5.7 Bottom cover

The bottom cover shown (see Figure 3.22) was made from a 0.9 mm aluminium material with dimensions of 300 mm x 600 mm. The cover was marked off using the scraper, marking-off paint, steel rule and engineer's square. The cover was then cut using the guillotine machine and the 10 mm lips bent at 90° using the bending machine. Lips were made on all four sides of the bottom cover so that it covered the top of the skeleton structure. Sixteen 4 mm holes were drilled using a 4 mm drill bit and a hand drill all around the lips. The cover had a 15 mm hole drilled at its centre, as shown in Figure 3.22, to connect the zigzagged saline water tube which supplies saline water to the rest of the system. The zigzagged saline water tube will be discussed later in the chapter.

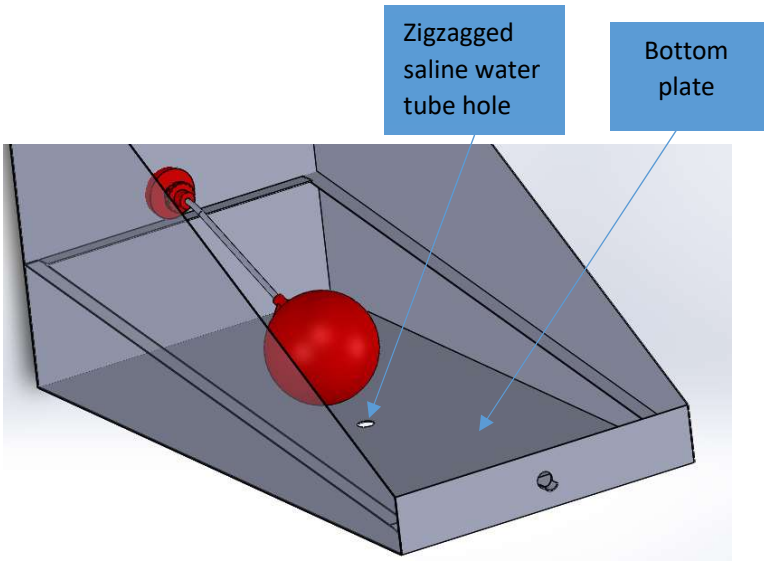

Figure 3.22: Bottom cover in 3D

Figure 3.23 shows stage 5 of the system with the basin solar still removed. Stage 5 was located just below the basin solar still in the multistage tower. The zigzagged saline water tube, protruding through the bottom cover of the basin still and extending downwards through all the stages, was to collect the pre-heated saline water from the basin still and supply it to the secondary tank. The rest of stages will be discussed later in the chapter. A water-resistant sealant sealed the mating surfaces of the bottom cover and the skeleton structure to prevent vapour leakage.

Figure 3.23: Stage 5 with zigzagged saline water tube

3.6 **Skeleton structure**

The skeleton structure, shown in Figure 3.24, as the main support of the multistage tower, had all the aluminium covers attached onto it. The structure was made from a galvanised square

tube with the dimensions of 16 mm x 16 mm and a thickness of 1.2 mm. The external dimensions of the overall structure were 1140 mm x 600 mm x 300 mm, height, length and width, respectively. Sloped square tubes of 582 mm length were installed at the lower end of the structure, positioned at an 8° slope from the horizontal to accommodate stage 1 tray. The lower ends of the tubes were installed 380 mm from the bottom of the structure while the upper end was 432 mm from the bottom of the structure. The horizontal cross tubes, 265 mm in length, were installed both at the top and bottom of the structure. The longitudinal tubes, 566 mm, were also installed at the top and bottom of the structure. Both the horizontal and cross tubes at the bottom of the structure were installed at 30 mm from the end.

The structure was accomplished by marking off using the marking-off paint, scraper, steel rule and engineer's square. The cutting was by an electrically powered steel hacksaw and the whole skeleton structure was put together by means of arc welding, as all joints of the structure were arc welded. The aim of installing the sloped and horizontal cross tubes was to enable ease of access into the system. Each cover of the system was attached independently which enabled the covers to be installed and removed independently without affecting the rest of the system. The skeleton structure was marked off and drilled with a 4 mm drill bit to accommodate the pop rivets which secure the covers in place.

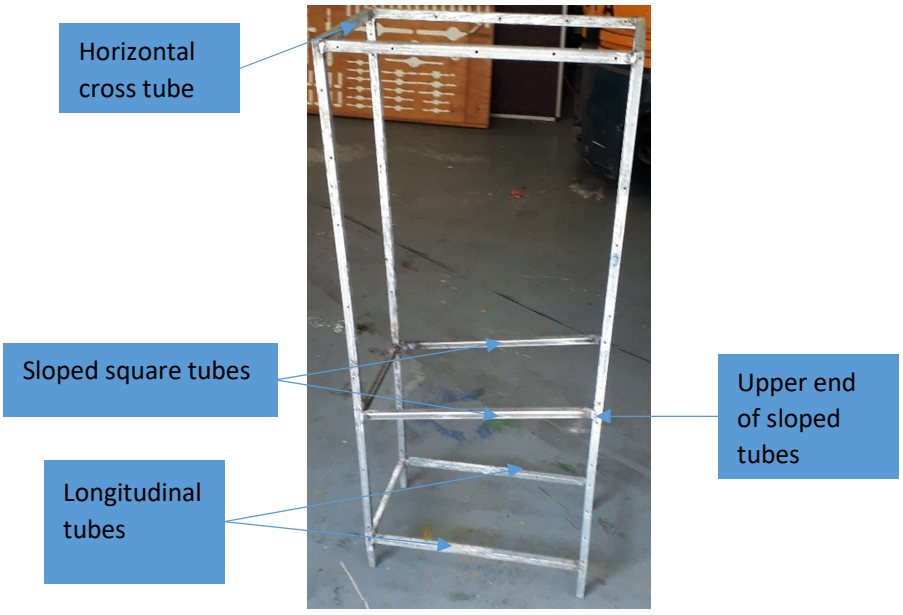

Figure 3.24: Skeleton structure

3.7 **Multistage tower covers**

3.7.1 Two-piece front covers

The two-piece front cover had an upper and lower cover, shown in Figure 3.25, before the U-shaped tubes were inserted through them. The covers were made from 0.9 mm thick aluminium sheet with a width of 265 mm. The 17 mm lips were bent to a 90° angle using a bending machine. The upper front cover had a length of 859 mm while the lower cover was 232 mm. The upper cover had six 4 mm holes along its length and three holes along its width to secure the covers onto the skeleton structure. The sizes were accomplished by marking off using the marking-off paint, scraper, steel rule and engineer's square. The cutting of the covers was achieved with a guillotine machine. The 4 mm holes were made by marking off with marking-off paint, centre punch and steel rule. A 4 mm drill bit and a hand drill were used to drill through the covers and cover lips. The covers were manufactured to fit snuggly onto the skeleton structure.

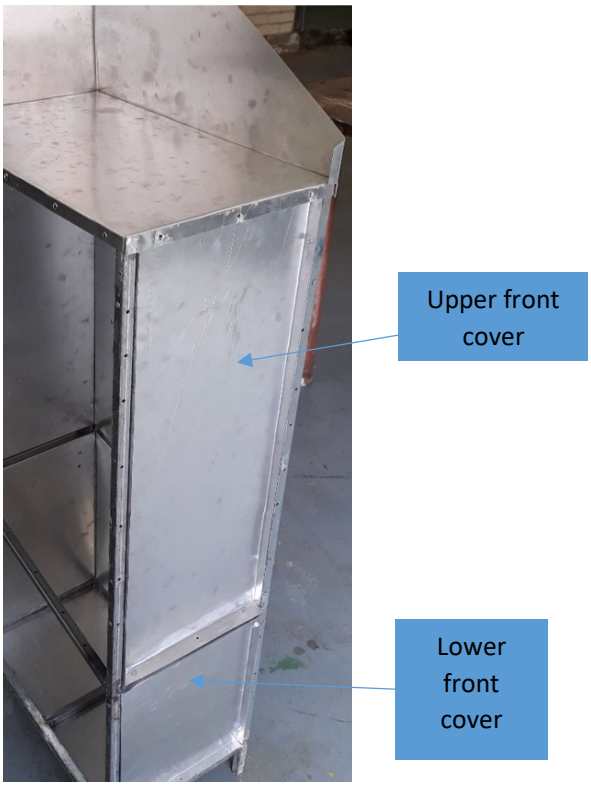

Figure 3.25: Front covers

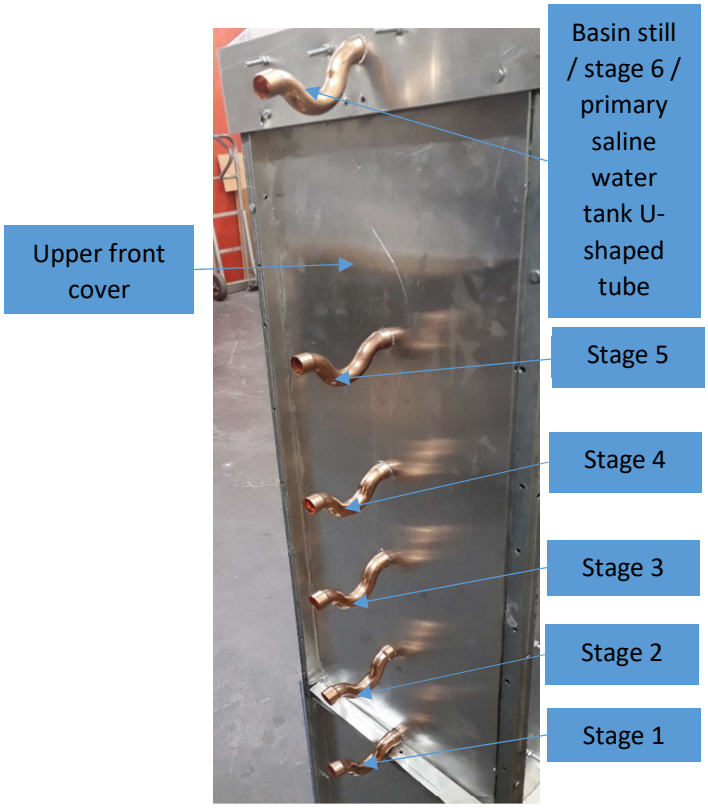

Figure 3.26: U-shaped distillate collector tubes

Five 15 mm holes were drilled at the centre, 132.5 mm from one end to the other across its width. The holes were lined vertically along the length of the upper front cover, as shown in Figure 3.26. These holes were to accommodate the distillate collecting U-shaped tubes. The holes were drilled to correspond with the distillate collecting points of the respective stage trays. Stage trays, as discussed later, were fixed onto this cover. The lower front cover form ed the secondary saline water tank and the evaporator's compartment at the bottom.

3.7.2 Two-piece back covers

The back covers (see Figure 3.27) were made from 0.9 mm thick aluminium sheet, at a width of 265 mm with 90° lips that are 17 mm long. The upper and lower covers were 784 and 308 mm in length. The sizes and shapes of the covers were achieved by marking off using the scraper, marking-off spray, engineer's square and a steel rule. The cutting was with a guillotine machine and finer smooth shapes were achieved by tin snip pliers. The bending of the lips was by bending machine and the covers were manufactured to fit tightly in between the square tubes of the skeleton structure. The stage trays were fixed onto the back cover by means of pop rivets. More discussion on the stage trays will come later in the chapter. After marking off, a 4 mm drill bit and hand drill were used to drill the holes on the cover and the lips. The lower back cover formed the secondary saline water tank and the evaporator's compartment.

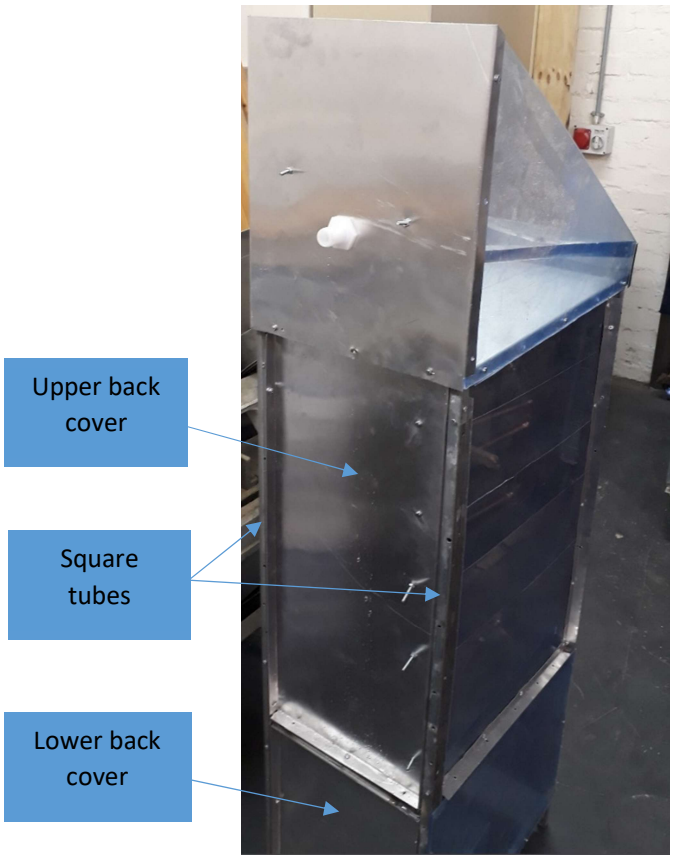

Figure 3.27: Back covers

3.7.3 Two-piece side covers

The multistage tower side covers, shown in Figure 3.28, were made from a 0.9 mm thick aluminium sheet. The upper and lower covers had a width of 568 mm width. The vertical length of the upper cover was 859 mm and the lower cover was 232 mm long. The cover was manufactured to follow the 8° inclined on the sloped square tubes, discussed under section 3.6 above. The shape and size of the covers was obtained using marking off instruments such as marking-off spray, steel rule, scraper and engineer's square. The cutting was by guillotine machine and finer details were accomplished by tin snip pliers. Both the upper and lower side covers had 17 mm lips bent at 90° using a bending machine. The cover and the lips were then drilled using a 4 mm drill bit and a hand drill. Stage trays were fixed onto the upper side cover, as discussed later in the chapter. The lower side cover formed the secondary saline water tank and the evaporator's compartment.

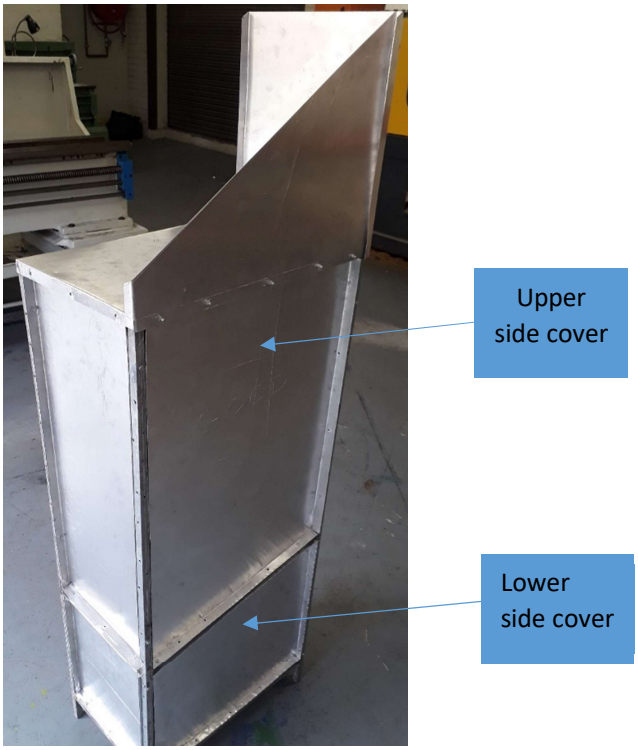

Figure 3.28: Side covers

Two 16 mm hot and cold tube holes were drilled on the lower side cover (see Figure 3.29). The tubes, connected to the evaporator, will be discussed later in the chapter. The holes were allowed the two tubes to pass through and connect to the solar collectors which will be discussed later in the chapter. The holes were accomplished by marking off using the centre punch, marking-off spray, steel rule, engineer's square, ball pen hammer and scraper. A 14 mm drill bit and a hand drill were used to drill the holes, and a round file to make the holes smooth. The holes were positioned 15 mm from the bottom and 86 mm from one end of the cover.

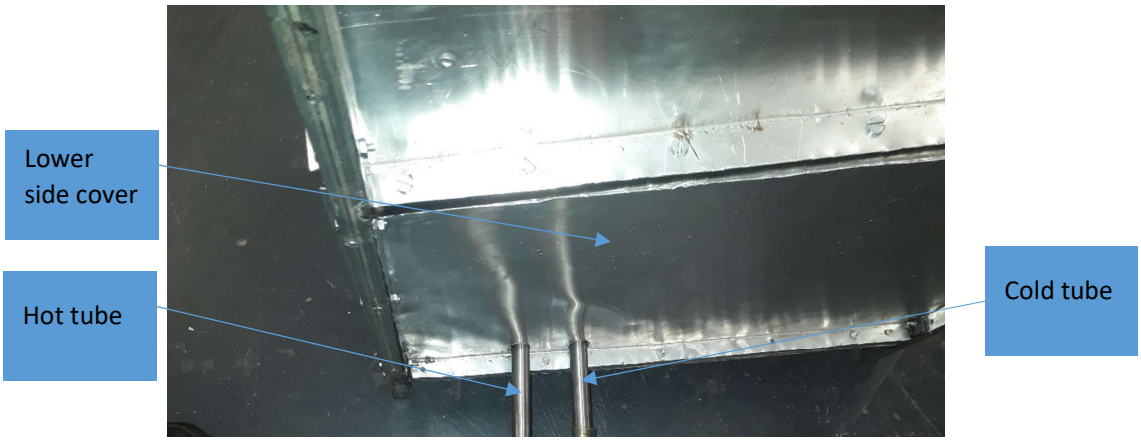

Figure 3.29: Side cover, hot and cold evaporator tubes

3.7.4 Stage covers (side covers)

These side covers are called stage covers as they separate each stage and provide sealing between the stages. The stage covers are different sizes (see Figure 3.30) as will be discussed under section 3.8. The stage covers were made from a 0.9 mm thick aluminium sheet. The sizes of the covers were achieved by marking off using the marking-off spray, engineer's square, steel rule and scraper. The initial cutting was achieved by a guillotine machine and smaller accurate cuts by tin snip pliers. The 10 mm lips were bent using the bending machine and smaller bends were achieved using pliers. The lips were drilled using a 4 mm drill bit and a hand drill, and two 4 mm holes were drilled on each cover. Two (4 x 12 mm) screws and nuts secured the covers in place on each stage cover. The covers were manufactured to fit tightly in the stage slots to prevent vapour leaks. A water-resistant sealant sealed off the mating surfaces to ensure no vapour leaks out of the stage or air leaks into the system.

Figure 3.30: Stage covers

3.7.5 Secondary saline water tank and evaporator compartment cover

The cover (see Figure 3.31), manufactured from a 0.9 mm aluminium sheet metal, was designed to fit tightly into the secondary saline water tank and evaporator compartment. Its shape was accomplished by marking off using a combined square, marking-off spray, steel rule, engineer's square and scraper. Initial cutting was by guillotine machine and final small cuts by a tin snip. The 17 mm lips all around the edges were bent using the bending machine. The sight glass slot corresponding to that of the secondary saline water tank (secondary saline water tank to be discussed later in the chapter) was made. Sight glass, of dimensions 113 x 10 mm, monitored the level of saline water in the secondary saline water tank. The slot was cut using the tin snip and the rough edges filed down with a flat file. A 25 mm thick polystyrene material of a similar shape to the cover minimised heat loss from the compartment.

Figure 3.31: Compartment cover

3.7.6 Multistage tower bottom cover

The multistage bottom cover (see Figure 3.32) was made from a 0.9 mm aluminium sheet metal. At 600 mm long and 300 mm wide, it was used to mount and support the secondary saline water tank and the evaporator. Its size was achieved by marking off using the marking-off spray, steel rule, engineer's square and scraper. It was cut using a guillotine machine, with finer cuts at each of its four corners made by tin snip pliers. The 17 x 17 mm cuts at the corners allowed it to fit in between the legs (square tubes) of the skeleton structure. The cover was then secured onto the skeleton structure using 4 x 20 mm screws to permit ease of access since screws are not permanent fasteners.

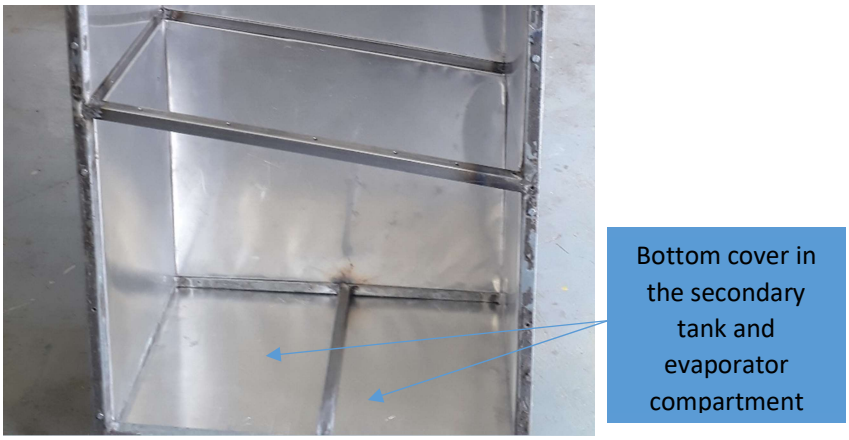

Figure 3.32: Multistage tower bottom cover

3.8 **Stage trays**

After fitting covers onto the skeleton structure, the incomplete multistage tower appears, as presented in Figure 3.33. The stage tray compartment was divided by five stage trays inclined at an angle equal to that of the sloped square tube (8°). The stage height was made different in anticipation of some stages receiving more vapour than others. Stage 1 was made larger than the rest of the stages. Stage 5 was the second largest because hot air and vapour tend to rise. In addition, this stage was cooled by the pool of saline water in the basin type solar still. Since the stages did not have saline water as waterbed, they relied on the surrounding ambient air for cooling. Stages which were anticipated to receive large quantities of vapour were enlarged to allow for cooling and the reduction of pressure in the stage.

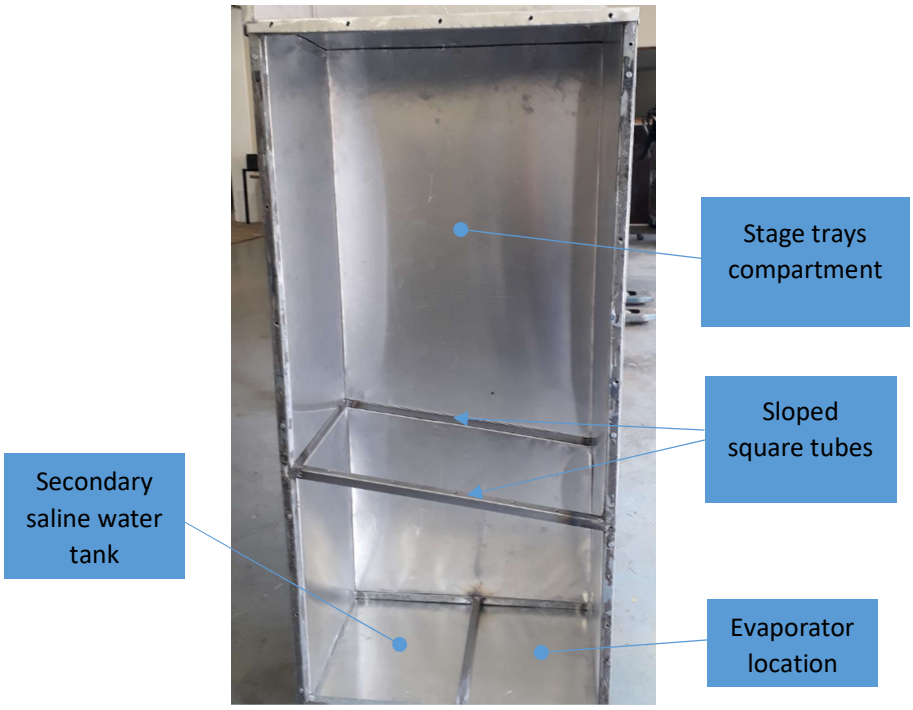

Figure 3.33: Covers fitted onto the skeleton structure

It can be seen from Figure 3.30 that stages 1 and 5 are a larger than the other stages. Stage trays shown in Figure 3.34 were made from a 0.9 mm aluminium sheet metal. The trays had a width and length of 337 mm and 500 mm, respectively. Their shape and sizes, achieved by marking off using the steel rule, engineer's square, scraper and a marking-off spray, were cut into sizes by a guillotine machine. Final sizes were achieved with tin snip pliers. The trays were bent in the middle along their lengths into a V-shape at 20° from the horizontal and from each side across their widths using a bending machine. The front lips were bent to approximately 84° from the flat surface of the tray to accommodate the inclination of the trays.

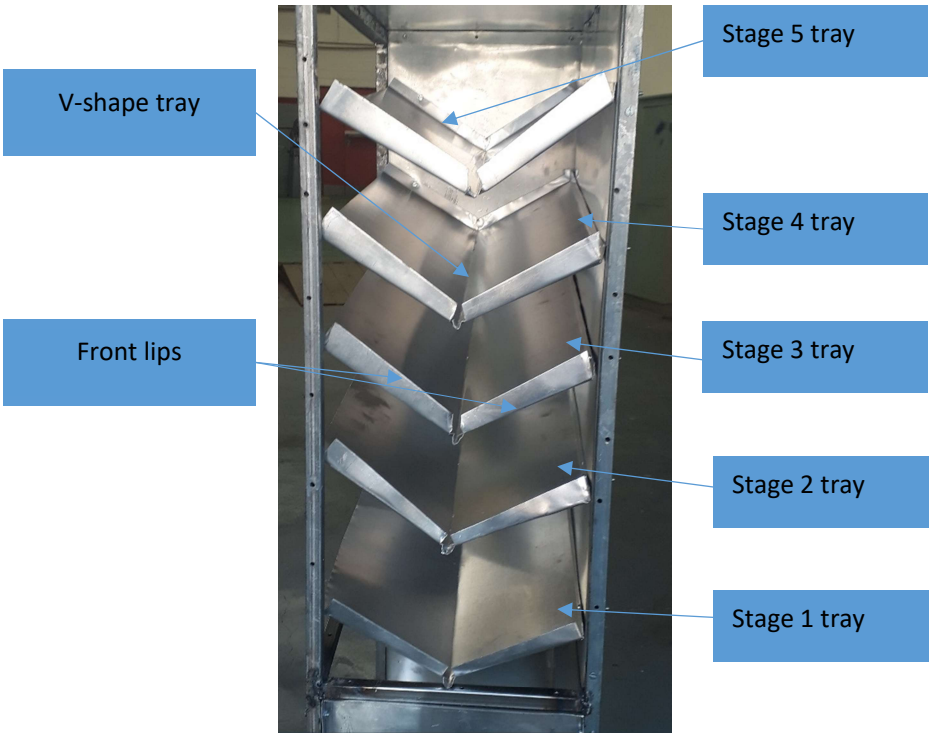

Figure 3.34: Stage trays

The side and the back lips (see Figure 3.35) were bent using a bending machine to approximately 108° and 115°, respectively, from the flat surface of the tray. The angles used were determined by the orientation of the V-shape tray in the multistage tower body. The lips were bent at approximately 17 mm, and 4 mm holes were drilled through the lips. The 12 holes were drilled all around the lips to secure the tray onto the upper side cover, upper back cover and upper front cover. Corresponding 4 mm holes were drilled on the upper side cover, upper back cover and upper front cover. Pop rivets of a 4 mm diameter secured the trays onto the covers. The sides of the trays with a 'straight end', shown in Figure 3.35, were not bent to accommodate the stage covers.

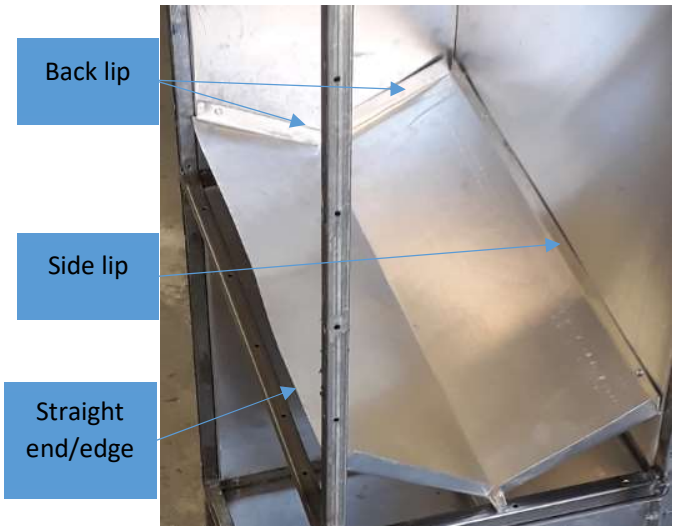

Figure 3.35: Stage trays

The distillate collecting trough on each tray (see Figure 3.36) was achieved with tin snip pliers. The trough was bent to be inserted into a U-shaped tube with internal diameter of 13.5 mm. The trough, 20 mm long and 25 mm wide, was used solely to collect the distillate produced and send it through the collecting tubes and into the distillate tank.

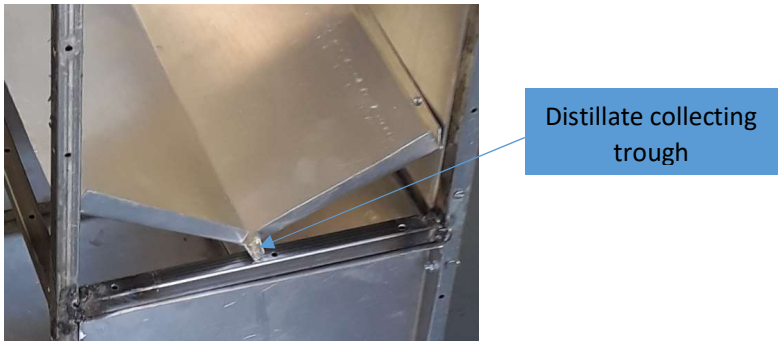

Figure 3.36: Distillate collecting trough

As discussed earlier, the stage sizes were different. Their heights, widths and lengths are shown in Table 3.1.

Table 3.1: Dimensions of the stages

Stage properties	Stage 1	Stage 2	Stage 3	Stage 4	Stage 5
Height (mm)	152	108	103	114	123
Width (mm)	268	268	268	268	268
Length (mm)	568	568	568	568	568
Volume (m^3)	0.0231	0.0164	0.0157	0.0174	0.0187

The stage trays were inclined at 8° from the horizontal, which was equal to the sloped square tube angle. This inclination allowed the collection of the distillate from the highest point to the lowest point of the tray. Condensed drops of fresh water fall onto the tray surface and collect at the centre (V-shape) section. The droplets then flow down an inclined tray to the lowest point where the trough was located. The inclined stage trays fitted onto the skeleton structure, shown in Figure 3.37, were secured inside the skeleton structure by means of 4 x 4 mm pop rivets.

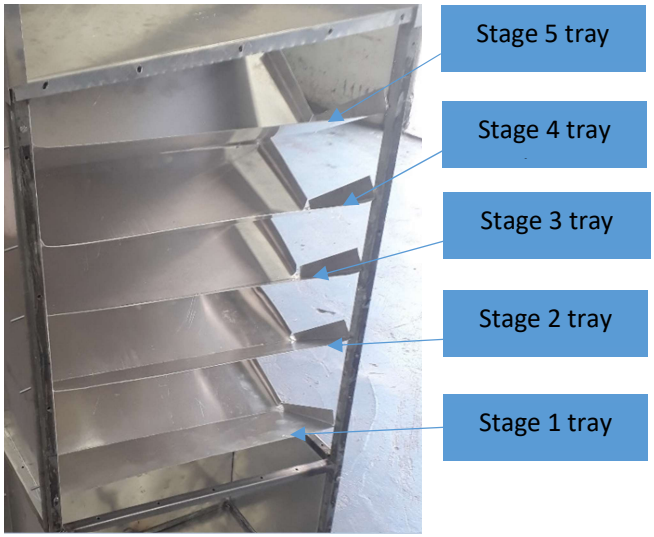

Figure 3.37: Inclined stage trays

On each tray, a 14.5 mm hole was drilled 68 mm from the back cover and 53 mm from the closest edge of the tray to accommodate the vapour transfer tubes. A 3D design (see Figure 3.38) shows the vapour transfer tubes used to transfer the vapour from one stage to the next. The vapour transfer tubes, made from copper material with 90° elbows and 15 mm external diameter, were tightly fitted in the holes. Figure 3.38 also shows the stage trays, as discussed above, as well as other system components. Some of these components will be discussed in the following sections.

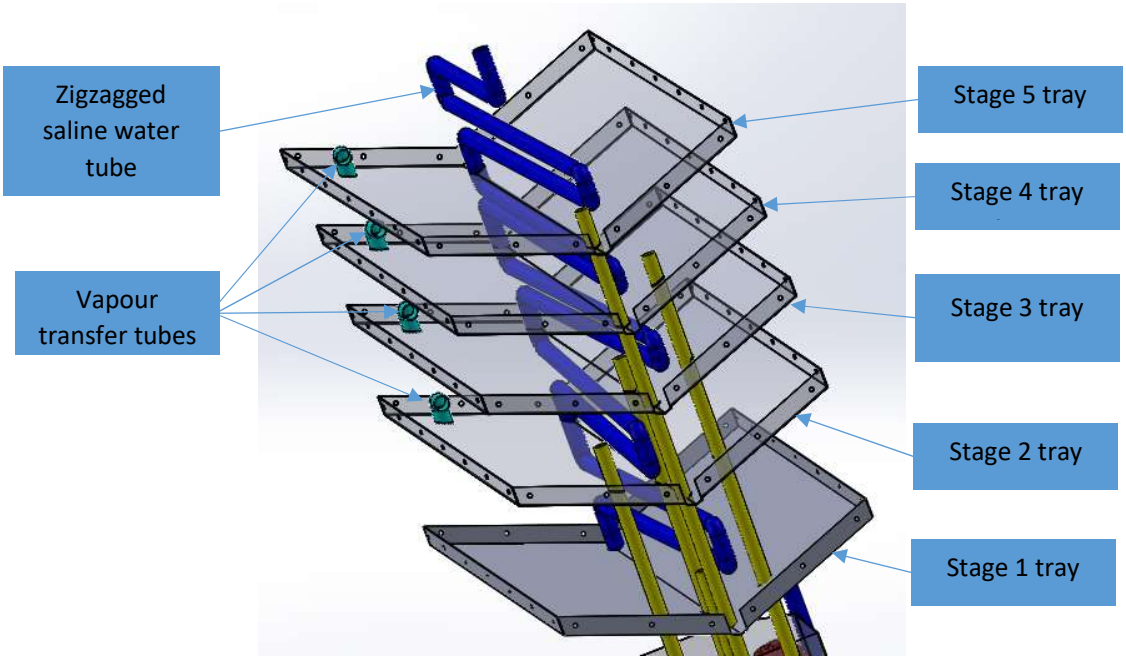

Figure 3.38: Stacked stage trays in 3D

Additional 15 mm holes were drilled at the centre of the stage trays to accommodate the zigzagged saline water tube. Each tray consisted of one hole located approximately 40 mm from one end of the tray along its length. After the zigzagged saline water tubes were inserted through the holes, a water-resistant sealant was applied to seal around the tube and form a vapour tight boundary.

Furthermore, 15 mm holes were drilled at one end of the trays through which the vapour make-up tubes protrude. The vapour make-up tubes will be discussed later in the chapter. The number of holes differs depending on which stage each tray was installed. Stage one had six holes, as shown in Figure 3.39, where all vapour make-up tubes and zigzagged saline water tube passes. The vapour make-up tube that supplies the vapour to stage 1 terminates in that stage. Stage 1 tray did not have a vapour transfer tube, so no vapour transfer tube was drilled.

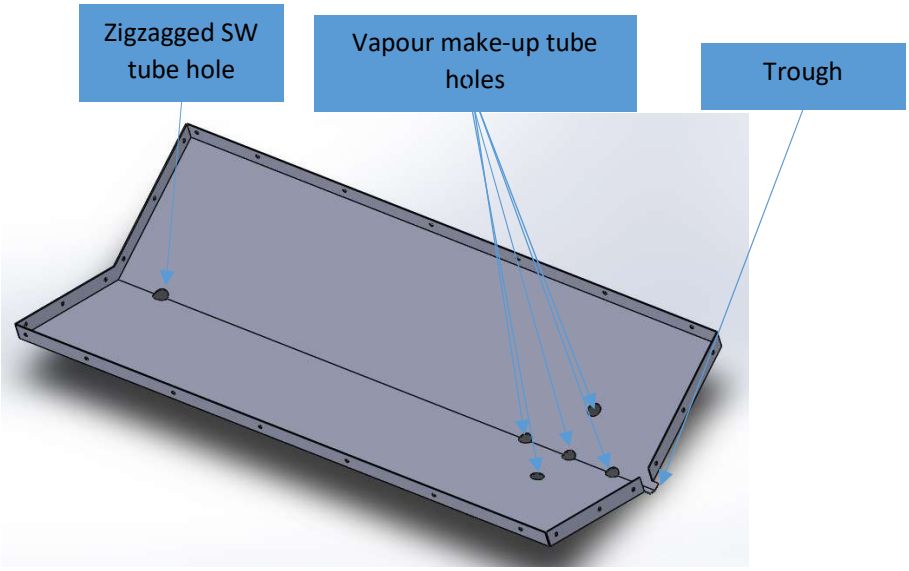

Figure 3.39: Stage 1 tray in 3D

Each tray had a trough at its lower end used for collecting the distillate (see Figure 3.39). Vapour make-up tubes, shown in Figure 3.40, are passing through the holes of stage 1 tray. A clear view of these tubes will be shown when the evaporator is discussed later.

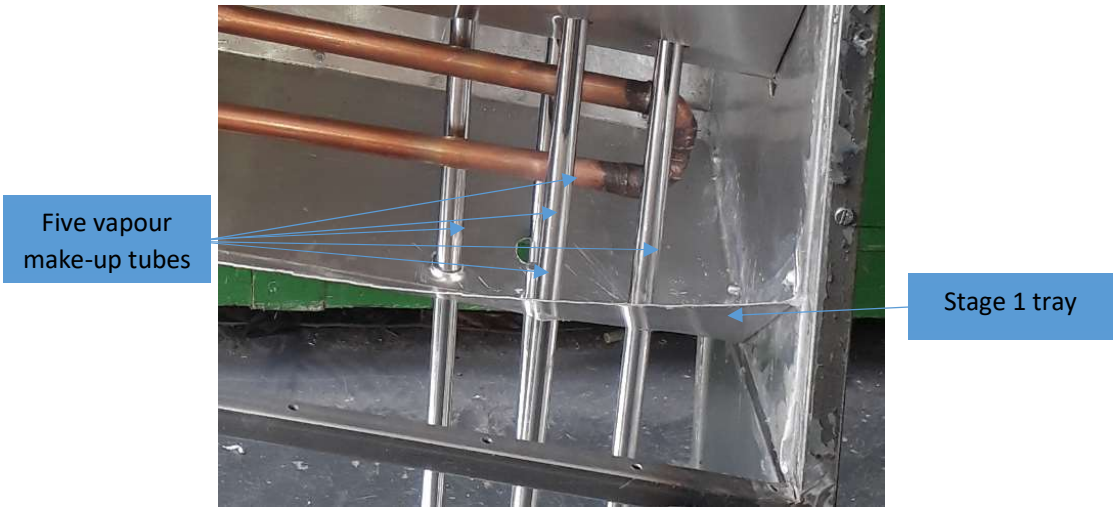

Figure 3.40: Stage 1 vapour make-up tube

Four vapour make-up tubes continue through the stage 2 tray and the tube that supplies vapour to this stage terminates in that stage (stage 2). Figure 3.41 shows the stage 2 tray with four vapour make-up tube holes, zigzagged SW tube hole and one additional hole for a vapour transfer tube hole. Since the vapour make-up tube supplying vapour to stage 1 terminated in that stage (stage 1), there are only four vapour make-up tubes on stage 2 tray.

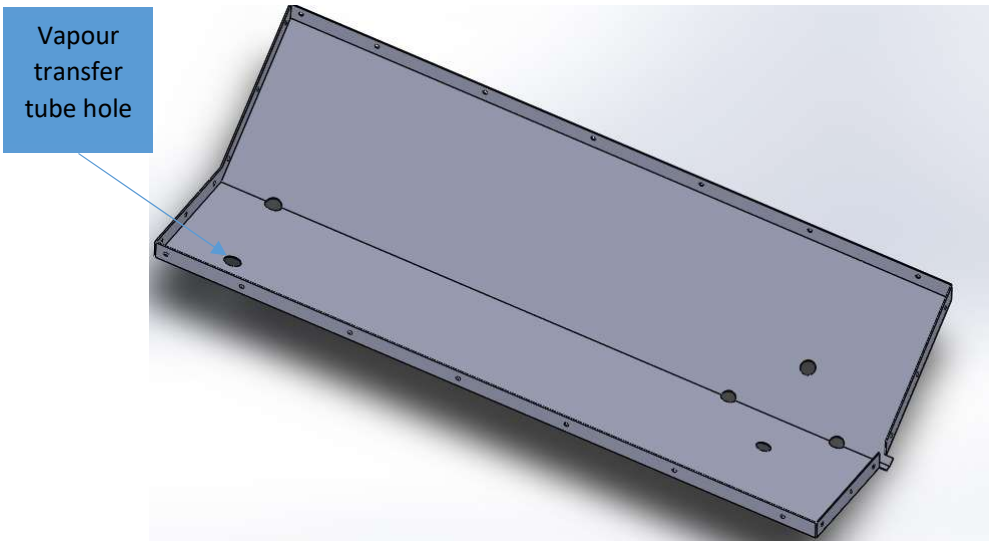

Figure 3.41: Stage 2 tray in 3D

Four vapour make-up tubes passing through stage 2 tray are shown in Figure 3.42. As in stage 1, the vapour make-up tube that supplies the vapour to this stage (stage 2) terminates in stage 2.

Figure 3.42: Stage 2 vapour make-up tube holes

Three vapour make-up tubes then continue through the stage 3 tray to the third stage. Again, the vapour make-up tube that supplies vapour to the third stage terminates in that stage (stage 3). Figure 3.43 shows the stage 3 tray with three vapour make-up tube holes, one zigzagged SW tube hole and a vapour transfer tube hole. The vapour make-up tube which supplies stage 1 and 2 terminated in those stages, so only three vapour make-up tubes continue to stage 3.

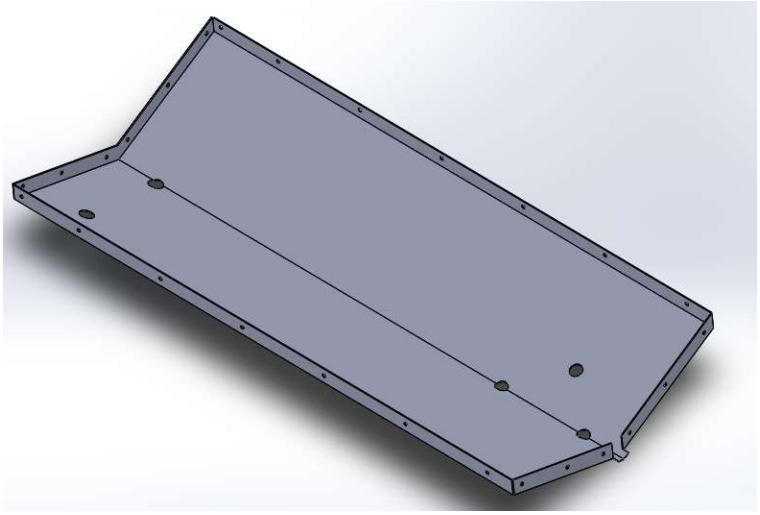

Figure 3.43: Stage 3 tray in 3D

Figure 3.44 shows the vapour make-up tubes passing through stage 3. In stage 3, the vapour make-up tube that supplies vapour in that stage terminates there in stage 3. Therefore, only two vapour make-up tubes continue on to the stage 4 tray.

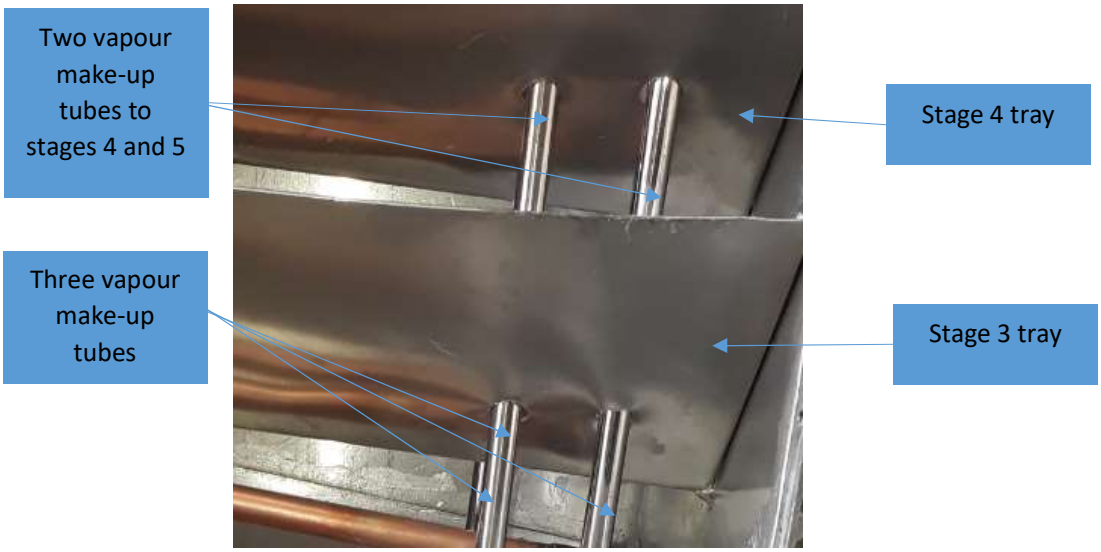

Figure 3.44: Stage 3 vapour make-up tube holes

Two vapour make-up tubes continue through to stage 4. Figure 3.45 shows the stage 4 tray with two vapour make-up tubes holes, zigzagged SW tube hole and a vapour transfer tube hole. As in the previous stages, the stage 4 vapour make-up tube terminates in that stage (stage 4) as well.

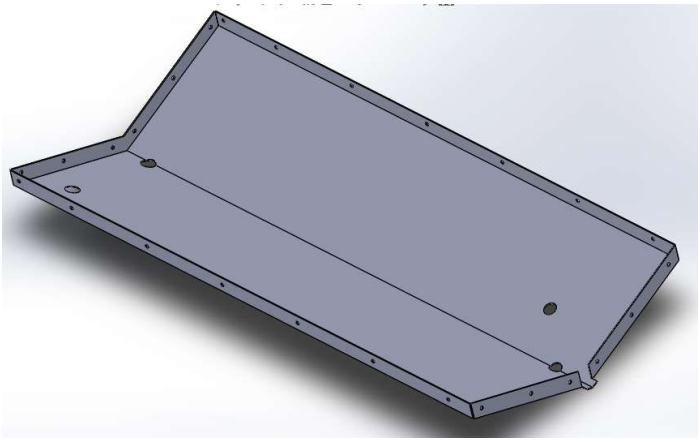

Figure 3.45: Stage 4 tray in 3D

Lastly, only one vapour make-up tube continues through stage 5 tray (not shown). This vapour make-up tube supplies the vapour in that stage (stage 5). Figure 3.46 shows the stage 5 tray with one vapour make-tube hole, vapour transfer tube hole and a zigzagged SW tube hole. Stage 5 was the highest stage amongst those supplied by the evaporator in terms of its location, situated farthest away from the evaporator, suggesting that it maintains a cooler temperature as compared to the lower stages.

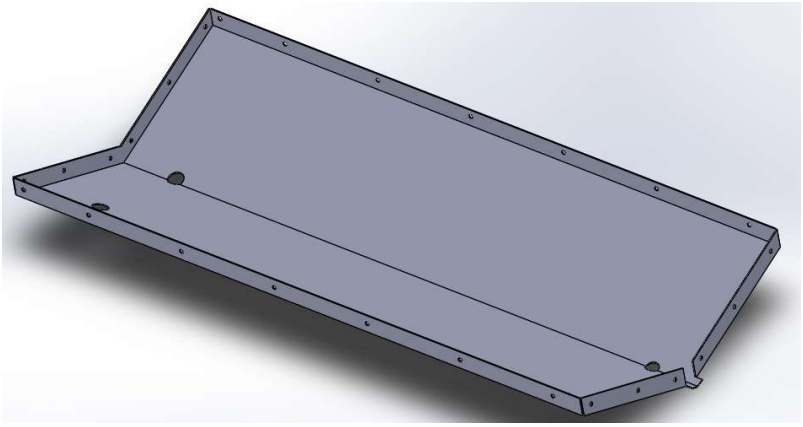

Figure 3.46: Stage 5 tray in 3D

3.9 **U-shaped tubes (cross over tubes)**

The U-shaped tubes and their purpose were briefly discussed above. When the distillate reached the distillate collecting trough of the stage trays, it then flows into the U-shaped tubes (see Figure 3.47). These U-shaped tubes were made from copper material with an external diameter of 15 mm and length of 75 mm. The U-shaped tubes were tightly fitted onto the distillate collecting trough and sealed with water-resistant sealant. There were six of these tubes in total, five connected onto the upper front cover and one onto the lower end of the basin type solar still. They play two roles in the system: the first role is collecting the distillate

produced by the system and guiding it into the distillate tanks. The second role is acting as vapour trap devices to prevent the vapour from escaping the stages (Jubran et al., 1999). The U-shaped section of the tube was filled with fresh water prior to the commencement of the operation of the system. This freshwater stayed inside the U-shaped section of the tube until distillate produced displaced it by pushing it out of the tube. The distillate then in turn stayed in this section of the tube until more distillate displaced it as well. When the distillate was produced, it flowed right into the tube and displaced the same amount as the freshwater/distillate in the tube section. The distillate and freshwater displacement continued throughout the operation until all fresh water was replaced and only the distillate remained inside the U-shaped section of the tube. It is clear from Figure 3.47 that the U-shaped tubes were slightly tilted downwards to encourage the flow of distillate out of the system. The downward tilt also help minimise the amount of distillate laying on the stage tray which will eventually vaporize or dry out.

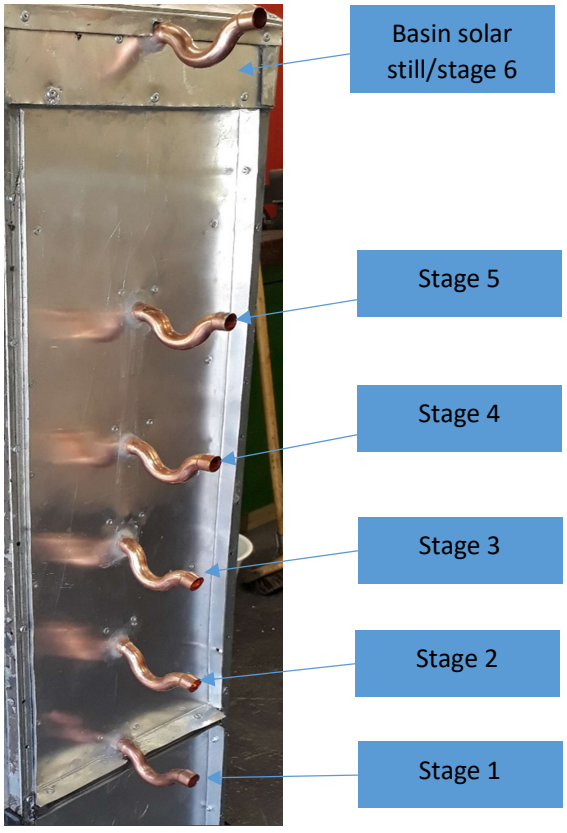

Figure 3.47: U-shaped tubes connections

3.10 Typical stage

A stage, just like the basin type solar still, is comprised of several components. A typical stage (stage 5) shown in Figure 3.48 consists of the components which make up the stage. Some of the components have already been discussed above in various sections. The figure shows

a top view of the fifth stage of the assembly with its components. Stage 2, 3, 4 and 5 had the same components, with the exception of stage 1. The only component that stage 1 did not have was the vapour transfer tube since it was the first stage of the assembly. Stage 5, like stage 2, 3 and 4 had the vapour make-up tube, vapour transfer tube, zigzagged saline water tube, four vertical covers and stage tray. The top view shows the fifth stage with the basin type solar still removed. Stage 5 was enclosed by four square tubes of the skeleton structure. All the joining or mating surfaces were treated with water-resistant sealant to prevent the vapour from escaping the stage while also preventing the surrounding air and other foreign materials from accessing the stage. The latent heat of condensation was transferred to the saline water flowing in the zigzagged saline water tube. Since there was no waterbed in the stages, some of the latent heat was lost through the walls of the stage to the surroundings.

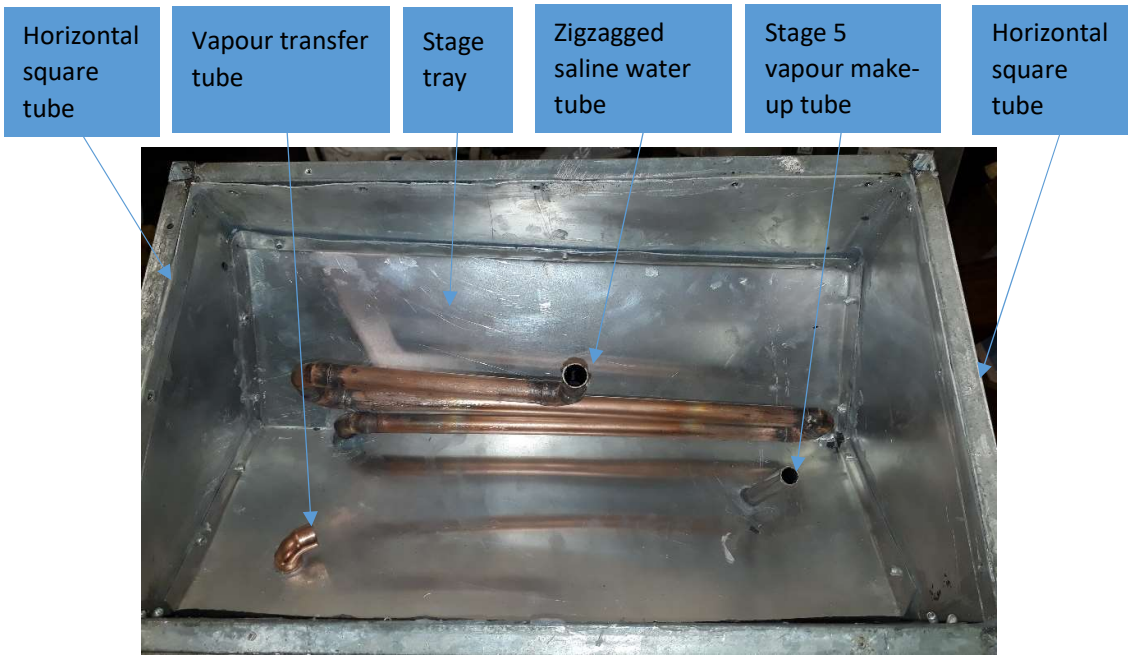

Figure 3.48: Typical stage

3.11 **Vapour transfer tubes**

Vapour transfer tubes were basically at 90° with a 15 mm external diameter copper fitting elbow, installed on four of the five stages (as previously shown in Figure 3.38). Stage 1 did not have a vapour transfer tube as there is no vapour being transferred to it as the first stage of the system. These tubes were used to transfer the vapour from one stage to the next if that particular stage experienced an excessive amount of vapour at a certain time during the operation. The excess vapour also increased the temperature of the condensing surfaces of the stage trays which stopped desalination all together. The vapour can only be transferred to the adjacent stage (next upper stage) as they were interconnected, or in other words, stage 1

can only transfer its excessive vapour to stage 2, stage 2 to stage 3, and so on. Stage 1 cannot transfer its excessive vapour directly into stages 3, 4 or 5. These tubes were tightly fit and water-resistant sealant secured the seal around them. These tubes (see Figure 3.49) were installed in four of the five stages.

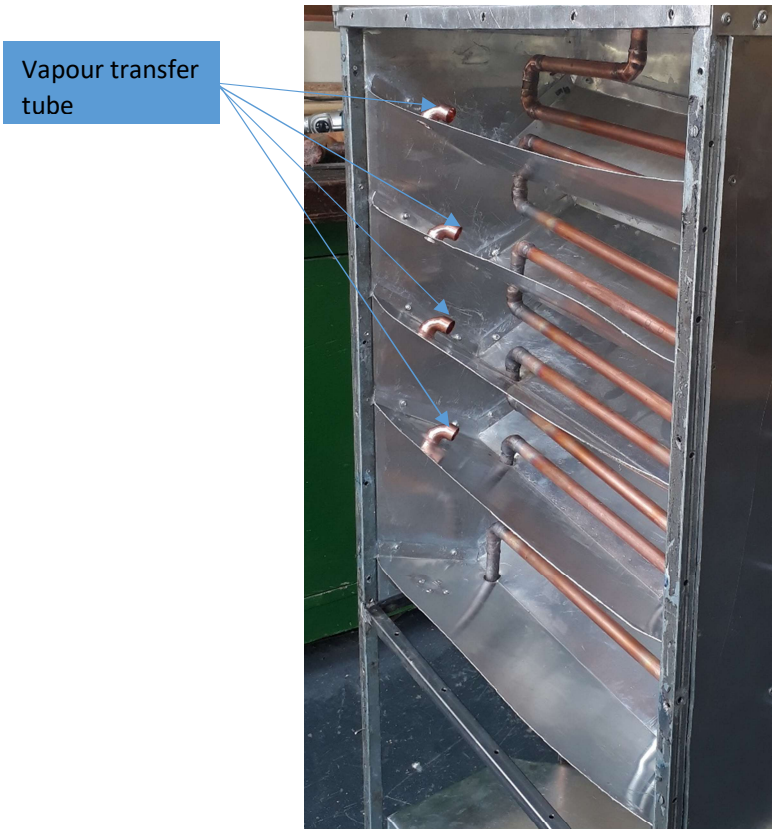

Figure 3.49: Vapour transfer tubes

3.12 **Zigzagged saline water tube**

The zigzagged saline water tube (see Figure 3.50), as mentioned in various sections, was made from copper material with an outside diameter of 15 mm. The tube and the copper elbows were joined by means of brazing. Acetylene gas and copper welding rods accomplished joining process. Each turn was accomplished by means of a 90° copper elbow with a 15 mm external diameter. The saline water tube, running through the system from top to bottom, played two roles in the operation of the multistage tower. The first role was collection of the pre-heated saline water from the basin type solar still to convey it to the secondary saline water tank at the bottom of the system. Since the saline water flowing in this tube traverses the stage filled with hot vapor from the evaporator, heat transfer took place between the condensing vapour (latent heat of condensation) and the saline water in the tube. Theoretically, each time the saline water passes through the stage, its temperature increases

slightly. The total length of the tube from one tip protruding in the basin type solar still to the secondary saline water tank is approximately 4963 mm (4.963 m).

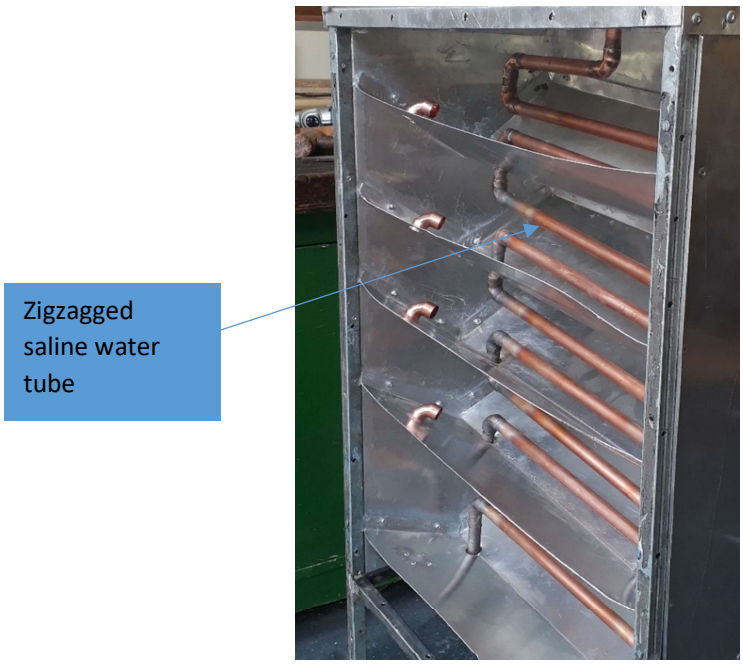

Figure 3.50: Zigzagged saline water tube

Instead of employing a single pass in each stage, a double pass was used to enhance the surface area of the tube (see Figure 3.51). Theoretically, the double pass increases the amount of time the saline water traverses the stage and thus increases the temperature of saline water further. The saline water completely flowed down to the secondary saline water tank under the influence of gravity. The float valve mechanism in the secondary saline water tank retarded the flow of saline water. The process of slowing the saline water was meant to expose the saline water to the hot vapour for longer. The flow appeared in droplet form when emerging in the secondary saline water tank though the float valve mechanism.

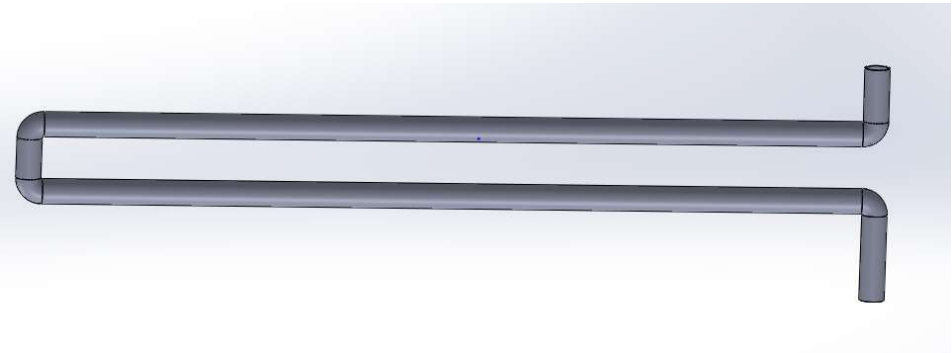

Figure 3.51: Zigzagged saline water tube double pass in 3D

The number of zigzagged saline water tube passes and the total length of the tube in each stage are presented in Table 3.2.

Table 3.2: Zigzagged saline water tube passes

Stage properties	Stage 1	Stage 2	Stage 3	Stage 4	Stage 5	Total
Passes	2	2	2	2	2.5	-
Length per pass (mm)	432	421	421	421	421	-
Total length of tube in a stage (mm)	1004	932	932	932	1163	**4963**

3.13 Secondary saline water tank and its components

3.13.1 The secondary saline water tank

This tank (see Figure 3.52), made from a 0.9 mm thick aluminium material, was shaped as a pentagon (five sides) and used to store pre-heated saline water from the basin solar still and through the stages. Its body, with a vertical height of 180 mm, was made from a single aluminium sheet. The total length of a single aluminium sheet was 756 mm. The shape and size of the tank were achieved by marking off using a steel ruler, engineer's square, marking-off paint and a scraper. The initial cutting was with a guillotine machine and the final sizes were achieved with tin snip pliers.

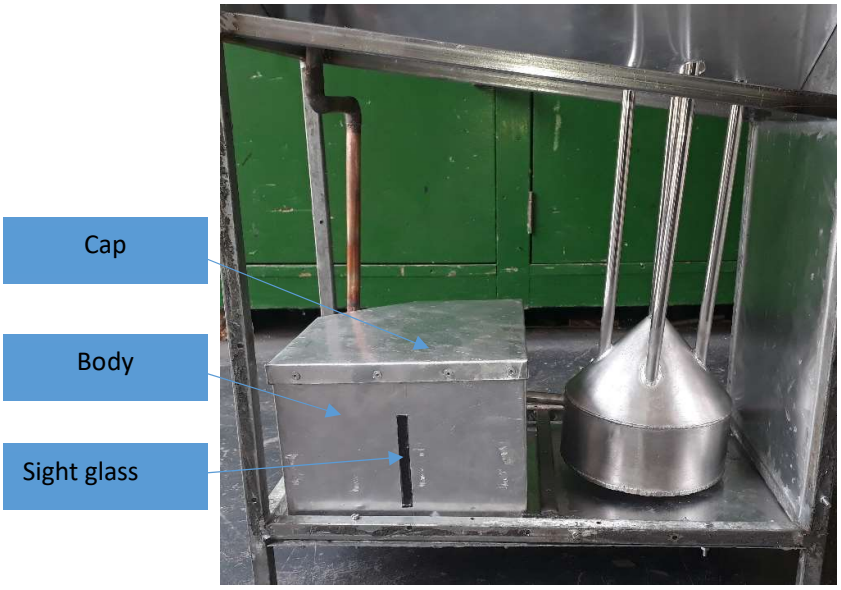

Figure 3.52: Secondary saline water tank

The pentagon shape was accomplished with a bending machine. Secondary SW tank had a maximum water capacity of 3.8 litres when fully filled. The sight glass for monitoring the

amount of saline water in the tank was achieved with a marking-off instrument. The cutting was initially done by an angle grinder and a cutting blade and thereafter, tin snip pliers. The sight glass slot was cut 30 mm from the bottom and 37 mm from the top, with a width of 10 mm. A 3 mm thick Perspex glass was used as a sight glass to monitor the level of saline water because of its transparent material. The Perspex glass, cut into a rectangular of 100 mm length and 20 mm width, was attached to the inner wall of the tank using the water-resistant sealant. It was left to dry for about 15 hours before water was poured to test for leaks. The body, made from a single aluminium sheet, was then drilled at both ends of the sheet using a 4 mm drill bit and a hand drill; this was to fix both ends to create an enclosure of a pentagon shape. A 3D view of the tank is presented in Figure 3.53. The figure shows the sight glass slot, float valve mounting hole and a saline water transfer tube hole.

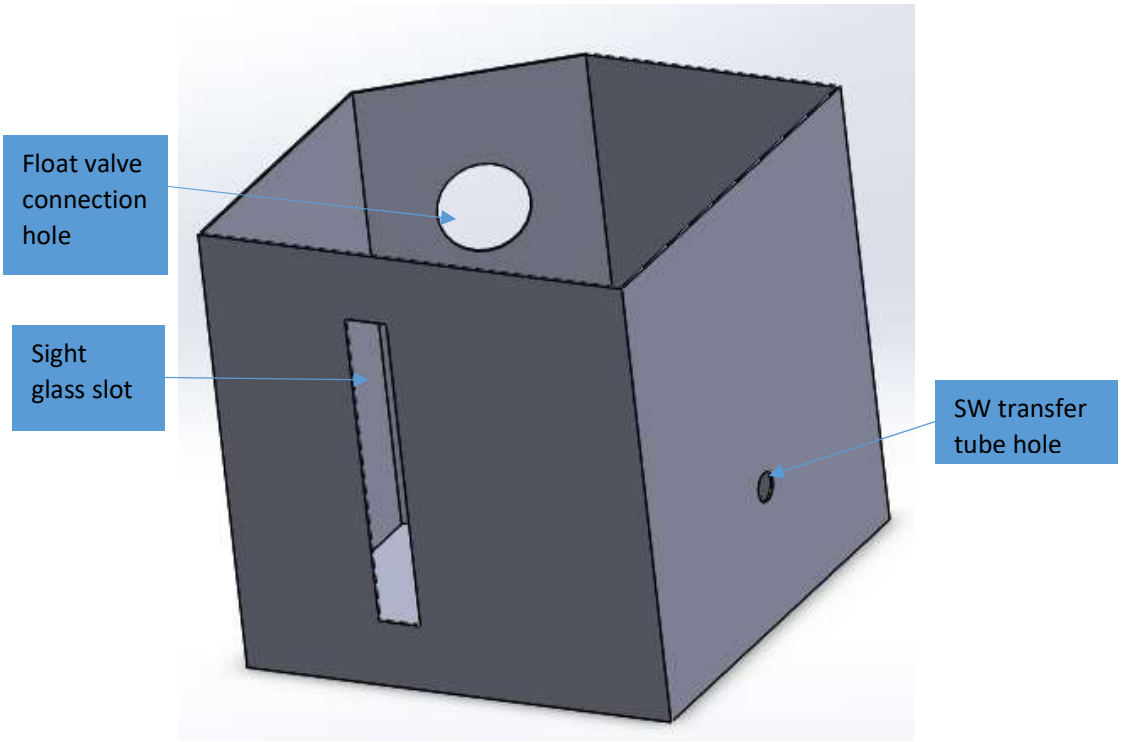

Figure 3.53: Tank lips in 3D

The tank was secured on the bottom cover (discussed under 3.7.6 above) of the multistage located underneath the secondary tank and the evaporator compartment. Several 4 mm holes were drilled using a 4 mm drill bit and a hand drill. A water-resistant sealant was applied to the mating surfaces and 4 x 4 mm pop rivets secured the tank. The tank was then painted with an aluminium paint to prevent corrosion and oxidation. A cap, shown in Figure 3.52, was manufactured in the same process as the body of the secondary saline water tank. However, the cap was altered into a two-piece cover for ease of access when cleaning or conducting maintenance. The altered two-piece cap (see Figure 3.54) has a ball float in the tank. The

figure also shows a thermocouple probe used for temperature reading in the secondary saline water tank.

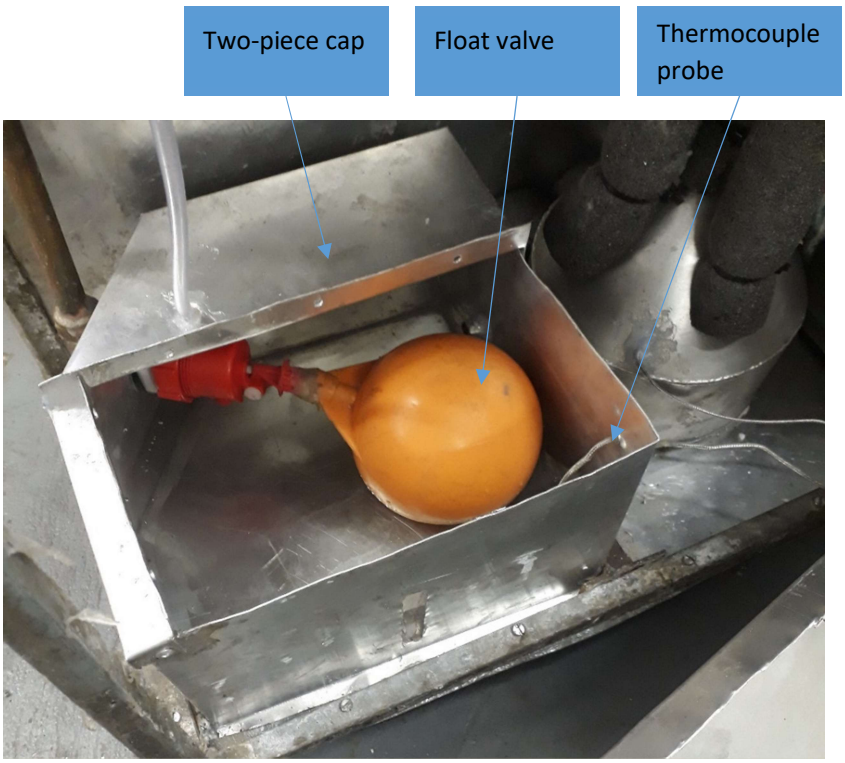

Figure 3.54: Two-piece cap

A 20 mm hole was drilled at the back of the secondary saline water tank using an 18 mm drill bit and a hand drill. A round file was used to achieve a smooth circular hole. A float valve fitting was threaded through the hole and adjusted accordingly. The fitting was then tightly connected to the zigzagged saline water tube (see Figure 3.55).

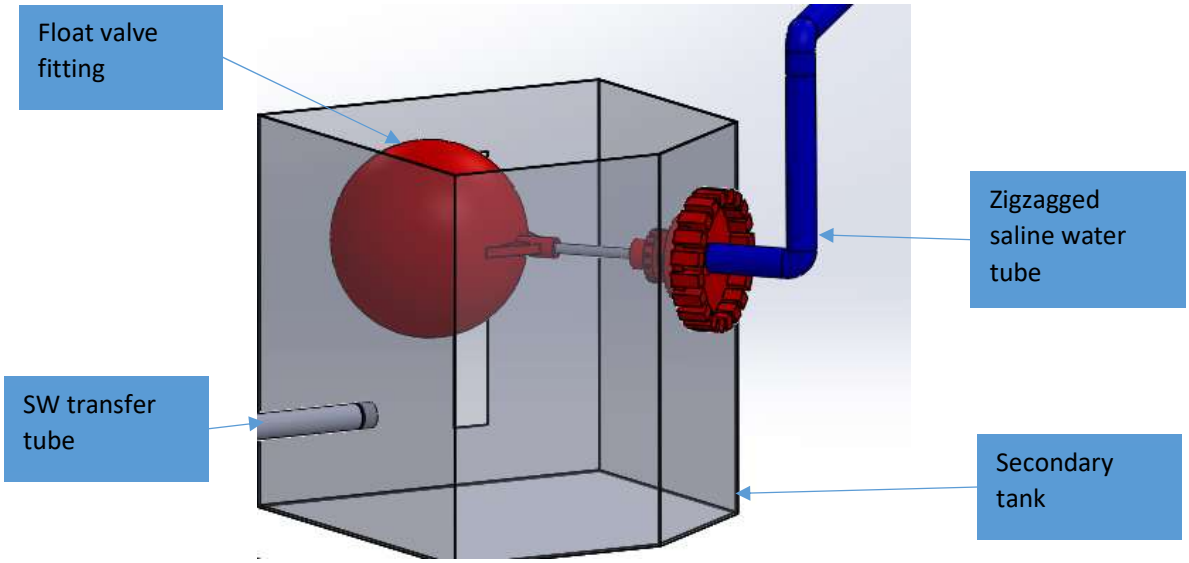

Figure 3.55: Zigzagged saline water tube connection in 3D

3.13.2 Float valve

The float valve in the secondary saline water tank was fitted with a ball float of 100 mm in diameter and a connecting rod 8 mm in diameter and 25 mm long. The valve (see Figure 3.56) was modified to fit into the secondary saline water tank. The length of the rod was reduced so that the valve could fit inside the tank. The float valve in the secondary saline water tank controls and regulates the saline water coming from the basin type solar still through the zigzagged saline water tube. It was also used to cut-off the flow of saline water from the basin type solar still when repair, maintenance or any problem was experienced in the lower part of the system.

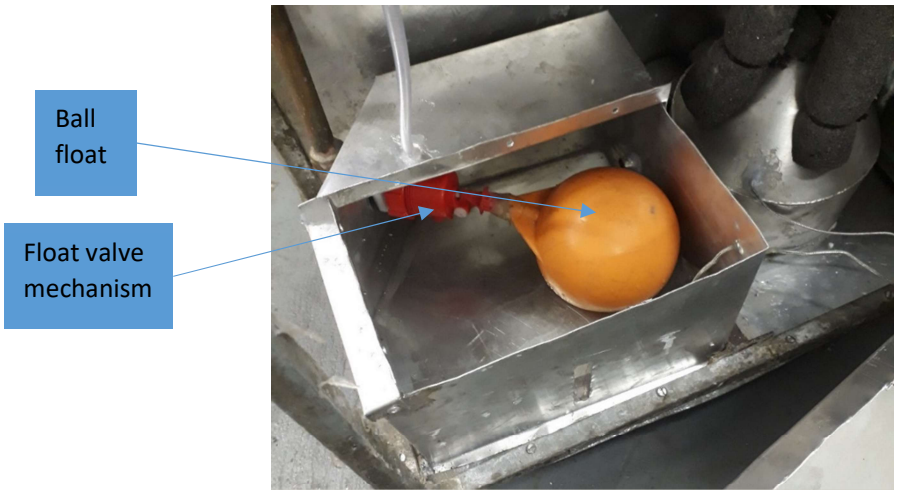

Figure 3.56: Float valve inside the secondary saline water tank

This valve was adjusted carefully to shut the saline water supply from the basin type solar still at a pre-determined level. The adjustment of the valve was crucial as too much supply of saline

water would simply add more cold saline water into the evaporator and reduce the evaporation rate. Maladjustment also means that a large amount of heated saline water in the evaporator was mixed with cold saline water. The introduction of a large amount of cold saline water in the evaporator means that vapour production was halted or reduced and the heating of this saline water must occur before vapour can be produced. Therefore, cold saline water in the evaporator affects the productivity of the entire system.

A 50 mm thick glass wool material (see Figure 3.57) insulated the saline water tank on the outer body. The insulation material was sandwiched between the outer body of the secondary tank and the surrounding outer covers of the system. The insulation also insulated the rest of the secondary tank and evaporator compartment.

Figure 3.57: A 50mm thick glass wool insulation material

3.13.3 Saline water transfer tube

The saline water transfer tube's purpose is to transfer the saline water from the secondary saline water tank into the evaporator. This tube was made from a 316-food grade stainless-steel material and welded onto the evaporator. The tube (see Figure 3.58 and Figure 3.59) had an external and internal diameter of 12.7 and 9.7 mm, respectively, a length of 63 mm, and was welded onto the evaporators. The saline water transfer tube hole on the secondary saline water tank was drilled 72 mm from the multistage bottom cover. The tube was positioned such that the end on the secondary tank side was higher than that of the evaporator side. The difference in height between the evaporator and the secondary saline water tank created an angle of inclination on the tube to allow the saline water to flow under the influence of gravity from the secondary tank to the evaporator.

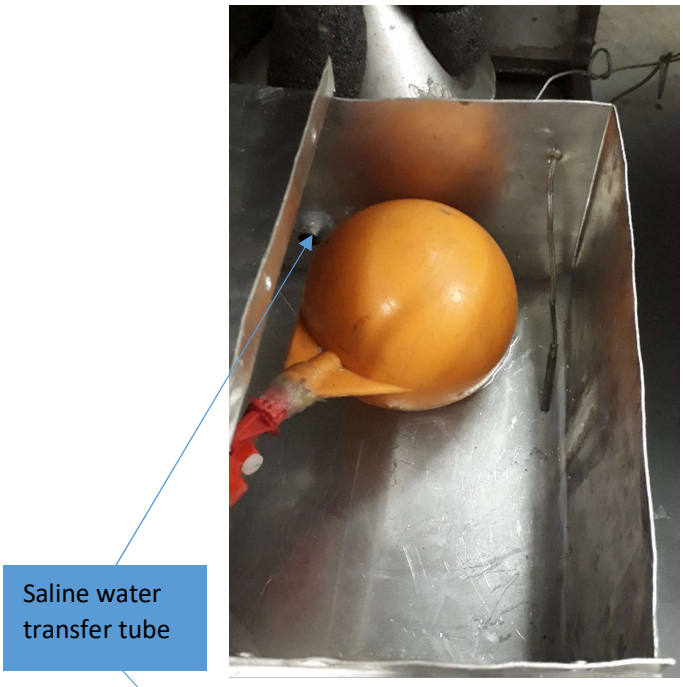

Figure 3.58: Inside view

Figure 3.59: Outside view

3.14 **Vapour make-up tubes**

Five vapour make-up tubes, connected to the evaporator by means of welding, protrude through the stage trays as previously discussed under section 3.8. They were made from a stainless-steel material similar to that of the saline water transfer tube. The vapour make-up tubes and the evaporator were made by an external company (outsourced). Their final sizes in length were measured using a tape measure, scrape, and a marking-off spray. They were then cut with a steel hacksaw and the ends filed with a fine flat file to remove rough edges.

The tubes, mounted on a cone shaped section of the evaporator, were to flush with the inside wall of the evaporator (see Figure 3.60). The flushing was done to avoid impeding the flow of the vapour from the evaporator to the stages.

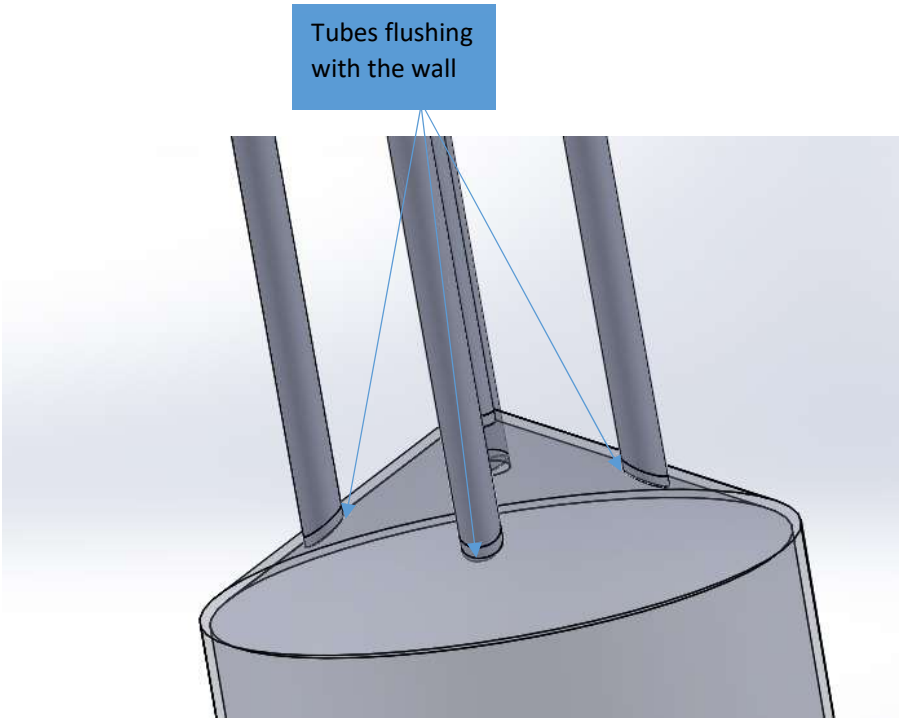

Figure 3.60: Vapour make-up tubes in 3D

The fitting of the vapour make-up tubes and the evaporator into the multistage tower will be discussed in the next section. These tubes differ in length depending on which stage they are supplying vapour to, as discussed under section 3.8. The basin solar still or stage 6 produced its distillate independently and was not supplied by the evaporator. Therefore, the basin type solar still did not have the vapour make-up tube connected to it. The vapour make-up tubes had 12.7 mm outside diameter and 9.7 mm inside diameter. The stage 1 vapour make-up tube was located at the centre of the cone shape section; the other four tubes were spaced equally at a radius of 50 mm around the circumference of the cone shaped section of the evaporator. Figure 3.61 show how the tubes were positioned at the top of the evaporator. The tubes numbering was counted clockwise when viewed from above, for instance, stage 3 tube came after stage 2 in the clockwise direction.

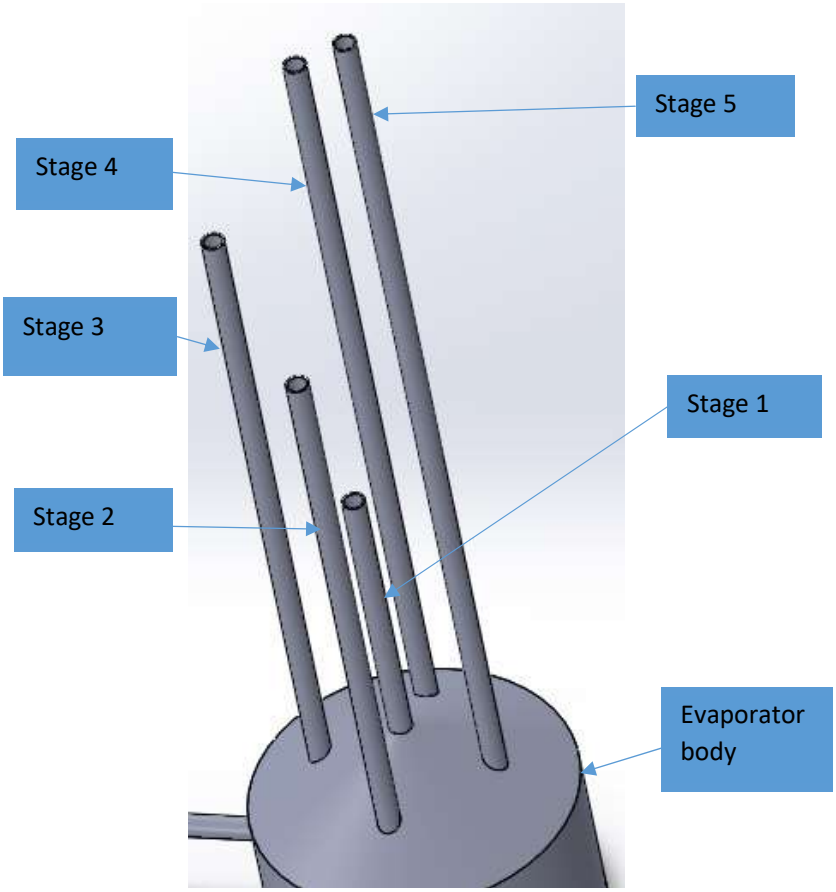

Figure 3.61: Vapour make-up tubes in 3D

3.14.1 Stage 1

The tube supplying vapour to this stage was the shortest among all four other tubes. Its length was due to the location of stage 1 at the bottom of the multistage tower. This tube, located at the topmost part of the cone shaped section of the evaporator, had a total vertical length of 294 mm from the top of the evaporator to just above stage 1 tray.

3.14.2 Stage 2

This tube was the second shortest as it terminated in stage 2 where it supplied the vapour. This tube, located adjacent to stage 1 vapour make-up tube, had a total length of 348 mm from its base to it top-most vertical tip which protrudes through the stage 2 tray.

3.14.3 Stage 3

The stage 3 vapour make-up tube was the third shortest tube, as it supplied vapour to stage 3. It had a total length of 459 mm from its base to its top-most tip which was in the third stage.

3.14.4 Stage 4

This tube was the fourth shortest or second longest tube in the vapour make-up tubing arrangement. The tube, supplying vapour to the fourth stage of the multistage tower, had a total length of 570 mm from its base to its top-most tip.

3.14.5 Stage 5

This vapour make-up tube was the longest tube amongst other four tubes. The tube had a total length of 681 mm from its base to its top-most tip.

3.14.6 The evaporator

The evaporator (see Figure 3.62), a cylindrical shaped object with an external diameter of 146 mm, was made from a food grade stainless steel with a thickness of 1.5 mm This material the evaporator was made from was similar to that of the vapour make-up tubes and saline water transfer tube. The cylindrical section of the evaporator had a vertical height of 60 mm, while the vertical height of the cone shaped section was 47 mm. The evaporator had an approximate 1.2 litres capacity to hold SW. Furthermore, in addition to the vapour make-up tubes and saline water transfer tube, the evaporator has two more other tubes – called “hot and cold tubes” – as one of them held relatively cold saline water and the other held heated water.

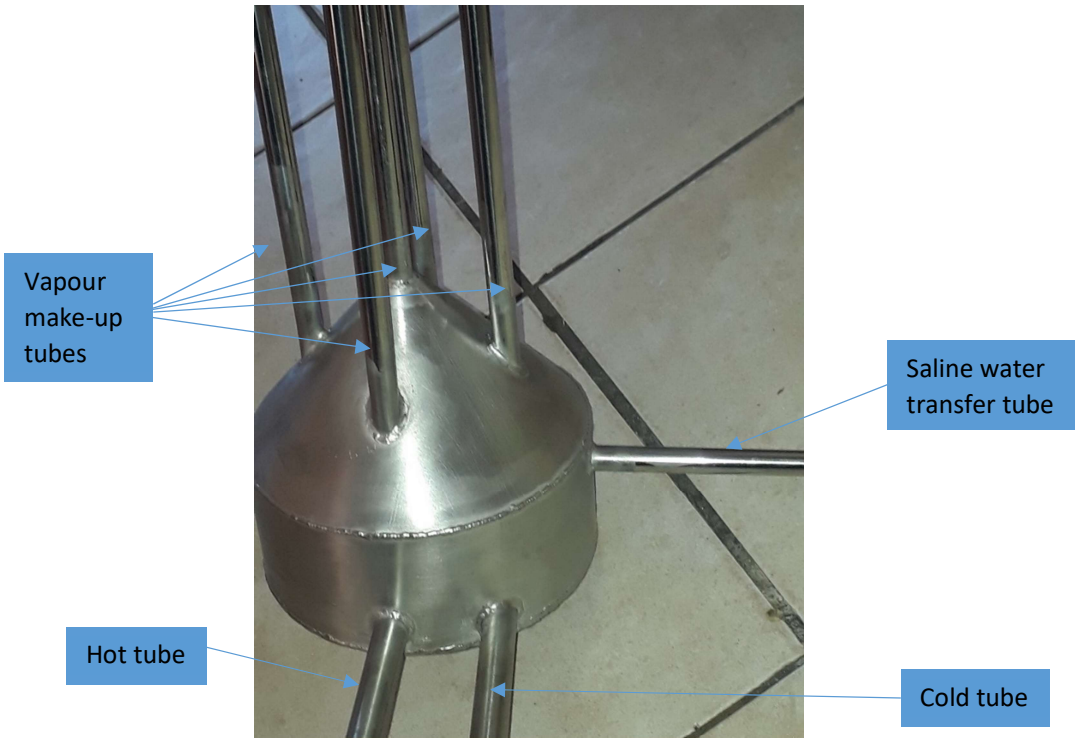

Figure 3.62: The evaporator

3.14.7 Saline water transfer tube connection to the evaporator

The saline water transfer tube, discussed under section 3.13.3, is now discussed with respect to its connection to the evaporator. This tube protruded through the cylindrical body of the evaporator on its side. It was then bent at 90° down (see Figure 3.63). The downwards facing portion of this 30 mm long tube is to minimise the back flow of saline water. Back flow occurs when water under pressure enters the evaporator, as some of this water tends to flow back into the secondary saline water tank. In addition, a non-return valve made in the Mechanical workshop from readily available material was connected to this saline water transfer tube to prevent a back flow from the evaporator. The opening of the downwards facing section was submerged under saline water in the evaporator so vapour cannot not flow back into the secondary saline water tank.

When the evaporator was full, excess saline water flowed back into the secondary saline water tank. The position of the tube was approximately 68 mm from the bottom cover of the multistage tower. The tube's position and it design restricted the amount of saline water entering the evaporator from the secondary saline water tank. In turn, saline water from the secondary tank stopped flowing and filled the secondary tank. Filling the secondary saline water tank to its pre-determined level caused the float valve to shut off the flow of saline water. Saline water flowing from the basin still through the zigzagged saline water tube was stopped. The flow of saline water was thus regulated and controlled in this manner.

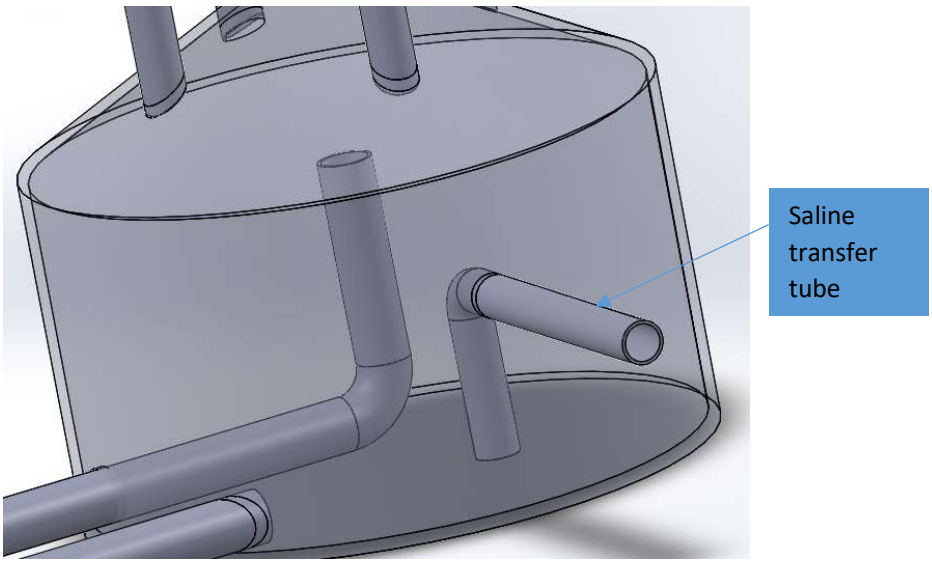

Figure 3.63: Saline water transfer tube in 3D

3.14.8 Hot and cold tubes

Figure 3.64 shows the actual hot and cold tube: the cold tube refers to the tube that carries relatively cold saline water as compared to the hot tube which carries the mixture of heated saline water and vapour. Both the cold and hot tubes were connected to the evacuated tube solar panel. Both tubes had an external and internal diameter of 15.88 mm and 12.88 mm, respectively.

Figure 3.64: Hot and cold tubes

The cold tube, 87 mm long, protruded through the body of the evaporator, as shown in Figure 3.65. The cold tube was not bent but straight and was installed with its centre 13 mm from the bottom of the evaporator base. The cold tube and the evaporator were positioned such that when the saline water entered the evaporator, it flowed through this tube under the influence of gravity towards the solar collectors. Moreover, the ejected saline water from the solar collector flowed through this tube for recirculation.

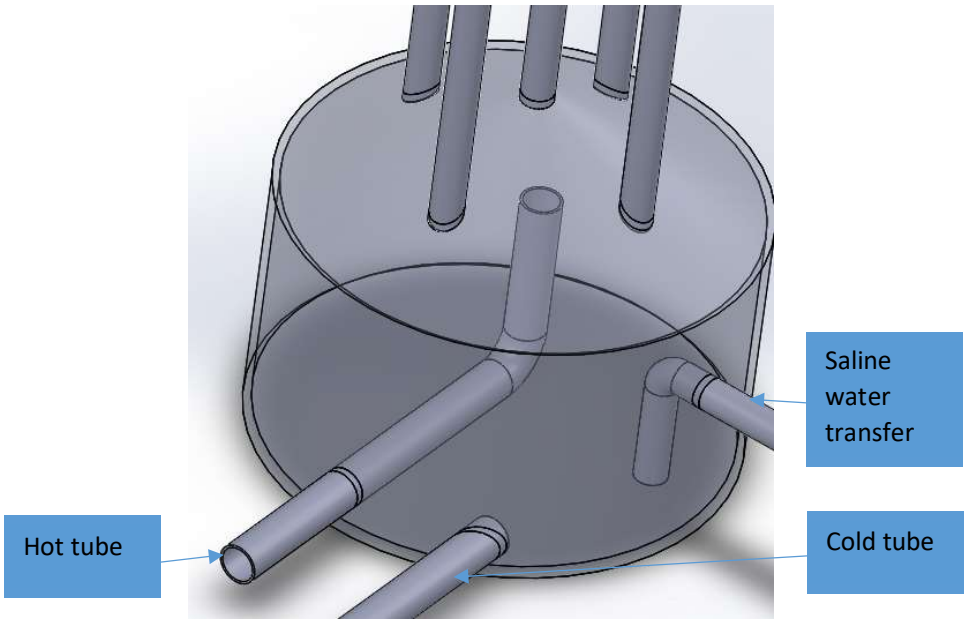

Figure 3.65: Hot and cold tubes in 3D

The hot tube (see Figure 3.66), bent 90° upwards, was 197 mm long and protruded through the body of the evaporator. The bent section of the tube, which was vertically up, was inside the evaporator. The horizontal section extended outside of the evaporator. The tube was not tilted but rather installed horizontally so the bent section was straight up. The end of the vertical section of the tube was directly below the stage 1 vapour make-up tube. The water vapour mixture flowed under pressure from the ETSC through the hot tube and into the evaporator. The water-vapour separation took place at the exit of the hot tube. The denser saline fell to the floor (base) of the evaporator while the lighter vapour ascended towards the vapour make-up tubes. The other driving force was the pressure build-up in the evaporator which then allowed the vapour to flow up into the stages through the vapour make-up tubes. The denser saline water, which fell onto the floor of the evaporator, was then recirculated through the cold tube into the ETSC for reheating. The cycle repeated every time the denser saline water entered the evaporator.

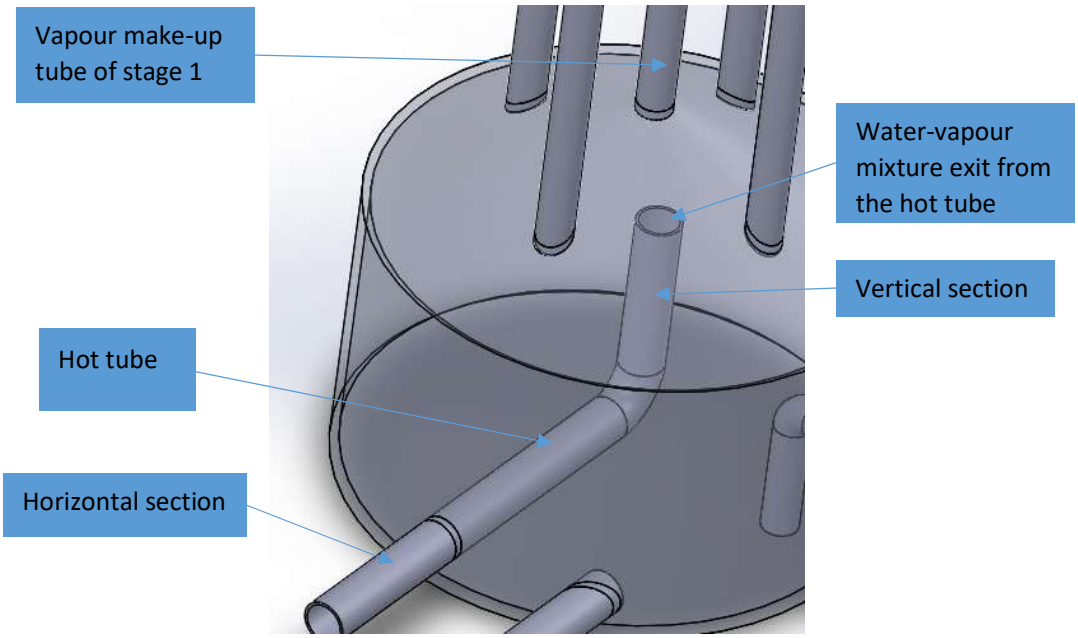

Figure 3.66: Hot tube in 3D

A 20 mm thick polystyrene insulation material was inserted underneath the evaporator to minimise heat loss. The polystyrene material (see Figure 3.67) is cut into a disc shape. Due to the inflexibility of this polystyrene material, it was unable to wrap around the evaporator and the vapour make-up tubes. So an alternative glass wool material (see Figure 3.57) was used to wrap the evaporator and the vapour make-up tubes for insulation purposes. The insulation material was sandwiched between the outer body of the evaporator and the surrounding outer covers of the condensing tower.

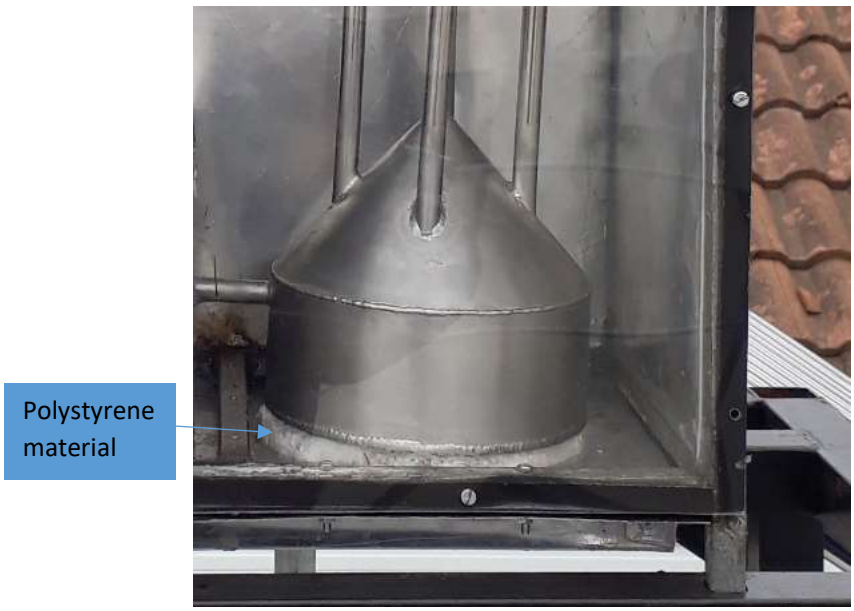

Figure 3.67: Polystyrene insulation material

3.15 External tubing

3.15.1 Evaporator connection to the external tubing

The saline water circulation from the evaporator was on the cold tube and returned via the hot tube, as shown in Figure 3.68 represented by blue and red arrows. The blue arrow represents relatively cold water from the evaporator to the ETSC, while the red arrow represents the hot water-vapour mixture flowing from the ETSC to the evaporator. The circulation of the saline water was clockwise direction viewed from above (see Figure 3.68). Saline water circulation was due to the thermodynamic principle of differential pressure. The mode of circulation was then termed “impulse circulation”. The circulation will be described under the non-return valve section.

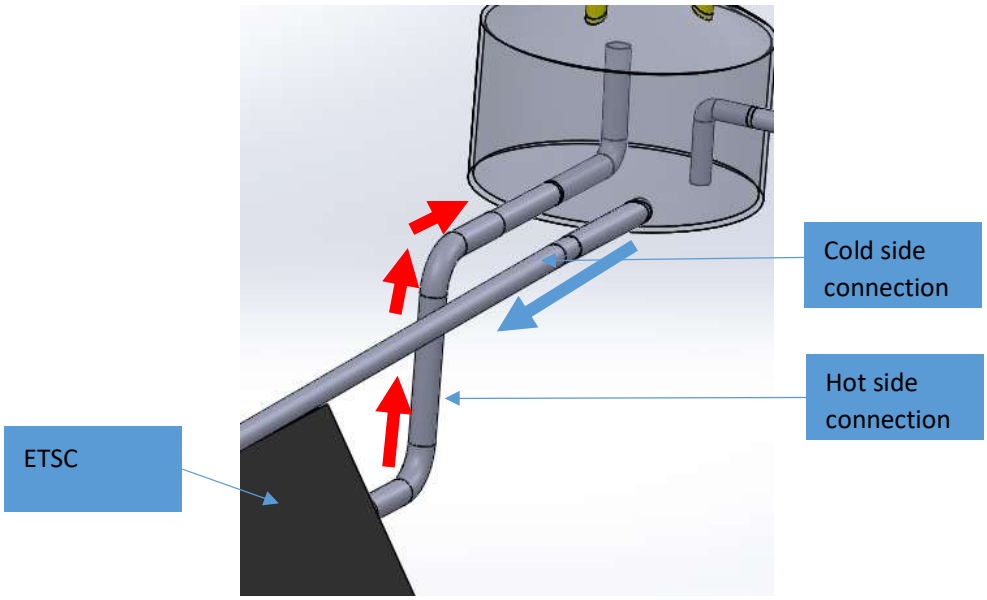

Figure 3.68: ETSC's connection to the evaporator in 3D

A transparent flexible hose, viewed from above in Figure 3.69, had an internal diameter of 16 mm and a length of 120 mm connected to the cold tube. This flexible hose was then connected to a copper tube with an external diameter of 15 mm. The transparent hose was used to observe and monitor the level of saline water flowing inside the tubing assembly. It was also to see if there were any foreign particles inside the tubing assembly as the saline water circulated. Furthermore, this was a point to prime the system with saline water so that the air pockets in the tubing assembly were removed. Furthermore, it was also a weak point on the tubing for protection of the system from excessive water pressure. The flexible hose will burst, allowing saline water under pressure to escape to the surrounding atmosphere.

Figure 3.69: Transparent flexible hose

The flexible hose was secured in place by two adjustable hose clamps (see Figure 3.70). The hose clamps were secured by means of a flat screwdriver or 8 mm ring spanner.

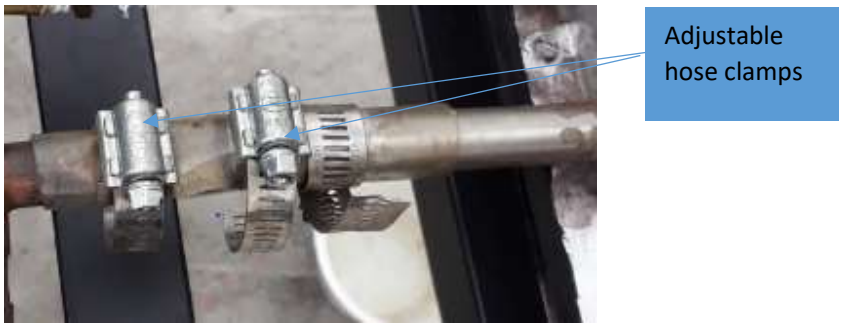

Figure 3.70: Hose clamps

3.15.2 Transparent flexible tube connection to a copper tube

A transparent flexible tube (as discussed above) was then connected to a copper tube with a total length of 1.85 m and external diameter of 15 mm (see Figure 3.71). One end was connected to the transparent flexible hose and secured using hose clamps; the other end was connected to the non-return valve by a 22 mm x 15 mm threaded brass fitting.

Figure 3.71: 15 mm copper tubing

This tube, as shown in Figure 3.72, connected with the evaporator. The tube was inclined at an angle of approximately 5° from the horizontal. The evaporator side was the higher point, the non-return valve side lower.

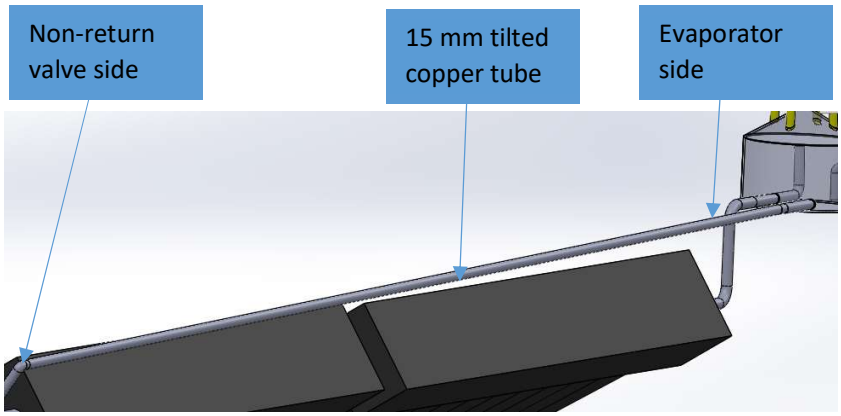

Figure 3.72: 15 mm copper tube at an incline in 3D

Two 90° copper elbows were fitted and welded onto the 15 mm tube by means of brazing. The copper tube was also tilted to create an inclined angle to allow saline water to flow under the influence of gravity, as illustrated in Figure 3.73. The 15 mm copper tube connection is shown in Figure 3.74.

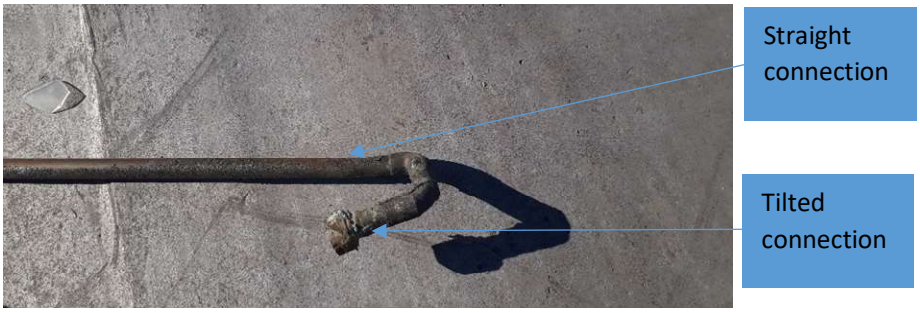

Figure 3.73: Tilted end of the tube

Figure 3.74: Tilted end connection

3.15.3 Non-return valve and its connections

A 20 mm diameter non-return valve (gate valve), as shown in Figure 3.75, induced the one-way direction of flow. The non-return valve was slightly inclined at an angle of about 12° from the horizontal, an angle necessary to keep the gate (swing) inside the valve opened. The connection between the non-return valve and the ETSC was achieved by welding a 45° copper elbow to a 55 mm long copper tube with a 15 mm diameter. The copper tube was fitted with a 22 mm x 15 mm threaded brass fitting on both ends. One end connects to the ETSC and the other connects to the non-return valve.

Figure 3.75: Non-return valve

The gate valve used in the system did not require high pressure (large force) to operate. The spring-loaded valve was unsuitable for this system as the saline water pressure from the evaporator was not high enough to operate it. In addition, the rubber seal inside the valve used to seal saline water and prevent the back flow was fragile to saline water, so the life span of the rubber was reduced. The valve was positioned so that the heated saline water which was at higher pressure was downstream, while the saline water that was yet to be heated was upstream. The hot tube was connected to the high-pressure side of the non-return valve.

When the saline water was heated in the ETSC, the pressure build-up in the solar collector manifold caused the saline water in the manifold to escape through the hot tube into the evaporator. The heat and pressure build-up inside the manifold forced the gate inside the valve to shut off saline water from the evaporator flowing through the cold tube. The gate also prevented any back flow of saline water from the manifold, creating a one-directional flow. When heated saline water escapes the manifold, it leaves a vacuum inside the manifold. This vacuum and the tilt effect open the gate (swing), allowing relatively cold saline water from the evaporator to enter. The heating cycle repeats, and heated saline water escapes the manifold due to a build-up in pressure. The gate (swing) inside the non-return valve only closes under the pressure created inside the ETSC manifold.

The non-return valve was the particular component that made it possible for the system to operate independently without electricity supply and pumps. Without this valve, there would be no one-directional saline water flow between the ETSC and the evaporator. The saline water from the evaporator flowed under the influence of gravity into the manifold of the ETSC. This was due to the slightly tilted angle from the horizontal surface of the 15 mm copper tube. A 25 mm thick insulation material covered the 15 mm whole external tubing assembly.

3.15.4 Solar collectors

Thermal energy was supplied by two ETSCs with aperture areas of 0.6 and 1.2 m^2, respectively. The ETSCs were tilted at an angle of 35° which was equal to the latitude of Cape Town, South Africa. The ETSCs (see Figure 3.76) are named collector A (ETSC-A) and B (ETSC-B) for ease of identification. The ETSC-A had 20 evacuated tubes with an aperture area of 1.2 m^2. ETSC-B had 12 evacuated tubes and an aperture area of 0.6 m^2. Both solar collectors had a manifold internal diameter of 22 mm. These two solar collectors were connected in series (Mahian et al., 2017). However, according to Reddy et al. (2012), there is more thermal energy losses in the series connected collectors. The losses lead to lower thermal energy collection by the series collected collectors. But on the other hand, the parallel connected collectors were reported are more efficient.

Figure 3.76: Evacuated tube solar collectors

3.15.5 ETSC series connector

The ETSCs were connected in series by means of brass fittings (see Figure 3.77). A male and female 22 x 15 mm threaded brass connection were used to achieve the series connection.

Figure 3.77: ETSC series connector

A 23 mm long copper tube with an external diameter of 15 mm was attached to the two threaded brass fittings. The total length of the two 22 x 15 mm and a 23 mm long tubes were 73 mm. ETSCs are shown in Figure 3.78 connected by the series connector.

Figure 3.78: ETSCs connected in series

3.15.6 Z-shaped connection

The external tubing connection was completed by a 215 mm long copper tube with a 15 mm external diameter. The tube, shown in Figure 3.79, had two welded 90° copper fittings which formed a Z-shape. The one end that was connected to the ETSC had a 22 x 15 mm threaded brass fitting with its compression ring. The other end was connected to the hot tube and had a 15 x15 threaded brass fitting. This Z-shape tube was installed vertically to prevent the flow of insufficiently heated saline water.

Figure 3.79: Z-shape connector tube

The saline water that passed through this tube and into the evaporator was sufficiently heated and flowed under pressure from the ETSC manifold. The connection intended to reduce the incondensable solids or heavy foreign objects that may be in the saline water. Large amounts of these foreign objects were limited in the lowest point of the entire tubing which was just after the non-return valve. This made cleaning the entire tubing system easier as opening the non-return valve releases all the foreign objects. A Z-shape connector is shown in Figure 3.80 connected to ETSC-B and a hot tube.

Figure 3.80: Z-shaped tube connection

3.16 A complete multistage desalination solar still

A complete multistage solar still system is shown in Figure 3.81. The system had an open loop external tubing connection which supplies the thermal energy. Thermal energy was supplied at the bottom of the system in the evaporator (Diaf et al., 2015). The total length of the external tubing was 6.36 m, including the ETSCs. The open loop re-circulated the saline water and thus no hot brine was discarded. The re-circulation of the saline water prevented the loss of thermal energy although loss occurred when the brine was being ejected from the systems reported in the literature. In addition, the saline water was constantly flowing rather than a stagnant pool of water. The fluid motion (convection) enhances the heat transfer rate. The motion of a fluid also prevents the salt build-up as it carries it away as it circulates. However, re-circulating the saline water without ejecting the brine increases the concentration of the salt content in the saline water and thus requires more thermal energy to heat and evaporate it.

Cleaning and flushing of the internal and external tubing in the system was required occasionally to aid in minimising the salt concentration as well as foreign particles that might have found their way in. The stage trays of the system were totally sealed from the outside environment and never met the saline water as the system was vapour based. For this reason, the stages were never cleaned, in fact, the only liquid flowing in the stages was the distillate produced. The multistage solar still operates at ambient pressure (no vacuum pressure).

Figure 3.81: A complete vapour-based MSS-SS

CHAPTER FOUR

EXPERIMENTAL TEST PROCEDURE USED ON THE MULTISTAGE SOLAR DESALINATION SYSTEM

This chapter discusses the experimental testing procedure used in analysing the performance of the vapour-based multistage solar still with stacked stages (MSS-SS). This chapter first lists the various equipment and instruments used during the testing procedure. It then briefly discusses the construction of the vapour-based MSS-SS. The data logging process and instruments are discussed thereafter, with discussion covering the various locations where the probes were installed. Subsequently, the chapter discusses the solar radiation collection process by means of a wireless weather station and its supporting components. The weather station was also collecting wind velocity and directions as well as ambient temperature. Moreover, the distillate collecting procedure and the electrical resistance of the distillate is discussed, followed by mathematical equations and analysis of the vapour-based MSS-SS performance. Lastly, the overall experimental procedure for the experimental tests is presented.

4.1 List of all equipment used during experimental tests

Table 4.1 lists all the data acquisition equipment during the experimental tests of a vapour-based MSS-SS.

Table 4.1: List of all equipment used in acquiring data from the vapour-based MSS-SS

Serial no.	Equipment and/or instruments	Type/make
1	Temperature data logger	12 channel BTM-4208SD data logger
2	Temperature probes	- x8 surface temperature probes - x4 liquid temperature probes
3	Weather station	- HP200 wireless weather station - Weather station's display console
4	Graduated cylinder	1000 litre capacity graduated at 10ml increments
5	Electrical multi-meter	MTD33
6	Distillate containers	x6 five-litre containers

4.2 Brief insight into the construction of the vapour-based MSS-SS

The vapour-based MSS-SS was constructed from standard everyday materials already available for purchase. Some items such as distillate containers had previously been used and so were thoroughly cleaned before use in the system. The MSS-SS was constructed to be simple and easy to operate. The only component specially manufactured for the system was the evaporator. The BSS and the ETSCs were positioned facing northwards at a certain

angle from the horizontal since South Africa is in the southern hemisphere. The system is illustrated in Figure 4.1 from the top to bottom starting with the external SW tank. The external SW tank was positioned higher for the purpose of supplying the SW under gravitational influence. That is, no electrical pumps were used to supply the SW. The SW flowed under gravitational influence into the BSS where the first pre-heating occurred. The flow from the external tank was regulated by the float valve located in the BSS. In addition to pre-heating the SW, the BSS was also producing its own distillate. From the BSS, some of the SW flowed into stage 5 through the copper zigzagged SW tube. In stage 5, the SW was further pre-heated by the incoming vapour from the evaporator into stage 5. The SW proceeded from stage 5 into stage 4 where the pre-heating continued. The pre-heating continued as the SW flowed into the lower stages (stage 3, stage 2 and stage 1) in a similar fashion as in stages 4 and 5. The flow of SW in the zigzagged SW tube was controlled and regulated by the float valve located in the secondary SW tank. The secondary SW tank was located in the secondary SW tank and evaporator compartment (see Figure 4.1).

In the secondary SW tank, the SW flowed into the evaporator due to water depth differential. That is, in the secondary SW tank, the SW level was higher than that of the evaporator. Therefore, the SW would flow due to SW pressure differential between the secondary tank and the evaporator. Furthermore, an in-house made one-way flow valve was manufactured to prevent a back flow from the evaporator. During the SW circulation in the external tubing and the evaporator, pressure built-up in the tube circuit. This pressure tended to force excessive heated SW back into the secondary tank. This back flow was undesired as it mixed with relatively cold SW in the secondary tank and reduced evaporation in the evaporator. Therefore, once the SW flowed passed the in-house made one-way valve, no flow back occurrence was observed. The increasing solar radiation from the morning hours increased the temperature of SW in the external tubing and the ETSC manifold. Due to increasing temperature in the manifold, the pressure also increased. The SW would start to move in a bid to equalize the pressure in the circuit. However, as discussed in Chapter 3, a non-return valve was installed on one side of the ETSCs preventing SW flow in one direction, and the only one way out of the tube and manifold due to increasing pressure was into the evaporator. Since the evaporator and the external tubing were constantly filled with SW, there was a constant flow in the tubing. That is, when the first batch of SW was jetted out of the manifold, it created vacuum pressure in the tubing. The negative pressure then sucked the next batch of SW into the ETSC manifold where it was heated up and escaped as the first batch.

In the evaporator, the separation of the lightweight vapour and the denser SW occurred. The vapour would begin ascending through the vapour make-up tubes, and the SW re-circulated

in the external tubing. After a full circulation of the SW in the external tubing, the SW in the tubing maintained a higher temperature which made evaporation efficient. Only a small quantity would drip into the evaporator from the secondary SW tank replacing the evaporated quantity. Therefore, the small relatively cold SW from the secondary SW tank did not have a considerable effect in changing the temperature of the SW already in the external tubing. In essence, each time the SW diminished due to evaporation in the evaporator, a replenishing small quantity would be sent from the secondary SW tank. In addition, since the secondary SW tank was not equipped to collect the distillate, it was not desirable to have evaporation taking place in it.

Figure 4.1: Vapour-based MSS-SS

The vapour generated in the evaporator would then flow vertically through the vapour make-up tube and into its respective stages. Upon entering the stages, the vapour would start the condensation process, which involved phase changes from gas to liquid. The V-shaped stage trays would guide the condensed liquid into the distillate collecting tubes (see Figure 4.1).

Finally, the condensate was collected in the distillate collecting containers and its quantity weighed.

4.3 Temperature data logger unit, temperature probes and the probes connections

This section discusses the temperature data acquisition process from the vapour-based MSS-SS during experimental tests. Next, it discusses the types of temperature probes used in acquiring the temperature data. Lastly, it discusses different components and compartments from which the temperature data was collected.

4.3.1 Temperature data logger

The temperature data logger is used in a solar still to indicate the temperatures of different points or compartments within a still during operation (Chen et al., 2017; Shalaby et al., 2016). There are various types of data loggers used in acquiring data from a solar still, as reported by many researchers (Li et al., 2018; Shalaby et al., 2016; Shafii et al., 2016). The temperature data logger (see Figure 4.1) with 12 channels was used to log the temperature data in a vapour-based MSS-SS. While the logger had various sensor type options such as J/K/T/E/R/S, the tests were undertaken using a K-type sensor mode. The lower and upper temperature limits of the K-type were -100°C and 1300°C, respectively. The temperature logger was powered by 8 x 1.5 V batteries or a direct current (DC) adapter. The 12 temperature probes connected to one end of the data logger were connected on different components of the system on the other end. The temperature on different points of the system was recorded continuously for certain time intervals. Some researchers use 30-minute intervals (Nishikawa et al., 1998). However, in the vapour-based MSS-SS, the temperature data was logged each 10-minute interval to increase the accuracy of the collected data. Even though the solar incidence recorded ceased soon after sunset, the temperature data was logged for 24 hours per day. The continuous recording of data after sunset was necessary to track the temperature of different components of the system for comparison purposes. Since the experimental tests were conducted outside, a watertight compartment protected the data logger unit from outside elements such as rain, winds and direct heat from the sun, essentially, from any possible damage. Further specifications of the temperature data logger are found in Appendix A-1.

Figure 4.2: Temperature data logger front view

The data logger was only switched off during maintenance of the vapour-based MSS-SS. The top view of the data logger showing the 12 channels to which the probes were connected is shown in Figure 4.3. The probe connections to the data logger were connected in such a way the evaporator was closest to it and the external SW the furthest. More details are discussed under the following sub sections.

Figure 4.3: Temperature data logger top view

4.3.2 Types of temperature probes

There were two types of K-type probes used to probe the temperature from different components of the system: surface and liquid probes. The liquid probes were divided into two types, as discussed below. The surface type probes were used to acquire data from the solid

surfaces of the MSS such as stage wall, stage trays and zigzagged SW tube, as shown in Figure 4.4 and Figure 4.5.

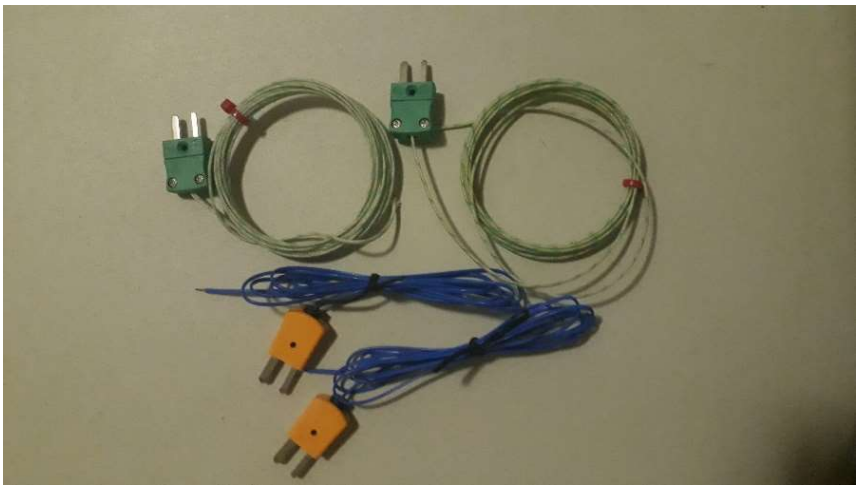

Figure 4.4: Surface temperature probes

Each probe was bought with an original length of 1m. However, due to some components to be probed being further away from the data logger unit, the probes wires were extended to reach different components and compartments. The evaporator was the closest to the location of the logger unit and the external tank was the furthest. The thermocouple probes were made from nickel aluminium and nickel chrome with 0.2 mm diameter probing ends. The temperature range of these probes were -100°C – 250°C.

Figure 4.5: Surface temperature probe

Figure 4.6 shows the liquid probe, the second type of temperature probe used in the vapour-based MSS-SS for data acquisition. Three of these probes were positioned throughout the

system, installed in the secondary SW tank, the evaporator and the BSS for data collection. These probes had a temperature range of -190°C – +260°C and were 2.5 m in length. The evaporator and secondary tank probes did not need any length extension, but the BSS probe was extended using a 1 m probe wire to reach the BSS.

Figure 4.6: Liquid temperature probe

In addition to the liquid probes discussed above, the external tank also had a liquid probe but dissimilar to those discussed above. Figure 4.7 shows a different make of the liquid temperature probe, the second type liquid probe. This probe was used in the SW tank to indicate the room temperature of SW during experimental tests. Since the external SW tank was positioned a distance away from the data logger, extension wires made the probe longer. There was only one of this K-type probe: the probing end was 150 mm long and the 3 mm in diameter; the temperature range was from -40°C – 1100°C.

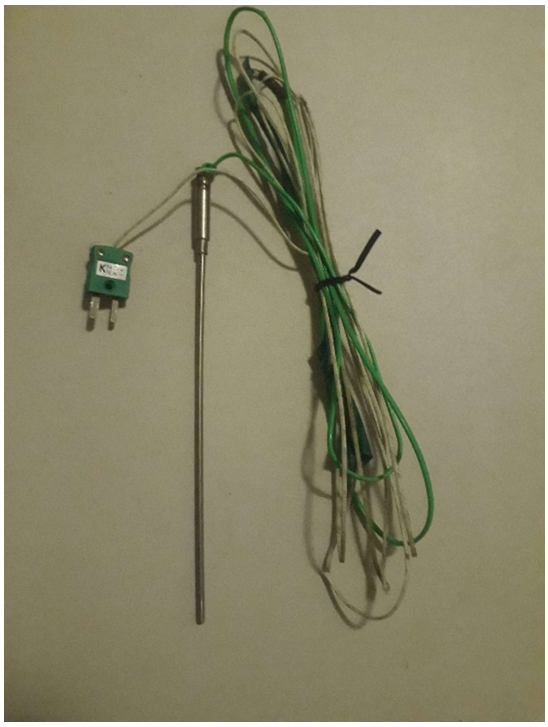

Figure 4.7: External SW temperature probe

4.3.3 Temperature probes connections

Table 4.2 presents the data logger channels and the corresponding component or compartment to which the probes were connected. The data logger channel numbering can be viewed in Figure 4.3. The probes were connected in such a way that the first channel was connected to the evaporator and the last channel to the external SW tank. The thermocouples were placed in best possible locations to measure temperature variations. The temperature at the selected location was regarded as the representative value of the surface measured. In the case of liquid probes, these probes were submerged under water and did not come into contact with a solid surface.

Table 4.2: Temperature probes connections

channel no.	Component/compartment	Probe type
1	Evaporator	Liquid
2	Secondary tank	Liquid
3	Stage 1	Surface
4	Stage 2	Surface
5	Stage 3	Surface
6	Stage 4	Surface
7	Stage 5	Surface
8	Basin condensing cover	Surface

9	Basin SW	Liquid
10	Stage 2 walls	Surface
11	Stage 2 tray	Surface
12	External SW tank	Liquid

4.3.3.1 Evaporator and secondary SW tank connections

Figures 4.8 and 4.9 show the evaporator and the secondary SW tank temperature probe connections. Both the evaporator and the secondary SW tank were drilled with a 4 mm drill bit to insert the probes through their bodies. The holes through which the probes protruded were sealed with adhesive (as discussed under section 3.2). Both the evaporator and the SW tank maintained full levels of SW. Therefore, the probes were always submerged under water. To maintain accuracy, the probes were cleaned during maintenance to prevent build-up on their cylindrical surfaces.

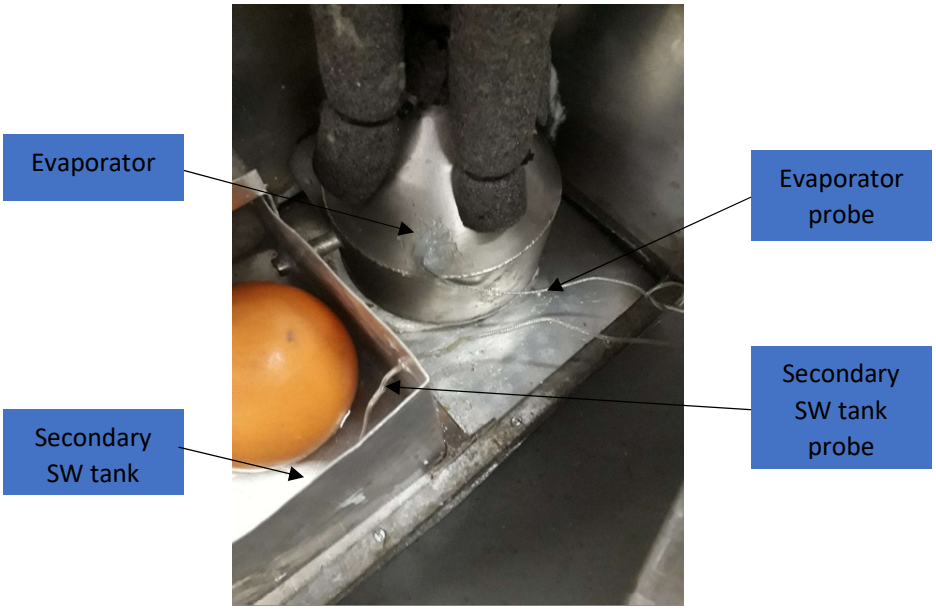

Figure 4.8: Liquid probes in the evaporator and secondary SW tank

During experimental tests, when the system was primed and filled with SW, accurate temperature readings were necessary. To obtain the most accurate reading from the temperature probes, the probes were adjusted such that they did not come into contact with solid surfaces. Contact between the probe and the inner walls of either the evaporator or the secondary SW tank could in fact interfere with the readings.

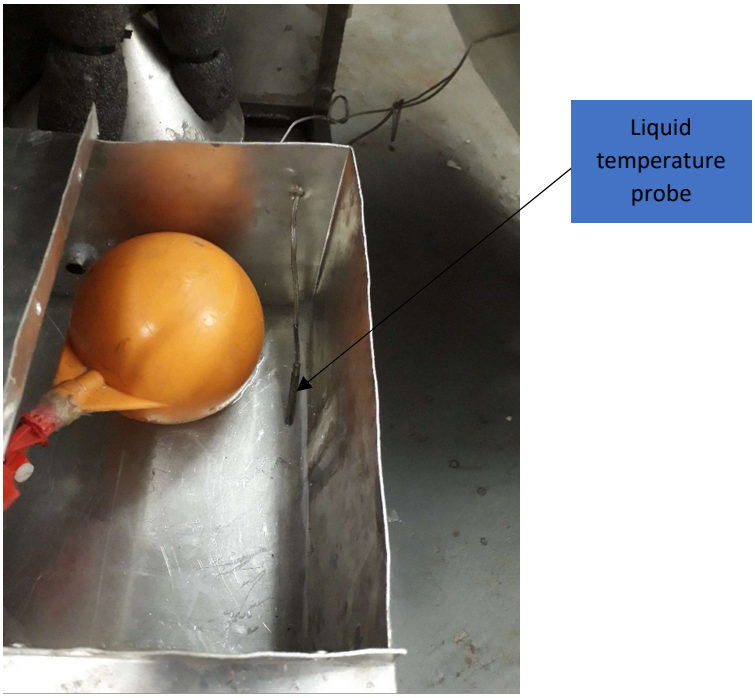

Figure 4.9: Liquid probe inside the secondary SW tank

4.3.3.2 Stage 1 to stage 5 probes

The probe types used in stage 1 to stage 5 were surface probes, inserted through the stage covers as shown in Figure 4.10. Small holes about 2 mm in diameter were drilled in the covers of the stages to accommodate the probes. The holes were then sealed using the adhesive to prevent vapour leaks. The zigzagged SW tube outside surface where the probes were placed was cleaned with sandpaper to ensure accurate temperature readings. The probes were inserted firmly through the stage covers so they did not come off when the stage cover was opened. The occasional opening and closing of stage covers will be discussed in the following section. Since these probes were extended lengthwise, insulation tape separated the wires and prevented exposure to the atmosphere. This was important to ensure accurate readings without external interferences.

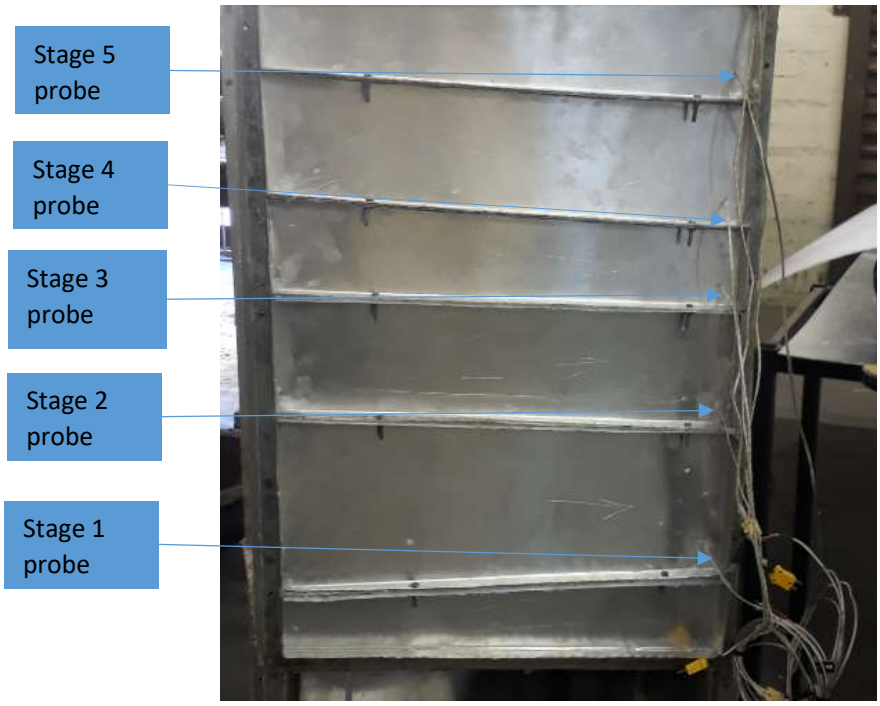

Figure 4.10: Surface temperature probes inserted through the stage covers

The probing ends of the sensors were secured onto the outside surface of the zigzagged SW tube, as shown in Figure 4.11, which shows the temporary installation of the probes using the insulation tape. For final installation, super glue secured the probing ends on the zigzagged SW tube. These probes were used to detect the temperature of SW as it flowed down from the BSS to the secondary SW tank.

Figure 4.11: Surface probes attached to the zigzagged SW tube's outer surface

The stage tray and stage wall probes were installed on stage 2 only due to the costs of purchasing more than one data loggers to probe each stage wall and stage tray. It was also because the data logger (as discussed in section 4.3) had only 12 channels and additional temperature probes would have required an additional data logger. In addition, the installation on stage 2 only was on the premise that the temperature of the vapour leaving the evaporator

and delivered to the stages was the same. This was reasonably assumed since the vapour source was common for all stages. However, as will be discussed in Chapter 5, the SW in the zigzagged SW tube differs in temperature. Therefore, it was not strictly accurate to assume that all stage walls and stage trays are at the same temperature value all the time. In other words, it was assumed that all stage temperatures would be the same as that of stage 2. Figure 4.12 shows the stage wall probe temporary installed with insulation tape. The stage tray probe can be seen in Figure 4.11.

Figure 4.12: Surface probes attached onto stage 2 wall

4.3.3.3 BSS temperature probes

While the BSS itself was not the focus of the study, it played various roles in the system. Its functions were, for example, to act as the primary SW tank in the MSS-SS, store SW for pre-heating and produce its own distillate passively. However, producing the distillate was not the primary focus for the BSS; the first two functions were. Probes were installed to collect temperature data from the SW in the basin as well as the condensing glass cover only. During experimental tests, it was noticed that the BSS saline water temperature was very high, indicating that the SW was almost at or was at boiling point. It was discovered that the cause of these elevated temperature values was because the liquid probe was laying against the BSS bottom cover. The probe was reading the surface temperature of the bottom cover heated by the incoming vapour to stage 5. Therefore, the probe was attached to a polystyrene material which can easily float on water (see Figure 4.13). This ensured that the probe did not come into contact with the bottom cover but floated on the SW. After the modifications, the probe temperature was moderate and in accordance with thermal energy supplied.

The surface probe (see Figure 4.13) was also measuring excessively high temperature values during experimental tests. To rectify this, the probe was prevented from the direct heating from sun's rays. A shadow was created by attaching the polystyrene material on the outside of the

condensing glass cover, directly opposite the probe, which then shadowed it from direct heating by the sun's rays and prevented increasing temperature readings. The temperature readings decreased and were in accordance with the SW temperature values.

Figure 4.13: BSS surface and liquid probes

4.4 Stage independence test procedure

One of the aims of this study was to develop a vapour-based MSS-SS with independent stages. It has been reported in the literature that the thermal energy supply from the bottom on the MSS-SS with stacked stages and waterbed caused low productivity in the upper stages. Low productivity was especially problematic during sunshine hours. The energy supplied from the bottom of the MSS-SS also caused a delay in the desalination process of the upper stages. That is, lower stages received thermal energy through latent heat of condensation much sooner than the upper stages. Therefore, the upper stages must wait for the lower stages to be heated-up and start the evaporation process since upper stages are dependent on lower stages for thermal energy supply through latent heat of condensation. Any loss or lack of thermal energy and resultant productivity of the lower stages would directly impact the upper stages.

To test the vapour-based MSS-SS stage independence, two methods were proposed. The first method was to open the stage covers (side covers) as discussed under section 3.7. The opening was to occur on the lower stages to observe the temperature behaviour and productivity pattern of the upper stages. This process took place for the whole day at the time. The testing procedure consisted of, firstly, stage 1 and stage 2 alternating process of exposing

them to the atmosphere. Secondly, stage 1 and stage 2 simultaneous process of exposing them. The stage atmospheric exposure imitated the loss of thermal energy in the lower stages (stage 1 and stage 2).

Additionally, a different testing procedure was conducted on the vapour make-up tubes, as reported in section 3.14. The vapour make-up tubes supplying vapour to stage 1 and stage 2 were shut off and the vapour prevented from reaching these stages. This process imitated the lack of productivity in the lower stages without any atmospheric exposure, that is, without any thermal energy loss to the atmosphere. The upper stages were then observed for temperature behaviour and productivity pattern. This experimental test continued for the whole day as in the first procedure of exposing the lower stages to the atmosphere. However, there were a number of prerequisites for these experiments to be conducted:

- Selected days for these experiments must have very different weather conditions (i.e., solar intensity, cloud cover, wind velocity) to observe the effect under varying weather conditions.
- In the case of the atmospheric exposure tests, stage covers are completely opened and with no distillate yield from those particular stages (stage 1 and stage 2).
- The vapour make-up tubes supplying vapour to stage 1 and stage 2 are completely shut during the vapour make-up tubes shut-off experimental observation.
- Other than the stages under experimentation, the system works in its full capacity, with no stoppages or half day experiments.
- During the atmospheric exposure experiments, the stages remain open for a full 24-hour period to observe temperature behaviour during daytime and night-time.
- During the vapour make-up tube shut off experiment, the tubes remain shut for a full 24-hour period.

4.5 Solar irradiance data collection

4.5.1 Wireless internet weather station (outdoor sensor)

During experimental tests of a solar still, various data is recorded to analyse the performance of the system. These data sets include solar radiation intensity, wind velocity and its direction and ambient temperature. The data is recorded continuously for different seasons of the year (Fath et al., 2013). Therefore, the outdoor installation (see Figure 4.14) consisted of all the data set measuring ability reported above. The weather station was installed on the roof of the Mechanical Engineering Department, Cape Peninsula University of Technology, Bellville campus. The figure shows the wind vane used for wind direction indication, the wind velocity

sensor to measure wind velocity and solar radiation sensor to measure the solar irradiance. The weather station was the HP2000 wireless weather station, with an outdoor temperature range of -30°C – 65°C and accuracy of +/- 1°C. The accuracy of wind velocity measurements above 5m/s was 10% and the solar radiation was 15%. The weather station was set to 5-minute intervals to increase accuracy of readings. A 1.75 m hollow tube was used for elevating the outdoor sensor which was installed according to the manufacturer's manual. The pole was to lift the station up so as to avoid obstruction from other surrounding objects. If the wind reaching the wind sensor was as a result of deflection from other surfaces, the wind direction and speed would be inaccurate. Therefore, elevation of the weather station ensured true wind velocity and solar radiation intensities, positioned so that the solar panel was facing north since South Africa in in the southern hemisphere. North facing was in accordance to the manufacturer's manual instructions. The full outdoor specifications of the weather station are presented in Appendix A-2.

Duffie and Beckman (2013) concur that the surface of the collector should face the equator. Depending on the geographical location (southern or northern hemisphere), the solar collector surface should face north in the southern hemisphere, meaning that the solar collector surface should face northwards. However, Duffie and Beckman (2013) continue, insisting that setting up the solar collector surface to receive maximum solar incident may not lead to maximum solar energy collection. Nevertheless, north facing surfaces have been reported as much better for the southern hemisphere. Moreover, as Shafii et al. (2016) reports that about 80% of solar energy is generated during sunshine hours (i.e., 08h30 in the morning to 5h00 in the evening), experimental tests are conducted during daytime to increase solar energy collection. Duffie and Beckman (2013) suggest that the most commonly available solar radiation data is measured on horizontal surfaces. Shalaby et al. (2016) report that solar radiation data was recorded using a high precision pyranometer to measure solar radiation on a 30° inclined surface.

In the current study, however, the global solar radiation was measured on a horizontal surface, as shown in Figure 4.15. The solarimeter, also reported by Singh et al. (2013), was used in the current study to capture the global solar radiation on a horizontal surface. The solar radiation varies based on time of day, time of year and latitude of the location where the solar still is situated (Mowla & Karimi, 1995). Solar radiation intensity depends on the latitude of the local area from which the still is operated (Sivakumar & Sundaram, 2013). Therefore, it was of paramount importance to consider geographical factors when installing the outdoor sensor.

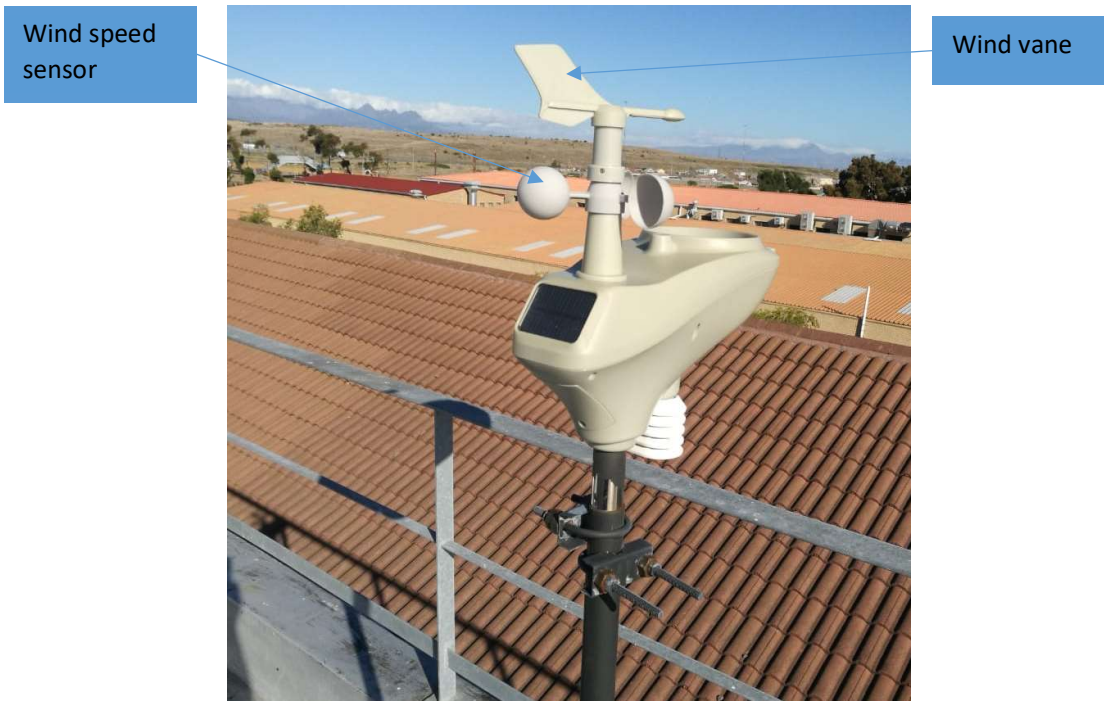

Figure 4.14: Wireless weather station

The wireless weather station in the current study can only measure the total global radiation on a horizontal surface. There is other, more advanced measuring equipment such as the pyranometer which can measure both the beam and diffuse radiation on a horizontal surface, but because of the high price of this advanced equipment, alternative means to predict the diffuse radiation have been developed (Maleki et al., 2017). Duffie and Beckman (2013) define beam radiation as the uninterrupted radiation coming from the sun and reaching the surface on ground, while diffuse radiation, also known as sky diffuse radiation, is radiation scattered in many directions before reaching the ground. Since the solar collectors receiving solar radiation are on an inclined plane, the beam and diffuse radiation must be converted. In an effort to convert these solar radiation components, many mathematical models have been developed over time. Some of these models were reported by Maleki et al. (2017). More details on various solar radiation components will be discussed in section 4.8.

Figure 4.15: Solar radiation sensor

4.5.2 Wireless weather station console unit

The console unit (see Figure 4.16) was kept in the watertight compartment with the temperature data logger for safety reasons. The display unit internet connections were wireless to the weather station installation. The wireless internet weather station was collecting various readings and sending them wirelessly to the display console. The maximum display unit range was 100 m on a flat surface for optimum operation. The console was powered by an electrical direct current (DC) adapter connected to the main electricity grid. The main disadvantage of connecting the console to the main grid was the occasional power outage, also known as 'load shedding'. When power cuts occurred, the console would automatically turn off. When the power returned, it would begin recording from the time it switched off with a power outage. Thus, the data recorded would be two to three hours behind. However, to ameliorate this, the console was re-set each morning during distillate collection time.

Figure 4.16: Wireless weather station console

4.6 Distillate collecting procedure

According to Shafii et al. (2016), the distillate produced by the solar still is collected in a graduated cylinder to keep track of the amount of produced water. In the vapour-based MSS-SS, the distillate yield was collected separately from each stage of the vapour-based MSS-SS. The graduated cylinder (see Figure 4.17) determined the quantity of the distillate yield in a day. The full capacity of the graduated cylinder was 1000 ml (1litre). The distillate collected from each stage was recorded separately to determine each stage productivity under a given solar intensity on a particular day. Figure 4.18 shows a complete MSS-SS rig for experimental tests. Each stage of the MSS-SS was fitted with the U-shaped tube filled with freshwater. Six flexible transparent hoses were connected to the stages on one end and connected to the 5-litre water containers. Figure 4.18 shows all six 5-litre water containers for collecting the distillate from individual stages. These flexible hoses differed in length depending on the stage to which it was connected. For instance, the BSS had the longest hose since it was the highest stage/tank. Stage 1 had the shortest hose since it was the closest to the ground.

The distillate was collected daily, at the end of each day. The experimental test day started in the morning when the first solar incident was recorded. The day ended the following morning before the first solar incident was recorded. In essence, the experimental day lasted for 24 hours each day. It relied on the sun rise and sunset information gathered from the weather station display console.

Figure 4.17: Graduated cylinder

This information was later confirmed with the solar irradiance data during data analysis. To keep the system operating at its optimum, the brine solution was flushed out on a weekly or bi-weekly basis. The flushing out of the brine was dependent on the electrical resistance tested on the brine solution. During days with high solar intensities like summer. The salinity levels would increase quicker than the cooler day of autumn, winter and spring. This quick increase was caused by intense evaporation of the SW water which then consumed more SW in the evaporator. During cooler days, where sometimes no distillate would be produced for more than one full day, the salinity levels would increase gradually. Thus, the flushing out was strictly dependent on weather conditions. Furthermore, flushing of the system was pre-planned and undertaken during the off-sunshine hours (at night or early in the morning, but preferably in the morning). Night-time flushing out of the system was avoided since the SW in the evaporator sustained higher SW temperatures which could have continued with the desalination process.

Figure 4.18: Vapour-based MSS-SS

4.7 Water quality tests

4.7.1 Distillate electrical resistance procedure

There are foreign substances existing in water which can be detected by conducting water quality analysis. Simonis and Nweze (2016) report three methods for testing the quality of water. The first, the chemical test, can detect the micro and micro substances dissolved in water. The second one, the physical test, can detect the colour, conductivity, odour or taste, turbidity, pH and hardness. The third method, the biological test, can detect the faecal coliform (human or animal waste). In the current study, however, the distillate produced by the vapour-based MSS-SS was continuously tested for electrical resistance. The aim was to find the extent to which the distillate will create resistance and register the values on the multi-meter (see Figure 4.19). According to Light et al. (2004), pure water has very low electrical conductivity. Since resistivity is the reciprocal of conductivity, this means that the lower the conductivity, the higher the resistivity of water. In addition, the dissolved solids in contaminated water aid in increasing the conductivity; this is contrary to pure water. Therefore, it is apparent, based on the report by Light et al. (2004), that water with high electrical resistance indicates that it contains less conductive elements in it, while water with low resistance indicates that there are more conductive elements contained inside. These conductive elements are in a

form of dissolved solids which increases electrical conductivity and thus reduces electrical resistance. There were three types of water tested for resistance: seawater, tap water and distillate produced by the MSS-SS. According to Light et al. (2004), with higher water temperatures between 75 – 100°C, higher accuracy in measuring is required to achieve the same accuracy of purity as when water is at 25°C. Therefore, in the current study, the SW or seawater was tested at room temperature before it was poured into the MSS-SS. Tap water was also tested at room temperature for comparison purposes. Both the seawater and the tap water were only tested once, and their values taken as fixed values. One beach was selected for collecting seawater for experimental purposes in the MSS-SS. As different seas are known to have different salinity levels (Morad et al., 2017), the seawater (in this work referred to as saline water) was collected from one place only. The closest beach with ease of access was Monwabisi beach in Khayelitsha. These three sets of water samples were also tested in the Chemistry laboratory at Cape Peninsula University of Technology (CPUT).

The resistance of the distillate was tested throughout the experimental tests of the MSS-SS. However, the chemistry laboratory tests were done only once for all three types of water samples. Since the distillate was collected from each stage separately (see Figure 4.18), six samples were taken each time from each stage. The separate stage samplings were to determine if the distillate level of resistance was the same for all the stages of the MSS-SS. The electrical resistance tests were done each time during the collection of the distillate during off-sunshine hours.

Figure 4.19: Digital multi-meter

4.7.2 Various water samples tested for pH levels

To test various water samples, eight 30 ml water sample containers were used to collect the samples. The water samples included seawater, tap water and distillate from all six stages of the vapour-based MSS-SS. The pH in water samples is the measure of the acid-base equilibrium (WHO, 2007). The pH water tests were conducted at the Chemical and Chemistry department, Cape Peninsula University of Technology, Bellville. The water samples were tested for two consecutive days to determine the mean values. The pH meter (see Figure 4.20) was used to measure different samples of water. During the tests, the temperature of each water sample was recorded. Appropriate pH levels of drinking water fit for human consumption is between 6.5 – 8.5. Natural waters can have lower pH due to acid rain or high pH in limestone areas. And pH levels may decrease as a result of increased water temperature (WHO, 2007). The DWAF (1996) acknowledges that chronic human health effects can occur at high aluminium concentration in water. The use of aluminium in water treatments results in high aluminium concentration in water. Because the vapour-based MSS-SS was constructed from aluminium materials, this may have increased the acid levels in water due to the high concentration of aluminium.

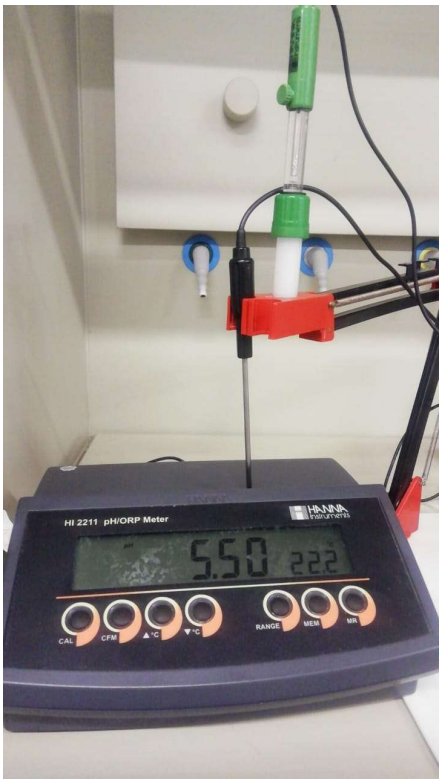

Figure 4.20: pH meter

4.8 Data reduction and determination of thermal energy input in vapour-based MSS-SS

It should be noted that the vapour-based MSS-SS was integrated with the passive BSS. However, the BSS was not the primary focus of the current research work and thus no mathematical equations were developed for it. Furthermore, the BSS have been widely reported in literature so the current study had no novelty concerning the BSS. The only novelty presented in this current work was that of the vapour-based MSS-SS and consequently, its mathematical equations are discussed in this section in detail. Unless expressly stated, the mathematical equations in this section were adapted from Maleki et al. (2017), Iqbal (1983), Diez et al. (2021) and Duffie and Beckman (2013). The sample results of the equations discussed in this section can be found in Appendices A-3 to A-5.

4.8.1 Estimation of the hourly solar radiation on a horizontal surface

Hourly global solar radiation is generally measured on a horizontal surface; hourly global solar radiation on inclined surfaces can be estimated by means of various models (Maleki et al., 2017). The weather station (as discussed in sub-section 4.5.1) used a solarimeter to capture the solar radiation on a horizontal surface. The solarimeter can generally be interpreted to mean pyranometer (Duffie & Beckman, 2013). However, the solarimeter used in this study had no disc shading and thus the sensor was purely recording the combination of the beam and diffuse radiation (total hemispherical solar). The total radiation on a horizontal surface, therefore, consists of the diffuse and beam or direct radiation. That is:

$$I_H = I_b + I_d \quad (\text{W/m}^2) \tag{4.1}$$

Where I_H, is the total radiation on a horizontal surface;

I_b, is the beam radiation on a horizontal surface; and

I_d, is the diffuse radiation on a horizontal surface.

4.8.1.1 Estimation of the hourly diffuse solar radiation on a horizontal surface

Maleki et al. (2017) suggests two categories into which the diffuse radiation on a horizontal surface can be classified: the parametric and decomposition models. When dealing with the parametric model category, there are specific environmental conditions that must be considered. On the other hand, when dealing with the decomposition model category, the only data required is that which pertains to global solar radiation. Under the decomposition model category, the models are guided by the correlation between the diffuse and the total radiation on a horizontal surface. This correlation is a function of the hourly clearness index ratio. Duffie and Beckman (2013) describe the hourly clearness index ratio of a particular hour's radiation

on a horizontal surface to the extra-terrestrial radiation of that hour. The hourly clearness index ratio can be written in equation form as follows:

$$M_t = \frac{I_H}{I_o} \quad (4.2)$$

Where M_t, is the hourly clearness index; and

I_o, is the extra-terrestrial radiation.

I_o, centred around an hour can be determined from the following equation:

$$I_o = \left(\frac{12\times60}{\pi}\right) I_{sc}E_o[(\omega_2 - \omega_1)sin\varphi sin\delta + cos\varphi cos\delta(sin\omega_2 - sin\omega_1)] \left(\frac{MJ}{m^2}\cdot h\right) \quad (4.3)$$

Where the solar constant is I_{sc} = 1367 W/m^2 and the eccentricity correction factor E_o is:

$$E_o = 1 + 0.033cos\left(\frac{2\pi n}{365}\right) \quad (4.4)$$

φ, Latitude of the location is the angular location at the north or south of the equator where north is positive and south negative.

δ, Declination angle is the angular position of the sun at solar noon.

ω, Hour angle, the ω_1 and ω_2, refers to the beginning and end of the time interval, measured in degrees. The hour angle is the angular displacement of the sun east or west of the local meridian. The earth rotates on its axis at 15°/hour, morning being negative and afternoon positive.

n, Number of the day in a year.

$$\omega_1 = \omega - \left[\frac{(\pi\times t_1)}{24}\right] \quad (4.5)$$

$$\omega_2 = \omega + \left[\frac{(\pi\times t_1)}{24}\right] \quad (4.6)$$

The time (t_1) is the period being considered: 1 for an hour and 0.5 for a 30-minute period (Diez et al., 2021).

$$B = \frac{2\pi(n-81)}{365} \quad (4.7)$$

The equation of time ET in minutes is as follows:

$$ET = 9.87sin2B - 7.53cosB - 1.5sinB \quad (4.8)$$

Local solar time, ST is determined as:

$$ST = 4(L_{st} - L_{loc}) + ET + LT \quad (4.9)$$

LT, local standard time;

L_s, standard meridian for a local zone, since South African time is 2 hours ahead of Greenwich Mean Time (GMT) and the meridians are a multiple of 15°. Therefore, standards meridian for South Africa is 2 x 15° = 30°; and

L_L, longitude of the local location in degrees.

Seasonal correction S_c, for solar time

$$S_c = 0.1645sin2B - 0.1255cosB - 0.025sinB \quad (4.10)$$

The hour angle equation is as follows:

$$\omega = \frac{\pi}{12}[(t + 0.06667(L_s - L_L) + S_c) - 12] \quad (4.11)$$

Time (t) is the standard time at midpoint of the period being considered (Diez et al., 2021).

The declination angle is calculated as follows:

$$\delta = 0.409sin\left[\left(\frac{2\pi n}{365}\right) - 1.39\right] \quad (4.12)$$

To find the hourly diffuse fraction (k_d) on the horizontal surface, the following equations from Diez et al. (2021) are used:

Where $M_t \leq 0.21 k_d = 0.995 - 0.081M_t$ (4.13)

$0.21 < M_t \leq 0.76, \quad k_d = 0.724 + 2.738M_t - 8.32{M_t}^2 + 4.967{M_t}^3$ (4.14)

$M_t > 0.76 \quad k_d = 0.18$ (4.15)

Furthermore, the hourly diffuse fraction is as follows:

$$k_d = \frac{I_d}{I_H} \quad (4.16)$$

$$I_d = k_d \times I_H$$

The diffuse radiation on a horizontal surface, I_d, can be computed from the above four equations, Equation 4.13 to Equation 4.16. The SI unit of the resultant diffuse solar radiation, I_d, is (W/m^2).

4.8.1.2 Estimation of the hourly beam radiation on a horizontal surface

Hourly beam radiation can be calculated from Equation 4.1, that is:

$I_H = I_b + I_d$

Then,

$I_b = I_H - I_d$ (W/m^2)

4.8.2 Estimation of the hourly solar radiation on an inclined surface

Maleki et al. (2017) explains various models proposed in the estimation of total solar radiation on a tilted surface. These mathematical models were basically classified into two categories. The first is the *isotropic model category* which assumes the diffuse radiation is uniform throughout the sky dome. The other, the *anisotropic model category,* considers circumsolar and horizon brightening radiation components. The current study applied the anisotropic model category as it was reported to be an improved model category.

4.8.2.1 Estimation of the hourly global solar radiation on an inclined surface

Unlike the global solar radiation on a horizontal surface, the total radiation an inclined surface, I_β, is constituted by three components. These solar radiation components are beam radiation, $I_{b\beta}$, diffuse radiation, $I_{d\beta}$, and reflected radiation I_r. The reflected radiation is comprised of reflection from surrounding components such as ground, trees and walls (Duffie & Beckman, 2013). Therefore:

$$I_\beta = I_{b\beta} + I_{d\beta} + I_r \quad \text{(W/m}^2\text{)} \tag{4.17}$$

4.8.2.2 Estimation of the hourly diffuse solar radiation on an inclined surface

There are various developed anisotropic models reported by Maleki et al. (2017). Since the current study adopted the use of the anisotropic diffuse model, the Hay's model was selected for the current study. The Hay's model states that the Hay's anisotropic index, f_{Hay}, is the ratio of the beam radiation on a horizontal surface to the extra-terrestrial radiation. That is:

$$f_{Hay} = \frac{I_b}{I_o} = \frac{I_H - I_d}{I_o} \tag{4.18}$$

Therefore, the diffuse radiation on an inclined surface, $I_{d\beta}$, based on the Hay's model, is calculated as follows:

$$I_{d\beta} = I_d \left[f_{Hay} \left(\frac{cos\theta}{cos\theta_z} \right) + \left(\frac{1+cos\beta}{2} \right) \left(1 - f_{Hay} \right) \right] \quad \text{(W/m}^2\text{)} \tag{4.19}$$

β, is the angle between an inclined/sloped surface and its horizontal.

θ is the angle of incidence, the angle between the beam radiation on a surface and a normal to that surface; and

θ_z, Zenith angle is the angle between the vertical and the line of the sun, the angle of incidence on a horizontal surface.

4.8.2.3 Estimation of the hourly beam solar radiation on an inclined surface

Beam radiation, $I_{b\beta}$, on an inclined surface is defined as the product of the beam radiation on horizontal surface, I_b, and the tilt factor, R_b. That is:

$$I_{b\beta} = I_b R_b \qquad (\text{W/m}^2) \tag{4.20}$$

Where the tilt factor is:

$$R_b = \frac{cos\theta}{cos\theta_z} \tag{4.21}$$

Furthermore, since θ is the incident angle of beam radiation on an inclined surface, the zenith angle, θ_z, is the angle between the normal to the horizontal surface (perpendicular to the horizontal surface) and the line of the sun rays.

Therefore:

$$cos\theta_z = cos\delta cos\varphi cos\omega + sin\varphi sin\delta \tag{4.22}$$

And:

$$cos\theta = \cos(\varphi + \beta) cos\delta cos\omega + sin(\varphi + \beta) sin\delta \tag{4.23}$$

4.8.2.4 Estimation of the hourly ground reflected radiation on an inclined surface

The ground reflected solar radiation components, I_r, is a result of reflectance from the surroundings. The snow-covered ground reflectance, ρ_g, is in order of 0.6 to 0.7 which is much higher than the non-snow-covered ground at 0.2. Therefore, with snow cover and high collector slope, the reflected solar radiation has a substantial contribution. This is contrary to when there is no snow cover and only a minimal collector slope (Duffie & Beckman, 2013).

The ground reflected solar radiation is therefore calculated as followed:

$$I_r = I_H \rho_g \left(\frac{1-cos\beta}{2}\right) \quad (W/m^2) \qquad (4.24)$$

4.9 Vapour-based MSS-SS energy balance equations

The vapour-based MSS-SS was integrated with the passive BSS for experimental purposes. This section discusses the thermal energy balance of the system separately: firstly, the energy balance of the solar collector and the evaporator (entry stage of the condensing tower); secondly, the energy balance of the stacked stages in the condensing tower; and lastly, the energy balance of the BSS. However, as stated earlier, the BSS was not the primary focus of the study. Therefore, existing mathematical equations found in the literature surveyed were used for the BSS without any modifications.

4.9.1 ETSC and evaporator energy balance

Figure 4.21 illustrates the thermal energy flow pattern inside the vapour-based MSS-SS, showing thermal energy supply from both the bottom (evaporator) and the top (BSS). The arrows and different colours of the arrows demonstrate the hottest section in terms of temperature and the least hot section of the system. The arrows indicate the flow direction and nature of flow. For instance, the red arrows between the ETSCs and the evaporator indicates the hottest section of the system. They also indicate that the SW recirculates in the external tubing. Orange arrows show the direction of vapour going into the stages, the second hottest. Dark green arrows showing SW flowing from the secondary tank is the third hottest after the vapour (orange colour). The light green arrows shows the SW flowing from the BSS though the stages and is the fourth hottest section of the system. Finally, the SW flowing from the external SW tank is the least hot section of the system. However, the SW from the BSS can get extremely hot (as discussed in Chapter 5).

Since the operation of the system typically involves transient or unsteady operating conditions, assumptions are made to minimise the variables and exclude factors that cannot be controlled. Below is the list of assumptions made for the vapour-based MSS-SS.

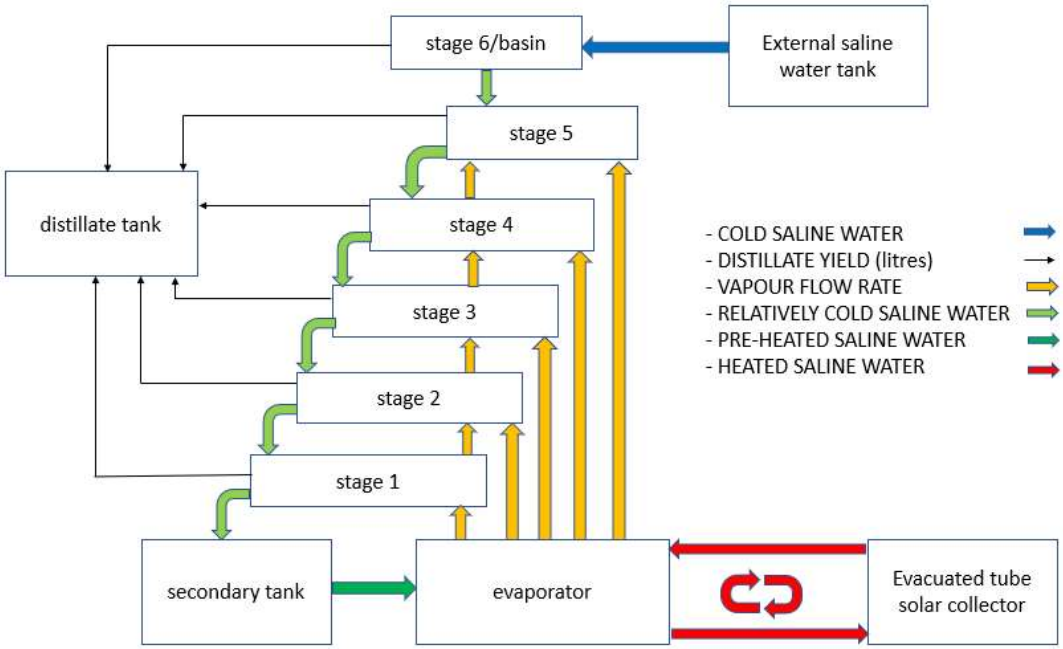

Figure 4.21: Vapour-based MSS-SS heat and mass transfer

4.9.1.1 Assumptions

- The amount of evaporated water is equal to the amount of condensed distillate.
- The effect of non-condensable gases released when the water is heated is neglected.
- The distillate leaves the desalination system at a temperature equal to that of a condensing surface.
- The energy balance of the system is done when the system has stabilised and is fully operational.
- Steady operating conditions are assumed.
- Vapour in the ith stage condenses completely and no transferring of vapour to the subsequent stage takes place.
- The zigzagged SW tube copper material effect on the heat transfer is negligible.
- The thermal energy flow path is as depicted in Figure 4.21.
- The SW temperature in the ETSC manifold is equal to that of the SW in the evaporator.
- The heating fluid temperature in the ETSC is equal to that of the SW.
- Thermal energy absorbed by the stage trays is considered as heat loss.

4.9.1.2 ETSC and saline water energy balance equation

In the ETSC, the area of solar radiation collection (the evacuated tubes) is not equal to the area of losses (the ETSC manifold). There are losses occurring in the evacuated tubes and the manifold which are not proportional. There are various factors to be considered in

determining the thermal energy captured and lost by the ETSC. A simpler approach is considering the overall ability of the ETSC to capture thermal energy. Therefore, Chen et al. (2017) concur that the total energy collected is represented by the total solar irradiance on a tilted surface, I_β, and the collector efficiency η. That is:

$$Q_{ETSC} = I_\beta \times \eta \ \text{(W/m}^2\text{)} \tag{4.25}$$

$$\eta = 0{,}803 - 2{,}01\left(\frac{T_m - T_a}{I_\beta}\right) - 0{,}0034\left(\frac{T_m - T_a}{I_\beta}\right)^2 \tag{4.26}$$

T_m is the average temperature of SW;

T_a is the ambient temperature; and

η is the collector efficiency.

4.9.1.3 Energy input into the evaporator

The thermal energy supplied by the ETSC through the saline water is the sum of the energy in the SW and the thermal energy (latent) for evaporation. Thermal energy losses between the ETSC and the evaporator are negligible. Adequate thermal insulation has been assumed between the collector and the evaporator. In addition, the ETSC and the evaporator were placed closed to each other thereby minimising losses to the surroundings. Therefore:

$$\dot{Q}_{ETSC} = I_\beta \times \eta = \left[\dot{m}_{sw} cp \frac{dT}{dt} + \dot{m}_e hf_g\right]_{evap} \ (\text{W/m}^2) \tag{4.27}$$

Global radiation on an inclined surface, I_β, represents total radiation collected over a time interval of an hour.

4.9.2 Energy input into the stages of the vapour-based MSS-SS

Since the SW was re-circulated in the evaporator and the external tubing, the term, $\dot{m}_{sw} cp \frac{dT}{dt}$, in Equation 4.27 is considered to be conserved in the SW and therefore, only the evaporative term, $\dot{m}_e hf_g$, delivers thermal energy into the stages. Then, the thermal energy input into the stages becomes as follows:

$$\left(\dot{m}_e hf_g\right)_{evap} = \dot{m}_{e1} hf_{g1} + \dot{m}_{e2} hf_{g2} + \dot{m}_{e3} hf_{g3} + \dot{m}_{e4} hf_{g4} + \dot{m}_{e5} hf_{g5} \tag{4.28}$$

In addition, the amount of evaporated water in the evaporator, $\dot{m}_e$, is equal to the sum of the evaporated water reaching the stages. That is:

$$\dot{m}_e = \sum \dot{m}_{e(1-5)} = \dot{m}_{e1} + \dot{m}_{e2} + \dot{m}_{e3} + \dot{m}_{e4} + \dot{m}_{e5} \tag{4.29}$$

Furthermore, the total amount of thermal energy leaving the evaporator through evaporation, $\left(\dot{m}_e hf_g\right)_{evap}$, is equal to the sum of thermal energy received by the stages. That is:

$$\dot{m}_e hfg_{evap} = \sum \dot{m}_e hfg_{(1-5)}$$

It becomes,

$$\dot{m}_e hfg_{evap} = \dot{m}_{e1} hfg_1 + \dot{m}_{e2} hfg_2 + \dot{m}_{e3} hfg_3 + \dot{m}_{e4} hfg_4 + \dot{m}_{e5} hfg_5 \quad (4.30)$$

Thermal energy carried by the SW from the ETSC was delivered to the evaporator. In the evaporator, the separation of the lightweight vapour and the denser SW occurred, as discussed in section 3.15. The denser SW was recirculated in the external tubing while the lightweight vapour ascended to different stages, as indicated by Equation 4.28 to Equation 4.30. In essence, only the vapour delivered the thermal energy into the stages of the vapour-based MSS-SS. Therefore, the energy balance of the condensing tower is as follows:

- Stage 1

$$\dot{m}_{e1} hfg_1 = \dot{m}_{sw1} cp_{sw} \frac{dT}{dt} + \dot{Q}_{loss,1} + \dot{m}_{dist1} cpT_{s1} \quad (4.31)$$

From left to the right of Equation 4.31, the evaporative energy into stage 1 is equal to the energy absorbed by SW in the zigzagged SW tube, thermal energy loss through the walls and stage tray, and the thermal energy in the distillate as it leaves the stage. Since it was assumed that the amount of evaporated water is equal to the amount of condensed water (distillate) in a stage, this means the mass of distillate, $\dot{m}_{dist1}$, is equal to the mass of evaporated water, $\dot{m}_{e1}$. That is:

$$\dot{m}_1 = \dot{m}_{dist1} = \dot{m}_{e1} \quad \text{(kg/s)} \quad (4.32)$$

Equation 4.31 is also true for all stages in condensing tower, stages 2 to 5. Re-arranging Equation 4.31 gives Equation 4.33.

$$\dot{m}_1 (hfg_1 - cpT_{s1}) = \dot{m}_{sw}\ cp_{sw} \frac{dT}{dt} + \dot{Q}_{loss,1} \quad (4.33)$$

- Stage 2

$$\dot{m}_e hfg_2 = \dot{m}_{sw2} cp_{sw} \frac{dT}{dt} + \dot{Q}_{loss,2} + \dot{m}_{dist2} cpT_{s2}$$

$$\dot{m}_2 (hfg_2 - cpT_{s2}) = \dot{m}_{sw2} cp_{sw} \frac{dT}{dt} + \dot{Q}_{loss,2} \quad (4.34)$$

- Stage 3

$$\dot{m}_e hfg_3 = \dot{m}_{sw3} cp_{sw} \frac{dT}{dt} + \dot{Q}_{loss,3} + \dot{m}_{dist3} cpT_{s3}$$

$$\dot{m}_3(hfg_3 - cpT_{s3}) = \dot{m}_{sw3} cp_{sw} \frac{dT}{dt} + \dot{Q}_{loss,3} \quad (4.35)$$

- Stage 4

$$\dot{m}_e hfg_4 = \dot{m}_{sw4} cp_{sw} \frac{dT}{dt} + \dot{Q}_{loss,4} + \dot{m}_{dist4} cpT_{s4}$$

$$\dot{m}_4(hfg_4 - cpT_{s4}) = \dot{m}_{sw4} cp_{sw} \frac{dT}{dt} + \dot{Q}_{loss,4} \quad (4.36)$$

- Stage 5

$$\dot{m}_e hfg_5 = \dot{m}_{sw5} cp_{sw} \frac{dT}{dt} + \dot{Q}_{loss,5} + \dot{m}_{dist5} cpT_{s5}$$

$$\dot{m}_5(hfg_5 - cpT_{s5}) = \dot{m}_{sw5} cp_{sw} \frac{dT}{dt} + \dot{Q}_{loss,5} \quad (4.37)$$

4.9.3 Energy efficiency

The following equations were adapted from Mbadinga (2015) in a study of a passive solar still under Cape Town, South Africa, weather conditions.

$$\eta = \frac{Thermal\ energy\ used\ in\ vaporising\ the\ SW\ or\ the\ useful\ energy}{Amount\ of\ solar\ incident\ on\ the\ condensing\ cover} \quad (4.38)$$

$$\eta = \frac{\dot{m}_e\ hfg_{evap}}{A_{cc} \int I_\beta\ dt}$$

Where, m_e, is the total evaporated water and A_{cc} is the condensing glass cover area in m^2. The global radiation on an inclined surface is I_β, as reported in section 4.8. The evaporative thermal energy hfg_{evap} equation was reported to have been adopted from Tiwari and Tripathi (2003). The evaporative thermal energy is determined as follows:

$$hfg_{evap} = 3.1615 \times 10^6 \times [1 - (7.616 \times 10^{-4} T_{sw})] \quad (4.39)$$

In the vapour-based MSS-SS experimental tests, the vapour temperature, T_v, was assumed to be equal to that of the evaporative surface of SW, T_{sw}. The evaporative surface is at the interface of stagnant pool of SW in the basin and the vapour. That is:

$$T_{sw} = T_v \quad (4.40)$$

Therefore, Equation 4.39 is for SW temperature, T_{sw}, above 70°C. For SW temperatures, T_{sw}, below 70°C, the equation becomes:

$$hfg_{evap} = 2.4935 \times 10^{6}\left[(1 - 9.4779 \times 10^{-4}T_{sw}) + \left(1.3132 \times 10^{-7}{T_{sw}}^{2}\right) - \left(4.7979 \times 10^{-9}{T_{sw}}^{3}\right)\right] \quad (4.41)$$

The distillate productivity, P_d, can be determined from:

$$P_d = \frac{V_t}{A_{cc}} \quad (4.42)$$

Where V_t is the total cumulative daily distillate yield in litres.

- Additional notes

If the distillate leaves the stage at a temperature equal to that of the condensing surface, then $T_{dist} = T_{cond.surface}$, the surface temperature, $T_{cond.surface}$, being the surface temperature of the stage walls, stage tray and the zigzagged SW tube. In addition, the condensation of vapour happens at constant temperature, hence $\dot{m}_e hfg_{evap}$.

4.10 Economic analysis of the MSS-SS

The economic analysis of the MSS-SS is carried out based on the methods reported in Chapter 2, in section 2.9. The equations guiding the cost estimation of the vapour-based MSS-SS are as follows:

$$CRF = \frac{i(1+i)^n}{[(1+i)^n - 1]} \quad (4.43)$$

$$FAC = P \times CRF \quad (4.44)$$

$$SFF = \frac{i}{[(1+i)^n - 1]} \quad (4.45)$$

$$S = 0.2P \quad (4.46)$$

$$ASV = SFF \times S \quad (4.47)$$

$$AMC = 0.15 \times FAC \quad (4.48)$$

$$AC = FAC + AMC - ASV \quad (4.49)$$

$$CPL = \frac{AC}{M} \quad (4.50)$$

4.11 Overall experimental set up of the vapour-based MSS-SS

Before the experimental tests were conducted, the vapour-based MSS-SS needed to be filled with SW. The system was primed with SW to remove air in the tubing of the system. Priming only took place when the system was to start the operation for the first time or after

maintenance. Once the system had been primed once, it would work continuously without any human assistance or intervention. The priming process is explained with the aid of Figure 4.22. The SW was filled in the external tank of the vapour-based MSS-SS. From the external SW tank, the SW flowed completely under the gravitational influence. The SW flowed from the external SW tank and into the BSS through a float valve which regulated the flow amount of SW. The float valve in the secondary SW water tank was fully opened to allow air out of the system. From the BSS the SW flowed through the zigzagged SW tube into the secondary SW tank. Once full flow was observed in the secondary SW tank, the valve was put into an operational position, meaning that the valve can open and shut on its own based on the level of SW in the secondary tank. Once the secondary SW tank is full, the SW starts to flow into the evaporator. The evaporator does not fill up before the external tubing is full as well. Therefore, only once the SW starts to flow from the evaporator hole, as in sub-section 4.3.3.1, (the liquid probe hole). The flow from the evaporator indicates that the whole system is fully primed and ready to start the operation.

Figure 4.22: Vapour-based MSS-SS condensing tower

The U-shaped tubes (see Figure 4.22) were also filled with freshwater before operation commenced. These tubes were filled only once before the start of the experimental tests. The water inside these tubes' rests in the U-shape portion of the tube and was not removed even during the maintenance. This water serves as the vapour trap device, as explained by Jubran et al. (2000), preventing the vapour from escaping the stages. Only the condensed distillate laying on the stage trays can displace the water from the U-shaped section of the tubes. Once

the entire system has been primed, the SW in the external tubing and the evaporator can start to circulate when heated by the ETSCs. Each time the SW reaches the evaporator, there is a separation of lightweight vapour and denser SW. The vapour is then delivered to the stages. When the vapour reached the stages, it is condensed and collected, as outlined under section 4.6. As the BSS was not the main focus of the study, only the basic equations found in the literature review were utilised to establish the productivity of the BSS based on the thermal energy input.

CHAPTER FIVE

EXPERIMENTAL TESTS RESULTS AND DISCUSSION

This chapter discusses the results obtained from the experimental tests conducted on the newly developed vapour-based multistage solar desalination system. The experimental tests for this current study were undertaken over a period of 10 months, beginning September 2020 through June 2021. As a result, the tests were conducted during spring, summer, autumn and winter in this sequence, under actual varying weather conditions in the field. The seasonal change and the variation of solar radiation were important factors in the distillate yield of the system. The MSS-SS was experimentally tested at the Cape Peninsula University of Technology (CPUT), Bellville campus, in Cape Town, South Africa. The performance of the MSS-SS system was tested under two scenarios: when the condensing tower was thermally insulated and when it was uninsulated. It is worth reminding that the daily performance of an MSS-SS system depends primarily on solar irradiance, so the variation of solar irradiance initiates the discussion.

The discussions are based on daily average solar irradiance on a horizontal surface. Sample calculations of the solar irradiance on an inclined surface are shown in Appendix A-3. The daily average solar irradiance was categorized into three groups: 1) low daily average solar irradiance; 2) moderate daily average solar irradiance; and 3) high daily average solar irradiance. The low daily average solar irradiance ranges between 0 W/m^2 and 199 W/m^2 while the range of moderate daily average solar irradiance is between 200 W/m^2 and 399 W/m^2. The high daily average solar irradiance range is between 400 W/m^2 and 600 W/m^2. It is also worth mentioning that as the data logged throughout the 10-month duration is quite intense, it would be difficult to present the whole realm of this data in this work. Therefore, the grouping of solar irradiance was used in selecting the specific days for the purpose of analysing the performance of MSS-SS system. As the availability of solar irradiance depends on various factors, the impact of wind speed and other factors are incorporated towards the end of this chapter.

Furthermore, in this work, when the solar irradiance curve increased and reached its highest point, this is referred as ‘crest’. The increasing curve represented the heating period where an increase in solar irradiance collection occurred. In addition, the non-fluctuating, or a curve with minimal fluctuations, represents a positive mode of thermal energy input into the evaporator. Alternatively, when the curve decreased and reached its lowest point, this is referred to as a ‘trough’. The decreasing curves represented the cooling down period of reduced solar irradiance collection. The fluctuating curve represents the impulse mode of thermal energy input (Feilizadeh et al., 2015).

5.1 Vapour-based MSS-SS performance under low solar insolation with the condensing tower thermally insulated

This current section starts by firstly discussing the solar irradiance responsible for temperature variations inside the condensing tower. This is followed by analysis of the evaporative and condensing surface temperature of the system. The evaporative and condensing surface temperature is comprised of the subsection that looks at the SW temperature variation as it flows through the system. The analysis of SW temperature is followed by the section that considers the stage wall and stage tray temperature variations. These subsections are crucial in discussion because they are perceived as having an influence in the distillate production. These subsections are then followed by discussion related to distillate production.

5.1.1 Daily solar irradiance

Figure 5.1 shows the solar irradiance curves for the 25th of Sept. 2020, 29th of May 2021 and 31st of May 2021, with average solar irradiance values of 145.1, 179.5 and 197.6 W/m^2, respectively. On the 25th of Sept. 2020, the first and last solar incidence was recorded around 06h50 am and 18h40 pm, respectively. The solar irradiance crest on the day was at 418 W/m^2 around 13h20 pm. Figure 5.1 demonstrate a moderately fluctuating solar radiation throughout the day.

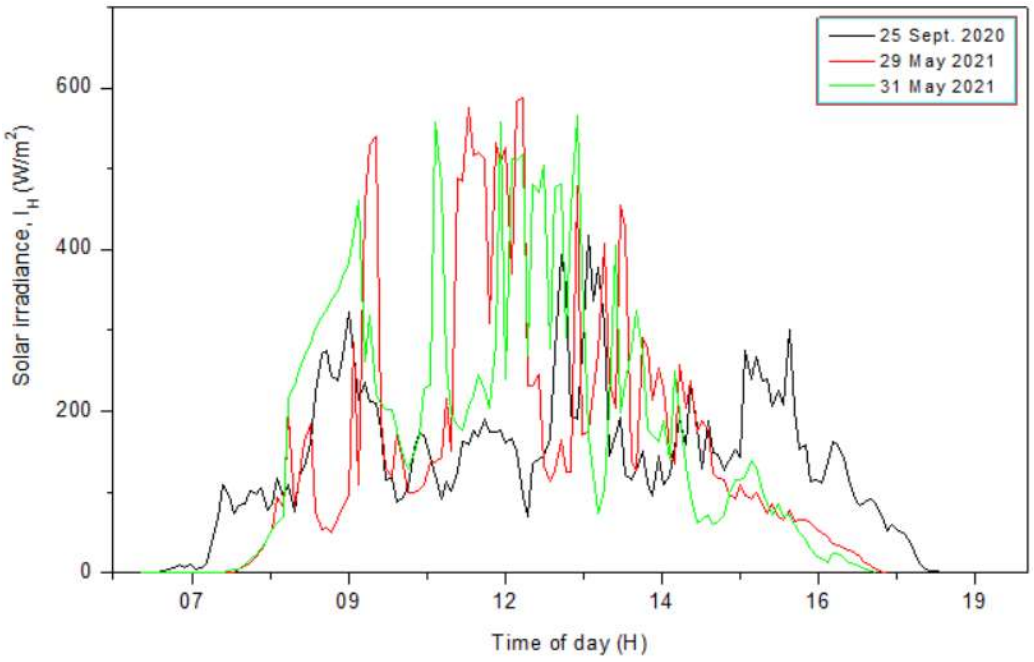

Figure 5.1: Solar irradiance vs time of day

On the 29th of May 2021, the average solar irradiance collected on the day was slightly higher at 179.5 W/m^2. The first and the last solar incidence were recorded around 07h50 am and 17h50 pm, respectively. The duration of the recorded solar irradiance was reduced by

approximately 1-hour and 50 minutes compared to that of the 25th of Sept. 2020. However, according to Figure 5.1, solar irradiance crests on the 29th of May 2021 reached a maximum of 586.7 W/m^2 around 12h20 in the afternoon, suggesting that the heating periods due to the solar irradiance crests on the 29th of May 2021 exceeded that of the 25th of Sept. 2020. Therefore, based on the premise that the higher the curve crest, the higher the thermal energy collected, there was increased thermal energy input into the condensing tower on the 29th of May compared to the 25th of Sept. 2020.

Amongst the three days in discussion, the highest average solar irradiance within the low solar irradiance range was 197.6 W/m^2 on the 31st of May 2021. The first and the last solar incidence was recorded around 07h50 am and 17h40 pm, respectively. Therefore, there was a reduction of 10-minutes in the duration of the recorded solar irradiance compared to that of the 29th of May 2021. There was an intense solar irradiance fluctuation throughout the day. Its highest crest was 566.1 W/m^2 reached around 13h00 pm.

The three graphs discussed in Figure 5.1 give evidence that the solar irradiance remained below the 600 W/m^2 mark. Furthermore, even though the average solar irradiance on the 31st of May 2021 was higher, there was prevalent heating periods on the 29th of May 2021, suggesting that the thermal energy collected on the 29th of May 2021 was higher compared to the 31st of May 2021. The higher thermal energy collection was also represented by the highest crest at 586.7 W/m^2. Moreover, the cooling down periods on the 31st of May 2021 were more prevalent compared to that of the 29th of May 2021, as shown in Figure 5.1. The solar irradiance crests on the 25th of Sept. 2020 were much lower than those of the 29th and the 31st of May 2021. Therefore, the rate of thermal energy input on the 25th of Sept. 2020 was lower compared to the 29th and 31 of May 2021. The low thermal energy input was a direct result of fluctuating solar irradiance and low solar intensities. These fluctuations were a direct result of cloud cover and other atmospheric activities during the day which resulted in the lower daily average solar irradiance (Mowla & Karimi, 1995; Kamal, 1988). Moreover, the amount of solar intensity reaching the earth's surfaces was dependent on the solar altitude angle. In winter periods, the solar altitude angle is low compared to the summer periods (Altarawneh et al., 2017; Iqbal, 1983).

5.1.2 Evaporative and condensing surface temperature behaviours

This section addresses the analysis of SW temperature as it flows through various parts of the system. This includes SW that flows through zigzagged copper tube, the stage walls and stage trays, as discussed under sections 3.7 and 3.12.

5.1.2.1 SW temperature behaviours

Figure 5.2 shows the evaporator SW and the stage SW temperature curves for the 25th of Sept. 2020. According to Figure 5.2, the evaporator SW temperature decreased throughout the day as a result of the solar irradiance in Figure 5.1. However, the BSS and the stage SW show a slight increase in temperature throughout the day due to the SW pre-heating from the BSS. The BSS SW temperature increase was due to the direct heating by the sun's rays on the day as it was exposed to the incoming solar radiation (Morad et al., 2015).

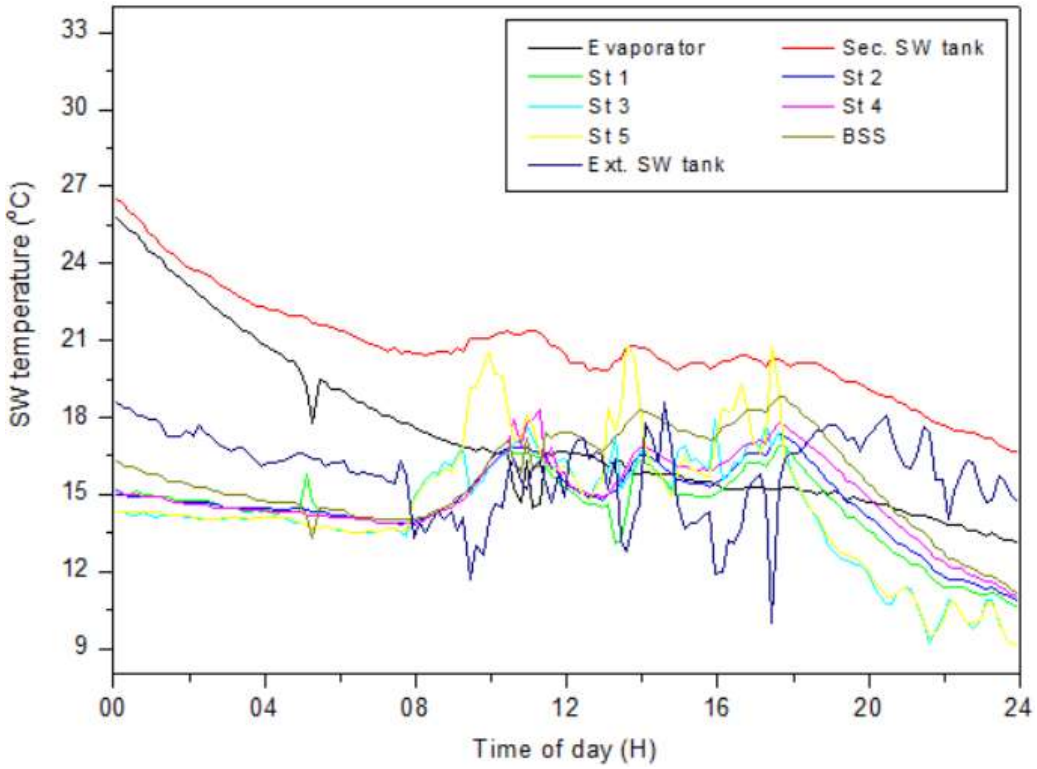

Figure 5.2: SW temperatures vs time of day

The SW temperature patterns in Figure 5.2 followed the solar irradiance patterns in Figure 5.1. The maximum stages SW temperature was such that they were 20.8, 18.3, 17.9, 17.4 and 16.9°C for stages 1 to 5, respectively, while that of the BSSSW was 18.8°C. This maximum SW temperature trend suggests that the thermal energy was supplied from the BSS through SW pre-heating. The pre-heated SW flowing down from the BSS caused the slight SW temperature increase in the stages as the SW flowed down through the stages. The instantaneous SW pre-heated in the stages caused the secondary SW temperature to maintain relatively higher SW temperatures (see Figure 5.2).

The evaporator SW and stage SW temperatures curves for the 29th of May 2021 are shown in Figure 5.3, with temperature variations based on solar irradiance presented in Figure 5.1. There was a slight decrease in the evaporator SW and stages SW temperature curves from

midnight until around 11h59 am but a gradual increase in temperature was observed around 12h00 pm with a sharp increase in evaporator SW temperature. The sharp temperature increase in the evaporator was due to the minimal SW quantity in the evaporator which increased and maintained elevated temperatures in the evaporator (El-Sebaii, 2011; Ahsan et al., 2014). Moreover, the evaporator SW temperature attained between 12h00 pm and 15h00 pm was approximately 92°C while other compartments reached maximum temperature less than that of the evaporator later in the day. Therefore, the higher the evaporator SW temperature, the higher the vapour production in the evaporator (Kabeel & EL-Agouz, 2011).

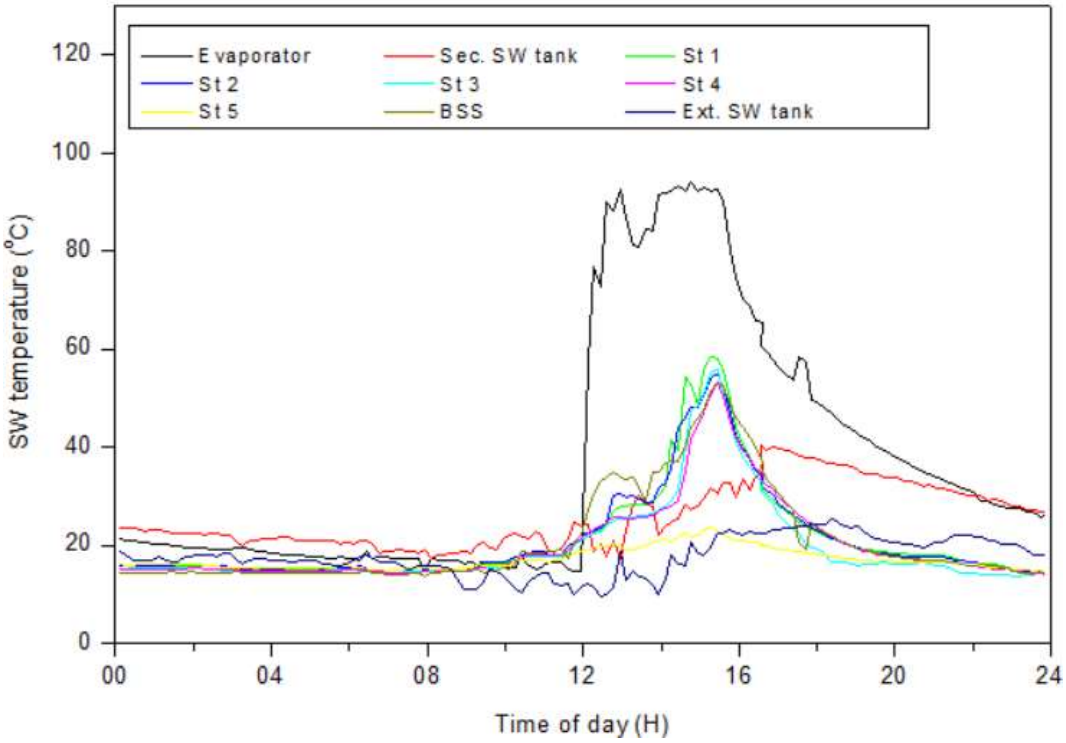

Figure 5.3: SW temperature vs time of day

There was a larger temperature difference between the stage SW and the evaporator SW, the stage SW was responsible for vapour condensation (Gnanaraj et al., 2017). Based on Figure 5.3, the notable stage's temperature gradient suggested that the maximum temperature reached by each stage depends on its location relative to the evaporator: the stage closer to the evaporator reaches higher maximum temperature compared to stages far from the evaporator. The stage SW temperature gradient was 58.6, 55.3, 56.1, 53.4 and 23.4°C, respectively, while that of the BSS was 53.4°C. The solar irradiance collected on this day was higher compared to that of the 25th of Sept. 2020. This increased solar irradiance changed the stage's SW temperature gradient compared to that of the 25th of Sept. 2020.

Figure 5.4 shows the evaporator SW and stage SW temperature curves for the 31st of May 2021. The evaporator and stage SW temperatures decreased from midnight until 09h30 am and started a gradual increase thereafter. There was a sharp increase in the evaporator SW temperature at 12h00 pm which was followed by the SW temperature curves at 12h40 pm. The evaporator SW reached and maintained maximum temperature of approximately 91.2°C between 12h50 pm and 14h50 pm. According to Figure 5.4, there was a larger temperature difference between the evaporator and the stage SW. Furthermore, the stage SW temperature gradients show the lower stages maintained higher temperatures relative to the lower stages. The stage SW temperature gradient for stages 1 to 5 was 65.6, 47.4, 44.2, 38.9 and 21.6°C, respectively, while that of the BSS SW was 38.2°C

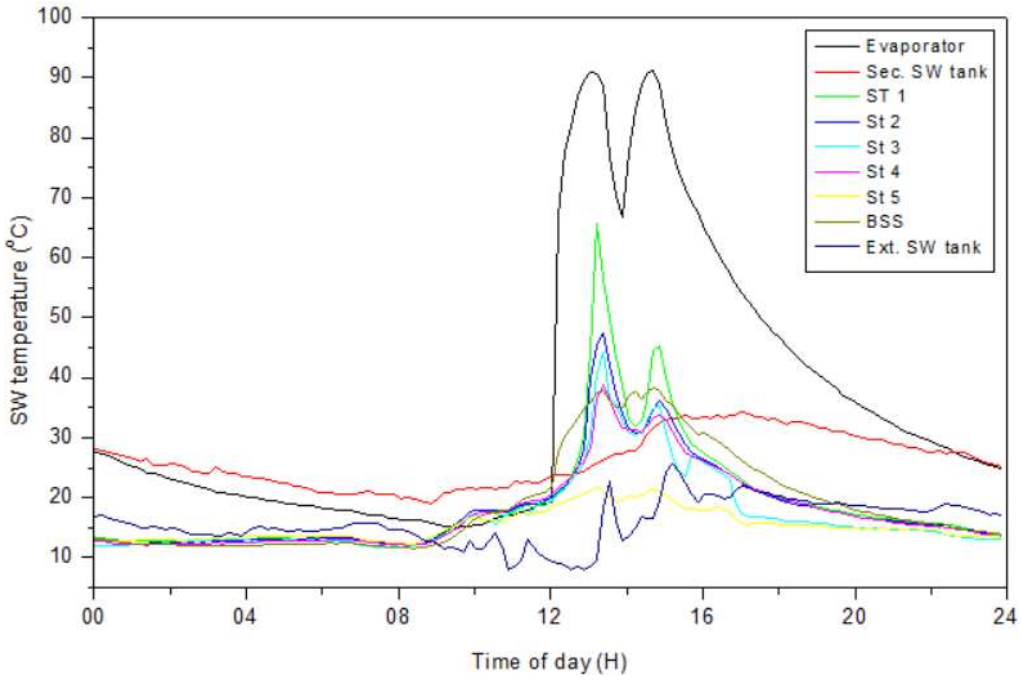

Figure 5.4: SW temperature vs time of day

Figure 5.5 presents the average SW temperature curves for the three days discussed above. The SW in the stages recovered the latent heat of condensation from the vapour while being pre-heated by the SW flowing from the BSS (Liu et al., 2014a). The average SW temperature profile of the 25th of Sept. 2020 shows that the upper stages maintained higher temperatures, indicating that heat was mainly supplied by BSS through SW pre-heating process. However, the SW temperature profiles for the other two days (29 May 2021 and 31 May 2021) show high temperatures maintained by lower stages, an indication that heat was mainly supplied by the evaporator through heat recovery process.

Increasing the solar irradiance increased the rate of thermal energy input into the condensing tower and therefore, increased the SW temperatures compared to that of the 25th of Sept.

2020. However, Figure 5.5 shows that despite the higher average solar irradiance on the 31st of May 2021, the SW temperature in the condensing tower was higher on the 29th of May 2021 compared to that of the 31st of May 2021. Furthermore, in Figures 5.3 and 5.4, stage SW temperature curves showed that thermal energy input on the 29th of May 2021 was higher. This higher rate of thermal energy input was a direct result of the solar irradiance curve progression and patterns in Figure 5.1. The higher solar irradiance crest curves, extremely low troughs and prolonged troughs contributed to the reduction of the rate of thermal energy input on the 31st of May 2021.

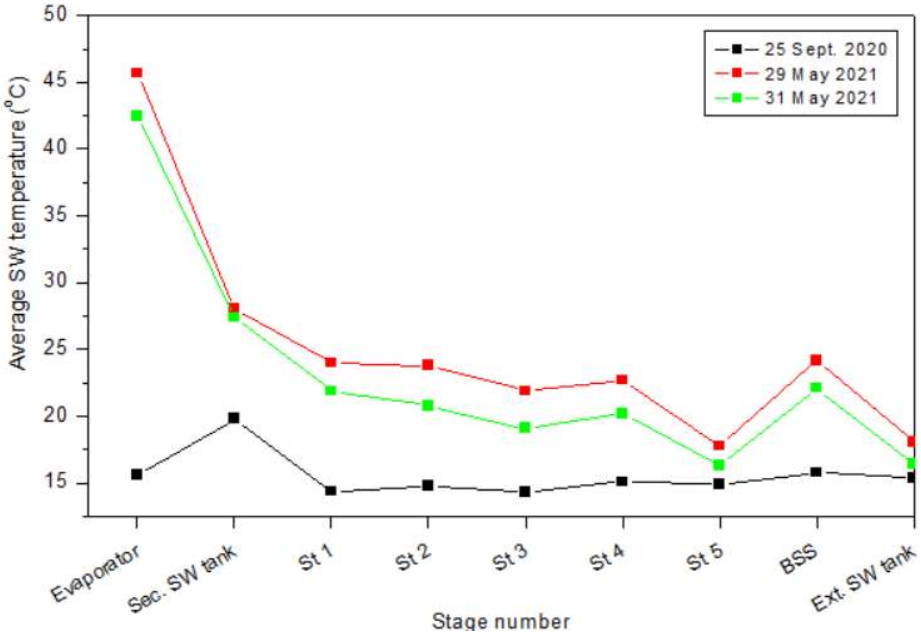

Figure 5.5: Average SW temperature vs stage number

5.1.2.2 Stage wall and stage tray

The stage walls and stage tray temperature probes were installed in stage 2 only as discussed in sub-section 4.3.3. The temperature profile for stage 2 SW, stage wall and stage tray (see Figure 5.6) for the 25th of Sept 2020 followed the same pattern throughout the day. The maximum temperature of 17.4, 17.7 and 17.8°C for stage SW, stage wall and stage tray were attained, respectively. Despite the above maximum temperatures, the curves in Figure 5.6 showed a changing pattern in terms of being the highest. However, later in the day, the stage SW curve was slightly higher than the other two curves.

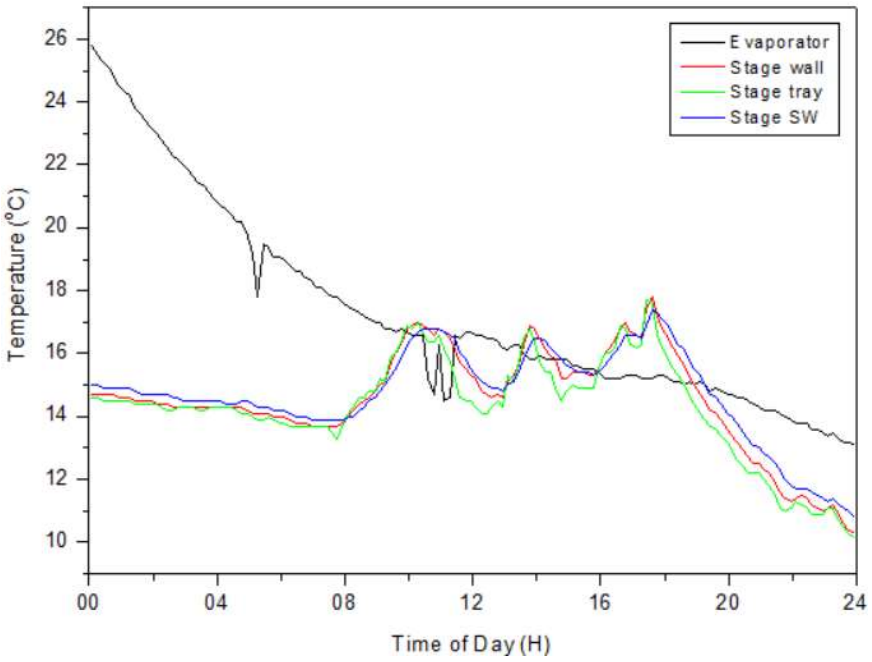

Figure 5.6: Evaporative and condensing surfaces vs time of day

The temperature profiles in Figure 5.6 suggested three possible causes for these SW temperature behaviours. Firstly, this could be a result of direct sun rays heating up the outside surface of the condensing tower. Since the stages were vapour tight, it caused heat build-up in the stages. Secondly, the temperature probes may be picking up the slight increase in temperature as the stages were being heated up by small quantities of incoming vapour from the evaporator. Thirdly, the origin of the increased temperature was the BSS through SW pre-heating as described earlier. However, Figure 5.6 shows that the stage wall temperature was mostly lower than the stage SW and the stage tray throughout the day.

The stage SW, stage wall and stage tray temperature curves for the 29th of May 2021 are shown in Figure 5.7. The maximum temperatures were 55.3, 55.1 and 56.3°C for stage SW, stage wall and stage tray, respectively. However, the maximum stage wall temperature was the lower than the stage SW and stage tray, indicating heat losses to the surroundings. Furthermore, the slightly higher stage SW temperature curve in Figure 5.7 may have been the result of both the SW pre-heating and heat recovery processes simultaneously. Figure 5.7 also reveals a changing curves pattern as the day progressed. Later in the day, the stage SW temperature curve was slightly higher while the stage was the lowest.

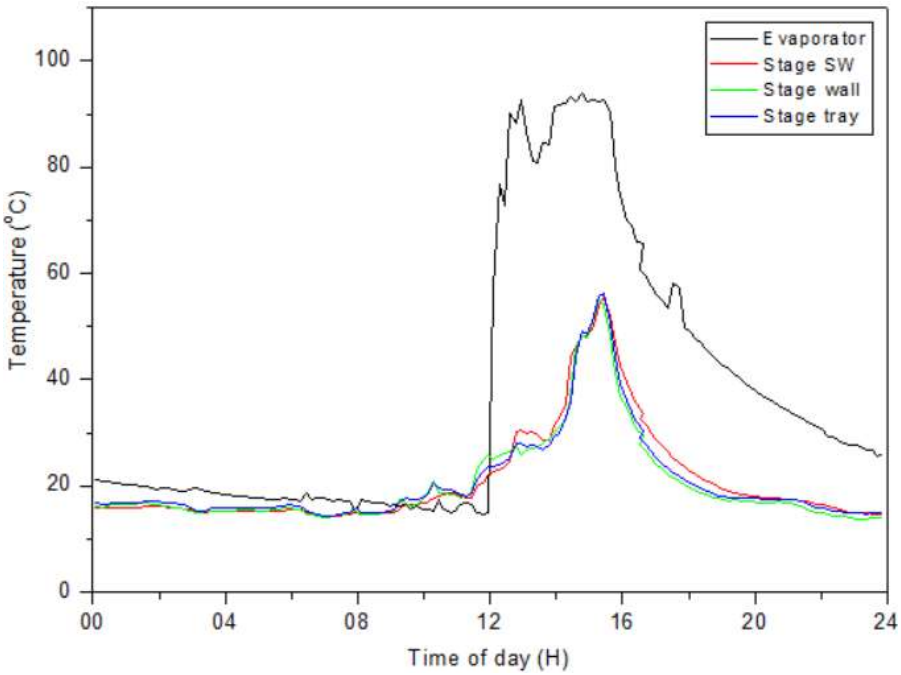

Figure 5.7: Evaporative and condensing surfaces vs time of day

Figure 5.8 shows the stage SW, stage wall and stage trays temperature curves for the 31st of May 2021. The stage wall and stage tray temperature curves followed the same path as stage SW temperature curve, discussed in Figure 5.4.

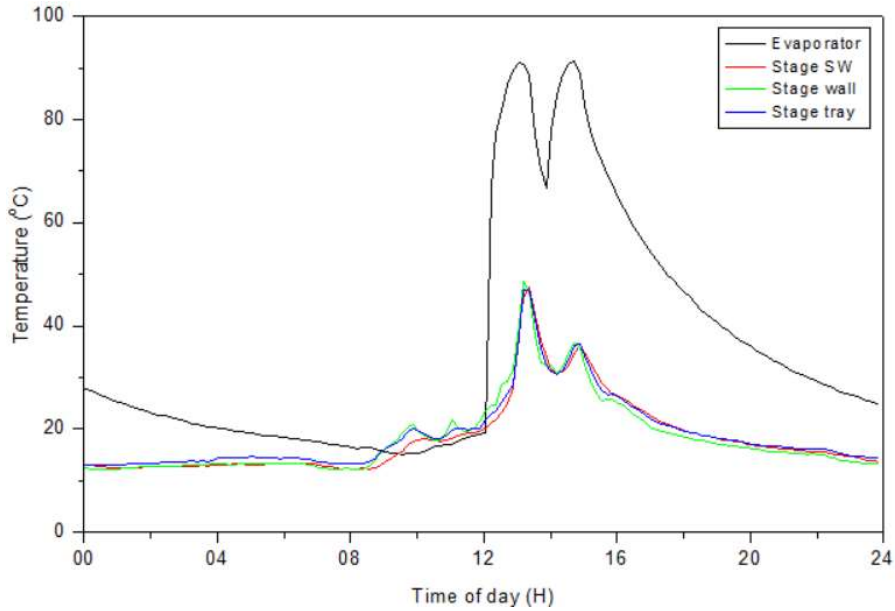

Figure 5.8: Evaporative and condensing surfaces vs time of day

Figure 5.8 shows that the stage wall was slightly higher in the morning and lower in the afternoon. The maximum stage SW, stage wall and stage tray temperatures were 13.7, 13.2

and 14.3°C, respectively. However, Figure 5.8 suggested that the curves were changing in terms of being highest throughout the day.

5.1.3 Daily cumulative distillate yield

Table 5.1 shows the distillate yield from the vapour-based MSS-SS. On the 25th of Sept. 2020, there were non-measurable (NM) distillate quantities from the stages. Thus, the average solar irradiance of 145.1 W/m^2 and the solar irradiance pattern shown in Figure 5.1 constituted the minimal operating conditions for the vapour-based MSS-SS. Moreover, on the 29th and 31st of May 2021, the daily cumulative distillate yield was 1190 and 580 ml, respectively, despite the higher average solar irradiance on the 31st of May 2021. Therefore, as seen in Figures 5.2 to 5.4 and 5.6 to 5.8, the system's components represented by the SW temperature curves were at low temperature in the morning.

The larger temperature gradient between the vapour and the vapour make-up tubes' inner walls caused the vapour to condense prematurely in the tubes creating a thermal boundary layer which prevented the bulk vapour in motion from reaching the stages. However, for the vapour to successfully reach the stages, thermal equilibrium, or close to it, must be achieved between the vapour and the vapour make-up tubes' inner wall. The flow of vapour or steam in a pipe dictate that there must be minimal temperature gradient between a fluid sufficiently far from the wall and in bulk motion relative to the inner walls of that pipe. The larger temperature gradient causes higher convective heat transfers between the two. This higher rate transfer of heat between the vapour or steam and the tube reduces the temperature of a fluid and thus causes it to condense when it reaches its dew point. Until thermal equilibrium or the temperature gradient is reduced, the vapour will continue condensing prematurely inside the tube (Çengel et al., 2008).

Therefore, the delays between the evaporator SW and the condensing surface temperature increase were interpreted as a result of the premature vapour condensation in the vapour make-up tubes. The low condensing surfaces temperature increase in Figures 5.4 and 5.8 suggested reduced vapour accessing the stages on the 31st of May 2021. To the contrary, the condensing surfaces were higher on the 29th of May 2021 (see Figures 5.3 and 5.7). Furthermore, as observed from Table 5.1, the distillate yield was consistent to an extent with the stage's SW temperature gradient on the 29th and 31st of May 2021. The stage distillate yield trend will be discussed later in the chapter. Moreover, Figure 5.5 proved that despite a low average solar irradiance on the 29th of May 2021 compared to that of the 31st of May 2021, the rate of thermal energy generated by the solar irradiance curve on the 29th of May 2021 was higher. Therefore, the solar irradiance curve patterns and progressions, as shown in

Figure 5.1, were crucial in increasing the amount of vapour reaching the stages. The daily distillate yield per stage for the entire experimental test period is shown in Appendix B-3.

Table 5.1: Distillate yield from the vapour-based MSS-SS

Day	Av. Daily Sol. Irradiance (W/m^2)	Stage distillate yield (ml)						Total (ml)
		St 1	St 2	St 3	St 4	St 5	BSS	
25 Sept. 2020	145.1	NM	NM	NM	NM	NM	NM	-
29 May 2021	179.5	560	100	170	30	250	80	1190
31 May 2021	197.6	250	30	120	20	30	130	580

Distillate collecting cylinder was graduated to 10 ml, the rounding off was used when the distillate was in between the graduated marks. NM-non measurable.

5.1.4 Summarised results

The effects of SW pre-heating from the BSS were apparent on the 25th of Sept. 2020 (see Figure 5.2). However, according to Figures 5.3 and 5.4, the condensing surfaces followed the evaporator SW temperature behaviour, suggesting that the heat recovery process of the latent heat of condensation was more dominant as the solar irradiance increased. The sharp decrease of the evaporative and condensing surfaces later in the day suggested increased heat losses and that the desalination process ceased soon after sunset midnight. Moreover, the evaporator operated at temperatures around 90°C from 12h00 pm to 15h00 pm and 12h50 pm to 14h50 pm on the 29th and 31st of May 2021, respectively, a behaviour suggesting that there was more vapour production on the 29th of May 2021 than on the 31st of May 2021. In addition, the evaporator SW temperature showed that it was sensitive to the fluctuating solar irradiance. There was a sharp decline in the evaporator temperature when the corresponding solar irradiance decreased to its troughs, a temperature decline observable in Figures 5.3 and 5.4. According to Figure 5.5, despite higher SW temperatures in the stages, the pre-heated SW temperatures in the secondary tank were 28.1 and 27.4°C on the 29th and 31st of May 2021, respectively. This low cumulative pre-heating may be associated with increased heat losses. The stage 2 SW, stage wall and stage tray temperature curves followed the same path. Therefore, it can be assumed that the stage wall and stage trays temperature curves of stages 1, 3, 4 and 5 followed that of the SW in their respective stages. For the 29th of May 2021, the overall thermal energy efficiency of the vapour-based MSS-SS was 18.23%, indicating increased energy losses from the system. The solar irradiance and the performance of the system sample calculations are shown in Appendices A-3 and A-4, respectively.

5.2 Vapour-based MSS-SS performance under moderate solar insolation with the condensing tower thermally insulated

This section, while set out similarly to section 5.1, considers the condensing tower temperature behaviours under moderate daily average solar irradiance.

5.2.1 Daily solar irradiance

The moderate daily average solar irradiance values were selected on 01 June 2021, 02 June 2021, 26 Sept. 2020, and 29 Sept. 2020 as 209.9, 246.1, 253.7 and 385.7 W/m^2, respectively. These values represent the average range of 200 – 399 W/m^2. Figure 5.9 shows that the first and the last solar incidences were recorded around 07h40 am and 17h40 pm, respectively, on the 1st of June 2021. The maximum and average solar irradiance on the 1st of June 2021 were 498 W/m^2 around 12h50 pm and 209.9 W/m^2, respectively. On the 2nd of June 2021, the first and last solar irradiance were recorded around 07h40 am and 17h40 pm, respectively. The maximum and average solar irradiances collected were 547.1 W/m^2 around 11h50 am and 246.1 W/m^2, respectively.

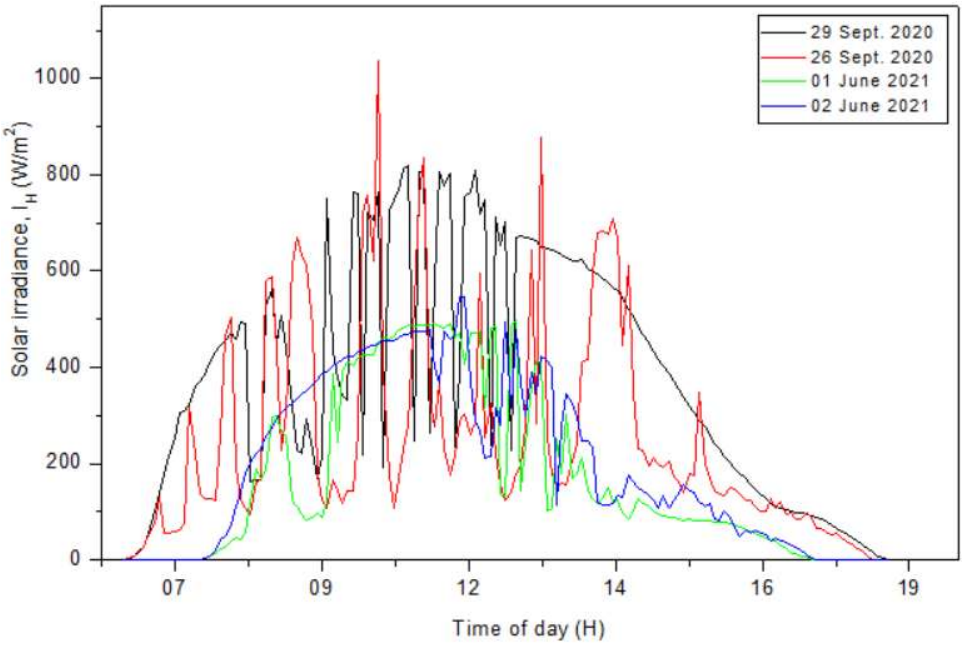

Figure 5.9: Solar irradiance vs time of day

On the 26th of Sept. 2020, the first and the last solar incidences were recorded at 06h30 and 18h40 in the morning and evening, respectively. The maximum instantaneous value of 1037 W/m^2 was recorded around 10h40 in the morning. The average daily solar irradiance was 253.7 W/m^2 on the day. On 29th of Sept. 2020, the first and the last solar incidences were recorded around 06h20 and 18h50 in the morning and evening, respectively. Therefore, the maximum and average solar irradiance values recorded on the day were 817.7 W/m^2 around 11h00 in the morning and 385.7 W/m^2.

Based on Figure 5.9, even though the average solar irradiance values from the 2nd of June 2021 and the 26th of Sept. 2020 were almost equal, their solar irradiance curves were vastly different. The crests of the curve on the 26th of Sept. 2020 were much higher than those of the 2nd of June 2021. This represented the difference between spring and winter. In addition, the

duration of the recorded solar irradiance was longer in the spring compared to the winter. Furthermore, compared to Figure 5.1, there were reduced fluctuations on the 1st and 2nd of June 2021. But even though there were fluctuations in spring curves, their crests were higher and the trough not as low as those in Figure 5.1. According to the discussion in section 5.1, an increased rate of thermal energy supply into the condensing tower is expected.

5.2.2 Evaporative and condensing surfaces temperature behaviours

5.2.2.1 SW temperature behaviours

An average increase in solar irradiance from 197.6 W/m^2 on the 31st of May 2021 to 209.9 W/m^2 on 1st of June 2021 resulted in the SW temperature behaviours shown in Figure 5.10. The stages SW temperature curves reveal the same behaviour as discussed under sub-section 5.1.2. That is, the SW in the stages started to increase around 08h00 in the morning while that of the evaporator was still decreasing (see Figure 5.10). The sharp increase in evaporator SW temperature occurred around 11h00 in the morning; stages 1 to 4 were delayed about 20 minutes before rapidly increasing. Meanwhile, the maximum evaporator SW temperature reached 91°C between 12h00 pm and 16h00 pm. Stages 1 to 5 reached maximum values of 97.7, 75.5, 66.6, 76.9 and 30°C, respectively. Figure 5.10 makes evident that stages 1 to 4 SW temperatures reached or exceeded that of the evaporator.

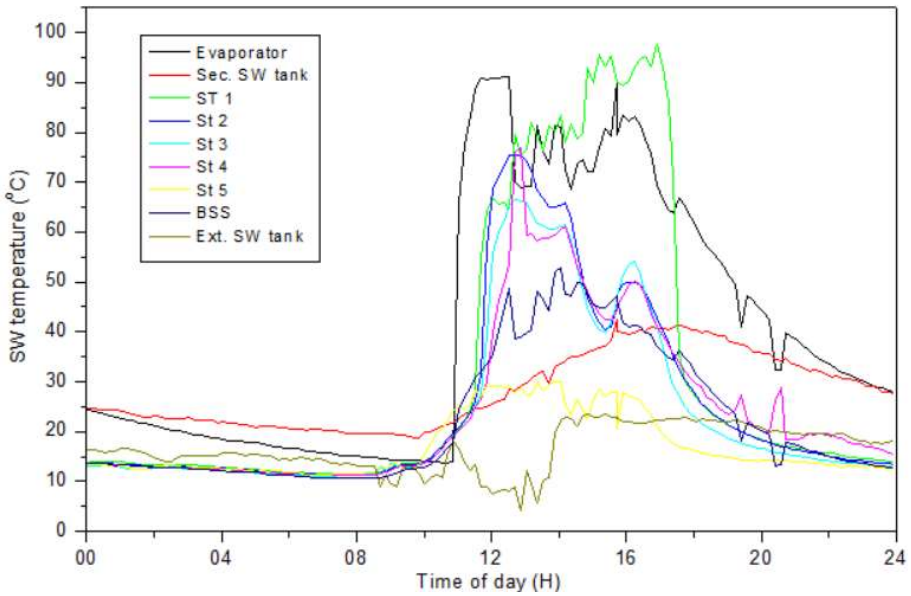

Figure 5.10: SW temperature vs time of day

While other stage SW temperatures decreased, stage 1 maintained elevated temperatures throughout the day, suggesting that the condensation in stages 2 to 4 was reduced or halted momentarily while that of stage 1 lasted longer. Stage 5 SW temperature remained low compared to the other stages. When the condensing surfaces equal or exceeds that of the

evaporative surfaces, the system is said to have reached “thermal damage condition”. Thermal damage condition occurs when the condensing surface temperature values approach, equal or exceed that of the evaporative surface (Shatat & Mahkamov, 2010). Under the lower solar irradiance, the system operated without reaching thermal damage condition. Therefore, increasing the rate of thermal energy input also excessively increased the temperatures of the cooling surfaces. Initially, the vapour was assumed to be supplied equally to all stages. However, since the temperature is directly proportional to its pressure, the thermal damage condition caused an increased in pressure in the stages (Çengel, 2003). Therefore, the vapour was redirected from the evaporator to those stages with moderate condensing surface temperature. In the stages with moderate SW temperatures, the condensing surfaces effectively condensed the vapour by maintaining cooler surfaces and thus, larger temperature differences. As the temperature difference is a driving force in the vapour condensation, the larger the temperature difference, the higher the vapour condensation rate (Sharshir et al., 2016a).

A further increase in the average solar irradiance to 246.1 W/m^2 on the 2nd of June 2021 resulted in the SW temperature curves in Figure 5.11. A decreasing trend of SW temperature from midnight until 08h00 am indicating heat losses can be observed in Figure 5.11. Furthermore, despite an increase in the average solar irradiance, only stages 2 and 4 reached thermal damage condition on the day. The evaporator reached its maximum temperature value of 93°C between 11h00 am and 15h30 pm. Meanwhile, the maximum SW temperature values of 71, 74.3, 65.6, 89.1 and 30.1°C were attained in stages 1 to 5, respectively.

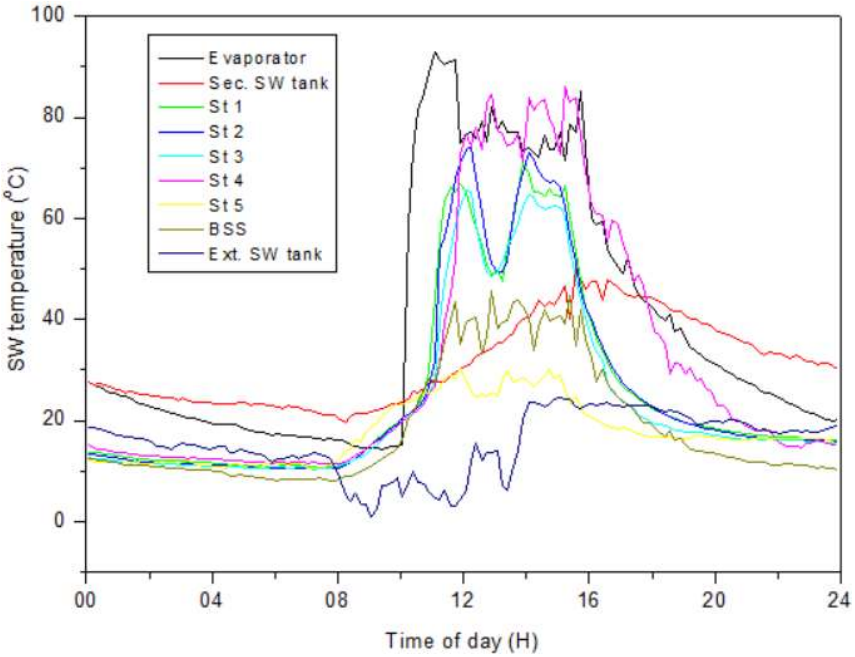

Figure 5.11: SW temperature vs time of day

Based on Figure 5.11, the condensation process in stage 4 was severely reduced or halted altogether due to the thermal damage condition. SW temperature behaviours began to change compared to all the previous discussed SW temperature figures. Figure 5.11 no longer showed that the lower stages maintained the highest SW temperatures. The external factors such as wind velocity and ambient air, not discussed yet, could have an impact on the SW temperature behaviours (Saeedi et al., 2015; Sharshir et al., 2016a). The average wind velocity and ambient air temperature for the 1st of June 2021 were 1.2 m/s and 14.5°C, respectively, while that of the 2nd of June 2021 were 2.1 m/s and 15.8°C, respectively. Since heat flows from a high temperature region to a low temperature region, the external factors must be considered despite the thermal insulation material on the condensing tower (Çengel, 2003). Additional data including the average wind velocity and the ambient air temperature is tabulated in Appendix B-1.

Figure 5.9 shows that the solar irradiance curve assumed both a positive and an impulse mode of thermal energy input and was higher than that of the 1st of June 2021. The increased average wind velocity to 2.1 m/s compared to 1.2 m/s could have had a significant impact on the SW temperature profiles as the average solar irradiance increased (Sharshir et al., 2016a). In addition, all the SW temperature figures (including Figure 5.11) show a sharp decline in the SW temperature in the condensing tower later in the afternoon, despite the use of the thermal insulation material; hence, the consideration of external factors.

The SW temperature behaviour on the 26th of Sept. 2020 is represented by Figure 5.12. The SW temperature was below 20°C since on the 25th of Sept. 2020 there was little thermal energy input into the condensing tower. A slight decrease in the SW temperature can be observed in Figure 5.12 until 09h40 am. The maximum evaporator SW temperature occurred between 10h50 am and 15h20 pm at 90.7°C. Figure 5.9 shows a heavily fluctuating solar irradiance curve representing cooling down periods and the impulse mode of thermal energy input into the condensing tower. Hence, the SW temperature behaviours in Figure 5.12 represent larger temperature differences between the evaporative and the condensing surfaces. Despite an increased in the average solar irradiance compared to the 1st and 2nd of June 2021, there was no thermal damage condition reached. Stage 1 to 5 attained their maximum SW temperatures of 73.6, 78.4, 72.3, 53.2 and 38.9°C, respectively. Furthermore, Figure 5.12 shows that under the impulse mode of thermal energy input, lower stages maintained a higher SW temperature despite increasing the average solar irradiance to 253.7 W/m^2.

Despite the low average wind velocity 1.7 m/s and average ambient air temperature of 12.5°C, the condensing tower only experienced a decreased temperature difference at 15h00 pm

when the solar irradiance assumed a positive mode of thermal energy input, momentarily. Table B-1 under Appendix B contains all other days experimentally tested.

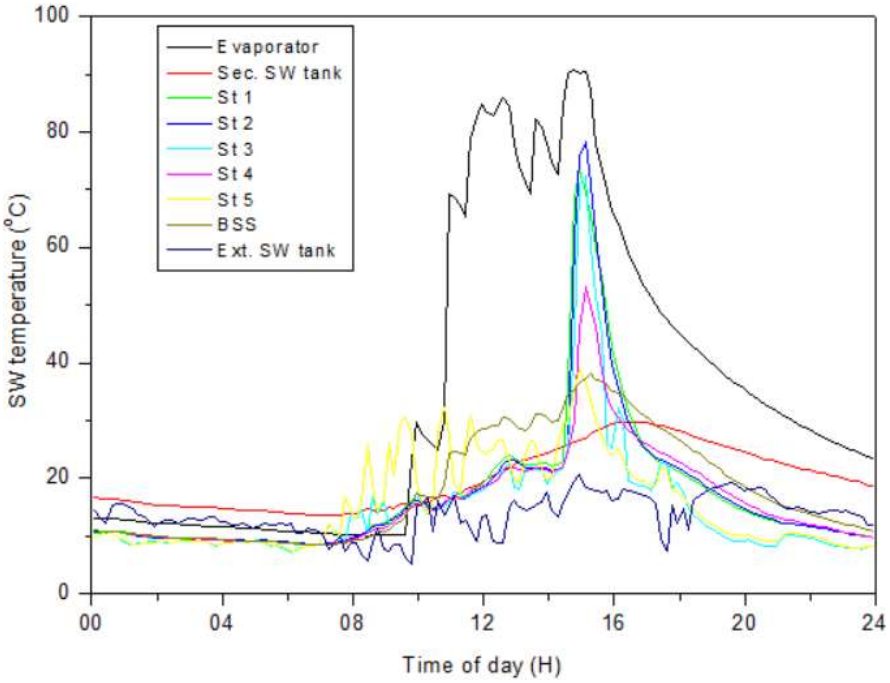

Figure 5.12 SW temperature vs time of day

On the 29th of Sept. 2020, the SW temperature curves, represented by Figure 5.13, were driven by the average solar irradiance of 385.7 W/m^2. The SW temperature curves showed a decrease in temperature from midnight until 07h00 am. The evaporator SW temperature increased sharply at 09h50 am. The evaporator attained it maximum temperature of 91.6°C between 10h50 am and 17h20 pm. Figure 5.13 also reveals that stages 2, 3 and 4 maintained the higher SW temperature values in the condensing tower.

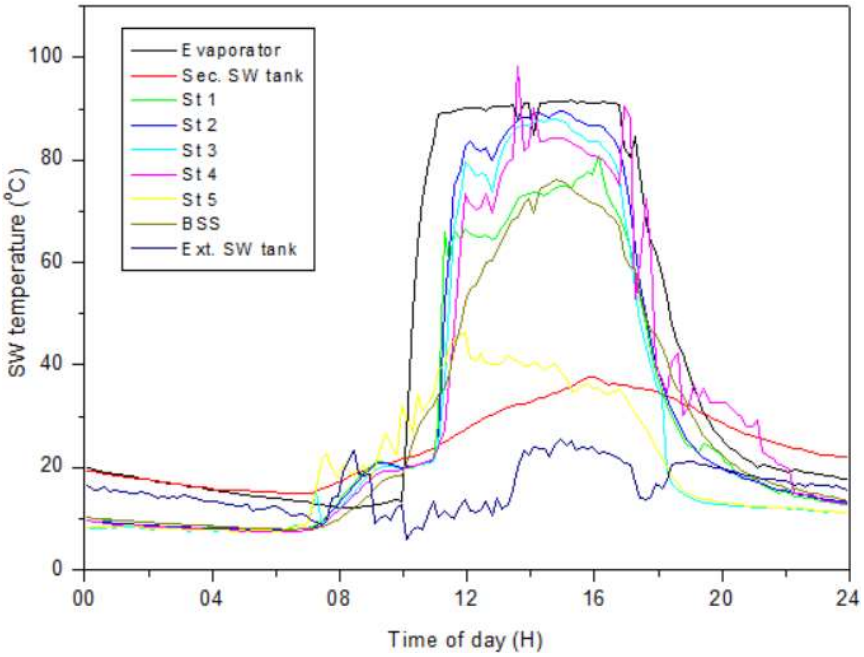

Figure 5.13: SW temperature vs time of day

Stages 1 to 5 SW temperatures were 81, 89.5, 88.1, 98.3 and 46.2°C, respectively. The condensing tower operated at thermal damage condition on the day. The combination of the impulse and positive mode of thermal energy input was evidently excessive for the condensing tower. In fact, some stages had already reached thermal damage under the average solar irradiance of 209.9 and 246.1 W/m^2. This was an indication that the SW in the zigzagged SW tube was insufficiently cool and condensed the vapour without reaching thermal damage condition, especially under positive mode of thermal energy input. Furthermore, despite the average wind velocity and ambient air temperature of 3.2 m/s and 15.5°C, the condensing tower reached thermal damage condition. Appendix B-1 presents additional data for the days experimentally tested. The condensing tower temperature behaviour indicated that in its current design, it cannot maintain an adequate temperature difference when thermally insulated.

5.2.2.2 Stage wall and stage tray

The condensing surfaces in Figure 5.14 represent the temperature behaviour of the condensing tower on the 1st of June 2021. Stage wall and stage tray temperature curves show an increase with increasing stage SW temperature. The stage 2 SW, wall and tray temperature were maximum at 75.5, 66 and 69.1°C, respectively. According to Figure 5.14, when the stage SW in the zigzagged SW tube reached thermal damage, the stage wall and tray were also approaching it. Therefore, it is safe to say stage walls and trays of stages 1, 3 and 4 (as shown in Figure 5.10) also reached thermal damage condition.

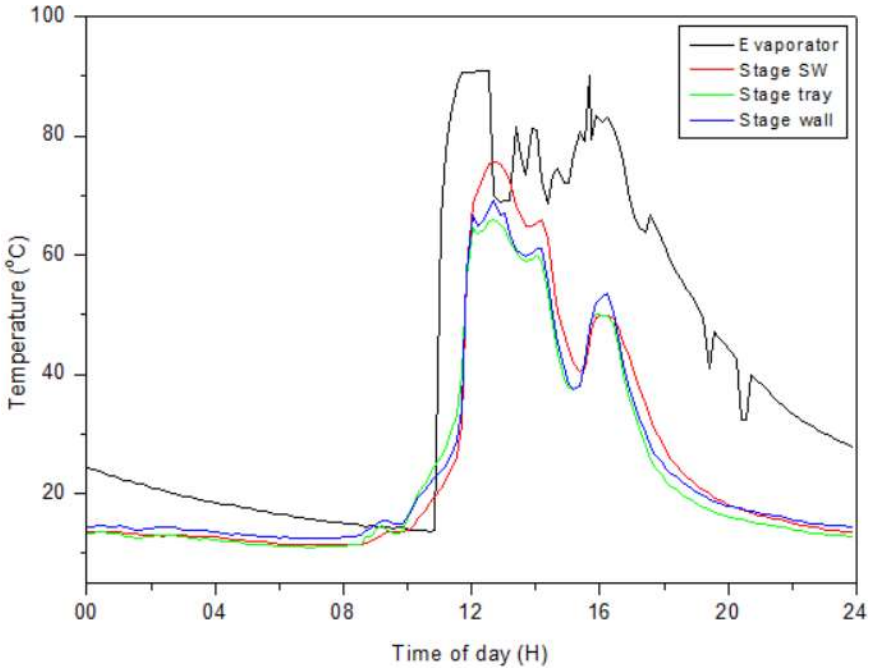

Figure 5.14: Evaporative and condensing surfaces vs time of day

The evaporative and condensing surfaces are shown in Figure 5.15 for the 2nd of June 2021. The stage SW, wall and tray temperatures were 74.3, 65 and 67.8°C, respectively. The evaporator curve in Figure 5.15 indicates a higher temperature throughout the day compared to the 1st of June 2021. This indicated a higher rate of vapour supply to the stages. Moreover, an increase in wind velocity to 2.1 m/s on the 2nd of June 2021 may have been the driving force in maintaining the stage wall and tray temperature low and thus, preventing thermal damage. Compared to the stage wall and tray on the 1st of June 2021 when the wind was only 1.2 m/s and a higher average solar irradiance, there was an increased temperature difference between the evaporative and condensing surfaces on the 2nd of June 2021.

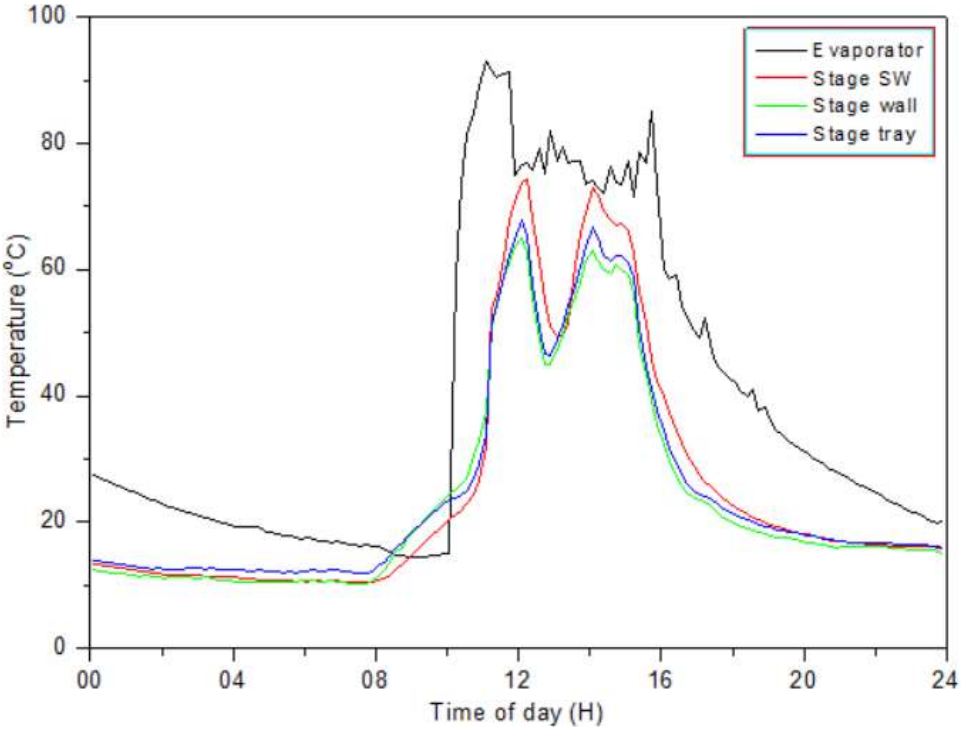

Figure 5.15: Evaporative and condensing surfaces vs time of day

Figure 5.16 represents the evaporative and condensing surface temperature behaviours for the 26th of Sept. 2020. The maximum of 78.4, 77.6 and 72.8 °C were momentarily attained by the stage 2 SW, wall and tray, respectively. The impulse mode of thermal energy input depicted in Figure 5.9 was the main driver in the larger temperature difference throughout the day. The wind velocity was relatively low compared to the 29th of Sept. 2020 to have meaningful impact. In fact, at only 209.9 W/m^2 average solar irradiance, the wind velocity of 1.2 m/s failed to maintain a larger temperature difference on the 1st of June 2021.

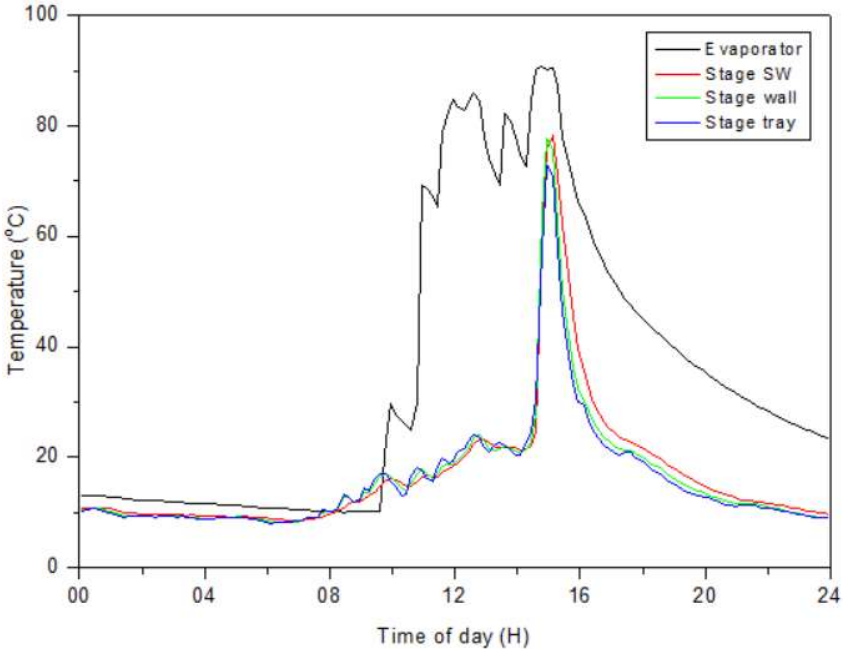

Figure 5.16: Evaporative and condensing surfaces vs time of day

The stage 2 SW, wall and tray maximum temperatures were 89.5, 88.6 and 85.4°C, respectively, as shown in Figure 5.17. The mode of thermal energy input assumed by the solar irradiance curve in Figure 5.9 for the 29th of Sept. 2020 caused a reduction in the temperature difference. Figure 5.17 suggests that stages 2, 3 and 4 experienced a critical reduction temperature difference with the evaporative surface.

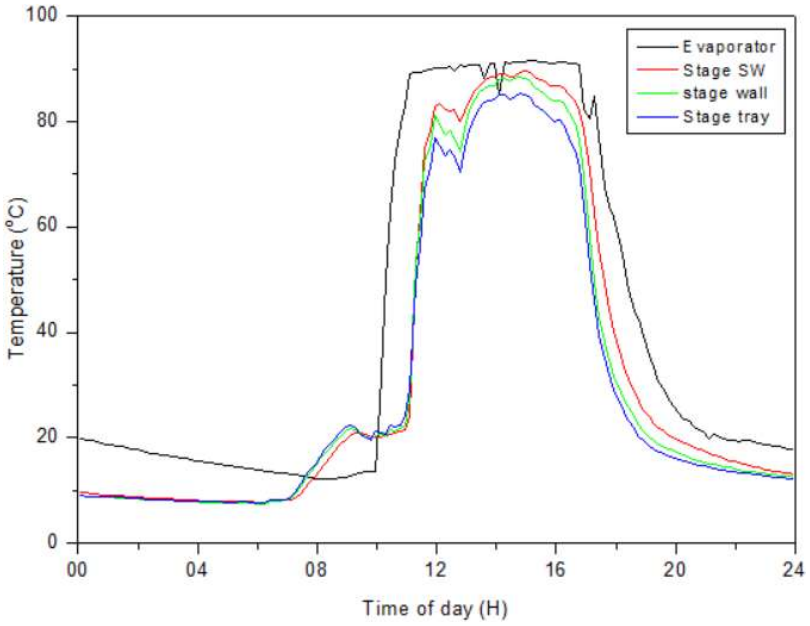

Figure 5.17: Evaporative and condensing surfaces vs time of day

The rate of vapour condensation in these stages was reduced, despite the higher average wind velocity at 3.2 m/s.

5.2.3 Daily cumulative distillate yield

Increasing the average solar irradiance further also caused an increase in the daily distillate yield of the condensing tower, as shown in Table 5.2. The distillate yield in Table 5.2 was a result of the low range (0 to 199 W/m^2) and the moderate range (200 to 399 W/m^2) of the average solar irradiance. Therefore, in terms of average values, and with reference to Table 5.2, increasing the solar irradiance by 5.9% between 197.6 to 209.9 W/m^2 caused an increase in the daily cumulative distillate yield by 100% from 580 to 1160 ml. Further increasing the average solar irradiance by 14.7% from 209.9 to 246.1 W/m^2 caused the daily cumulative distillate yield to increase by 48.3% from 1160 to 1720 ml. Increasing the average solar irradiance by 3% from 246.1 to 253.7 W/m^2 caused a substantial increase in the total distillate by 195.93% from 1720 to 5090 ml. A further increase in average solar irradiance by 34.2% from 253.7 to 385.7 W/m^2 caused the total distillate yield to increase by 6.8% from 5090 – 5460 ml. However, as discussed earlier, the extent of productivity of the vapour-based MSS-SS was primarily dependent on three aspects: the values of the crest of the solar irradiance curves, that is, how high the crest can reach on a day; the frequency of heating periods as the solar irradiance fluctuated up to its crest and down to its trough; and the frequency of cooling periods as the solar irradiance fluctuated throughout the day.

Table 5.2: Distillate yield from the vapour-based MSS-SS

Day	Av. Daily Sol. Irradiance (W/m^2)	Stage distillate yield (ml)						Total (ml)
		St 1	St 2	St 3	St 4	St 5	BSS	
25 Sept. 2020	145.1	NM	NM	NM	NM	NM	NM	-
29 May 2021	179.5	560	100	170	30	250	80	1190
31 May 2021	197.6	250	30	120	20	30	130	580
01 June 2021	209.9	50	150	210	140	470	140	1160
02 June 2021	246.1	160	390	510	60	380	220	1720
26 Sept. 2020	253.7	980	1120	1070	680	900	340	5090
29 Sept. 2020	385.7	1020	1040	1050	590	1280	480	5460

Distillate collecting cylinder was graduated to 10 ml, the rounding off was used when the distillate was in between the graduated marks. NM-not measurable

Under the mode of thermal energy input represented on the 29th of Sept. 2020, stage 5 was the most productive stage. This is potentially a direct result of the larger temperature difference (Sharshir et al., 2016a). On the 26th of Sept. 2020, however, the solar irradiance crests were reaching as high as 1037 W/m^2 and troughs as low as 100 W/m^2. This mode of thermal energy input proved to be more productive as increasing the average daily solar irradiance by 3% from 246.1 to 253.7 W/m^2 caused an increase in the total distillate by 195.93% from 1720 to 5090 ml.

5.2.4 Summarised results

In comparison with the SW pre-heating and heat recovery under the low range of average solar irradiance, there was a further increase under the moderate solar irradiance range. The SW in the secondary SW tank attained its highest temperature of 50.2°C on the 2nd of June 2021. However, there was a decline on the 26th and 29th of Sept. 2020 as the secondary SW tank only reached a maximum of 29.7 and 37.6°C, respectively. This may have indicated a limit to the extent the SW can be pre-heated in the vapour-based MSS-SS current design. Furthermore, the cooling down periods represented by the intensely fluctuating solar irradiance on the 26th of Sept. 2020 may have affected the SW pre-heating process. The condensing tower still showed a sharp decrease of both the evaporative and condensing surfaces later in the day, indicating increased heat losses to the surroundings. Furthermore, due to the increased thermal energy input, the evaporator temperature reached its maximum valued of 93°C on the 2nd of June 2021. However, further increasing the average solar irradiance showed no further increase in the evaporator temperature. The evaporator temperature maintained its highest SW temperature for longer on the 29th of Sept. 2020 between 10h50 am and 17h20 pm, representing a longer duration for vapour production in a day.

On the 29th of Sept. 2020, there was reduced sensitivity between the fluctuating solar irradiance and the evaporator SW temperature curve (see Figures 5.9 and 5.13). Furthermore, the highest solar irradiance crests and the cooling down periods (troughs) in Figure 5.9 were the direct result 195.93% distillate yield between the 2nd of June 2021 and 26 Sept. 2020. Under the moderate average solar irradiance, the mode of thermal energy input depicted by Figure 5.9 for the 26th of Sept. 2020 may be the most suitable to prevent thermal damage while increasing the condensing tower's productivity. However, it had shown to have minimal effects in terms of SW pre-heating. Based on Figures 5.13 and 5.17, except for stage 5, the temperature difference between the evaporative and condensing surfaces reduced drastically. Appendix B-1 provides average solar irradiance, wind velocity, ambient air temperature and cumulative distillate yield on the rest of the days experimentally tested.

5.3 Vapour-based MSS-SS performance under high solar insolation with the condensing tower thermally insulated

This section covers the average solar irradiance defined as from 400 – 600 W/m^2. The vapour-based MSS-SS is expected to operate under similar conditions as observed under Figures 5.13 and 5.17 due to an increased rate of thermal energy input.

5.3.1 Daily solar irradiance

Figure 5.18 shows the solar irradiance curves for the 24th of Sept. 2020 with the average solar irradiance of 418.9 W/m^2. The solar irradiance curve demonstrated a non-fluctuating curve relative to all other curves discussed so far. The non-fluctuating curve represented a positive thermal energy supply to the vapour-based MSS-SS. The first and the last solar incidences were recorded around 06h40 am and 18h40 pm, respectively. The maximum solar irradiance value of 745.1 W/m^2 was attained around 12h00 noon.

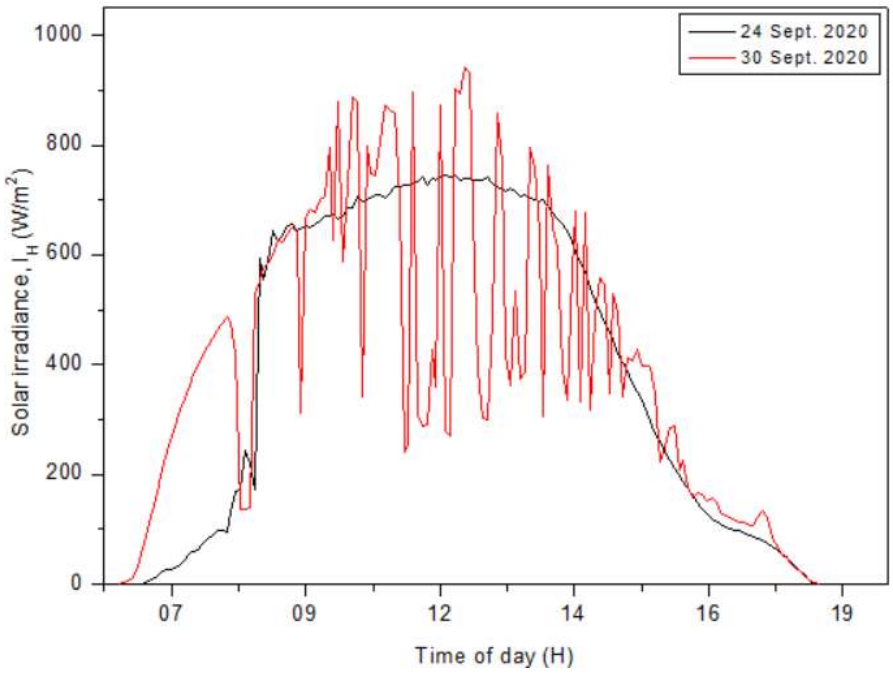

Figure 5.18: Solar irradiance vs time of day

On the 30th of Sept. 2020, the average solar irradiance curve was 412.2 W/m^2. The solar irradiance curve was fluctuating with minimal cooling down periods (see Figure 5.18). The first and last solar incidence was recorded around 06h20 am and 18h40 pm. The maximum solar irradiance value was 941.1 W/m^2 reached around 12h30 pm.

5.3.2 Evaporative and condensing surfaces temperature behaviours

5.3.2.1 SW temperature behaviours

The SW temperature behaviour under the average solar irradiance of 412.2 W/m^2 on the 30th of Sept. 2020 is shown in Figure 5.19. The SW temperatures show a decline in temperature from midnight until 06h50 am, when they started a steady increase until 09h50 am. Meanwhile the evaporator SW temperature showed a steady decline until 09h20 am when it increased sharply thereafter. There was, therefore, about a 30-minutes delay between the evaporative and condensing surfaces temperature sharp increase. Figure 5.19 shows that the temperature profile in the stages was such that the lower stages maintained higher temperature than the

upper stages. The stages 1 to 5 SW temperature maximum values were 109.3, 93.7, 94, 90.4 and 56.9°C, respectively. Meanwhile, the evaporator SW temperature reached its maximum at 90.9°C between 09h40 am and 16h30 pm. The condensing tower operated at thermal damage which has exceeded the conditions observed in Figures 5.13 and 5.17 for the 29th of Sept. 2020. The stage 1 SW temperature behaviour resembled that of Figure 5.10 for the 1st of June 2021.

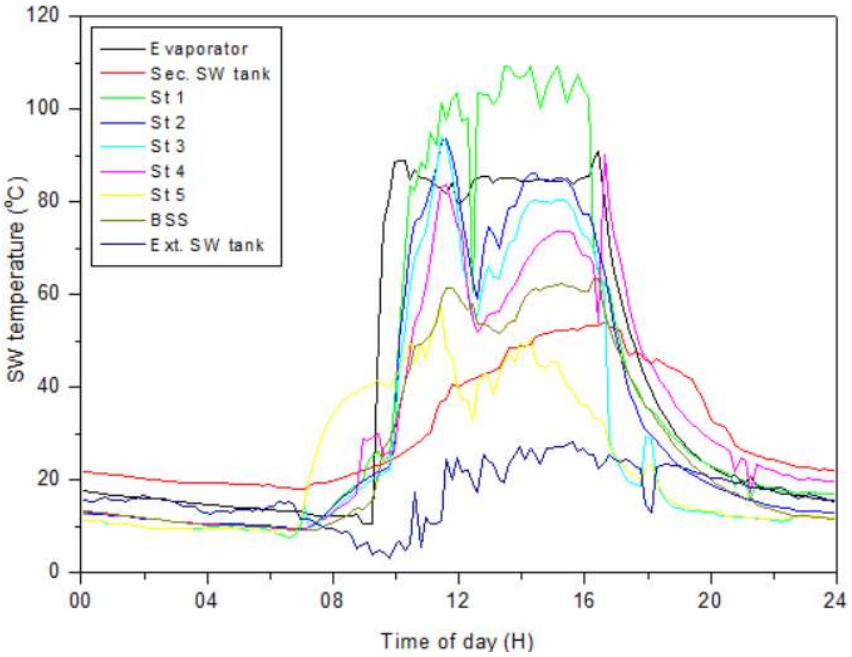

Figure 5.19: SW temperature vs time of day

According to Figure 5.19, stage 5 was the only stage that maintained sufficient temperature difference with the evaporator temperature and thus, condensation was effective. Furthermore, despite stage 4 being relatively further away from the heat source (the evaporator), it was prone to reaching the thermal damage. There was no apparent cause for this behaviour except that the arrangement of vapour make-up tubes on the evaporator might have an influence on this. Moreover, under low and moderate average solar irradiance, the condensing surfaces tended to sharply decrease earlier than the evaporator temperature, except for on the 29th of Sept. 2020. Figure 5.19 also shows a reduced time-delay between the sharp decline in the evaporative and condensing surfaces, an indication of the increased thermal energy input into the condensing tower. However, the sharp decline in temperature later in the afternoon still revealed the extent of heat losses from the condensing tower. On the 30th of Sept. 2020, the average wind velocity and the ambient air temperature was 2.4 m/s and 15.4°C, respectively, as shown in Appendix B-1.

The 24th of Sept. 2020 SW temperature behaviours are represented by Figure 5.20. Accordingly, a further increase in the average solar irradiance to 418.9 W/m^2 resulted in stages

1 to 4 reaching thermal damage condition. In the previous figures (Figures 5.13 and 5.19), one or two stages reached or exceeded that of the evaporator. However, data in Figure 5.20 indicates only stage 5 maintained a larger temperature difference, evidence that a thermally insulated condensing tower could not effectively operate at the rate of thermal energy represented by Figure 5.18. The delays in sharp increase and decline observed between the evaporative and condensing surfaces temperatures were reduced in Figure 5.20 compared to the earlier figures presented.

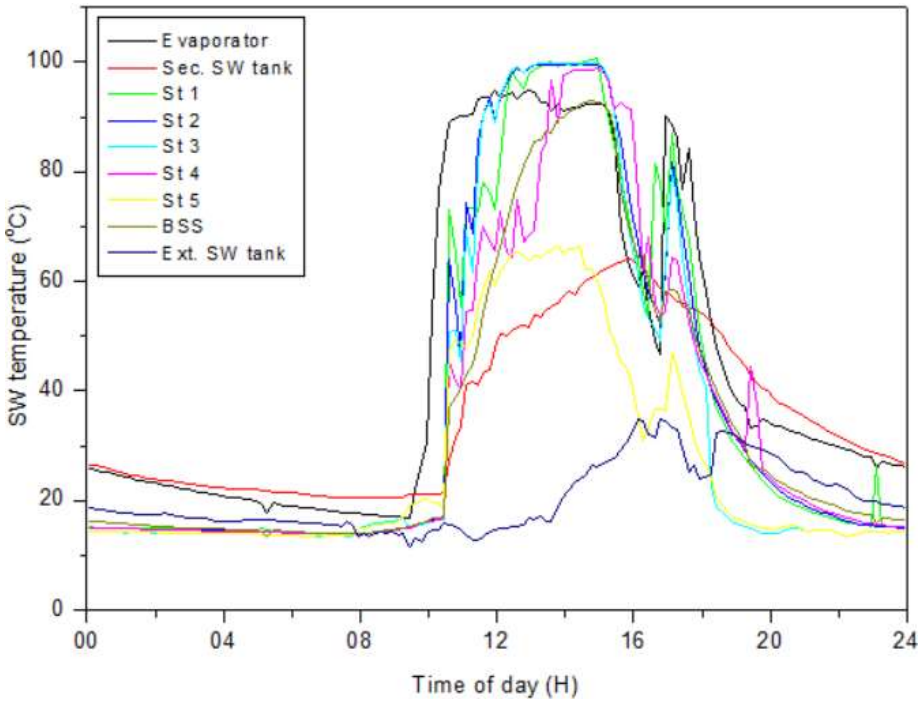

Figure 5.20: SW temperature vs time of day

The evaporator SW temperature reached a maximum of 94.7°C between 10h40 am and 17h50 pm, a 1.7°C increase from the maximum evaporator SW temperature value on the 2nd of June 2021. Meanwhile, stages 1 to 5 reached their maximum SW temperatures of 100.8, 99.6, 99.8, 98.8 and 30.1°C, respectively. The average wind velocity and ambient air temperature were 1.5 m/s and 19.3°C, respectively, as tabulated in Appendix B-1. Therefore, the increased rate of thermal energy input, higher average ambient air temperature and low average wind velocity resulted in the SW temperature behaviours presented in Figure 5.20, necessitating the removal of the thermal insulation material from the condensing tower.

5.3.2.2 Stage wall and stage tray

The evaporative and condensing surfaces temperature curves for the 30th of Sept. 2020 are shown in Figure 5.21. Based on Figures 5.19 and 5.21, stage 1 wall and tray had reached thermal damage while that of stages 2, 3 and 4 were intermittent in their thermal damage status. Stage 2 SW, stage wall and tray maximum temperatures were 93.7, 94.3 and 92.8°C,

respectively. The stage wall and tray both maintained temperatures a few degrees below that of the SW (see Figure 5.21) but sharply declined earlier than the SW temperature later in the afternoon, thereby maintaining a relatively larger temperature difference.

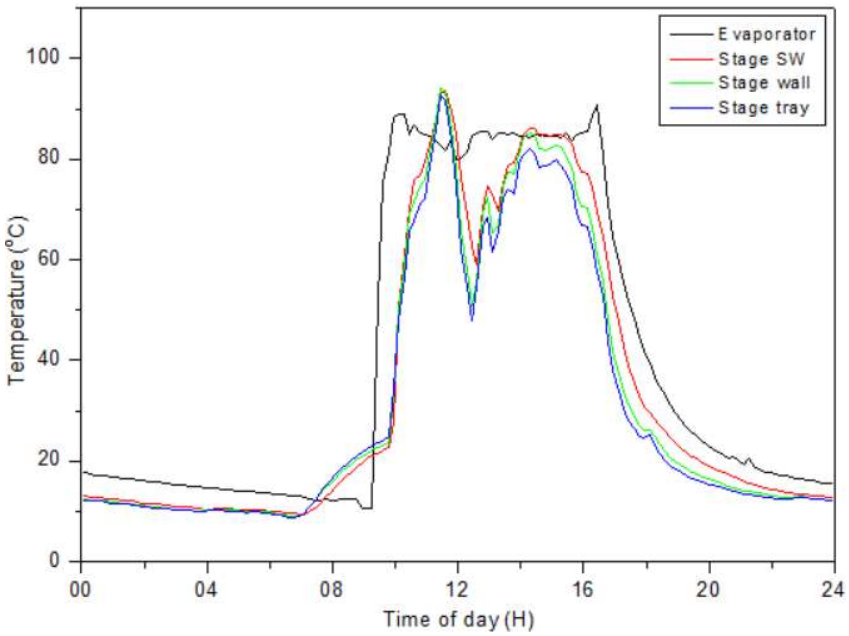

Figure 5.21: Evaporative and condensing surfaces vs time of day

For the 24th of Sept. 2020, the evaporative and condensing surface temperatures are represented by Figure 5.22. According to Figure 5.2, stage 2 remained at thermal damage for most of the day, an indication of ineffective condensation process which reduced or halted it altogether. Even though care was taken to ensure vapour tightness in the adjoining surfaces of the stages, the thermal damage (see Figure 5.22) may show a situation where the uncondensed vapour leaked through the stages. Since the temperature of a fluid is directly proportional to it pressure, an increase in temperature also caused an increase in pressure (Çengel, 2003). Therefore, based on Figures 5.19 and 5.22, stages 1 to 4 may have experienced the vapour leak phenomenon. The maximum temperatures were 99.6, 100.3 and 100.1°C for the stage SW, wall and tray, respectively. Thus, Figure 5.22 constitutes a scenario wherein the desalination process was greatly reduced in the condensing tower except for stage 5.

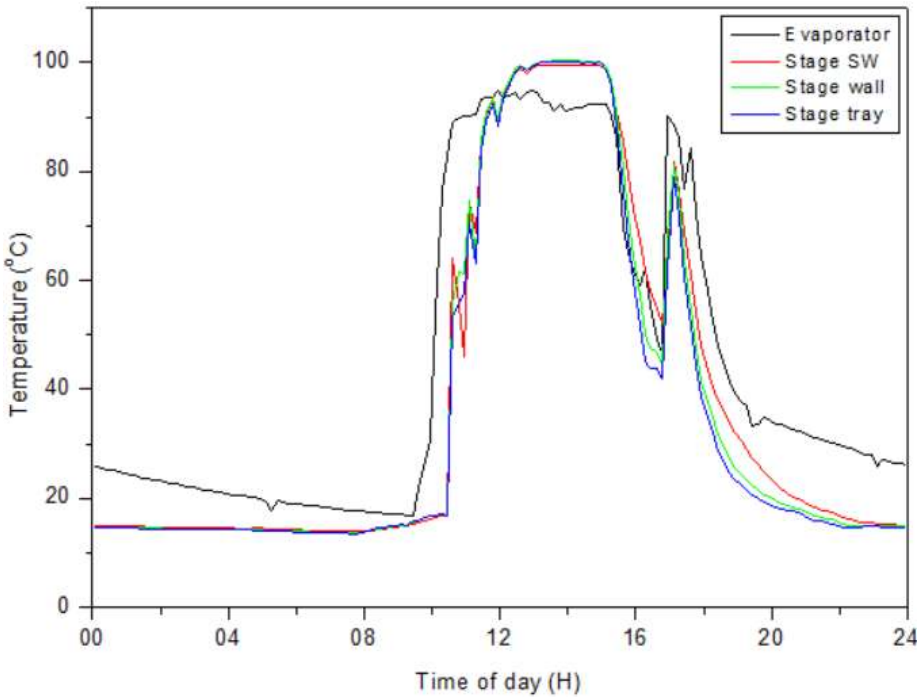

Figure 5.22: Evaporative and condensing surfaces vs time of day

5.3.3 Cumulative distillate yield

To get the full picture, this sub-section will discuss the distillate yield on the 24th and 30th of Sept. 2020. The data is tabulated similarly to sub-section 5.2.3. Table 5.3 shows that increasing the average solar irradiance further to 412.2 W/m^2 enhanced the distillate yield. However, a further increase to 418.9 W/m^2 when the condensing tower was thermal insulated, meant a decrease in distillate yield. For instance, increasing the average solar irradiance by 6.4% from 385.7 to 412.2 W/m^2 increased the distillate yield by 2.3% from 5460 to 5590 ml. However, when the average solar irradiance was increased further by 1.6% from 412.2 to 418.9 W/m^2 while the condensing tower was thermal insulated, the distillate yield dropped by 7.3% from 5590 to 5180 ml. The decrease in the total cumulative distillate yield at 418.9 W/m^2 was a result of the thermal damage condition experienced (see Figure 5.20). The condensing tower operated at thermal damage for longer periods of time on the 24th of Sept. 2020 compared to those in Figure 5.19. However, a question arises in these discussions: if the evaporator produced higher quantities of vapour which caused the system to operate at thermal damage, where does the vapour go? The answer is twofold: firstly as discussed earlier, when the stage cannot condense the vapour, the incoming vapour was re-directed to another stages. The second answer, though, is that the vapour may have been leaking out of the stages undetected.

Table 5.3 shows that the distillate yield trend of the stages changed with changing average solar irradiance. However, it was not just the average solar irradiance that dictated which stage was more productive on a day. It was mainly the solar irradiance curve crests, troughs and overall patterns that dictated the distillate yield in the stages. For instance, even though 197.6 W/m^2 was higher than 179.5 W/m^2, the distillate yield on the 29th of May 2021 showed that more quantities of vapour reached the upper stages than on the 31st of May 2021.

Table 5.3: Distillate yield from the vapour-based MSS-SS

Day	Av. Daily Sol. Irradiance (W/m^2)	Stage distillate yield (ml)						Total (ml)
		St 1	St 2	St 3	St 4	St 5	BSS	
25 Sept. 2020	145.1	NM	NM	NM	NM	NM	NM	-
29 May 2021	179.5	560	100	170	30	250	80	1190
31 May 2021	197.6	250	30	120	20	30	130	580
01 June 2021	209.9	50	150	210	140	470	140	1160
02 June 2021	246.1	160	390	510	60	380	220	1720
26 Sept. 2020	253.7	980	1120	1070	680	900	340	5090
29 Sept. 2020	385.7	1020	1040	1050	590	1280	480	5460
30 Sept. 2020	412.2	880	1120	1180	640	1260	510	5590
24 Sept. 2020	418.9	760	990	1030	570	1470	360	5180

Distillate collecting cylinder was graduated to 10 ml, the rounding off was used when the distillate was in between the graduated marks. NM-not measurable

On any given day, stages 3 and 5 tended to be the most productive stages in the system. This distillate yield pattern was directly linked with the condensing surfaces and the SW in the zigzagged SW tube in the stages. As discussed earlier, in a vapour-based MSS-SS, the stages that maintained lower temperatures for the zigzagged SW tube tended to be more productive. The theory of vapour redirection from the evaporator to those stages with moderate temperatures can be observed in Table 5.3. Despite stage 5 being further away from the evaporator, its cooler condensing surfaces enabled larger temperature difference and thus a higher rate of condensation. Due to the SW temperature and condensing surface temperature curves, the thermal insulation material was removed from the body of the condensing tower for average solar irradiance 400 – 600 W/m^2. Even though removing the thermal insulation material increased heat losses, it was necessary as the condensing tower could not condense the vapour effectively. This ineffective vapour condensation is demonstrated in Figures 5.10, 5.11 and 5.13 as well as 5.19 to 5.20. Any average solar irradiance at or above 400 W/m^2 was considered too high for the thermally insulated condensing tower. Table B-1 and B-3 in Appendix B show the rest of the days experimentally tested.

5.3.4 Summarised results

The condensing tower revealed that the condensing tower partially reached thermal damage at the beginning of the moderate solar irradiance range. The thermal damage condition increased as the average solar irradiance increased. It reached about 80% thermal damage condition in terms of the number of stages when operating under higher solar irradiance range. Furthermore, the thermal condition caused the uppermost stage (stage 5) to remain the most

productive stage in the condensing tower. Due to the failure to effectively condense the vapour in the stages, there was a reduction in the daily cumulative distillate yield of 7.3% between the 24th and 30th of Sept. 2020. The rate of thermal energy produced by the upper solar irradiance values of the moderate range and the lower solar irradiance values of the high range of solar irradiance proved excessive for the condensing tower in its current design. Increasing the average solar irradiance further caused a marginal increase of 1.7°C in the evaporator in terms of its maximum SW temperature on the 24th of Sept. 2020 compared to the 2nd of June 2021. However, there was a further increase in the SW pre-heating as the SW in the secondary tank reached a maximum of 54.1 and 64°C for the 24th and 30th of Sept. 2020. In terms of heat recovery, the condensing tower reaching thermal damage was an indication that the heat recovery had decreased or ceased. The latent of condensation can only be effectively recovered when there is sufficient temperature difference between the hot and cold fluid (Çengel et al., 2008).

5.4 Vapour-based MSS-SS performance under high solar insolation with the condensing tower thermally uninsulated

This section will discuss the performance of the vapour-based MSS-SS condensing tower without any thermal insulation material, focusing particularly on the high daily average solar irradiance ranging from 400 – 600 W/m^2. As demonstrated in sections 5.2 and 5.3, the vapour-based reached thermal damage conditions at moderate to higher solar irradiance. For discussion, four days were selected with average solar irradiance as 482.7, 518.7, 560.3 and 585 W/m^2 on 14 Dec. 2020, 04 Feb. 2021, 11 Nov. 2020 and 13 Jan. 2021, respectively.

5.4.1 Daily solar irradiance

The solar irradiance curves are presented in Figure 5.23 for the 14th of Dec. 2020, 4th of Feb. 2021, 11th of Nov. 2020 and 13th of Jan 2021. On the 14th of Dec. 2020, the average solar irradiance value was 482.7 W/m^2. The first and the last solar incidences were recorded around 05h30 am and 19h50 pm, respectively. The solar irradiance curve demonstrated a combination of the minimal and intense fluctuations relative to all curves in Figure 5.23. Moreover, its maximum crest was recorded at 1271 W/m^2 at 12h40 pm. The duration for the recorded solar irradiance on the day was around 14 hours and 20 minutes.

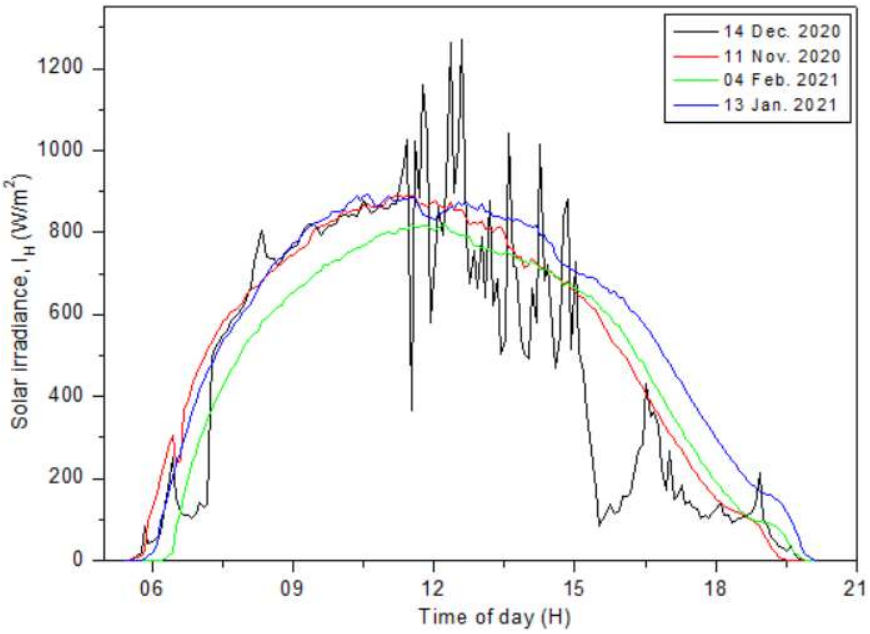

Figure 5.23: Solar irradiance vs time of day

Figure 5.23 shows that the solar irradiance curve on the 4th of Feb. 2021 was lower and had minimal fluctuations throughout the day compared to that of the 14th of Dec. 2020. The first and the last solar incidences were recorded around 06h12 am and 20h00 pm, respectively. Therefore, the duration of recorded solar irradiance on the day was 13 hours and 45 minutes. Moreover, the maximum solar irradiance crest recorded on the 4th of Feb. 2021 was 819 W/m^2 around 11h30 am.

The solar irradiance curve representing the recorded solar irradiance on the 11th of Nov. 2020 is shown in Figure 5.23. The solar irradiance curve on the 11th of Nov. 2020 reveals minimal fluctuations throughout the day, representing positive thermal energy input in the vapour-based MSS-SS. The first and last solar incidences were recorded around 05h30 am and 19h20 pm, respectively. The total duration of the recorded solar irradiance was 13 hours and 50 minutes. The maximum solar irradiance crest recorded on the 11th of Nov. 2020 was 890.5 W/m^2 around 11h30 am.

On the 13th of Jan. 2021, the solar irradiance curve had minimal fluctuations (see Figure 5.23). The first and last solar incidences were recorded around 05h40 am and 20h00 pm, respectively. The total duration for the recorded solar irradiance was 14 hours and 20 minutes. This duration was the longest recording amongst the selected days for discussions. In addition, the maximum solar irradiance was recorded at 892 W/m^2 around 13h30 pm.

5.4.2 Evaporative and condensing surfaces temperature behaviours

5.4.2.1 SW temperature behaviours

The SW temperature behaviours (see Figure 5.24) were driven by the average solar irradiance of 482.7 W/m^2 on the 14th of Dec. 2020. The SW temperature curves in Figure 5.24 show a similar trend of a steady decrease from midnight until 07h50 am. However, the evaporator and the secondary SW tank show that they were much higher at midnight indicating residual heat in the SW from the previous day. The SW temperature curves in Figure 5.24 were a result of the solar irradiance curve in Figure 5.23 with the mixture of intense and minimal fluctuations. Despite a further increase in the average solar irradiance from 418.9 W/m^2 to 482.7 W/m^2, Figure 5.24 shows that the condensing tower never reached thermal damage condition. Stage 1 temporarily reached 87.2°C earlier in the day. Stages 1 to 5 attained their maximum temperatures of 87.2, 77, 73.8, 81.7 and 38.3°C, respectively.

Meanwhile, the evaporator SW temperature reached 92.8°C between 09h50 am and 15h20 pm. The removal of the thermal insulation material also caused the early sharp decrease of the condensing surfaces relative to the evaporative curve. The average wind velocity and the ambient air temperature were 3 m/s and 20.1°C, tabulated in Appendix B-1. With the absence of thermal insulation material, the effect of the condensing tower cooling through convective heat transfer as the wind blew past the condensing tower was increased (Sharshir et al., 2016a).

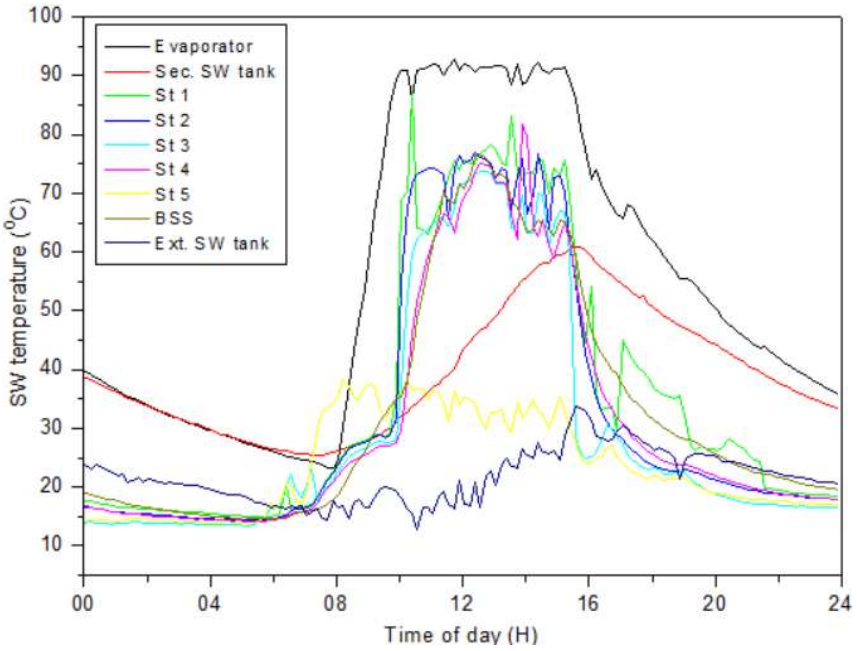

Figure 5.24: SW temperature vs time of day

At an average solar irradiance of 518.7 W/m^2 on the 04th of Feb. 2021, the SW temperature behaved (see Figure 5.25). At midnight, the evaporator and secondary SW tank temperature

remained higher, as shown in Figure 5.25. Furthermore, the SW in the stages showed minimal decline from midnight until 07h40 am. Increased average ambient air temperature may have direct impact on the sustained heat in the SW (Saeedi et al., 2015). Figure 5.23 shows that the solar irradiance curve had minimal fluctuations and thus minimal cooling down periods. Therefore, the mode of thermal energy input was positive and resulted in the SW temperature curves in Figure 5.25. The SW temperature behaviours in Figure 5.25 resembled that of Figures 5.10 and 5.11 in terms of stages 1 and 4 reaching thermal damage. However, unlike Figures 5.10 and 5.11, stages 2 and 3 SW temperatures remained relatively low on the day.

The average wind velocity and ambient air temperature were 4.9 m/s and 23.1°C. These external factors may have played a role in retaining some of the stages at low temperatures. The maximum SW temperature of stages 1 to 5 were 90, 74.8, 65.1, 93.9 and 40.9°C, respectively. The evaporator SW temperature was maximum at 91.3°C between 10h10 am and 18h20 pm. The condensing surfaces started their sharp decrease much earlier than that of the evaporator. This decrease, despite the higher rate of thermal input, may have been due to the higher average wind velocity on the day.

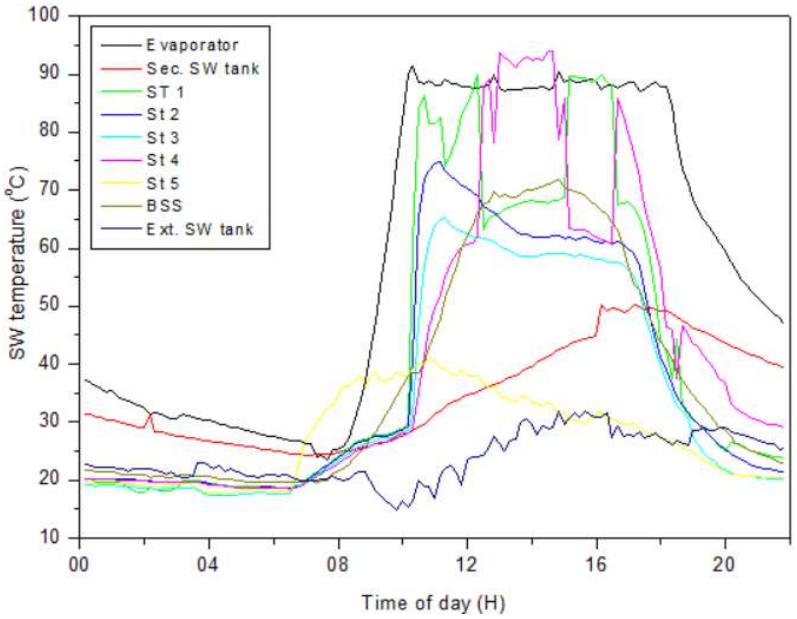

Figure 5.25: SW temperature vs time of day

According to Figure 5.26, the evaporator and the secondary SW temperature remained higher than that of the stages. The decline in temperature occurred from midnight until 05h50 am for stages and 08h00 am for the evaporator. Moreover, the temperature difference between the evaporator and the SW temperature decreased earlier in the day. However, despite the average solar irradiance of 560.3 W/m^2 on the 11 of Nov. 2020, the condensing tower never reached thermal damage condition on the day.

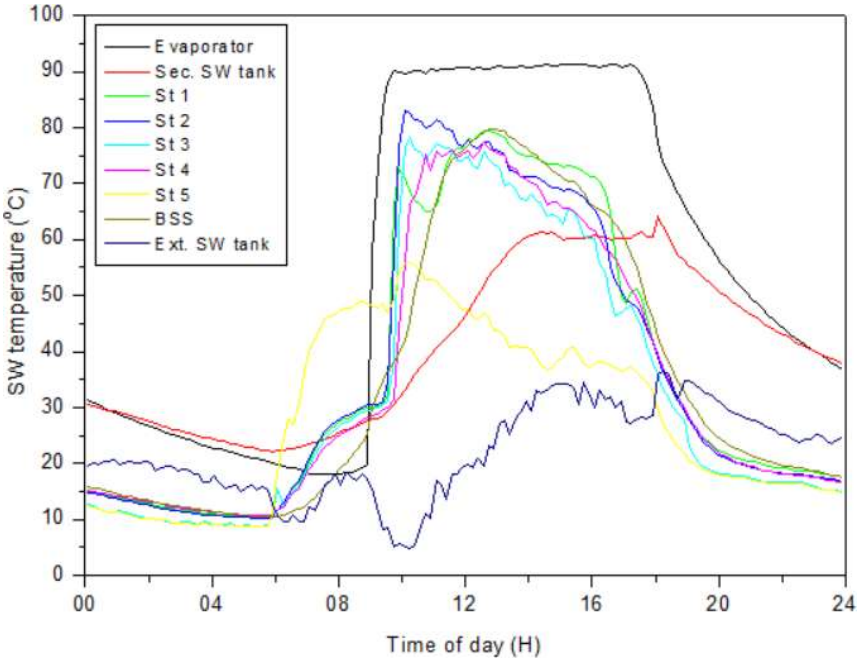

Figure 5.26: SW temperature vs time of day

The average wind velocity had decreased to 2 m/s from 4.9 m/s on the 4th of Feb. 2021. Meanwhile, the average ambient air temperature was 22.4°C compared to 23.1°C on the 4th of Feb. 2021. Figure 5.23 shows minimal solar irradiance fluctuation on the day which translated to a positive mode of thermal energy input. The maximum evaporator SW temperature was 91.2°C between 09h30 am and 17h30 pm. Stages 1 to 5 attained their maximum temperature values of 79.5, 83.1, 78.2, 77.5 and 55.9°C, respectively.

Under the average solar irradiance of 585 W/m^2 on the 13th of Jan. 2021, the SW temperatures behaved (see Figure 5.27). On this day, a steady decrease in SW temperature started at midnight and terminated at 05h00 and 06h20 for the condensing and evaporative surfaces, respectively. Furthermore, despite the removal of the thermal insulation material, stage 1 SW temperature consistently exceeded that of the evaporator throughout the day. The SW in stages 1 to 5 reached a maximum of 110.9, 78.9, 75.4, 80.4 and 55.2°C, respectively. The condensation process in stage 4 was momentarily affected while that of stage 1 continued for longer as they reached thermal damage. The evaporator SW temperature reached its maximum of 90.2°C between 10h00 am and 18h15 pm.

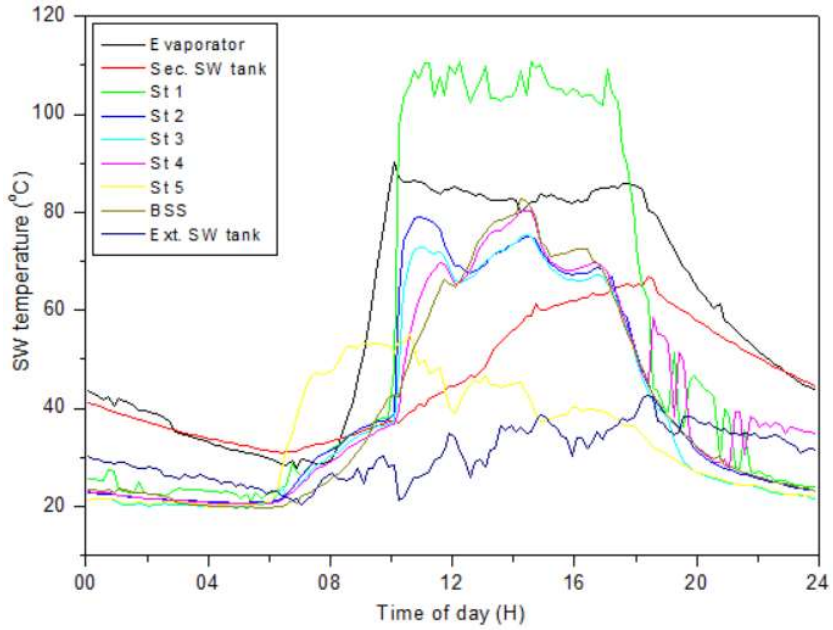

Figure 5.27: SW temperature vs time of day

The average wind velocity and ambient air temperature were 3.1 m/s and 29.3°C, respectively. Given the positive mode of thermal energy input represented in Figure 5.23, there was reduced temperature difference in the condensing tower. Moreover, except for stage 1 SW, the rest of the stage's SW temperatures show an early sharp decline in the day, suggesting increased heat losses caused by the external elements.

5.4.2.2 Stage wall and stage tray

The condensing surfaces temperature behaviours are presented in Figure 5.28 for the 14th of Dec. 2020. According to Figures 5.24 and 5.28, the average wind velocity of 3 m/s in conjunction with the removal of the thermal insulation material prevented thermal damage condition. The stage SW, wall and tray temperatures were maximum at 77, 72 and 75.1°C, respectively. Despite an increase in the average solar irradiance, the condensing tower never reached thermal damage.

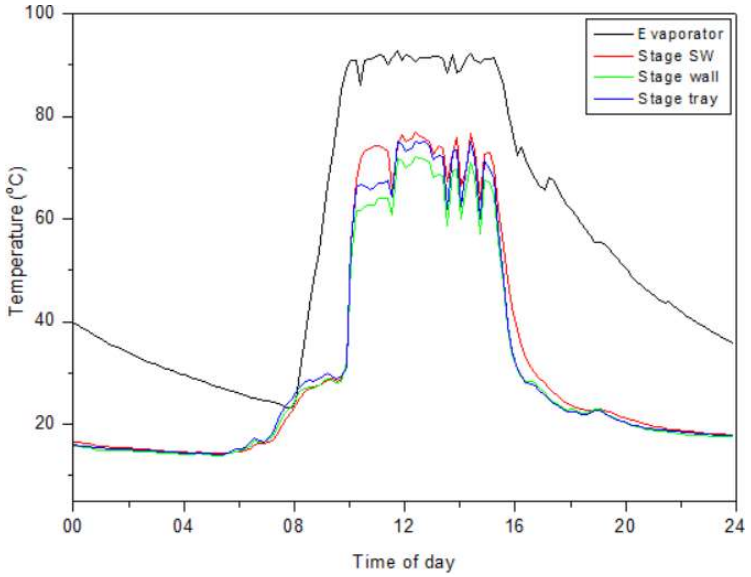

Figure 5.28: Evaporative and condensing surfaces vs time of day

A further increase in an average solar irradiance caused stage 1 and 4 to reach thermal damage (see Figure 5.25) on the 4th of Feb. 2021. However, as shown by Figure 5.29, stages 2, 3 and 5 maintained a larger temperature difference. Therefore, the condensation process was only affected in stages 1 and 2. The maximum of 74.8, 63.5 and 70.7°C were attained by stage SW, wall and tray, respectively. This larger temperature difference was a direct result of thermal insulation material removal and the average wind velocity at 4.9 m/s. According to Figure 5.29, there was an increased temperature difference between the stage SW, wall and tray, indicating increased heat losses as well as sufficient cooling of the condensing surfaces as heat generally flows from a high temperature region to a low temperature region (Çengel, 2003).

Figure 5.29 also gives evidence that the external elements had more influence on the condensing tower absent of thermal insulation material, despite an increase in average solar irradiance to 518.7 W/m^2 with a positive mode of thermal energy input as depicted in Figure 5.23.

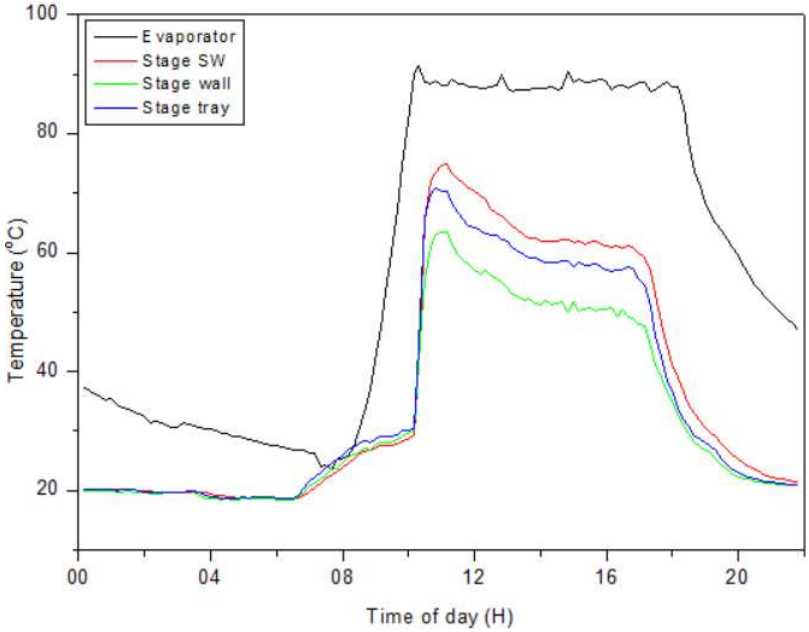

Figure 5.29: Evaporative and condensing surfaces vs time of day

At an average solar irradiance of 560.3 W/m^2 on the 11th of Nov. 2020, the condensing surfaces behaved as shown in Figures 5.26 and 5.30. The stage SW, wall and tray maximum temperatures were 83.1, 78.8 and 83.1°C, respectively. A decrease in average wind velocity to 2 m/s from 4.9 m/s caused a reduction in temperature difference between stage SW, wall and tray. However, on this day, none of the stages reached thermal damage condition despite a positive mode of thermal energy input, depicted in Figure 5.23.

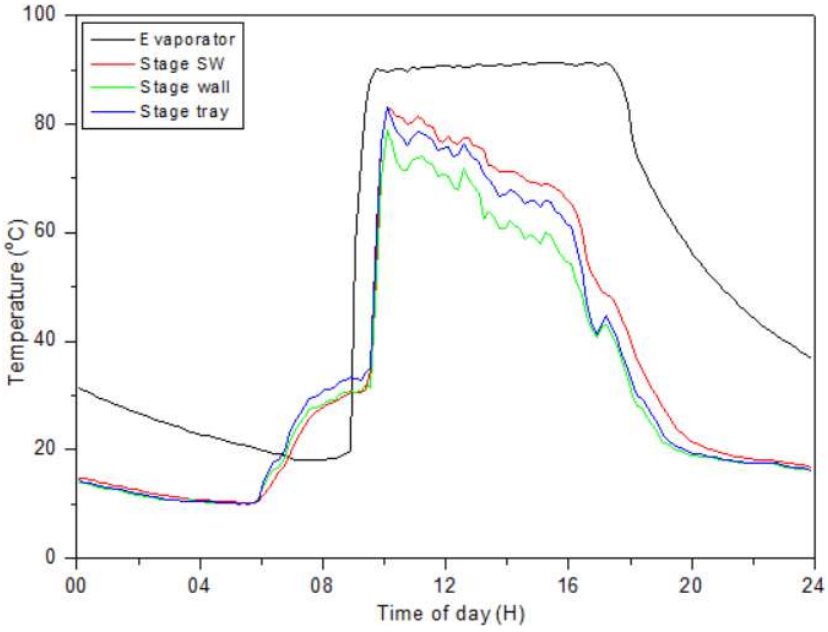

Figure 5.30: Evaporative and condensing surfaces vs time of day

The evaporative and condensing surfaces on the 13th of Jan. 2021 are represented by Figures 5.27 and 5.31 where the average solar irradiance was 585 W/m^2. The maximum stage SW, wall and tray temperatures were 78.9, 72.2 and 77.2°C, respectively. According to Figures 5.30 and 5.31, there was a reduction in temperature difference between the evaporative and condensing surfaces on the 13th of Jan 2021. The condensing tower was being cooled by an average wind velocity of 3.1 m/s. However, this average wind velocity was evidently insufficient to maintain cooler temperatures in stage 1, as shown in Figure 5.27.

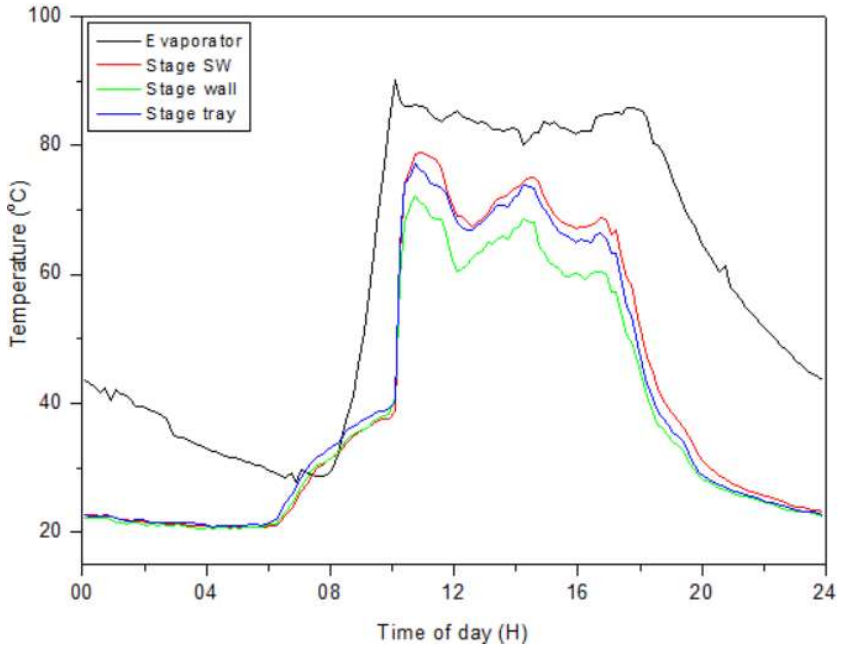

Figure 5.31: Evaporative and condensing surfaces vs time of day

5.4.3 Daily cumulative distillate yield

This current sub-section discusses the distillate yield from the high average solar range of 400 to 600 W/m^2. Under the high solar irradiance range, the condensing tower was thermally uninsulated. It then compares the distillate yield from the low, moderate and higher insolation ranges. Table 5.4, showing the distillate yield from the vapour-based MSS-SS on various days, reveals that the total cumulative continued to increase with the increase in average solar irradiance, which maximised at 7790 ml (approx. 7.8 litres). This increase in distillate yield, however, was at the expense of increased heat losses to the surroundings. When the average solar irradiance was increased by 13.2% from 418.9 to 482.7 W/m^2, the distillate yield increased by 23.03% from 5180 to 6730 ml. A further increase by 6.94% from 482.7 to 518.7 W/m^2 resulted in a marginal increase of 0.6% from 6730 to 6770 ml. This marginal increase might have been due to the thermal damage condition in stages 1 and 4, as shown in Figure 5.25, which may have caused vapour leaks into the surroundings. An increase by 7.4% from

518.7 to 560.3 W/m^2 caused the cumulative distillate yield to increase by 7.5% from 6770 to 7320 ml. From 560.3 to 585 W/m^2, there was an increase of 4.2%, and in turn an increase of 6.03% from 7320 to 7790 ml.

Table 5.4: Distillate yield from the vapour-based MSS-SS

Condensing tower	Solar insolation	Date	Av. Daily Sol. Irradiance (W/m^2)	Stage distillate yield (ml)						Total (ml)
				St 1	St 2	St 3	St 4	St 5	BSS	
insulated	Low	25 Sept. 2020	145.1	NM	NM	NM	NM	NM	NM	-
		29 May 2021	179.5	560	100	170	30	250	80	1190
		31 May 2021	197.6	250	30	120	20	30	130	580
	Moderate	01 June 2021	209.9	50	150	210	140	470	140	1160
		02 June 2021	246.1	160	390	510	60	380	220	1720
		26 Sept. 2020	253.7	980	1120	1070	680	900	340	5090
		29 Sept. 2020	385.7	1020	1040	1050	590	1280	480	5460
	High	30 Sept. 2020	412.2	880	1120	1180	640	1260	510	5590
		24 Sept. 2020	418.9	760	990	1030	570	1470	360	5180
Uninsulated		14 Dec. 2020	482.7	920	1310	1290	850	1480	880	6730
		04 Feb. 2021	518.7	840	1320	1380	920	1730	580	6770
		11 Nov. 2020	560.3	860	1310	1460	980	1780	930	7320
		13 Jan. 2021	585	760	1550	1630	910	1880	1060	7790

Distillate collecting cylinder was graduated to 10 ml, the rounding off was used when the distillate was in between the graduated marks. NM-not measurable

Table 5.4 shows that with an overall increase in the average solar irradiance by 225.91% from 179.5 to 585 W/m^2 the cumulative distillate yield increased by 554.62% from 1190 to 7790ml. In addition, removing the thermal insulation allowed for an increased temperature difference at high solar irradiance compared to when it was thermally insulated. With reference to Table 5.4, the cumulative distillate yield on the 24th of Sept. 2020 had decreased to 5180 ml due to the thermal damage condition in the system. However, from the 14th of Dec. 2020 to the 13th of Jan. 2021, according to Table 5.4, the distillate yields consistently increased, even while, due to the thermal damage condition and other related technical challenges, some stages produced more distillate than others. Additional data on the cumulative distillate yield can be found in Appendix B-1.

The desalination was dependent on the evaporation rate from the evaporator and its SW temperature. Under high solar irradiance range, the evaporator SW temperature remained as high as 43.5°C by midnight at the end of the day, an indication that the desalination process in the condensing tower continued for longer under an increased rate of thermal energy input and ambient air conditions (see Figures 5.24 to 5.27). Furthermore, as demonstrated by Figure

5.32, the higher the average SW temperature, the higher vapour production. Higher vapour production translated to higher distillate output. However, this higher vapour output was at the expense of increased heat losses as the thermal insulation material was removed. Moreover, the temperature curve on the 26th of Sept. 2020 demonstrated the most appropriate conditions for the vapour-based MSS-SS to operate under.

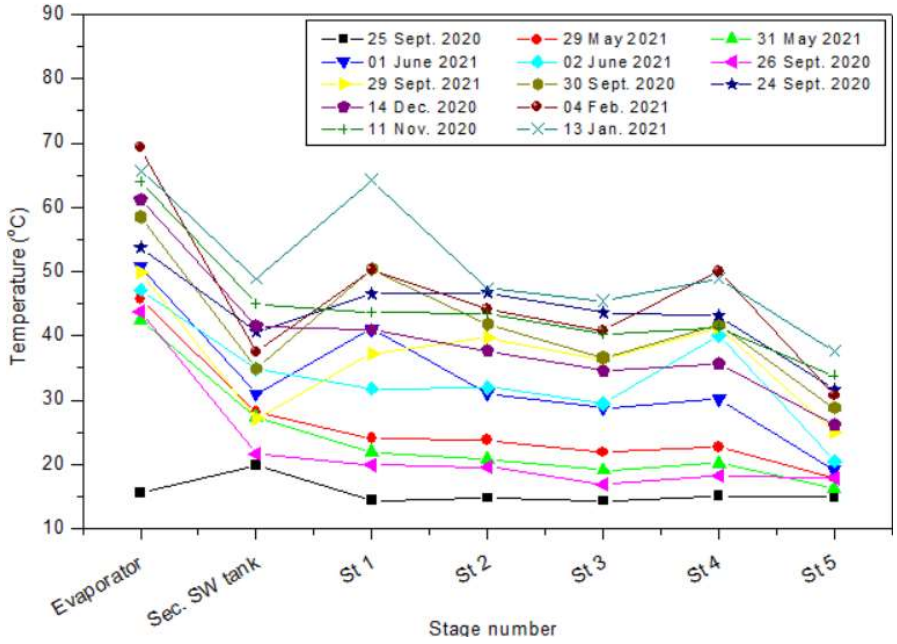

Figure 5.32: Average SW temperature vs stage number

5.4.4 Summarised results

Figure 5.32 shows that despite increasing the overall average solar irradiance by 69.3%, the SW pre-heating in the secondary tank increased by 59.6% from 19.8 to 49°C, on average, on the 25th of Sept. 2020 to the 13th of Jan. 2021. This was as a result of increased heat losses from the condensing tower. The maximum SW temperatures, representing SW pre-heating in the secondary SW tank, were 61, 50.1, 64.3 and 66.8°C for the 14th of Dec. 2020, 4th of Feb. 2021, 11th of Nov. 2020, and 13th of Jan. 2021, respectively. Moreover, heat recovery was unquantifiable under the uninsulated condensing tower due to increased heat losses to the surroundings. The removal of the thermal insulation material was an indication that the vapour-based current design lacked a insufficient cooling medium to recover heat with the thermal insulation. Furthermore, the steady decrease in SW temperature under higher solar irradiance range suggested that the desalination process in the condensing tower continued for longer. The SW temperature could reach as high as 43.5°C around midnight.

The evaporator SW temperature maintained an elevated SW temperature around 90°C for longer periods of time (i.e., 10h00 am and 18h15 pm) on the 13th of Jan. 2021, prolonging

vapour production on this day compared to those under low and moderate ranges. Further, it has been demonstrated that the stage wall and tray tend to follow the same path as that of the stage SW. Under uninsulated conditions and depending on the external elements, the stage wall temperature remained lower, indicating effective cooling from the outside relative to the stage SW and tray.

The discussions have revealed limits to the operation of the vapour-based MSS-SS. These limits can be described as minimum and maximum operating conditions. The conditions on the 25th of Sept. 2020 represented the minimum operational limit while the maximum was dependent on various factors (i.e., mode of thermal energy input, wind velocity, the crests and troughs of the solar irradiance curves). Further discussions on these limits will be covered later in the chapter.

5.5 **Effect of minimal saline water in the evaporator**

In the existing solar stills, the SW temperatures increased and reached their maximum values around mid-day or later in the day, a result of factors such as the larger body of SW in the solar still and the nature of the solar irradiance progression from the morning (Gnanaraj et al., 2017; Shatat & Mahkamov, 2010). Larger bodies of SW have a greater capability to store thermal energy compared to small bodies of water (Morad et al., 2015). Comparing a larger and smaller body of water, the smaller body of water tends to be heated much faster when an equal rate of thermal energy is applied. It then maintains elevated temperatures for longer compared to the larger body as long as the rate of thermal energy supply is consistent. Therefore, a solar still with minimal SW in its basin maintains elevated temperatures which increase the vapour production (Velmurugan, 2015; Kabeel & EL-Agouz, 2011). The solar stills that maintain and operate at elevated SW temperatures above 70°C are classified as 'high temperature solar stills' (Sampathkumar et al., 2010).

Based on the above, the SW was directly heated the by ETCs manifold. Approximately 0.5 litres (0.5 kg) of SW was heated at a time and impulsively circulated, as described in sub-section 3.15.3. Each time the SW was heated and impulsively circulated, it ended up in the evaporator where the liquid probe thermocouple was installed to probe the SW temperature. Therefore, the effects of minimal SW in the system were as follows.

5.5.1 Sensitive to the fluctuating solar radiation

As observed under sections 5.1 to 5.4, due to the low thermal energy storage capacity of the minimal SW in the ETSC, it closely fluctuated according to the solar irradiance. Since the evaporator was the supplier of the vapour to the stages, the entire system became operationally sensitive to the fluctuating solar radiation. This phenomenon can be observed especially in Figures 5.4 and 5.12. Moreover, the operational sensitivity is demonstrated in Figure 5.33. It can be observed that the evaporator SW temperature curve tended to rise and fall as the solar irradiance reached its crests and troughs, respectively. Furthermore, later in the day, the fluctuations of the solar irradiance curves were reduced and assumed the positive mode of thermal energy input, as was the evaporator SW temperature curve.

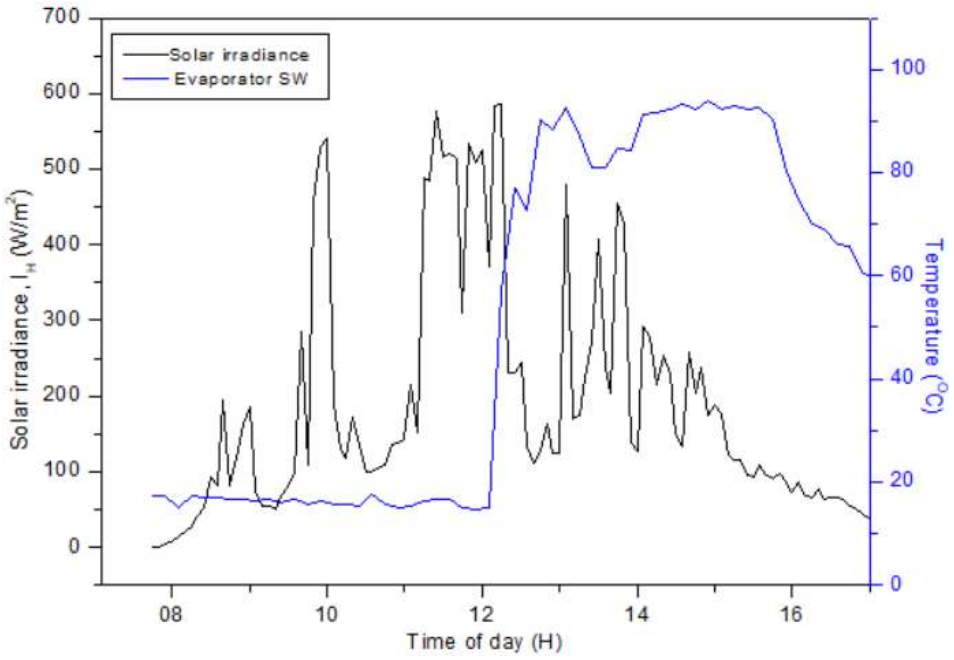

Figure 5.33: Operational sensitivity vs time of day

Based on these solar irradiance fluctuations, it is believed that the rate of vapour supply to the stages also fluctuates according to the evaporator SW temperature curve. That is, the supply of vapour was intermittent and according to the evaporator SW temperature curve. Fluctuating condensing surfaces are discussed under sections 5.1 to 5.4. Moreover, according to Figure 5.33, there was a slight delay between the solar irradiance curve rise or fall and the evaporator SW temperature. This delay may represent the time required for the heat to be transferred between the ETSCs and the impulsively circulating SW in an open loop circuit.

However, it can be observed (see, for instance, Figures 5.13 and 5.17) for the 29th of Sept. 2020 that as the rate of thermal energy input increased, the operational sensitivity diminished. The evaporative and condensing surfaces maintained non-fluctuating behaviours even though

the solar irradiance was fluctuating heavily (see Figure 5.9). Similar behaviour can be observed on the 24th of Sept. 2020 and 14th of Dec. 2020 as well. This diminishing behaviour was a direct result of the limited thermal energy storage of the impulsively circulating SW in an open loop. However, at low range of the average solar irradiance, the solar irradiance fluctuations were detrimental to the amount of vapour reaching the stages due to the premature condensation in the vapour make-up tubes.

5.5.2 SW temperature rapid increase

In the entry stage of the existing MSS-SS with waterbed, the SW temperature increased according to the solar irradiance patterns. Moreover, the SW temperature in the entry stages tended to increase gradually and maximised as the solar irradiance maximised somewhere at midday or later in the afternoon. The gradual increase in the SW was caused by the larger body of SW in the entry stage as well as the solar irradiance progression throughout the day. The quantity of the SW in the entry stage ranged from 12 to 20 kg (Schwarzer et al., 2009; Singh et al., 2012; Estahbanati et al., 2014; Chen et al., 2017; El-Bahi & Inan, 1999; Kaushal et al., 2016). According to the literature reviewed, the existing MSS-SS systems reached their SW temperature peaks in the entry stage once around mid-day and then began to decline, as reported by Estahbanati et al. (2014) and Chen et al. (2017). Figure 5.34 shows the evaporator SW temperature behaviours in the vapour-based MSS-SS.

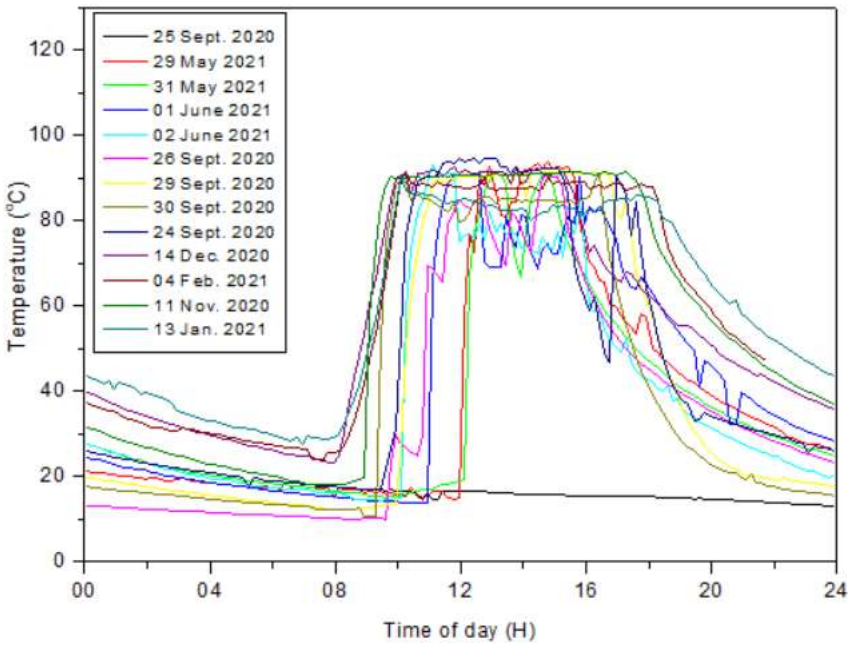

Figure 5.34: Evaporator SW sharp increase vs time of day

The vapour-based MSS-SS had as little as 0.5 kg of SW heated at a time which was impulsively circulated in the ETSCs. Figure 5.34 shows that the SW temperature increased sharply through the year from the spring of 2020 to winter of 2021.

The vapour-based MSS-SS did not experience the steady SW temperature increase which maximised late in the day at the same time that the solar irradiance was at maximum. Therefore, the vapour-based MSS-SS maintained a higher SW temperature around 90°C soon after its sharp increase in the morning. The higher SW temperatures were maintained throughout the day and according to the prevailing solar irradiance of the day. The maintained higher SW temperatures in the vapour-based MSS-SS caused enhanced vapour production in the evaporator for longer periods of time, especially in summer. This increased vapour production caused increased distillate production in the condensing tower (Franco & Saravia, 1994). The only challenge with the vapour-based MSS-SS was the thermal damage condition which represented the maximum operational limitations of the system.

According to Figure 5.34, under higher range of solar irradiance, the evaporator SW temperature started its sharp increase much earlier in the morning. Furthermore, under the high range of solar irradiance, the decrease in the evaporator temperature later in the day occurred much later. The decrease in evaporator SW temperature assumed an almost steady decline rather than a sharp decline, an indication that the evaporator SW temperature maintained higher temperatures throughout the day and into the evening. Therefore, the vapour production and the desalination process lasted longer and continued well into the night as the evaporator SW temperature was at 43.5°C on the 13th of Jan. 2021.

Under low to moderate solar irradiance range, the evaporator SW sharp increase occurred as late as 12h00 noon. The decrease in the evaporator SW temperature occurred much earlier in the day and assumed a sharp decline. Therefore, time was limited for vapour production on such days. Moreover, upon decreasing later in the day, the evaporator SW temperature attained temperatures of as low as 13.1°C by midnight, an indication that desalination ceased soon after sunset due to insufficient thermal energy reaching the stages as a result of premature vapour condensation in the vapour make-up tubes.

5.6 Pre-heating and heat recovery process in the vapour-based MSS-SS

The process of SW pre-heating and heat recovery was an integral part of the vapour-based MSS-SS operations. The extent of SW pre-heating and heat recovery was displayed in Figure 5.32, on average. By definition, SW pre-heating referred to the extent to which the SW increased its temperature while flowing from the external SW tank, through the stages and into the secondary SW tank. Two mechanisms were responsible for pre-heating the SW, the first was the direct heating by the sun's rays in the BSS. The second mechanism was through

heat exchange between the vapour releasing its latent heat of condensation and the SW in the stages absorbing it. Since there were five stacked stages in the condensing tower, theoretically the SW was supposed to increase its temperature six times in total, including that of the BSS before reaching the secondary SW tank.

Heat recovery referred to the ability of the cooling medium (SW inside the condensing tower) to recover thermal energy from the vapour by completely condensing it. When the SW recovered the thermal energy from the vapour, it would also increase its temperature, thereby pre-heating. Theoretically, the heat recovery would occur five times inside the condensing tower before the SW reached the secondary SW tank. Therefore, the extent of SW pre-heating and heat recovery were reflected in the secondary SW temperature values on a day. However, as discussed in sections 5.1 to 5.4, The SW pre-heating process was so effective on other days that the SW in the stages reached or exceeded the evaporator and caused thermal damage. Meanwhile, the heat recovery ability of the SW diminished as the SW in the stages increased in temperature. That is, when there was a larger temperature difference between the vapour and the SW, heat recovery was effective. However, when there was a reduced SW temperature difference due to SW temperature increase, the heat recovery was ineffective, and the condensing tower reached thermal damage.

Table 5.5 shows the average temperature data for the pre-heated SW in the condensing tower. Column 11, in particular, shows the temperature difference between the external SW tank and the secondary SW tank. As mentioned earlier, the SW was being pre-heated as it flowed through the condensing tower. Columns 5 to 9 show the pre-heating and heat recovery in stages 1-5 of the condensing tower. For instance, on the 24th of Sept. 2020, the heat recovery and SW pre-heating resulted in a 19°C SW temperature increase as it flowed through the condensing tower on average; that is, the difference between the SW in the external SW tank before it entered the condensing tower at 21.6°C and the final pre-heated SW in the secondary SW tank at 40.6°C. Under an ideal situation, the sum of SW temperature increments in the BSS and stages 1-5 are equal to the cumulative SW temperature increase in the secondary SW tank. In fact, in an ideal situation, the SW temperature in the secondary SW tank should be equal to or slightly below that of the evaporator shown in column 12. That is, the vapour entered the stage with the same temperature as that of the evaporator. Therefore, if all that heat was absorbed by the SW in the stages, plus the effect of pre-heating from the BSS, then the SW reaching the secondary SW should be close to that of the evaporator. However, due to heat losses and the vapour flow patterns to the stages, some stages' SW tended to decrease in temperature. As observed from Table 5.5, the SW temperature did not increase with each stage as it flowed through it.

For instance, on the 24th of Sept. 2020, the BSS was at 41.6°C in column 4. However, stage 5 SW temperature in column 5 was at 31.7°C. Moreover, stage 4 SW temperature in column 6 was recorded at 43.1°C. There was an increase in SW temperature in stage 3, represented by column 7 to 43.6°C. A further increase in stage 2 in column 8 to 46.7°C but a slight decline in stage 1 in column 9 to 46.6°C.

Table 5.5: Average SW temperature in the condensing tower for various days

1	2	3	4	5	6	7	8	9	10	11	12
	Date	**Ext. SW tank (°C)**	**BSS (°C)**	**St 5 (°C)**	**St 4 (°C)**	**St 3 (°C)**	**St 2 (°C)**	**St 1 (°C)**	**Sec. SW tank (°C)**	**ΔT (°C)**	**Evap. Temp. (°C)**
insulated	25 Sept. 2020	15.4	15.8	14.9	15.1	14.3	14.8	14.4	19.8	**4.4**	15.6
	29 May 2021	18.1	24.2	17.8	22.7	21.9	23.8	24.0	28.1	**10**	45.7
	31 May 2021	16.4	22.1	16.3	20.2	19.1	20.8	21.9	27.4	**11**	42.5
	01 June 2021	17.3	26.9	19.1	30.2	28.8	31.1	41.1	31.0	**13.7**	50.8
	02 June 2021	15.9	22.6	20.5	40.0	29.5	32.0	31.8	34.9	**19**	47.2
	26 Sept. 2020	13.9	21.1	17.9	18.2	16.9	19.6	19.9	21.6	**7.7**	43.7
	29 Sept. 2020	16.7	36.1	25.0	41.4	36.3	39.7	37.2	27.1	**10.4**	49.9
	30 Sept. 2020	17.9	33.7	28.8	41.7	36.6	41.8	50.4	34.9	**17**	58.5
	24 Sept. 2020	21.6	41.6	31.7	43.1	43.6	46.7	46.6	40.6	**19**	53.7
	14 Dec. 2020	22.1	37.7	26.2	35.6	34.6	37.7	41.0	41.5	**19.4**	61.3
	04 Feb. 2021	24.9	44.2	30.7	50.1	40.8	44.1	50.2	37.5	**12.6**	69.3
	11 Nov. 2020	23.2	42.0	33.8	41.3	40.3	43.4	43.6	45.0	**21.8**	64
	13 Jan. 2021	31.7	45.9	37.5	48.8	45.4	47.4	64.2	49.0	**17.3**	65.7

It should be noted that the SW in the stages was pre-heated by vapour from the evaporator as well as the already pre-heated SW from the stages above. However, on a day such as the 25th of Sept. 2020, there was minimal SW pre-heating and heat recovery (see Figure 5.2). The increased SW in the secondary SW tank was due to the thermal energy stored in the secondary tank already. Due to the cooling periods on the 26th of Sept. 2020, represented by Figure 5.12, the SW pre-heating effects was minimal as the secondary SW was only pre-heated by 7.7°C.

When the thermal insulation material was removed, the pre-heating process revealed only marginal improvements due to the enhanced heat losses through the stage walls of the condensing tower. The highest increase was 21.8°C on the 11th of Nov. 2020 when the system was uninsulated. With thermal insulation, the highest SW pre-heating occurred while the system operated at thermal damage. With regards to recovering the latent heat of condensation, the process was effective. However, due to the small quantity of cooling SW in the stages, the effectiveness of the heat recovery process was diminished as the system approached thermal damage condition. Thus, removal of the thermal insulation material prevented thermal damage condition but adversely affected the heat recovery process.

5.7 Distillate yield trend on the stages of the vapour-based MSS-SS

In the MSS-SS with waterbed, the lower stage of the condensing tower tended to yield higher distillate compared to the upper stages (Adhikari et al., 1995; Jubran et al., 2000; Schwarzer et al., 2009; Shatat & Mahkamov, 2010; Ahmed et al., 2009). However, it has been experimentally established that the vapour-based MSS-SS showed a different trend all together. At this point of the vapour-based MSS-SS development, while the trend is not fully known, the vapour redirection from the evaporator to those stages with moderate condensing surface temperatures remain a likely cause for the trends observed.

5.7.1 Distillate yield trends due to low average solar irradiance

Table 5.6 shows the distillate yield data due to low solar irradiance, as defined in section 5.1. The distillate yield from each individual stage varied based on the prevailing solar irradiance of the day. The distillate yield per stage for the entire period covering the duration of the experimental tests is tabulated in Appendix B-3.

Table 5.6: Distillate yield per stage of the MSS-SS

Condensing tower	Date	Av. Daily Sol. Irradiance (W/m^2)	Stage distillate yield (ml)						Total (ml)	Most productive stage
			St 1	St 2	St 3	St 4	St 5	BSS		
insulated	17 June 2021	122.7	NM	NM	NM	NM	NM	NM	NM	N/A
	06 Nov. 2020	125.6	NM	NM	NM	NM	NM	NM	NM	N/A
	16 June 2021	139.1	NM	NM	NM	NM	NM	NM	NM	N/A
	25 Sept. 2020	145.1	NM	NM	NM	NM	NM	NM	NM	N/A
	31 Mar. 2021	155.5	80	50	30	10	50	150	370	St 1
	27 May 2021	164.4	20	40	80	0	150	140	430	St 5
	13 June 2021	173.6	200	80	190	20	230	130	850	St 5
	09 June 2021	176.1	240	330	330	180	190	110	1380	St 2/St 3
	28 May 2021	179.2	70	50	40	0	50	100	310	St 1
	29 May 2021	179.5	560	100	170	30	250	80	1190	St 1
	21 May 2021	187.4	280	230	190	130	90	140	1060	St 1
	24 May 2021	195.0	110	30	50	0	50	120	360	St 1
	31 May 2021	197.6	250	30	120	20	30	130	580	St 1

Figure 5.35 graphically represents the distillate yield data in Table 5.6. At low average solar irradiance, the distillate yield trend suggests that stages 1, 3 and 5 were the most productive stages in the condensing tower. According to Table 5.6 and Figure 5.35, stage 1 was the most productive stage on all the days except on the 27th of May 2021, 9th of June and 13th of June 2021. The enhanced productivity of stage 1 in the condensing tower suggested that the thermal energy input was at its minimal since stage 1 was the lowest stage in the condensing

tower. Stages 3 and 5 took turns in the number 2 spot after stage 1 in terms of the most productive stage in the condensing tower. Stage 5 was the most productive stage only twice: on the 27th of May 2021 and 13th of June 2021. Stage 3 never took first spot but was second to stages 1 or 5 depending on the day in terms of its productivity. The productivity of stage 2 was similar to that of stage 3. It was either equal or just below the productivity of stage 3. Stage 4, however, always remained the least productive stage in the condensing tower. Based on Table 5.6 and Figure 5.35, the vapour-based distillate yield trend at low solar insolation was such that stages 1, 5 and 3 were the most productive stages in their respective order.

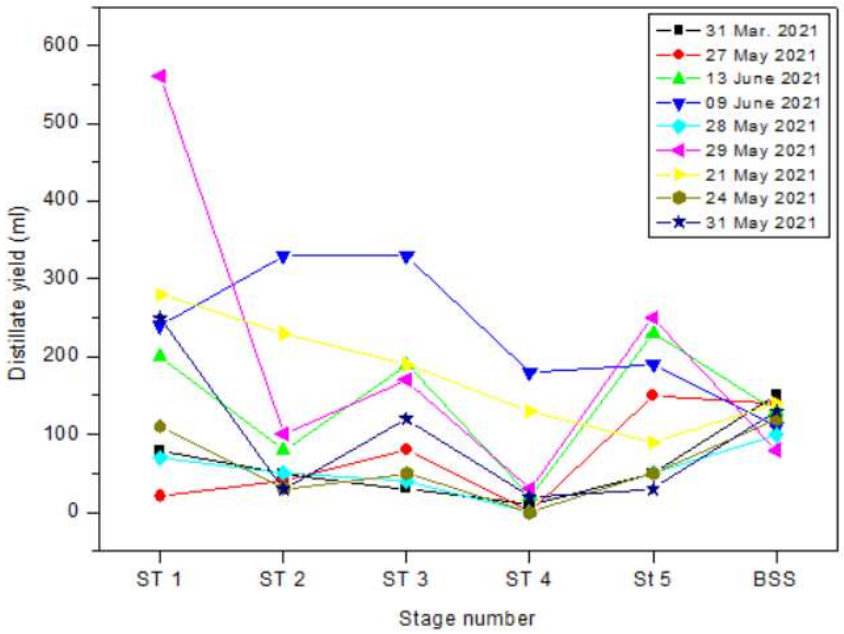

Figure 5.35: Distillate yield vs stage number

The daily cumulative distillate yield trends are shown in Figure 5.36 for the low average solar irradiance. Figure 5.36 shows the cumulative distillate yield of both the MSS-SS stages and that of the MSS-SS stage combined with that of the BSS. The cumulative distillate yield pattern was not proportional to the increasing average solar irradiance. The cumulative distillate yield was primarily influenced by the solar irradiance curve progression throughout the day. That is, the higher the solar irradiance curve crests, the higher the rate of thermal energy input into the condensing tower. The effects of the average solar irradiance on the distillate yield can be observed from Table 5.4 for the 2nd of June 2021 and 26th of Sept. 2020.

The lesser the solar irradiance fluctuations, especially under low average solar irradiance, the higher the rate of thermal energy input. The solar irradiance curve with minimal fluctuations also translated to a positive mode of thermal energy input. Therefore, Figure 5.36 shows that even though the average solar irradiance on the 9th of June 2021 was only 176.1 W/m^2, the distillate yield on that day was the highest at 1380 ml (see Table 5.6). Days such as the 31st

of March 2021, 28th of May 2021 and 24th of May 2021 had average solar irradiance values of 155.5, 179.2 and 195.0 W/m^2.

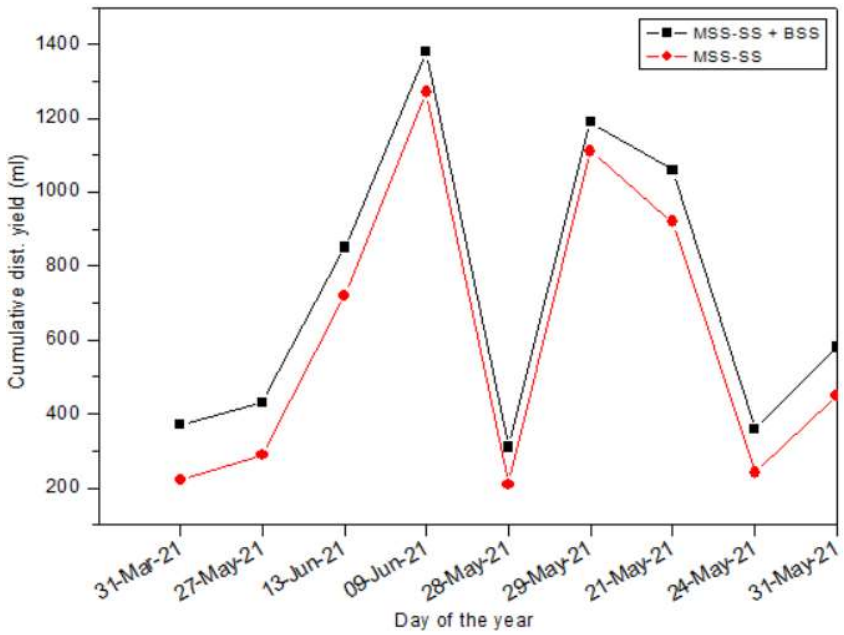

Figure 5.36: Cumulative distillate yield vs day of the year

These three days had the lowest cumulative distillate yields, as shown in Table 5.6. The solar irradiance on these days fluctuated intensely which allowed for cooling down periods in the condensing tower.

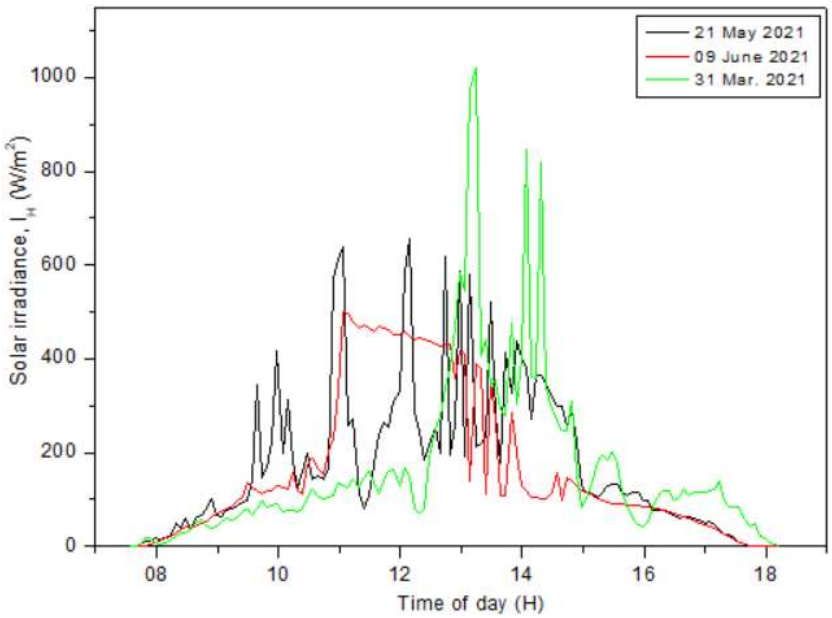

Figure 5.37: Solar irradiance vs day of the year

The solar irradiance troughs on the 21st of May 2021 and the 31st of March 2021 were much lower than the 9th of June 2021. Therefore, cooling down periods were increased on the 31st of March 2021 and 21st of May 2021. Meanwhile, the solar irradiance curve on the 9th of June 2021 shows lesser fluctuations and thus positive thermal energy input. Based on these three dates, the effect of cooling down periods can be observed on the productivity of the solar still. These cooling down periods were evidently detrimental to the productivity of the vapour-based MSS-SS.

5.7.2 Distillate yield trends due to moderate average solar irradiance

Table 5.7 shows the distillate yield data under moderate solar irradiance. The tabulated data in Table 5.7 was used to generate the graphical representation in Figures 5.38 and 5.39.

Table 5.7: Distillate yield per stage of the MSS-SS

Date	Av. Daily Sol. Irradiance (W/m^2)	Stage distillate yield (ml)						MSS-SS+BSS (ml)	MSS-SS (ml)	Thermally insulated	Most productive stage
		St 1	St 2	St 3	St 4	St 5	BSS				
15-Mar-21	209.5	220	280	240	130	80	170	1120	950	Yes	St 2
01-Jun-21	209.9	50	150	210	140	470	140	1160	1020	Yes	St 5
30-May-21	234.6	700	230	340	80	330	140	1820	1680	Yes	St 1
02-Jun-21	246.1	160	390	510	60	380	220	1720	1500	Yes	St 3
26-Sep-20	253.7	980	1120	1070	680	900	340	5090	4750	Yes	St 2
08-Oct-20	268.8	1110	1190	980	650	940	460	5330	4870	No	St 2
04-May-21	273.0	370	350	430	80	800	340	2370	2030	Yes	St 5
16-May-21	283.6	520	220	340	110	700	310	2200	1890	Yes	St 5
11-Dec-20	291.9	860	980	890	650	1110	410	4900	4490	No	St 5
23-Apr-21	299.4	580	870	780	560	450	380	3620	3240	Yes	St 2
31-Jan-21	316.9	980	1320	1200	580	1440	570	6090	5520	No	St 5
05-Nov-20	320.3	1070	1060	1170	590	1080	640	5610	4970	No	St 3
18-Feb-21	323.7	1090	1180	1190	840	1530	510	6340	5830	No	St 5
01-Dec-20	324.2	1090	1160	1020	670	1030	580	5550	4970	No	St 2
01-Oct-20	337.2	1150	1080	1230	610	1100	400	5570	5170	Yes	St 3
08-Mar-21	338.8	670	950	870	480	690	360	4020	3660	Yes	St 2
14-Oct-20	358.1	1130	1210	1120	810	1160	540	5970	5430	No	St 2
04-Mar-21	377.9	1010	1090	1100	670	810	270	4950	4680	Yes	St 3
29-Sep-20	385.7	1020	1040	1050	590	1280	480	5460	4980	Yes	St 5
08-Apr-21	388.0	690	1210	1170	640	820	440	4970	4530	Yes	St 2
09-Apr-21	388.7	530	1210	1130	560	620	380	4430	4050	Yes	St 2
08-Nov-20	390.7	1030	1150	1080	830	1020	640	5750	5110	No	St 2
23-Jan-21	392.0	1030	1330	1360	590	1440	500	6250	5750	No	St 5
05-Apr-21	395.0	620	1330	1280	860	450	540	5080	4540	Yes	St 2
27-Mar-21	396.0	760	850	1000	820	590	530	4550	4020	Yes	St 3
28-Oct-20	396.0	900	1100	1130	820	1050	660	5660	5000	No	St 3

Figure 5.38 shows the distillate yield due to moderate solar irradiance between 200 and 299 W/m^2. Figure 5.39 presents the distillate yield data for solar irradiance ranging from 300 to 399 W/m^2. For readability, the data has been broken down to two figures: 5.38 and 5.39. The distillate yield pattern in Figure 5.38 represents the spring, early summer, autumn and early

winter. The distillate is around the average of 200 W/m^2 and falling within autumn or winter tended to follow the same distillate yield trend as in Figure 5.55. These curves in Figure 5.58 show that stages 1, 3 and 5 tended to be most productive stages. These distillate yield trends with stages 1, 3 and 5 as the most productive stages (see Figures 5.55 and 5.58) were the direct results of heavily fluctuating solar irradiance. That is, the rate of thermal energy input into the condensing tower was reduced due to the low solar irradiance trough, as shown in Figure 5.57. Therefore, even though the average solar irradiance had surpassed 200 W/m^2, its lower crests, intense fluctuations and cooling periods spurred stages 1, 3 and 5 to be the most productive stages. However, as observed in Figure 5.35, the distillate yield trend on the 9th of June 2021 was different even though it was only at 176.1 W/m^2. The distillate yield trend on the 23rd of Apr. 2021 was closely similar to that of the 9th of June 2021 (see Figure 5.38). The distillate yield trend on the 9th of June 2021 and 23rd of Apr. 2021 show an increase rate of thermal energy input into the condensing tower.

According to Figure 5.39, the spring and summer, with average solar irradiances from 200 to 299 W/m^2, had different distillate yield trends to those of autumn and early winter. The difference in solar irradiance curves in spring and early winter were presented in Figure 5.9. As the rate of thermal energy input into the condensing tower increased, the distillate yield trend changed (see Figure 5.38) for the 8th of Oct. 2020, 26th of Sept. 2020 and 11th of Dec. 2020.

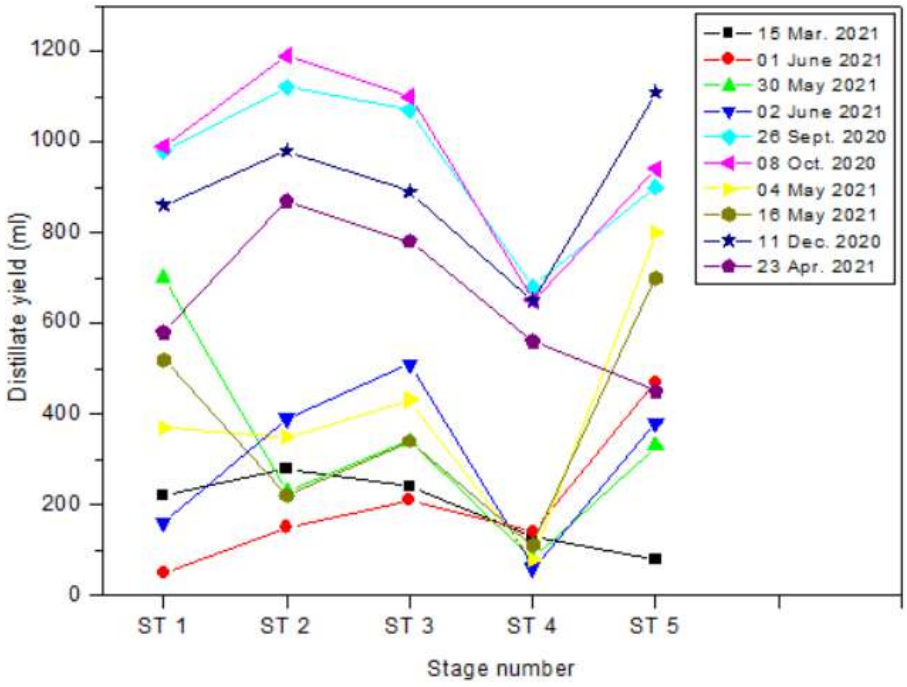

Figure 5.38: Distillate yield vs stage number

Even though the average solar irradiance values were within a 200 to 299 W/m^2 range, the distillate yield increased significantly in spring and early summer (see Figure 5.38) compared to autumn and winter. The distillate yield trend shows that stage 2 became the most productive stage under spring (see Figure 5.38) for the 26th of Sept. 2020 and 8th of Oct. 2020. Stages 1 and 3 were exchanging the number two spot after stage 2, and stage 5 was the fourth most productive stage in the system. However, in the early summer, stage 5 became the most productive stage in the system followed by stages 2 and 3, respectively.

A further increase in average solar irradiance to above 300 W/m^2 shows that the distillate yield maintained an almost consistent trend. Figure 5.39 presents the distillate yield as a result of the average solar irradiance from 300 to 399 W/m^2. The distillate yield trends in spring and summer (Figure 5.39) followed those of the 26th of Sept. 2020 and 8th of Oct. 2020 (Figure 5.38). However, Figure 5.39 shows that stage 5 distillate yield was beginning to surpass that of stage 2 as shown on the 5th of Nov. 2020. The most productive stages were between stages 2 and 5 as the rate of thermal energy input increased, an indication that except for stage 5, the rest of the stages were experiencing thermal damage conditions. The condensing surfaces of stage 1-4 were behaving similar to those in Figures 5.19 and 5.20, regardless of whether or not the condensing tower was thermally insulated. As the solar intensity increased further, stage 4 showed a constant decline in its productivity. Stages 1 and 4 were prone to reaching thermal damage condition, as discussed in section 5.2.

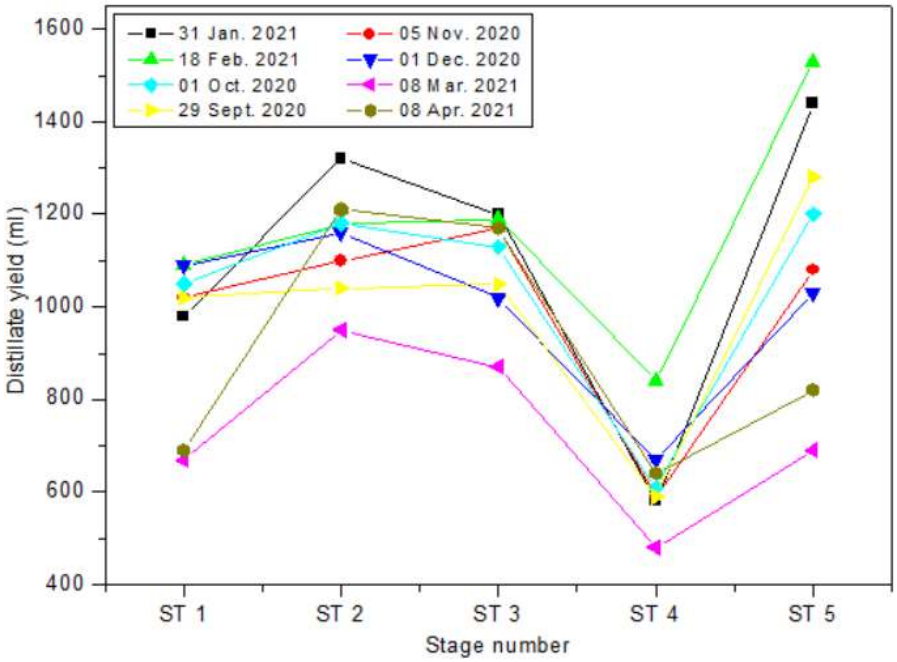

Figure 5.39: Distillate yield vs stage number

Even though there were some fluctuations, the daily cumulative distillate yield trend shown in Figure 5.40 indicates an increasing trend as the average solar intensity increased. Figure 5.40 was plotted according to Table 5.7 starting with the distillate yield corresponding to the lowest average solar irradiance to those corresponding to the highest average solar irradiance in Table 5.7. The graph presented in Figure 5.40 shows the curves of both the MSS-SS stages alone and the combined MSS-SS stages with the BSS distillate yield. As stated in sub-section 5.7.1, the distillate yield was not solely the function of the increasing solar irradiance but also the solar irradiance patterns throughout the day. For instance, it can be observed from Table 5.7 that the average solar irradiance on the 23rd of Apr. 2021 was 299.4 W/m^2, while those of the 26th of Sept. 2020 and 11th of Dec. 2020 were 253.7 and 291.9 W/m^2, respectively.

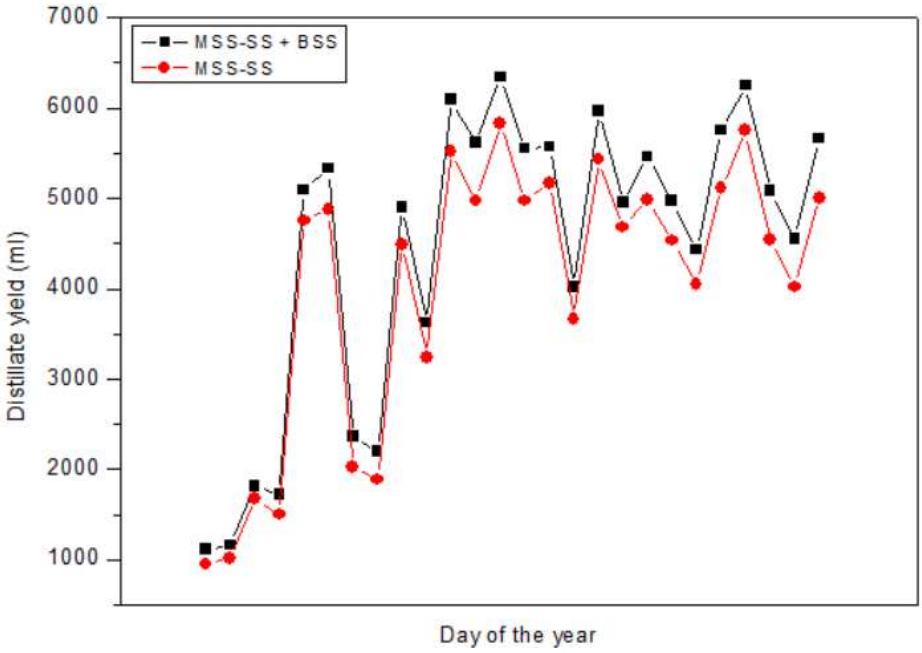

Figure 5.40: Cumulative distillate yield vs day of the year

The cumulative distillate yield from the MSS-SS stages alone were 3240, 4750 and 4490 ml for the 23rd of Apr. 2021, 26th of Sept. 2020 and 11th of Dec. 2020, respectively; hence, the cumulative distillate yield trend in Figure 5.40. Moreover, according to Figure 5.40, the higher distillate yield occurred in spring and summer. Unlike Figure 5.36, where the daily cumulative distillate yield trends were heavily fluctuating even though the average solar irradiance was increasing, Figure 5.40 shows an increasing pattern with increasing average solar irradiance.

5.7.3 Distillate yield trends due to high solar irradiance

Table 5.8 presents the data under high solar irradiance from 400 – 600 W/m^2 on the vapour-based MSS-SS. The data in Table 5.8 is discussed in conjunction with Figures 5.41 and 5.42. As observed from Table 5.8, late autumn and winter months did not have average solar irradiance for high solar insolation.

Table 5.8: Distillate yield per stage of the MSS-SS

Date	Av. Daily Sol. Irradiance (W/m^2)	Stage distillate yield (ml)						Total (ml)	Thermally insulated	Most productive stage
		St 1	St 2	St 3	St 4	St 5	BSS			
07-Apr-21	400.2	920	780	940	640	570	660	4510	Yes	St 3
15-Oct-20	405.5	990	1000	1160	990	1550	490	6180	No	St 5
02-Oct-20	410.8	890	1100	1120	690	1300	330	5430	Yes	St 5
30-Nov-20	434.9	1020	1150	1160	720	1380	670	6100	No	St 5
03-Apr-21	411.7	150	920	1160	930	590	600	4350	Yes	St 3
24-Sep-20	418.9	760	990	1030	570	1470	360	5180	Yes	St 5
17-Mar-21	459.7	750	1270	1780	860	1030	850	6540	Yes	St 3
21-Nov-20	479.3	1070	1310	1290	700	1280	650	6300	No	St 2
09-Dec-20	484.7	990	1210	1230	650	1660	780	6520	No	St 5
08-Feb-21	492.2	1120	1370	1440	740	1350	560	6580	No	St 3
10-Feb-21	504.9	960	1250	1230	810	1460	740	6450	No	St 5
04-Nov-20	514.1	1030	1190	1240	920	1320	750	6450	No	St 5
04-Feb-21	518.7	840	1320	1380	920	1730	580	6770	No	St 5
19-Jan-21	525.6	1010	1330	1320	820	1540	660	6680	No	St 5
02-Dec-20	532.5	980	1330	1420	780	1610	920	7040	No	St 5
11-Nov-20	560.3	860	1310	1460	980	1780	930	7320	No	St 5
13-Jan-21	585	760	1550	1630	910	1880	1060	7790	No	St 5

According to Figure 5.41, the distillate yield data shows that stage 5, 3 and 2 were the most productive stages, in that respective order. Moreover, the distillate yield data trends in Figure 5.41 did not differ much from data in Figure 5.39. As the solar irradiance increased, stage 5 maintained its most productive status. Table 5.8 makes apparent that just above the average of 500 W/m^2, stage 5 became the most productive stage. Figure 5.41 shows that despite the higher average solar irradiance on the 17th of March 2021 and 7th of Apr. 2021, the curves show a different trend. On these two days, stages 3 and 2 were the most productive. In fact, these two days followed the same trend as the autumn and winter days in Figure 5.38. However, the distillate yield trend for the 2nd of June 2021 and 4th of May 2021 were closely similar to those in Figure 5.41, a similarity likely due to the fact that in autumn and winter the condensing tower was thermally insulated. Therefore, at high average solar irradiance, temperatures in the condensing tower behaved as though the thermal insulation material was present. That is, even though the condensing tower was not thermally insulated in late spring and summer, the intensity of heat reduced the temperature difference between the evaporative and condensing surfaces such that the condensing tower behaved similar to Figures 5.10, 5.11 and 5.13. Furthermore, the distillate yield on the 7th of April 2021 was lower than other stages. Therefore, the increase in distillate yield not only depended on the increasing average solar irradiance, but also the crests, fluctuations and troughs. In spring and summer, the distillate yield trend did not change for high average solar irradiance.

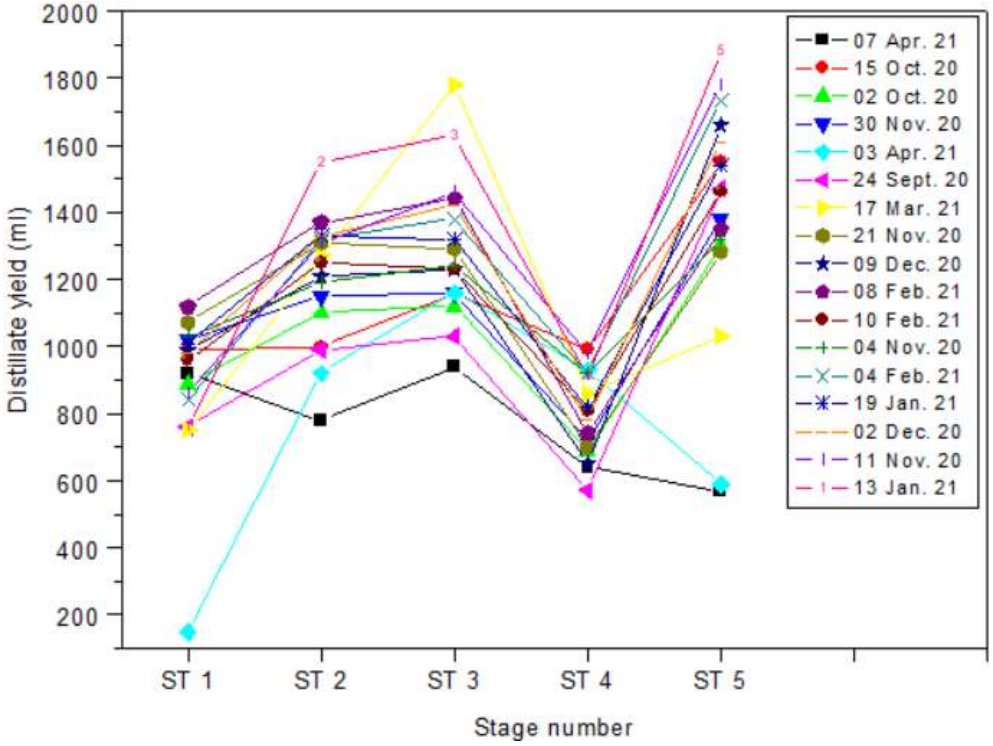

Figure 5.41: Distillate yield vs stage number

Figure 5.42 shows the cumulative distillate yield based on the high average solar insolation. The data in Figure 5.42 was arranged from the lowest average solar irradiance to the highest, as tabulated in Table 5.8. There were notable decreases of daily cumulative distillate decrease on the 2nd of Oct. 2020 and 3rd of April 2021. These decreases occurred even though the average solar irradiance was increasing. Therefore, above the average value of the solar irradiance, as mentioned earlier, the progression of the solar irradiance curve through the day had a larger impact on the 2nd of Oct. 2020. On the 3rd of April 2021, in addition to the solar irradiance progression, the crests of the curves were decreasing compared to that of the spring and summer (see Figure 5.9). Moreover, the cumulative distillate yield trend had evolved from intensely fluctuating (Figure 5.36) to moderate fluctuating curves (Figures 5.40 to 5.42) with minimal variations.

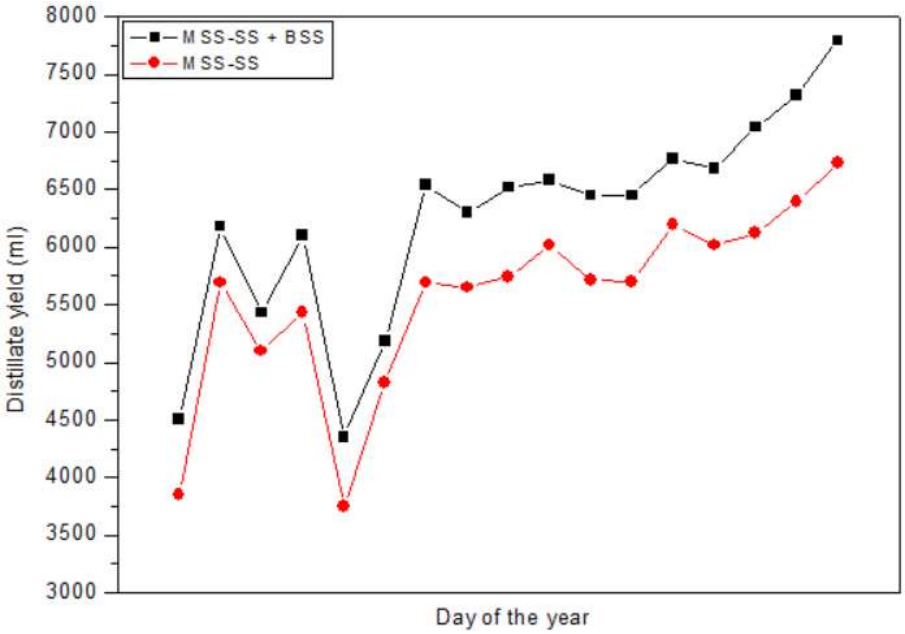

Figure 5.42: Daily cumulative distillate yield vs day of the year

5.7.4 Daily cumulative distillate yield trend

Figure 5.43 shows the daily cumulative distillate yield trend from Sept. 2020 to June 2021 from the vapour-based MSS-SS. Figure 5.43 shows that the cumulative distillate yield trend increased with the increasing average solar irradiance from spring to summer. Moreover, when the solar irradiance intensity, and therefore the average solar intensity, started a decline towards autumn, the daily cumulative distillate yield also showed a decline. According to Figure 5.43, the BSS was more productive at higher solar intensities than average and low solar intensities. Furthermore, in spring and summer, there was less cumulative distillate yield from day to day, indicating that despite the varying daily average solar irradiance in spring and summer, the condensing tower received sufficient thermal energy for the desalination process. Contrarily, in early autumn until winter, the cumulative distillate yield showed larger variations from day to day, suggesting that some days the productivity of the condensing tower was reduced according to the rate of thermal energy input. It also revealed that as the autumn progressed, the solar intensity lessened. The productivity in the BSS was reduced as a result of decline solar intensity. The daily cumulative distillate yield data in Figure 5.43 is also tabulated in Appendix B-3.

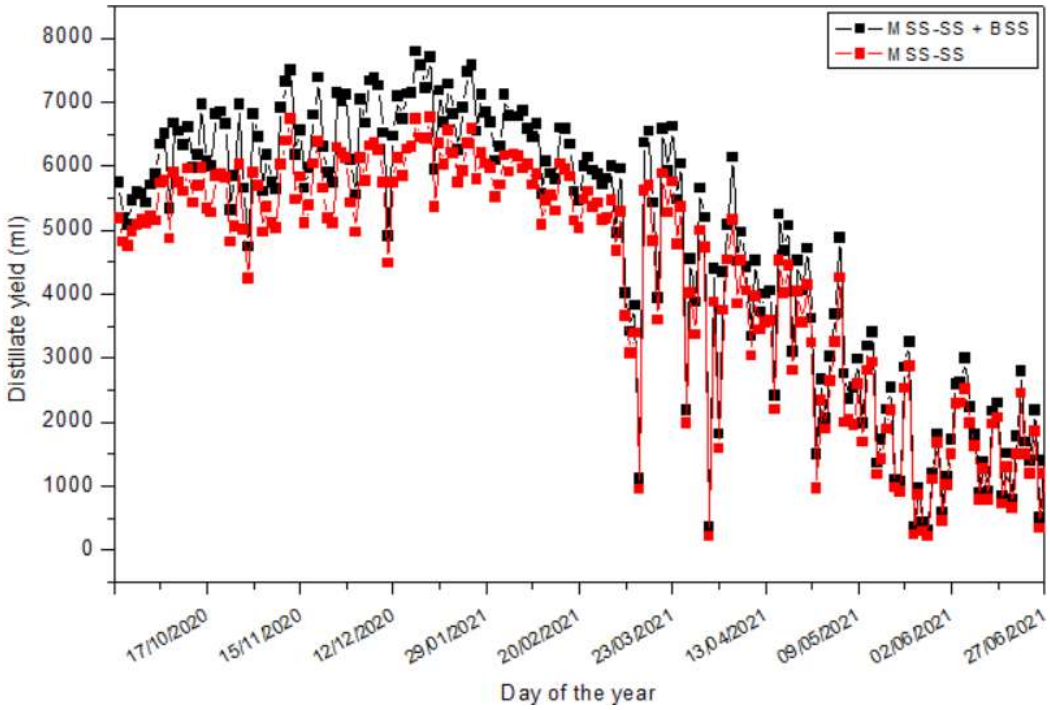

Figure 5.43: Distillate yield vs stage number

5.8 Independence of the stages of a vapour-based multistage solar still vs dependent stages of a multistage with waterbed

The independence of stages was experimentally tested through observations of temperature and productivity variations in the stages. There were two experimental tests conducted: one the atmospheric exposure of stages 1 and 2 and the other, the shutting off of vapour supply from stages 1 and 2. The atmospheric exposure was done by opening and exposing one or two stages to the atmosphere and observing the temperature and productivity behaviour of the remaining stages. The observations began in September 2020 (spring) and continued to December 2020. Further similar experiments were conducted for winter. The experiments were conducted on selected days, preferably with little cloud cover, over a number of days.

Early spring, autumn and winter can be regarded as cooler seasons with relatively low solar incidence, while summer months are hot with high solar incidence. Due to longer daytime in summer, solar radiation was available for long periods of time. In addition, solar radiation variations were lesser in summer and it was relatively stable. In terms of the existing MSS-SS, Estahbanati et al. (2014) reports that the lower stages tend to be more productive than the upper stages. The low productivity of the upper stages is associated with the thermal energy supply at the bottom of the system. Thus, upper stages receive and maintain moderate temperatures compared to the lower stages. The upper stages totally depend on the lower stages for thermal energy supply. Therefore, these current experimental observations were

seeking to address the scenario of vapour leak and or vapour losses in the lower stages and observed the productivity of the upper stages. In addition, the current experimental tests sought to establish the extent to which the upper stages were dependent on the lower stages.

Estahbanati et al. (2014) report low heat transfer efficiency between the stages as a result of heat loss from the walls, vapour condensing on the walls and other parts/components where it cannot be collected, droplets dropping back into the pool of saline water, removal of some thermal energy with freshwater (distillate) and a device operating in an unsteady mode resulting in the storage of some energy at the end of the experiment. This current study can add that the disposal of brine solution during operation also removes some thermal energy along with it. The are some common trends in both the vapour-based and a multistage with waterbed in the stages, including loss of thermal energy through the stage walls, removal of some thermal energy with the distillate (freshwater) and a device's operation in an unsteady mode.

5.8.1 Atmospheric exposure experimental tests

5.8.1.1 Spring experiment (28 Sept. 2020)

Figure 5.44 shows a graphical representation of the SW pre-heating in the zigzagged SW tube through the stages of a vapour-based MSS-SS. On this particular day, the 28th of Sept. 2020, thermal insulation material was applied on the body of the condensing tower. Stages 1 and 2 were opened and exposed to the atmosphere for a whole day. The average solar irradiance, wind velocity and ambient air temperature values were 371.6 W/m^2, 1.3 m/s and 13.4°C, respectively. According to Figure 5.44, stages 1 and 2 show that the SW in the zigzagged SW tube remained much cooler on the day at a maximum of 46.3 and 61°C, respectively. These maximum values occurred around 14h10 and 15h50 for stages 1 and 2, respectively. Meanwhile stages 3, 4 and 5 reached a maximum at 93, 95.7 and 49.6°C, respectively. Therefore, opening and exposing stages 1 and 2 to the atmosphere did not have any direct effect on the SW temperature curves on stages 3, 4 and 5.

Moreover, based on the SW temperature profile in sections 5.1 to 5.4, the SW temperature curve profiles of stages 1 and 2 were different in Figure 5.44. The opening of the stages 1 and 2 increased heat losses to the atmosphere. Thus, the secondary SW tank was at maximum at 32.8°C. There was an increased thermal energy collected in the BSS, stages 5, 4 and 3 as stages 1 and 2 were exposed to the atmosphere. There was also a decrease in the secondary SW temperature in terms of its maximum value. For instance, when the system was fully operational under the solar irradiance of 385.7 W/m^2 on the 29th of Sept. 2020, the maximum SW temperature value was 37.6°C. The decrease in the maximum SW temperature value in

the secondary was due to both opened stages and the decreased average solar irradiance from 385.7 to 371.6 W/m^2.

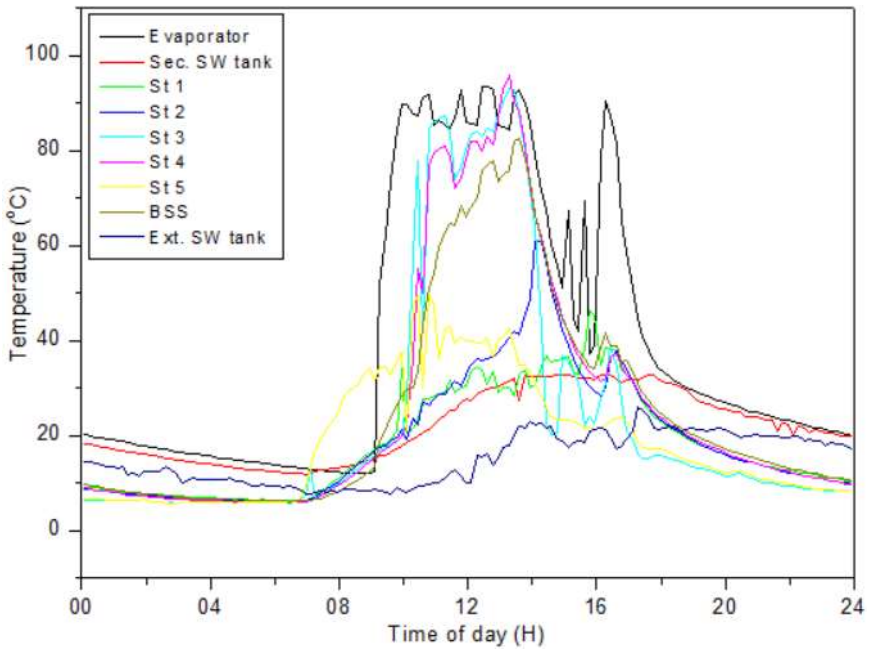

Figure 5.44: SW temperature vs time of day

Since the stages 1 and 2 were exposed to the atmosphere, no distillate was produced in these stages. That is, the vapour and thermal energy were lost to the atmosphere from these two stages. Moreover, the temperature is directly proportional to its pressure, that is, the higher the temperature, the higher the pressure (Çengel, 2003). Initially, the vapour was assumed to be equally supplied to all stages of the condensing tower. However, due to the thermal damage condition in some stages, the vapour was redirected to the stages that had not reached thermal damage.

It was assumed that stages experiencing thermal damage condition had higher condensing surfaces temperature and increased pressure, rendering some stages more productive than others. Under the atmospheric exposure experiment, the condensing tower experienced a decrease in the daily distillate yield directly correlated with the assumption that since stages 3 and 4 had reached thermal damage condition, the vapour was redirected to stages 1, 2 and 5. However, only stage 5 was operational in terms of producing the distillate. The vapour lost to the surroundings was, therefore, the cause of decline in the productivity of the condensing tower. The redirecting and the varying productivity of stages as the solar irradiance increased can be observed in Tables 5.7 and 5.8.

5.8.1.2 Summer experiment (09 Feb. 2021)

Data from under summer weather conditions when the condensing tower was thermally uninsulated is shown in Figure 5.45, on the 9th of Feb. 2021. The average solar irradiance, wind velocity and ambient air temperature values were 501.2 W/m^2, 5.9 m/s and 23°C, respectively. Due to the absence of the thermal insulation material and the effects of convective cooling by the wind, all stage SW temperature values remained moderate. Moreover, due to an increased rate of thermal energy input, as shown by the evaporator temperature curve in Figure 5.45, the exposed stages 1 and 2 SW temperature curves were much closer to those of the operational stages (i.e., stages 3, 4 and 5). The higher average wind velocity caused substantial cooling and prevented thermal damage condition. The maximum SW temperature values of stages 1 and 2 were 65.5 and 54.7°C, respectively. Those of stages 3, 4 and 5 were 64.8, 80.1 and 41°C, respectively. Figure 5.45 shows that despite exposing stages 1 and 2 to the atmosphere under a high rate of thermal energy supply, the SW temperature tended to increase regardless in stages 1 and 2.

Under summer conditions, then, with an average solar irradiance of 501.2 W/m^2, stages 1 and 2 reached higher SW temperatures. Moreover, since none of the stages experienced thermal damage condition, the re-direction of the vapour was minimal compared to Figure 5.44. However, compared to other days when the condensing tower was fully operational, there was a slight decline in the daily distillate yield of the system.

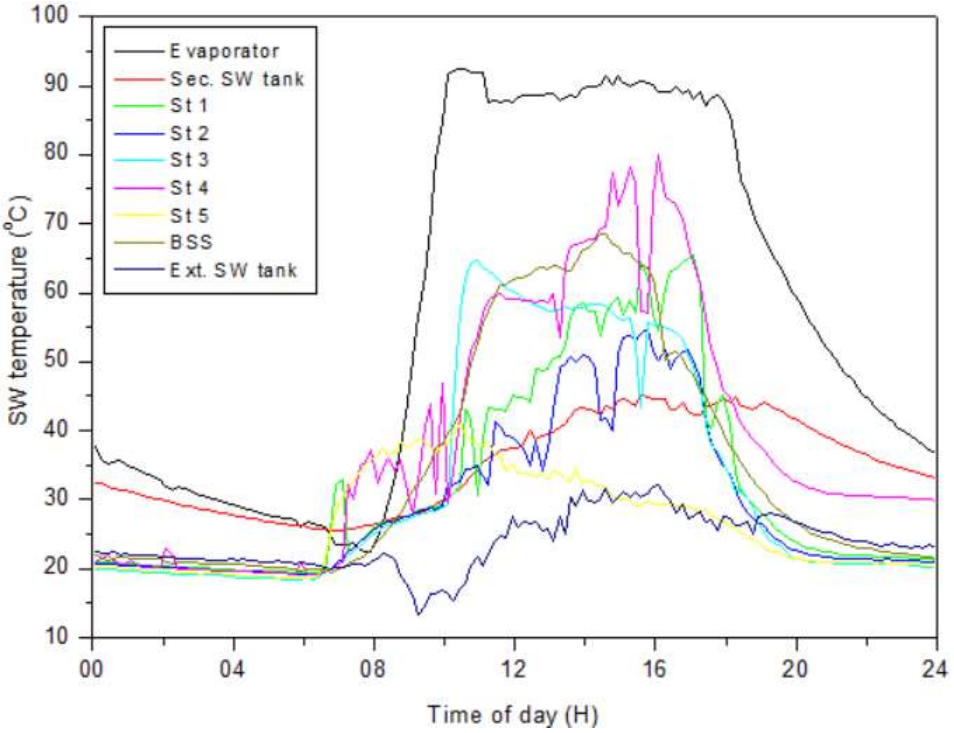

Figure 5.45: SW temperature vs time of day

The secondary SW tank maximum temperature was 45°C, an increase from 32.8°C in Figure 5.44. However, comparing Figure 5.25 with an average solar irradiance of 518.7 W/m^2, its secondary SW temperature was maximum at 50.1°C. There was a decline in the overall pre-heating and heat recovery in the stages due to the high average wind velocity at 5.9 m/s and the exposed stages 1 and 2. Furthermore, the SW temperature curves in the exposed stages were much different to those in Figure 5.25. The SW temperature curves in Figure 5.45 indicated an intermittent heating and cooling in the exposed stages due to the combination of the pre-heated SW from the BSS, the vapour supply from the evaporator and the exposed stages in the condensing tower.

5.8.1.3 Winter experiment (11 June 2021)

The experimental tests in winter did not show any fixed patterns (see Figure 5.46). The SW temperature curves in Figure 5.46 represented the 11th of June 2021 when the condensing tower was thermally insulated. The average solar irradiance, wind velocity and ambient air temperature values were averaged at 228.7 W/m^2, 1.1 m/s and 18.6°C. Each day tested under winter conditions tended to experience heavy fluctuations and increased distillate yield losses. This unclear and unstable pattern was also observed in sub-section 5.7.1 under low average solar irradiance.

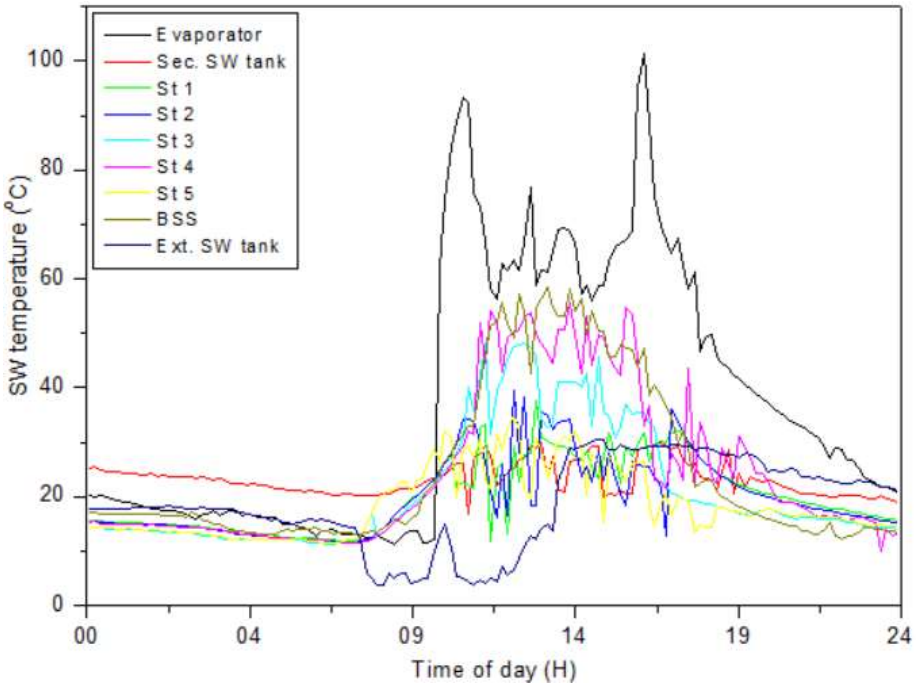

Figure 5.46: SW temperature vs time of day

Despite the average solar irradiance of 228.7 W/m^2 falling in the moderate range, the condensing tower SW temperature behaviour was similar to that of low solar insolation. This condensing tower behaviour was a direct result of substantial heat losses due to exposed

stages 1 and 2. These heavy SW temperature curve fluctuations were not only due to the exposed stages (stages 1 and 2), but also to the nature of the solar irradiance. As discussed earlier, under low solar insolation, the components of the condensing tower cooled down rapidly due to insufficient thermal energy supply. These fluctuations of SW temperature curves were moderate under Figures 5.44 and 5.45. However, despite these heat losses, stages 3 and 4 show that they operated at thermal damage condition for some time on the day with instantaneous surges. Due to the intermittent nature of the thermal energy reaching the stages, their SW temperature curves showed increased cooling down periods.

Due to the moderate rate of thermal energy input, the vapour make-up tubes tended to cool faster. As mentioned earlier, the cooling down of the condensing tower was counterproductive in terms of distillate yield. Furthermore, stages 1 and 2 SW temperature were maximum at 37.8 and 39.6°C, respectively. Operational stages 3, 4 and 5 had maximum SW temperatures of 39.2, 55.7 and 34.7°C, respectively. The maximum secondary SW tank temperature was 29.9°C. However, under the average solar irradiance of 209.9 W/m^2 on the 2nd of June 2021, the secondary SW tank maximum temperature was 50.2°C. There was a considerate amount of thermal energy lost to the surrounding. Therefore, the heat recovery and SW pre-heating processes were affected substantially by vapour lost to the atmosphere. The results of the atmospheric exposure of stages 1 and 2 show that these stages behaved similar to those of the 29th of May 2021 and 31st of May 2021 even though the average solar irradiance had increased to 228.7 W/m^2. The SW in the zigzagged SW tube was heated intermittently and in turn cooled down rapidly. Therefore, the average solar irradiance of 228.7 W/m^2 under the atmospheric exposure experiment can be regarded as falling under low solar insolation range.

5.8.1.4 Summarised results

The experimental tests of stage independence were not conducted in autumn as the temperature data logger unit was unavailable since it was being calibrated. In addition, the approach used to experimentally test the independence of stages was unreliable as some aspects were unknown or varying with time. For instance, the extent to which the thermal energy was lost could not be quantified at this point. The SW temperature curve behaviours could not be repeated under the same rate of thermal energy input and pattern as the solar intensity changed from day to day. The effects of wind velocity on the exposed stages on the condensing tower, and the effects of wind velocity on solar stills have been widely reported in the literature. Therefore, wind blowing into the opened stages would play a significant role in cooling the stage walls, vapour make-up tubes and SW in the zigzagged SW tube. However, the wind direction could not be controlled nor repeated to obtain reliable results. Therefore, the tests were general and were aimed at establishing the extent of the stage's independence during operation. Based on this aim, the results are summarised below.

The results from these atmospheric exposure experiments show that the combination of low-to-moderate solar intensity and high wind velocity had detrimental effects on the yield of the upper stages. In fact, even when the average wind velocity was as low as 1.1 m/s, there was rapid cooling in the condensing tower (as in Figure 5.46). The results further show that during days with low solar intensities and high wind velocities, the vapour make-up tubes supplying vapour to the upper stages and passing through stages 1 and 2 tended to cool down momentarily. When these tubes cooled down, they reduced the amount of vapour reaching the stages (as demonstrated in Figure 5.46). However, during high solar intensity and low wind velocities, the effect of exposing the lower stages to the atmosphere were negligible. Figure 5.45 shows that at high solar insolation, the rate of thermal energy input was so high that even the average wind velocity of 5.9 m/s could not keep the condensing surfaces temperatures as low as in Figure 5.46. The exposed stages showed an increase in SW temperature through the day (see Figure 5.45). Therefore, the removal of the thermal insulation material and exposing stages 1 and 2 to the atmosphere could not sufficiently cool down some of the stages. The overall results show that the daily distillate yield from the upper stages was reduced by 5.8% to 41.3% under low solar intensity and high wind velocity compared to similar average solar irradiance under the same season. During days with high solar intensity such as in summer, the daily distillate yield decreased from 0.8 – 12.4% under similar solar intensities under the same season. Low wind velocity did not have a significant effect on cooling the vapour make-up tubes under high solar intensity. However, under low solar intensity, the pre-heating of the SW was affected by as much as 40.2% compared to the moderate to high solar intensity.

5.8.2 Shutting off vapour supply to the lower stages

When the second experimental observation was made, no atmospheric exposure was allowed. That is, all stages were sealed and isolated from outside elements and influences. Stages 1 and 2 vapour make-up tubes were plugged or shut off preventing any vapour supply to these stages. On the 21st of Jan. 2021, the average solar irradiance, wind velocity and ambient air temperature values were 478.4 W/m^2, 3.3 m/s and 22.4°C, respectively. A singular figure (Figure 5.47) showing the SW temperature curve progression throughout the day is presented, as the SW temperature curves in Figure 5.47 were quite different to those established in sections 5.1 to 5.4.

Figure 5.47 shows where the theory of the vapour redirection in the condensing tower was conceptualized based on the SW temperature curves. That is, when the vapour could not flow through a certain vapour make-up tube, it was redirected from one vapour make-up tube to the other. Since the vapour make-tubes of stages 1 and 2 were shut off, all the vapour from the evaporator was redirected to stages 3, 4 and 5. As a result, the condensing surfaces of

the condensing tower increased significantly (seen Figure 5.47). Stages 3 and 4 operated close to thermal damage condition due to the increased rate of thermal energy input. Furthermore, the evaporator SW temperature curves show a positive thermal energy supply; that is, minimal or no cooling periods due to the solar irradiance curve progression. Despite the absence of the thermal insulation material and the average wind velocity of 3.3 m/s, stages 3 and 4 operated at elevated temperatures. Moreover, the condensing surfaces in Figure 5.47 were much higher than those in Figure 5.26 where the average solar irradiance was 560.3 W/m^2. Due to these increased rates of thermal energy supply, stage 3, 4 and 5 attained the maximum SW temperature values of 83.8, 85.7 and 59.4°C. The maximum value of 59.4°C in stage 5 was the highest of any discussed so far. Stages 1 and 2 SW temperatures reached maximum at 70.8 and 65.7°C, respectively. It should be noted that the SW temperature in stages 1and 2 was only pre-heated by the SW flowing from the BSS. Since the vapour make-up tubes were plugged off, the SW in these stages was not pre-heated by the vapour directly.

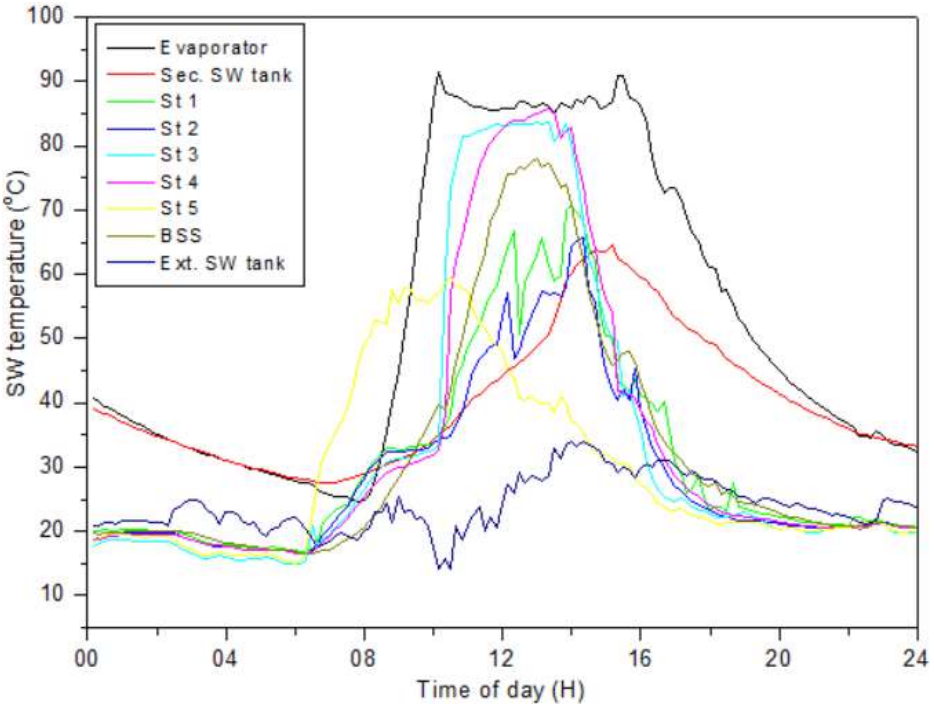

Figure 5.47: SW temperature vs time of day

The results from this test show no productivity loss in the upper stages due to the shutting down of the lower stages. In fact, about 7.1 – 15.4% increase in the daily cumulative distillate yield was observed. These results support the vapour redirection theory in the condensing tower. The most significant distillate yield increase was observed in stage 5. In the literature, it was reported that the upper stages depend on the lower stages for thermal energy supply. Therefore, should any thermal energy loss occur in these lower stages, the waterbed-based MSS-SS would be greatly affected. The experimental observations of the vapour-based MSS-

SS were to determine the extent to which the upper stages depend on the lower stages under quality of distillate.

5.9 Quality of the distillate

5.9.1 Electrical resistance

After the seawater (saline water) was collected from the ocean, it was tested for electrical resistance using a multi-meter as discussed in Chapter 4. The SW was tested at room temperature before it was poured into the vapour-based MSS-SS. Tap water was also tested at room temperature as well for comparison purposes. Both the SW and tap water electrical resistance tests were done only once and the values taken as fixed values, as discussed under section 4.7. The higher electrical resistance in water indicates reduced total dissolved solids (TDS). Low electrical resistance indicates increased presence of the TDS in water (Light et al., 2004). Some of the electrical resistance results of the distillate are tabulated in Table 5.9. The electrical resistance experiments were conducted for approximately two months. Due to other experimental observation conducted, the electrical resistance experiments were only conducted in the autumn of 2021. The rest of the electrical resistance results can be found in Appendix B-4.

The electrical resistance of tap water and of the SW were recorded and fixed at 128.6 x 103Ω and 14.2 x 10^3Ω, respectively. Even though the BSS electrical resistance results are included in Table 5.9, the focus is on the stacked stages. The BSS results were merely for comparison purposes. According to Table 5.9, the electrical resistance of the distillate had no notable relationship with the varying average solar irradiance. Therefore, there was no clear pattern to follow in terms of the correlation between solar intensity and electrical resistance. However, in most days, stage 4 distillate maintained higher electrical resistance results compared to other stages (see Table 5.9). It is not clear whether stage 4, always at higher temperatures in sections 1 and 2, had any connections to its electrical resistance. However, those results cannot be conclusive as stage 1 was also operating close to thermal damage condition, as in sections 5.2 to 5.4, under moderate to high solar intensities.

Table 5.9: Distillate electrical resistance results per stage of the MSS-SS

Date	Av. Sol. Irradiance (W/m^2)	ST1	ST 2	ST 3	ST 4	ST 5	BSS
		Ohms (Ω) (x10^3)					
26-May-21	208.3	78.7	82.9	649	194.3	64.3	115.5
14-May-21	269.6	98.6	154.8	847	969	173.2	908
26-Mar-21	301.4	33.8	65.5	132.7	469	81.2	111.9
01-May-21	338.8	80.3	688	186.1	950	106.1	687
30-Apr-21	340.2	99.8	178.1	982	1160	139.3	838
04-Mar-21	377.9	36.1	45.4	91.7	392	57.4	56.6
16-Apr-21	386.6	76.1	73.0	109.7	472	71.2	69.5
21-Mar-21	404.6	65.3	72.3	434	705	74.6	132.9

01-Apr-21	411.1	76.6	88.6	191.3	587	94.9	151.2
AVERAGE		76.2	175.4	441.5	688.3	100.6	376.8

On the 4th of March 2021, all stages showed a decline in the electrical resistance, implying that the distillate contained increased TDS. Since the SW was re-circulated in the open loop circuit and not disposed of, the SW in the evaporator and the open loop circuit accumulated salt and other foreign content. As discussed under section 4.6, the flushing out of the brine solution was conducted weekly or bi-weekly depending on the electrical resistance results. Therefore, not only on the 4th of March 2021, decrease in the electrical resistance can be observed on other days on a week or bi-weekly basis (see Appendix B-4). However, as the winter of 2021 approached and low evaporation in the evaporator due to low solar intensity, the brine disposal period exceeded two weeks.

Figure 5.48 shows the graphical representation of the electrical resistance data in Table 5.9. Except for the 1st and 26th of May 2021 (see Figure 5.48), all other curves show the same pattern which suggests that stage 4 produced the distillate with the least amount of the TDS. Furthermore, from stages 1-4, Figure 5.48 shows a trend that suggests that the electrical resistance increased with increasing stage number. That is, stage 1 distillate had the lowest electrical resistance and stage 4 distillate had the highest. However, stage 5 suggested that its electrical resistance was closely similar to that of stages 2 and 3. The cause of this trend cannot be established at this point. Moreover, these electrical resistance curves in Figure 5.48 were inversely proportional to the distillate yield some stages. For instance, from Figures 5.35, 5.38, 5.39 and 5.41, stage 4 almost always produced the least amount of distillate, but its electrical resistance was higher. Stages 2, 3 and 5 almost always produced the most distillate in the condensing tower but their electrical resistance was lower than that of stage 4. Even though there were no specific links to the increasing solar intensity, these electrical resistance results appeared to be influenced indirectly by the rate of thermal energy supplied.

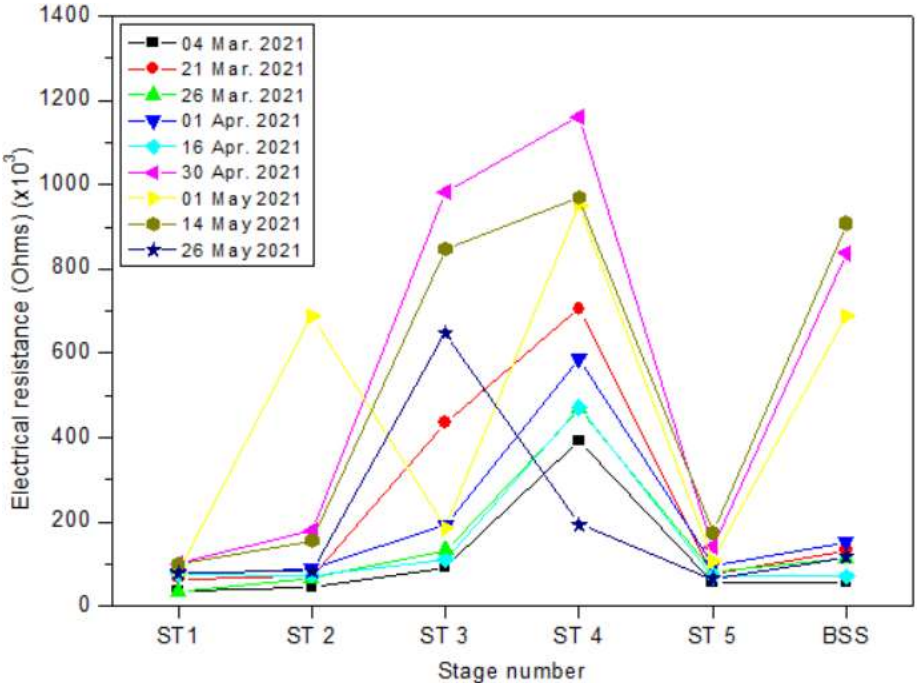

Figure 5.48: Distillate electrical resistance vs stage number

5.9.2 pH levels in the distillate

The pH levels were measured as indicated in sub sub-section 4.7.2, with results indicating that the samples had a high acid concentration. This concentration may have been due to the aluminium and copper materials used to construct the condensing tower. The use of aluminium material in water treatment results in high aluminium concentration (DWAF, 1996). Thus, the acid level in the samples showed a lower pH reading compared to the accepted guidelines of between 6.5 – 8.5. Only one of the three tests, the physical test, reported by Simonis and Nweze (2016) was performed. The biological tests were not conducted on the distillate samples. Table 5.10 shows the temperature and pH readings of the water samples tested. The readings were inconclusive at best due to the huge fluctuations recorded between the two days of testing. Therefore, the mean pH values (see Table 5.10) were used to calculate the average between the two days. The high acid concentration in the distillate samples may have emanated from the aluminium particles in water which caused a decrease in pH readings. Table 5.10 shows that the water treatment process had increased the acid concentration in the water far above that of the SW. The low pH levels indicate that the vapour-based MSS-SS be constructed from food grade stainless steel materials to eradicate the high acid concentration in water. The pH values in the table also indicate that the distillate needs post-treatment to attain a final product of water at an acceptable level for consumption.

Table 5.10: Distillate pH results per stage of the MSS-SS

Description	04 May 2021		05 May 2021		pH mean value
	pH level	Temp. (°C)	pH level	Temp. (°C)	
BSS	6.33	21.4	5.39	21.0	5.86
Stage 5	6.75	21.7	4.87	20.8	5.81
Stage 4	7.84	22.2	5.11	21.0	6.48
Stage 3	7.87	22.1	5.67	21.2	6.77
Stage 2	7.76	22.6	5.91	21.0	6.84
Stage 1	6.67	22.1	5.99	21.6	6.33
Tap water	7.19	22.0	6.93	22.0	7.06
Seawater	7.90	22.2	8.10	22.2	8

5.10 Contamination in the condensing tower of the vapour-based MSS-SS

In the literature, it was reported by Adhikari et al. (1995), Schwarzer et al. (2001) and Soni et al. (2017) that the stages of the MSS-SS tend to accumulate salt deposits due to salt water (waterbed) in the stages. This salt residue accumulation was reported to affect the heat transfer ability through the stages. The build-up on the tray surface also caused fouling over time which in turn affected the heat transfer ability of the tray (Chen et al., 2017). It also required stage maintenance in the form of flushing and washing off the salt deposits using some chemical solution or water. The ineffectiveness of heat transfer through the stages was reported to further cause low distillate production in the condensing tower. Therefore, an experimental investigation was conducted to establish whether the salt residue or any foreign elements accumulated in the vapour-based MSS stages. This experiment was conducted simultaneously with the independence of stage experiment reported under section 5.8 for stages 1 and 2. For stages 3, 4 and 5, the experimental observations were undertaken during system maintenance.

As the contamination experiments were based on observations, no numerical data was available. The vapour-based MSS-SS was experimentally tested for approximately 10 months (Sept. 2020 – June 2021). The entire condensing tower and the stages were sealed and isolated from outside contamination such that no dust particles could access the stages. The stage walls, trays and the zigzagged SW tube were monitored for any forms of build-up and contamination over time. Therefore, during the entire 10 months, no salt deposits or any contamination was ever discovered in the stage wall, tray or zigzagged SW tube. The only visible marks on the stage walls and trays, in fact, were the dried-up condensate as shown in Figures 5.49 and 5.50. The pictures in Figures 5.49 and 5.50 were taken on the 9th of Feb. 2021, six months after the commencement of the experimental tests.

Figure 5.49: Stage 2 trays and zigzagged SW tube

The marks left by the dried-up condensate appear nearly white on the stage walls and trays (see Figures 5.49 and 5.50). This change in colour was suspect to the increased acid level in distillate, as alluded to in sub-section 5.9.2.

Figure 5.50: Stage 2 wall and tray

The lack or non-contamination by salt deposits on the stage walls, trays and zigzagged SW tube suggested no maintenance requirements in the stages as reported in the literature. It was therefore concluded that, based on observation, the vapour-based MSS-SS required no stage maintenance and no fouling took place on the zigzagged SW tube for a period of almost 10 months during experimental tests.

5.11 Contamination in other compartments

5.11.1 External tubing and the evaporator maintenance

While the investigations under section 5.10 found no sign of salt deposit contamination in the stages, the opposite was the case in the external tubing and evaporator. Furthermore, under the current study, the brine solution ejection from the system was based on the evaporation rate in the evaporator driven by the prevailing solar intensity, increased electrical resistance in the brine solution compared to the 14.2 x $10^3\Omega$ of the SW, and decreasing distillate yield from the system. Further analysis of the brine was beyond the scope of this current work. Salt

build-up was prevalent in the tubing and the evaporator. To avoid thermal energy loss by removing heated brine solution, the brine solution was ejected during the early hours of the morning before the first solar incident was recorded. As Estahbanati et al. (2014) report, the removal of some thermal energy with freshwater (distillate) also contributes to low thermal heat transfer efficiency in the condensing tower. The current study further adds that the removal of heated brine solution during the system's operation also contributes to the thermal energy losses. Therefore, brine solution was removed early in the morning. The SW with high salinity in the tubing was flushed out with unheated seawater. In other words, the system was flushed and primed simultaneously by the less salty water collected from the sea.

The inspections on the fouling of the ETSCs manifold were visual inspections. That is, during maintenance, the external tubing connecting the ETSCs was inspected. Due to the difficulty in obtaining clear pictures inside the ETSC's manifold, the enlarged pictures of the non-return valve and series connector (discussed in sub-sections 3.15.3 and 3.15.5) are shown in Figures 5.51 and 5.52, respectively.

Figure 5.51: Non-return valve contamination

Most of the contamination shown in Figures 5.51 and 5.52 was floating in the SW in the tubing. When it circulated during the operation of the system, it tended to circulate with it. Under the dynamic mode of operation, the salt deposit sticking to the surfaces was minimised by the bulk fluid motion as it washed it away (Salem, 2013). When the brine solution was flushed out, most of the contamination was ejected with it. However, some of it remained in the tubing (see Figures 5.51 and 5.52). The contamination left in the tubing was cleaned and removed during maintenance. Additionally, since SW was used as raw water, the swing's rubber seal in the non-return valve was damaged after a period of between three to four months. This rubber seal needed to be replaced as it could no longer create a perfect sealing for one-directional flow. The durability and salt resistance of this seal was monitored during the experiments. An indication that the sealing was no longer perfect was pick-up when the SW started to flow in

both directions. However, no definite period of time was established before it failed, only an approximate in conjunction with constant monitoring.

Figure 5.52: ETSC series connector contamination

Since the evaporator was welded (see Figure 3.62) as discussed in sub-section 3.14.6, the inside of the evaporator was inaccessible. However, as in Figure 4.8 and discussed in sub sub-section 4.3.3.1, the evaporator had a 4 mm hole drilled in its body where the liquid probe was inserted. Figure 5.53 pictures an enlarged evaporator with the liquid probe inserted.

Figure 5.53: Evaporator contamination

The only indication of the accumulation of the salt content inside the evaporator and the external tubing SW was the crystalized salt content coming out from the 4 mm drilled hole in the evaporator, suggesting that the sealing around the probe was insufficient to resist the pressure of SW in the evaporator. However, the hole was never perfectly sealed as the crystalized salt content was beneficial to reducing the level of salinity in the SW. Furthermore,

the crystalized salt content could be further processed for consumption. This 4 mm evaporator hole also served as a point where the brine solution could be tested for electrical resistance, as discussed in sub-section 5.9.1.

5.11.2 SW circulation in the external tubing and the evaporator

The continuous circulation of SW in the external tubing and the evaporator was observed to aid in reducing the salt deposits from sticking to the surface of the tubes and the evaporator. Salem (2013) concurs that the dissolved salt deposits or solids that accumulate on the surface of the tray under dynamic mode of operation are continuously washed away. The dissolved solids were continuously circulated with the SW water and so no heavy build-up was observed in the external tubing or evaporator. The majority of the dissolved salt and other solid contaminants were collected when the brine solution was being flushed. On close inspection, the ETC inner walls and heat transferring tubes in the manifold consisted of minor build-up of contaminants. However, this investigation was not the primary focus of the study and therefore further investigations are necessary.

5.11.3 Secondary SW tank, external SW tank and BSS maintenance

The secondary SW tank was the equivalent of the stages of the MSS-SS with waterbed in the stages. Outside of the BSS and the external SW tank, the secondary SW tank was the only compartment with a stagnant pool of SW. An extensive salt build-up was encountered in this tank. This tank was cleaned more frequently than any other compartment in the condensing tower. The BSS showed a moderate contaminant build-up compared to the secondary SW tank, primarily due to the fact that the SW from the BSS was constantly supplied to the secondary SW tank. The zigzagged SW tube was connected at the bottom of the BSS which meant that the majority of the solids flowed down into the secondary SW tank. However, the secondary SW tank was situated at the bottommost part of the system, so all the solids and contaminants settled in it and required occasional removal.

5.12 Impulse circulation to replace electrical pumps (circulation in the entry stage)

According to Çengel et al. (2008), heat transfer through convection involves bulk fluid motion and the higher the fluid velocity, the greater the heat transfer. The concept of impulse circulation in a solar still came as solution to the necessity for maintaining minimal SW in the evaporator. The larger pool of SW tended to gradually increase its temperature and reached its maximum somewhere in the afternoon or thereabout (Gnanaraj et al., 2017; Morad et al., 2015; Schwarzer et al., 2009; Estahbanati et al., 2015; Chen et al., 2017). Several researchers recommend the use of a pump for SW circulation purposes in a solar still (Ahsan et al., 2013). Pumps are used to circulate the SW or heat transfer fluids (HTF) under forced mode circulation (Tiwari & Sahota, 2016; Sampathkumar et al., 2010). However, the vapour-based multistage

system employed a thermodynamic principle to circulate the SW instead of pumps. The vapour-based multistage system had an open loop external tubing circuit which supplied the thermal energy through heated saline water. Due to the small quantity of SW being heated in the solar collector manifold at a time, circulation of SW was initiated at low solar intensity. As a result of low and fluctuating solar radiation, the SW would impulsively circulate as the swing inside the non-return valve opened and shut instantaneously.

Thermal energy was supplied from the bottom of the system in the evaporator (Diaf et al., 2015). The circulation (flowing waterbed) at the base (entry stage) of the vapour-based solar still can be closely associated with an inclined basin solar still (Sathyamurthy et al., 2015). However, unlike the inclined basin solar still in which the SW is directly heated by the sun, there is no direct solar radiation transmitted from the sun's rays to the SW in the vapour-based MSS-SS entry stage. Moreover, under very high solar intensity, the impulse effect would cease, and the SW would flow rapidly and continuously without any impulse action. The impulse circulation was used throughout the experimental test period and never failed as long as there was enough heat in the ETSC's manifold. However, no measuring instruments such as pressure gauges or flow rate meters were used to study the concept in detail. Nevertheless, it was able to satisfy the basic need of circulating SW through pressure differential caused by heating in the solar collector manifold. The pressure differential principle worked as long as there was adequate solar radiation available. It was experimentally observed that the impulse circulation concept was only functional under certain solar intensities.

Figure 5.54 shows the average solar irradiance and the cumulative distillate yield curves from Sept. 2020 to June 2021. Figure 5.54 was plotted using the data in Table B-1 under Appendix B. Figure 5.54 only aims to show the correlation between the daily cumulative distillate yield and the prevailing solar irradiance. The solar irradiance curve was responsible for all the evaporator SW temperature curves discussed earlier in the chapter. It was also responsible for the daily cumulative distillate yield trend, as shown in Figure 5.54 Moreover, it was discussed that there was a minimal average solar irradiance that could cause the condensing tower to yield the lowest quantity of the distillate. As shown in Table 5.6, the vapour-based MSS-SS was entirely unproductive between 122.7 to 145.1 W/m^2. However, as the solar irradiance increased to 155.5 W/m^2, the smallest system started to produce some distillate. Therefore, according to Figure 5.54, all the average solar irradiance below 155.5 W/m^2 can be considered as below the minimal value that can cause the system to begin production. In other words, below the minimum average solar irradiance value that could not initiate the impulse circulation in the open loop circuit and deliver sufficient thermal energy to the evaporator through SW. However, the average solar irradiance below the minimal value did not mean that the evaporator SW temperature would behave similar to that of Figure 5.2 on

the 25th of Sept. 2020 where the average solar irradiance was 145.1 W/m^2. For instance, on the 16th and 17th of June 2021, the average solar irradiance values were 139.1 and 122.7 W/m^2, respectively. These average solar irradiance values were able to produce fluctuating evaporator SW temperature curves. That is, compared to the 25th of Sept. 2020, on the 16th and 17th of June 2021, the impulse circulation was initiated. However, there was insufficient solar intensity to sustain the circulation of SW in the open loop circuit.

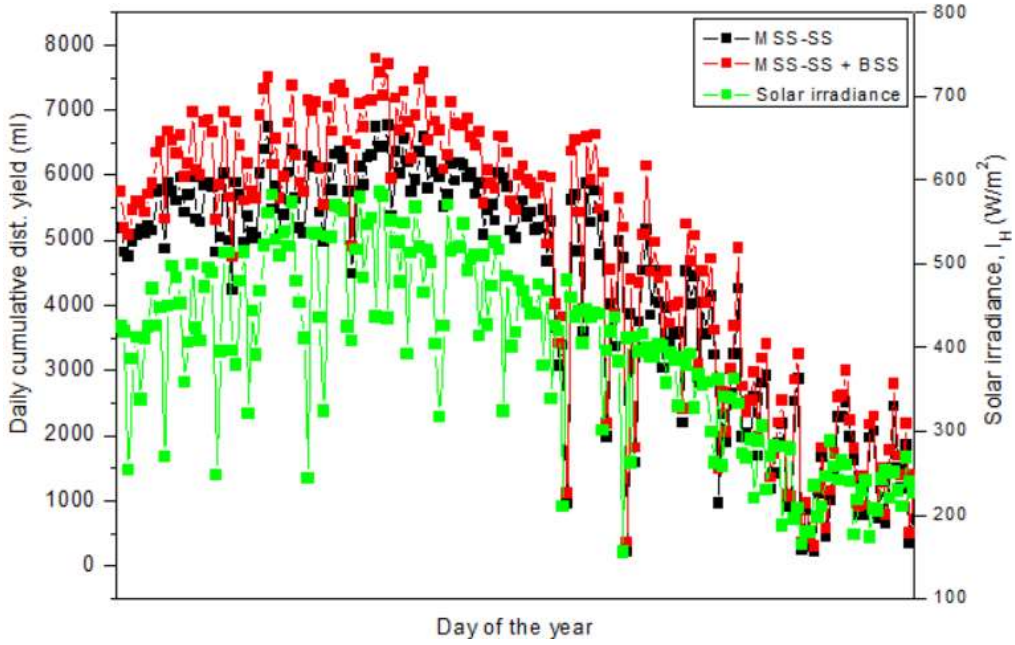

Figure 5.54: Evaporator contamination

As stated at the beginning of this section, at very high solar intensities, the impulsive actions of the SW circulation ceased, and the SW flowed continuously as in any pipeline. This continuous flow of SW was a direct result of elevated and maintained SW temperatures as shows by the curves such as those in Figures 5.24 to 5.27. Furthermore, this continuous flow also meant a consistent thermal energy supply to the evaporator which can be defined as positive thermal energy supply. Hence, the condensing surfaces were unable to cool the vapour fast enough which resulted in thermal damage condition. However, the pattern of thermal energy supply shown in Figure 5.9 was an ideal pattern at higher solar intensities. It is necessary for the TES to store excessive thermal energy to prevent the thermal damage condition. Throughout the experimental tests, there were never any measuring instruments such as pressure gauges and flow rate meters for measuring the working of the impulse circulation. For instance, it was never established as to under what solar intensity values does the impulse circulation start and stop, or under what solar intensity value did the impulse effect stop and the continuous SW flow in the open loop circuit begin. However, the combination of

the minimal SW in the entry stage and the impulse circulation showed that the vapour-based MSS-SS can produce the distillate for most days of a year.

5.13 Standalone ability of the vapour-based MSS-SS

Standalone ability refers to the ability of a solar still to operate without any external sources except for those intended to be used. For instance, in a renewable energy system like a solar still, the primary source of energy is solar energy. Anything beyond that can be considered as an external source. As an example, the vapour-based MSS-SS was experimentally tested for 10 months. During that time, no external sources were employed to assist the desalination process, confirming that the vapour-based MSS-SS can be used anywhere so long as there is adequate solar radiation available. The impulse circulation concept played a major role in enabling the vapour-based MSS-SS to function as a standalone system. In addition, the remotely controlled SW valves within the system ensured the operation without any supervision. For a small-scale system, it can fully replace pumps, electrical switches and other related and complicated units (Schwarzer et al., 2009). Therefore, it can be asserted that the attempt to develop a standalone system was a success.

5.14 Direct heating of SW in the solar collector

Schwarzer et al. (2009) explain that distilled water is used as heat transfer fluid to avoid corrosion in the ETC manifold. The experimental investigation of the vapour-based MSS-SS eliminated any additional heating agents such as HTF. The direct heating in the ETSCs ensured maximum heating of the SW. The major challenge in the direct SW heating was the contamination, as discussed in sub-sections 5.11.1 and 5.11.2. However, the suspension of the salt deposits and any other contaminants in the SW minimised the concentration of the contamination in the external tubing. Moreover, the circulation of the SW also aided in minimising the contaminants from solidifying in the external tubing inner walls. This was observed in comparison with the secondary SW tank, the BSS, and the external SW tank where the SW was stagnant or with no bulk fluid motion. In addition, some of the salt was observed coming out from the evaporator, as discussed in subsection 5.11.1. However, as reported by Chen et al. (2017), the contamination caused fouling in the system. This fouling reportedly reduced heat transfer efficiency of the system components. Therefore, it should be acknowledged that even with minimal contamination in the external tubing, the heat transfer efficiency in the ETSC's manifold was affected. However, the extent of deficiency of the ETSCs was never established as this was beyond the scope of this current study.

5.15 Integrating the BSS with the MSS-SS for SW preheating

Chen et al. (2017) report that the SW temperature of the last tray of the MSS-SS was momentarily higher than the stages below. This higher SW temperature was attributed to the direct heating by the sun's rays. The BSS was integrated with the vapour-based MSS-SS as the last stage, again as reported by Chen et al. (2017). It should be noted that the BSS in the current research work was not specifically studied but acted as the primary pre-heating compartment for the SW. At best, it produced a fraction of the total distillate of the entire system. The BSS had the third largest amount of stagnant pooled SW after the external SW tank and the secondary SW tank. The heating of the SW in the BSS was accomplished by both indirect and direct heating. As discussed in section 5.1, the SW in the BSS was heated by the incoming vapour into stage 5 in addition to the direct heating by sun rays.

In this section, focus is on three curves, namely, the external SW tank, the BSS and the stage 5 curves. Using Figure 5.2 as an example, the three possible causes discussed earlier in the chapter are revisited. That is, the increase in the SW temperature curve of stage 5 in the morning before that of the evaporator was attributed to, firstly, direct sun's rays heating the outside surface of the condensing tower. Since the stages were vapour tight, this caused heat build-up in the stages. Secondly, the temperature sensors may be picking up the slight increase in temperature as the SW in the stages was being heated by small quantities of incoming vapour. Thirdly, according to Figure 5.2, the BSS SW temperature began to increase in the morning, whereas the evaporator curve continued to decline throughout the day. The SW flowing down through the zigzagged SW tube may be causing that increase in SW temperature.

However, according to Figure 5.10 for instance, both the BSS and the evaporator contributed to the pre-heating of the SW. The thermal energy from the BSS can be regarded as dominant in the morning. But as soon as the SW temperature started a rapid increase around 11h20 in the late morning, the effects of the BSS SW pre-heating contributions were not apparent. Therefore, since the thermal energy was supplied from both the BSS and the evaporator, especially considering Figure 5.2, the effects of the BSS, specifically in terms of SW pre-heating, could not be established. The apparent influence from the BSS to stages of SW was apparent early in the morning. Moreover, stage 5 showed a clear response from the BSS thermal energy supply. Stages 1 to 4 SW temperature trends showed minimal response, especially stage 3 (see Table 5.5) by the average temperatures. That is, both SW temperature curves in the BSS and stage 5 started to increase before any other curves early in the morning.

The BSS was influenced by the high average solar irradiance with positive mode of thermal energy, as shown by Figures 5.20, 5.24, 5.26 and 5.27. The BSS SW temperature curves

followed the same path as the stages on the above-mentioned figures. This was evidence that the BSS acted as both the heat recovery compartment and fed the system with pre-heated SW. At low to moderate solar insolation, the BSS SW temperature curves followed their own path. Figure 5.55 shows the SW pre-heating on the days discussed in Table 5.4, plotted in ascending order from the lowest average solar irradiance to the highest. The temperature curves in Figure 5.55 show that when the thermal insulation material was removed from the condensing tower, the pre-heating effects in stage 5 also decreased despite the BSS continuing with the same pattern. Therefore, the ability of the BSS to supply pre-heated SW was limited by the heat losses in stage 5.

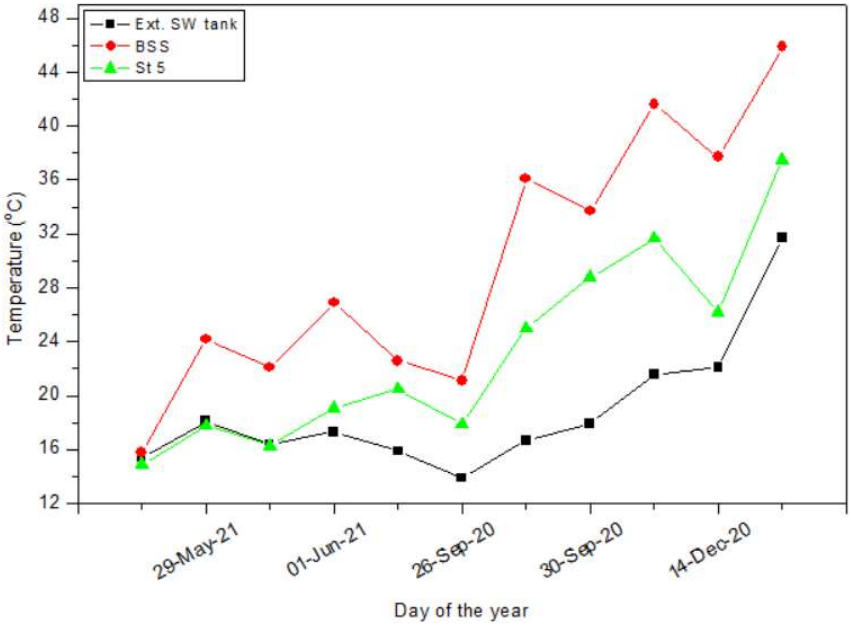

Figure 5.55: Average SW temperature vs day of the year

5.16 Effect of the height of the vapour-based MSS-SS

One of the observed impediments to the vapour flow and ultimately the daily cumulative distillate yield was the total height of the system (Ahmed et al., 2009). Total height refers to the vertical height between the evaporator and the last stage (stage 5). All the stages were supplied through vapour make-up tubes with the vapour. Therefore, the further away the stages were from the evaporator, the longer the vapour make-up tube must be. This ultimately meant that the vapour must travel a longer vertical distance (upwards) to reach the stages. In addition, the vapour had a larger area (vapour make-up tube surface area) to heat-up before it reached the stage. As discussed earlier, for the vapour to reach the stages, thermal equilibrium must be established between the vapour and the vapour make-up tubes. The vapour not only heats the tube, but it must also maintain the tube's temperature to prevent premature condensation in the tubes. In other words, the vapour must maintain thermal

equilibrium between itself and the tube's inner walls. Otherwise, the vapour will condense inside the tubes and fail to reach its destination. In fact, in a vapour-based MSS-SS, vapour condensing prematurely and failing to reach its destination was observed at low solar intensities. For instance, at lower solar intensities such as those on the 16th and 17th of June 2021, the evaporator SW temperature increased (see Figure 5.56). However, no distillate was produced as not enough thermal energy was produced to overcome the thermal obstacles. Ideally, the thermal insulation material should create a thermal boundary layer to prevent heat losses and thus prevent prolonged vapour premature condensation in the vapour make-up tubes.

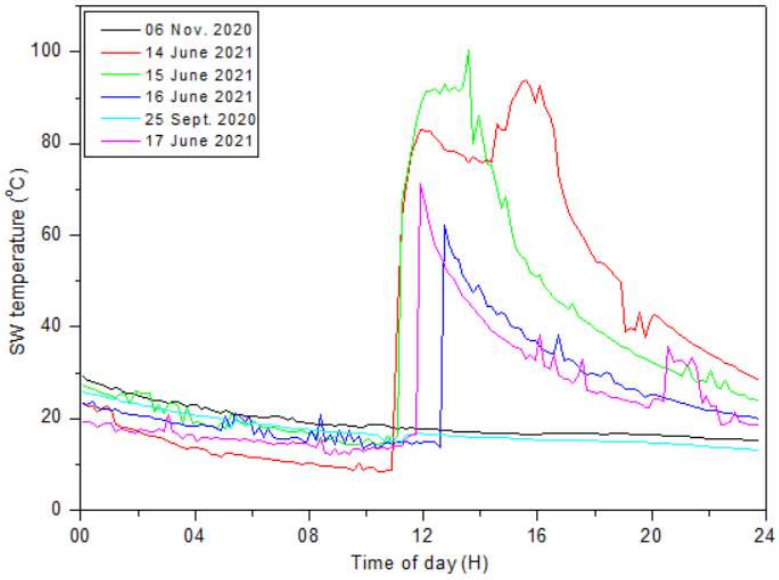

Figure 5.56: Evaporator SW temperature vs time of day

At higher solar intensities with higher rates of thermal energy input, the obstacles caused by the vertical height were overcome more effectively. In fact, at moderate to higher solar intensities, some stages even reached thermal damage and the thermal insulation material had to be removed. At higher solar intensities, the upper most stage (stage 5) tended to be the most productive stage in the condensing tower. This was the opposite at low solar intensities as stage 1, 2 and 3, in that respective order, tended to be more productive. Therefore, in respect of the vapour-based MSS-SS, the challenges caused by the lengths of the vapour make-up tubes and ultimately the total vertical height of the system diminished with increasing solar intensity. These challenges were not fixed under any solar intensity values but rather transitional.

5.17 Economic analysis of the vapour-based MSS-SS

The distillate cost per litre or kg had been reported in the literature. However, due to different construction requirements from the various systems, the costs reported fluctuated. For instance, Saeedi et al. (2015) reported that in India, bottled water cost Rs. (Rupees) 10/kg while the cost of distilled water using a PV/T active solar still was Rs. 1.93/kg. There was a possibility of reducing the cost of distilled water to Rs. 1.5/kg when heat recovery and SW preheating occurred in the active solar still. On the other hand, Soni et al. (2017) reported that for an adaptable wind/solar powered hybrid system, the cost ranged from Rs. 0.5 – 1.2/kg. The cost of the distillate of the vapour-based MSS-SS was computed using the equations reported in Chapter 4, section 4.11. The analysis was done by Microsoft excel using the average distillate yield values. The CPL results are tabulated in Appendix B7. For the purpose of analysis, 260 clear sky days were assumed. The bank's landing interest rate, i, was estimated at 15% for funding. The system's estimated life expectancy in number of years, n, was assumed to be 12 years.

Due to other experimental tests, repairs and maintenance on the vapour-based MSS-SS, the system was either non-operational or not fully operation. For instance, with the experimental observation discussed in section 5.7, the condensing tower was not producing the distillate at its full capacity. Moreover, during maintenance and repairs, the system was stopped altogether from producing the distillate. Therefore, the days with interruptions were excluded from the estimation of the CPL.

When considering all the days when the system was producing the distillate at full capacity, the daily cumulative distillate yield was 7790 ml (4.9 litres) and 6730 ml (6.73 litres) for the MSS-SS plus the BSS and the MSS-SS stages alone, respectively. In addition, the days when the distillate yield was deemed non-measurable (NM) were excluded from the productive days. The daily cumulative distillate yield values considered the maximum distillate yield which occurred on the 13th of Jan 2021. The capital cost for the vapour-based MSS-SS was estimated to be R38 000 plus the collection of raw water at R 2000 (South African Rands).

When the vapour-based MSS-SS was assumed to operate at its optimum, the distillate yield values were 7790 ml and 6730 ml for MSS-SS plus the BSS and MSS-SS stages only. However, based on the actual data, the vapour-based MSS-SS was estimated to produce 4887.94 ml/day excluding the yield from the BSS on average. The MSS-SS stages plus the BSS yield was found to be 4329.6 ml/day. The CPL for the MSS-SS stages alone was found to be R4.69/litre. Meanwhile, the CPL for the MSS-SS plus the BSS combined was found to be R4.05/litre. Therefore, producing distilled water from the MSS-SS stages alone was more expensive when compared to the MSS-SS plus the BSS. According to the DWS (2019)

national water and sanitation master plan, the municipal cost of producing water was R6/m^3. Therefore, the vapour-based MSS-SS in its current design was too expensive compared to the municipal costs to produce water. When the CPL was converted to US dollars per litre ($/litre), the costs were 0.33 and 0.28$/litre for the MSS-SS stages and the combined MSS-SS plus the BSS. Comparing the CPL of 0.33 and 0.28$/litre to that of the desalination systems tabulated in Table 2.9, the vapour-based MSS-SS show that its CPL is higher. The sample calculations of the CPL are provided in Appendix A-5 and the calculated CPL results are tabulated in Appendix B-2.

CHAPTER SIX
CONCLUSIONS AND RECOMMENDATIONS

6.1 Conclusion

A vapour-based MSS-SS system integrated with a passive single slope solar still (BSS) was developed based on literature reviewed. The BSS was modified slightly to accommodate the float valve for regulating SW flow from the external SW tank. Different parts of the system were manufactured, as outlined in Chapter 3, and the system was constructed, assembled and experimentally tested under Cape Town weather conditions at Cape Peninsula University of Technology (CPUT), Bellville. The experimental tests were conducted through four seasons – over a full year, beginning spring (Sept. 2020) to winter (June 2021). Based on the aims and objectives of the current study, the conclusions follow.

A vapour-based MSS-SS was successfully developed and experimentally tested under actual weather conditions. It was established that the distillate yield trend from the stages varied with the prevailing daily average solar irradiance. At low average solar irradiance between 0 W/m^2 to 199 W/m^2, the lower stages (i.e., stage 1) proved to be the most productive stage in the system. This was associated with the low rate of thermal energy input into the condensing tower through the evaporator. In fact, there was a minimum operating condition in terms of the average solar irradiance which was estimated to be approximately 145.1 W/m^2. Under this average of 145.1 W/m^2, the condensing tower produced non-measurable (NM) quantities of distillate. Furthermore, the observed obstacle for vapour flowing through the vapour make-up tubes under low average solar irradiance was the temperature gradient between the vapour and the vapour make-up tubes inner walls. This larger temperature gradient caused premature vapour condensation in the vapour make-up tubes and prevented the vapour from successfully reaching the stages, especially the upper stages. This premature vapour condensation had a direct impact of the daily cumulative distillate yield. Therefore, the distillate yield recorded ranged from NM to 1380 ml (1.38 litres) under the low average solar irradiance. This daily cumulative distillate yield of 1380 ml comprised of the MSS-SS stages yield at 1270 ml and 110 ml from the BSS. Moreover, the numerically calculated overall vapour-based MSS-SS thermal energy efficiency was at 18.23%, as shown by the sample results in Appendix A-4, while thermally insulated.

However, at moderate average solar irradiance ranging between 200 W/m^2 to 399 W/m^2, the distillate yield trend changed and stages 2 and 3 were the most productive stages. This was an indication of an increased rate of thermal energy supply into the condensing tower. This was evident by the thermal damage condition experienced by some of the stages (i.e., stages

1 and 4). At moderate average solar irradiance, the condensing tower also revealed that the cooling SW in the zigzagged SW tube was inadequate for the amount of vapour contained by the vapour, hence, thermal damage condition. In fact, the partial thermal damage condition was experienced at average solar irradiance values of as low as 209.9 W/m^2. However, the average solar irradiance value was not the final deciding factor, the solar irradiance curve patterns throughout the day were instrumental in causing the thermal damage condition. Factors such as the mode of thermal energy input (positive of impulse), the crests, the troughs and the period between the last crest and the next were instrumental. Despite the partial thermal damage experienced by the condensing tower, there was an increased daily cumulative distillate yield under the moderate range of the average solar irradiance. In addition, the distillate improved further when operating under uninsulated conditions within the average solar irradiance range.

The maximum under this range was 5830 ml (5.83 litres) on the 18th of Feb. 2021 for the MSS-SS stages, and 510 ml (0.51 litres) for the BSS driven by the average solar irradiance of 323.7 W/m^2. When thermally insulated, the maximum distillate yield was 5690 ml (5.7 litres) on the 17th of Mar. 2021 for the MSS-SS stages, and 820 ml (0.82 litres) for the BSS driven by the average solar irradiance of 301.8 W/m^2. Even though not directly proven, the thermal damage condition was suspected as causing vapour leaks from the stages rendering relatively low distillate output from the thermally insulated condensing tower. The maximum operating conditions were observed within the moderate solar irradiance range. However, since there was more than one factor contributing to thermal damage – such as the small quantity cooling SW in the stages, the mode of thermal energy input, wind velocity and ambient air temperature – the maximum operating conditions were dependent. For instance, on the 1st of June 2021, the condensing tower partially reached thermal damage at an average solar irradiance of 209.9 W/m^2. However, on the 26th of Sept. 2020, at an average of 253.7 W/m^2, there was no thermal damage condition.

Under higher average solar irradiance ranging from 400 W/m^2 to 600 W/m^2, the condensing tower was completely uninsulated. The condensing tower in its current design had already reached its maximum operating conditions, hence, the removal of the thermal insulation. The difference in condensing surface behaviours can be observed in sections 5.3 and 5.4 under the high range of solar irradiance and with and without thermal insulation material. Under the uninsulated conditions, the wind velocity played a significant role in increasing the temperature difference between the evaporative and condensing surfaces in the condensing tower. Furthermore, the maximum daily cumulative distillate yield was recorded at 6730 ml (6.73 litres) for the MSS-SS stages, and 1060 ml (1.1 litres) for the BSS driven by an average solar

irradiance of 585 W/m^2. When the condensing tower was thermally insulated under the high range of solar irradiance it tended to behave as demonstrated under section 5.3. The CPL estimated for the higher average solar range on the 13th of Jan. 2021 without any thermal insulation material was R4.69 per litre for the MSS-SS stages. Meanwhile, it was R4.05 per litre for the MSS-SS and the BSS. These results are shown in Appendix A-5.

In terms of the stages' dependency/independency, it was experimentally observed that the upper stages were not operating entirely independently when increased heat loss (i.e., atmospheric exposure) was experienced in the lower stages. Under relatively cooler and windy days with low average solar irradiance, there was a notable decline in the daily cumulative distillate yield during atmospheric exposure experiments. This distillate yield decline was associated with the cooling of the vapour make up tubes which supplied the vapour to the upper stages. The cooling of the vapour make-up increased the temperature gradient between the vapour and the vapour make-up tubes' inner walls, resulting in the premature vapour condensation of the vapour in the vapour make-up tubes. As a result, there was a reduction of about 5.8 to 41.3% of the distillate yield. The decline of about 41.3% occurred under the combination of an impulse mode of thermal, low rate of thermal energy input and higher wind velocity. Moreover, as discussed in section 5.6, the SW pre-heating was also affected by the increased heat loss from the condensing tower.

When there were no increased heat losses in the lower stages (i.e., atmospheric exposure), the upper stages showed a different distillate yield trend altogether. Plugging off the vapour make-up tubes of stages 1 and 2 redirected the vapour from the plugged off stages to those that were operational, likely due to the pressure difference between the evaporator and the operational stages. The vapour redirection was also observed when the condensing tower reached thermal damage condition. That is, the stages which maintained moderate temperature tended to be more productive under moderate to higher average solar irradiance. There was an increase in the distillate yield ranging from 7.1 to 15.4% compared to normal operating stages driven by an approximately equal average solar irradiance. However, these values depended on various factor such as the mode of thermal energy input (positive of impulse), the crests, the troughs and the period between the last crests. It has been established that the stages of the vapour-based MSS-SS can operate fully when the lower stages are not. They were only affected by the increase in heat loss to the surroundings due to the vapour leaks and atmospheric exposure of the lower stages.

In terms of the contamination in the stages of the condensing tower, observations made during the experimental tests determined no contamination in the stages in terms of salt deposits or

foreign particles. The stages were sealed, and the pure water vapour accessed the stages through the vapour make-up tubes. Furthermore, the U-shaped tubes which contained water, as discussed in section 3.9, acted as the vapour trap devices thereby preventing any foreign particles from accessing the stages. Therefore, as discussed in section 5.10, the stages experienced no salt deposit or any foreign contamination; no maintenance was required. In addition, the zigzagged SW tube experienced no fouling, as shown in section 5.10, and therefore, the heat transfer between the vapour and the SW in the zigzagged SW tube was not affected by salt deposit contamination. With respect to other compartments of the condensing tower such as the BSS, secondary SW tank and the external SW tank, there was contamination and these compartments required cleaning and maintenance.

In terms of the developing a standalone system, based on the experimental tests, a standalone system was successfully developed. The vapour-based MSS-SS operated without any additional external sources with regards to electricity or otherwise. For a period of 10 months and even more, the system was driven by the impulse circulation (pressure differential) which required only the heat from the sun (solar irradiance). However, as discussed earlier, under a certain average solar irradiance, not enough heat was collected and thus no SW circulation, no SW temperature increase and ultimately, no distillate yield. This was referred to as a 'minimal operating condition' of the system. Moreover, the standalone ability was enhanced by the remotely controlled SW flowing from the external tank, BSS, stages, secondary SW tank and into the evaporator. The size of the external tank determined how long the system could operate before requiring human intervention to refill the SW.

In terms of minimising human intervention in the operation of the system, as alluded to above, to increase the time the system can operate without any human assistance, a simple but effective concept of float valves was integrated into the condensing tower. With the 20-litre capacity of the external SW tank, discussed under section 3.3, the system operated up to a week under a moderate range of solar irradiance, that is, when consecutive days had moderate range of the average solar irradiance (i.e., 200 to 399 W/m^2) which caused moderate to high evaporation rates in the evaporator. Under high average solar irradiance range (i.e., spring and summer), the system could operate from three to five days. However, at low average solar irradiance, the operational period was longer depending on the average solar irradiance on those consecutive days. Therefore, the combination of the impulse circulation and the float valve did not need a manual open or shut, or a start or stop of any components of the vapour-based MSS-SS.

In terms of brine solution re-circulation, the effects of recirculating the brine solution was that it maintained SW temperatures in the evaporator at high levels. That is, in addition to the pre-heated SW in the secondary SW tank, the re-circulated brine solution further heated the SW from the secondary SW tank as it entered the evaporator, preventing a reduction in the rate of evaporation by maintaining higher SW temperatures in the evaporator. From sections 5.1 to 5.4, it is evident that the secondary SW temperature remained relatively lower than that of the evaporator. Furthermore, the evaporation rate in the evaporator depended on the prevailing average solar irradiance and so did the salt content accumulation in the external tubing. However, as discussed in sub-sections 5.11.1 and 5.11 2, there was minimal salt content build-up on the inner surfaces of the external tubing associated with the SW circulation which kept the dissolved solids suspended in SW. There was a degree of contamination, as shown by Figures 5.51 and 5.52. Additionally, the crystallised salt was ejected through the evaporator hole, discussed under Figure 5.53. When the flushing out of SW was carried out or during maintenance, small foreign particles were observed from the brine solution. These small particles were perceived to be washed off the inner surfaces of the tubing as the SW circulated. Even though inconclusive, the impulse circulation of the SW potentially aided in reducing the fouling in the entire tubing.

In terms of minimising the quantity of SW heated by the solar collector at a time, it can be observed that the minimal SW began to respond to the thermal energy supplied and produced some distillate at as low as 155.5 W/m^2 on average on the 31st of March 2021. The distillate yield and the solar irradiance curve results are presented in Table 5.6 and Figure 5.37, respectively. This was a direct result of heating and impulsively circulating approximately 0.5 kg of SW at a time. The minimal SW, as discussed under section 5.5, had an advantage of increasing its temperature rapidly and maintaining values around 90°C throughout the day. This translated to enhanced evaporation in the evaporator and thus increased vapour production. However, its main disadvantage was its sensitivity due to its small capacity to store thermal energy. As such, it tended to fluctuate according to the prevailing solar irradiance resulting in a fluctuating vapour supply to the stages. Moreover, the sharp decline in its SW temperature later in the day revealed increased heat losses which may have been due to inadequate thermal insulation as well as the minimal SW quantity in the system. Sharp increases were observed to occur much earlier in late spring and summer which increased the vapour production duration beyond late autumn and winter. The sharp decline under late spring and summer conditions was reduced and the SW maintained a higher temperature around midnight at the end of the day. However, the study was unable to incorporate the measuring device for the SW flow rate in the external tubing as per the objective.

In terms of creating a circulating waterbed in the entry stage, also known as a dynamic mode as defined under Figure 2.1, the SW circulation was linked with factors such as contamination in the open loop, standalone ability, minimising human intervention, recirculating brine solution and a minimal SW quantity in the entry stage. The convective heat transfer which involved bulk fluid in motion was the primary reason for circulating the SW in the open loop circuit. However, in the interest of narrowing the study to the development of the vapour-based MSS-SS, the effects of the flowing waterbed over the stagnant waterbed were not specifically studied. Nevertheless, the SW was successfully circulated by means of pressure differential before and after the non-return valve, as discussed under sub sub-section 3.15.3. The SW circulation, which yielded some small quantities of distillate, was initiated as average solar irradiance of 155.5 W/m^2 and above. The circulation of the SW enabled the factors mentioned above to be a realised. Thus, a prerequisite for minimal operating conditions was the failure of the heated SW to be delivered into the evaporator and initiate the desalination process which was around 145.1 W/m^2 on average. However, the solar irradiance curve progression was instrumental in the producing adequate heat to start the desalination: at low average solar irradiance, the positive mode of thermal input was desirable.

In terms of directly heating the SW open loop circuit, the direct heating eliminated the need for an additional heating transfer fluid (HTF) in the open loop circuit, as discussed under section 5.14. It reduced the cost component of the overall installation and operation. In theory, it minimised the heat loss that would have occurred between the ETSCs, HTF and SW. The increase in the salinity in the SW depended on the evaporation rate in the evaporator. On consecutive days with high average solar irradiance, the flushing out of SW was carried out in a week or less. However, under low to moderate average solar irradiance, the flushing out process took 14 days or more. The fouling in the tubing was as described under section 5.11.1. For all the days the system was experimentally tested, the evaporator SW temperature typically fell within the range of 90 to 95°C, occasionally exceeding boiling point and reaching 101.3°C, as shown in Figure 5.46.

6.2 Recommendations

The changing daily distillate yield trend of the stages under varying daily solar irradiance was perceived to be associated with the ability of stage surfaces to effectively cool down and condense the vapour. Due to thermal damage condition occurring in the condensing tower, a decreased distillate yield was experienced in those stages which were operating at thermal damage condition. The moderate temperature maintained by stage 5 shows that this stage tended to yield more distillate. Therefore, it is recommended that increased cooling SW in the stages be implemented to recover the latent heat from the vapour without reaching thermal damage. This increase in cooling water could also change the distillate yield trend as it were and prevent thermal damage condition.

In terms thermal damage conditions or maximum operating conditions, it was observed that the condensing tower partially reached thermal damage conditions as low as 209.9 W/m^2 on average. Firstly, it is recommended that a thermal energy storage device be augmented at moderate and higher average solar irradiance to prevent thermal damage conditions. This is due to the much larger collector area-to-basin (CBA) ratio. It was evident that the system could not operate at higher rate of thermal energy input, as shown in Figures 5.19 and 5.20 (Feilizadeh et al., 2015). Secondly, as described in the previous paragraph, the amount of cooling SW in the stages was grossly inadequate; this was shown by the condensing tower reaching thermal damage condition at an entry level of the moderate average solar irradiance. Thus, it is recommended that the amount of incoming SW from the external tank through the BSS and the stages be increased significantly to sufficiently cool the vapour without the system reaching thermal damage condition. Furthermore, the small quantities of cooling water require that the thermal insulation material be removed to prevent thermal damage condition and wind velocity be used as a cooling medium.

In terms of the material for construction of the system linked with quality of the distillate, a food-grade material is recommended to eradicate any post-treatment processes of the distillate produced by the system. Aluminium and copper material tended to react with SW and cause further contamination in water. Material such as stainless steel (food-grade material) is recommended for used in the system. Replacing material such as aluminium, copper and plastic tubes with food-grade material may eradicate the need for post-treatment and eliminate the associated costs.

It is recommended that an appropriate weather station such as the Campbell Scientific-SP-LITE silicon pyranometer used by Mbadinga (2015) be used to accurately measure the total and diffuse solar radiation components on a horizontal surface. The estimation equations used

in the current study showed numerous errors in computing the various components of solar radiation.

Experimentally testing the independence involved various factors in the process such the non-uniform daily solar irradiance, wind velocity, wind direction and ambient conditions. As the results took those factors into account, they may have overestimated the decrease in the distillate yield. An indoor simulation with uniform thermal energy supply may yield conclusive results. Therefore, it is recommended that the stage dependency/independency experiment be conducted under simulated conditions.

An improved float valve which can operate and regulate SW with low SW depth is recommended in the BSS. This improved valve will ensure the system is maintained with the pre-set quantity of SW in the system to prevent over-heating due to insufficient water. Furthermore, a larger external SW tank will ensure a longer period of operation for the system. It is also recommended that float valves be constructed from suitable material to withstand elevated temperature in a range of 90-100°C in both the BSS and the secondary SW tank.

The sealing rubber material of the non-return valve, shown in Figure 3.16.3, revealed deterioration over time with constant contact with SW. When the sealing rubber was worn out, it could not seal SW properly; the one directional flow was affected. It is therefore, recommended that the sealing rubber material be made from material resistant to SW; this will ensure that the life span of the sealing rubber is elongated. Furthermore, due to low operating pressure of the external tubing, the spring-loaded non-return valve was unsuitable in the circulation of SW. The swing type no-return valve proved more appropriate for the vapour-based set-up. In addition, since no SW pumps were used, the SW was circulated by means of pressure differential. Therefore, the non-return valve should be positioned as shown in Figure 3.74. The upstream (inlet side) must be positioned higher than the downstream (outlet side). This position encouraged the bulk flow of SW from the evaporator into the ETSCs.

Another recommendation is a study to establish the extent of the effects of the vapour make-up tube in terms of premature vapour condensation in the tubes. This will assist in determining an ideal overall height of the condensing tower, as discussed under section 5.16. It was observed that the lower stages tend to be more productive at low average solar irradiance. This was associated with the length of the vapour make-up tubes to the upper stages. Therefore, reducing the overall height of the condensing tower and the vertical lengths of the vapour make-up tubes will allow more vapour to access the stages.

When the system heats and evaporates the saline water, it leaves behind salt residue which may have a negative effect on the effectiveness of the solar panel to heat and evaporate saline water. The system must be flushed occasionally to remove the excess salt in the ETSC manifold, tubes and the evaporator. Citric or oxalic acids are not harmful and so can be used to reduce fouling in the tubing (Salem, 2013). The crystallized salt residue that is left behind after heating, evaporating and condensing the vapour can be extracted from the system, dried and after thorough analysis of the residue, can be used as salt for domestic purposes.

The impulse circulation should be studied further to learn more about its characteristics. It has been reported in the literature that heat exchange through convection had the highest rate of heat transfer compared to the other two mechanisms (radiation and conduction). Thus, the combination of SW circulation and minimal SW in the evaporator may have an added advantage over the stagnant waterbed.

Bibliography

Abdelkareem, M.A., Assad, M.E.H., Sayed, E.T., Soudan, B., 2018. Recent progress in the use of renewable energy sources to power water desalination plants. *Desalination*, 435, 97-113.

Abdenacer, P.K., Nafila, S., 2007. Impact of temperature difference (water-solar collector) on solar-still global efficiency. Desalination, 209 (1-3), 298-305.

Abdessemed, A., Bougriou, C., Guerraiche, D., Abachi, R., 2019. Effects of tray shape of a multi-stage solar still coupled to a parabolic concentrating solar collector in Algeria. *Renew. Energy*, 132, 1134-1140.

Abujazar, M.S.S., Fatihah, S., Rakmi, A.R., Shahrom, M.Z., 2016. The effects of design parameters on productivity performance of a solar still for seawater desalination: A review. *Desalination*, 385, 178-193.

Aburideh, H., Deliou, A., Abbad, B., Alaoui, F., Tassalit, D., Tigrine, Z., 2012. An experimental study of a solar still: Application on the sea water desalination of Fouka. *Procedia Eng.,* 33, 475-484.

Adeala, A.A., Huan, Z., Enweremadu, C.C., 2015. Evaluation of global solar radiation using multiple weather parameters as predictors for South Africa provinces. *Therm. Sci.,* 19 (suppl. 2), 495-509.

Adhikari, R.S., Kumar, A., Garg, H.P., 2000. Techno-economic analysis of a multi-stage stacked tray (MSST) solar still. *Desalination*, 127 (1), 19-26.

Adhikari, R.S., Kumar, A., Sootha, G.D., 1995. Simulation studies on a multi-stage stacked tray solar still. *Sol. Energy*, 54 (5), 317-325.

Ahmed, M.I., Hrairi, M., Ismail, A.F., 2009. On the characteristics of multistage evacuated solar distillation. *Renew. Energy*, 34 (6), 1471-1478.

Ahsan, A., Imteaz, M., Thomas, U.A., Azmi, M., Rahman, A., Daud, N.N., 2014. Parameters affecting the performance of a low cost solar still. *Appl. Energ.,* 114, 924-930.

Al-Abbasi, M.A., Al-Karaghouli, A.A., Minasian, A.N., 1992. Photochemically assisted solar desalination of saline water. *Desalination*, 86 (3), 317-324.

Al-Hinai, H., Al-Nassri, M.S., Jubran, B.A., 2002a. Effect of climatic, design and operational parameters on the yield of a simple solar still. Energ. Convers. and Manag., 43 (13), 1639-1650.

Al-Hinai, H., Al-Nassri, M.S., Jubran, B.A., 2002b. Parametric investigation of a double-effect solar still in comparison with a single-effect solar still. Desalination, 150 (1), 75-83.

Aliyu, A.K., Modu, B., Tan, C.W., 2018. A review of renewable energy development in Africa: A focus in South Africa, Egypt, and Nigeria. *Renew. and Sust. Energ. Rev.,* 81, 2505.

Alkaisi, A., Mossad, R., Sharifian-Barforoush, A., 2017. A review of the water desalination systems integrated with renewable energy. *Energy Procedia*, 110, 268-274.

Al-Karaghouli, A., Renne, D., Kazmerski, L.L., 2009. Solar and wind opportunities for water desalination in the Arab regions. *Renew. and Sust. Energ. Rev*., 13 (9), 2397-2407.

Alkhadra, M.A., Gao, T., Conforti, K.M., Tian, H. and Bazant, M.Z., 2020. Small-scale desalination of seawater by shock electrodialysis. Desalination, 476, 114219.

Al-Nimr, M.A., Dahdolan, M.-E., 2015. Modeling of a novel concentrated solar still enhanced with a porous evaporator and an internal condenser. Sol. Energy, 114, 8-16.

Al-Othman, A., Darwish, N.N., Qasim, M., Tawalbeh, M., Darwish, N.A., Hilal, N., 2019. Nuclear desalination: A state-of-the-art review. *Desalination*, 457, 39-61.

Alsehli, M., Choi, J.K., Aljuhan, M., 2017. A novel design for a solar powered multistage flash desalination. *Sol. Energy,* 153, 348-359.

Al-Shammiri, M., 2002. Evaporation rate as a function of water salinity. *Desalination*, 150 (2), 189-203.

Al-Tabbakhand, A.A., Mohammed, A.A., 2017. Experimental Investigation of an Evacuated Tube Solar Air Collector. *Adv. in Natural and Appl. Sci*., 11 (11), 62-71.

Altarawneh, I., Rawadieh, S., Batiha, M., Al-Makhadmeh, L., Alrowwad, S., Tarawneh, M., 2017. Experimental and numerical performance analysis and optimization of single slope, double slope and pyramidal shaped solar stills. *Desalination*, 423, 124-134.

Arunkumar, T., Jayaprakash, R., Denkenberger, D., Ahsan, A., Okundamiya, M.S., Tanaka, H., Aybar, H.Ş., 2012. An experimental study on a hemispherical solar still. *Desalination*, 286, 342-348.

Asmus, P., 2005. Intermittency solutions: Making Intermittent renewable sources work for California… and the USA. *Refocus*, 6 (2), 36-38.

Aves, M., 2011. Experimental enhancement of single slope solar still (Doctoral dissertation, King Fahd University of Petroleum and Minerals (Saudi Arabia)).

Ayoub, G.M., Malaeb, L., 2014. Economic feasibility of a solar still desalination system with enhanced productivity. *Desalination*, 335 (1), 27-32.

Baatjies, W.J. 2014. Management of water shortages in selected municipality in the Eden district, South Africa. MTech thesis, Cape Peninsula University of Technology, Cape Town.

Badenhorst, H., 2018. Solar energy for desalination and water purification using carbon materials. Water Research Commission, Pretoria, South Africa. [Online] Available from: http://www.wrc.org.za/wp-content/uploads/mdocs/2467-1-17.pdf [Accessed 05 February 2020].
Badran, A.A., Al-Hallaq, I.A., Salman, I.A.E., Odat, M.Z., 2005. A solar still augmented with a flat-plate collector. *Desalination*, 172 (3), 227-234.
Badran, O.O., Al-Tahaineh, H.A., 2005. The effect of coupling a flat-plate collector on the solar still productivity. *Desalination*, 183 (1-3),137-142.
Bait, O., Si–Ameur, M., 2016. Numerical investigation of a multi-stage solar still under Batna climatic conditions: effect of radiation term on mass and heat energy balances. *Energy*, 98, 308-323.
Binns, J.A., Illgner, P.M., Nel, E.L., 2001. Water shortage, deforestation, and development: South Africa's working for water programme. *Land Degrad. Develop.* 12, 334; 342.
Bos, R., Roaf, V., Payen, G., J Rousse, M., Latorre, C., McCleod, N., Alves, D., 2016. Manual on the Human Rights to Safe Drinking Water and Sanitation for Practitioners. p. 24. IWA Publishing.
Bosman, H.H., 1983. Spectral differences in glass and perspex thermopile shields and the effects on solar radiation measurements. *Agric. Meteorol.,* 28 (1), 65-74.
Bouzaid, M., Ansari, O., Taha-Janan, M., Mouhsin, N., Oubrek, M., 2019. Numerical analysis of thermal performances for a novel cascade solar desalination still design. *Energy Procedia*, 157, 1071-1082.
Bundschuh, J., Hoinkis, J. eds., 2012, p. 6. Renewable energy applications for freshwater production. CRC Press.
Buros, O.K., 2000. The ABCs of desalting. Topsfield, MA: International Desalination Association. [Online] Available from: https://water.ca.gov/LegacyFiles/pubs/surfacewater/abcs_of_desalting/abcs_of_desalting.pdf [Accessed 18 April 2020].
Bwapwa, J.K., 2018. Review on main issues causing deterioration of water quality and water scarcity: case study of South Africa. Environ. Manag. Sustain. Dev., 7 (3), 14-15.
Campione, A., Gurreri, L., Ciofalo, M., Micale, G., Tamburini, A., Cipollina, A., 2018. Electrodialysis for water desalination: A critical assessment of recent developments on process fundamentals, models, and applications. Desalination, 434, 121-160.
Cengel, Y. and Heat, T.M., 2003. *A practical approach*. New York, NY, USA: McGraw-Hill.
Çengel, Y.A., Turner, R.H., Cimbala, J.M. and Kanoglu, M., 2008. *Fundamentals of thermal-fluid sciences* (Vol. 703). New York: McGraw-Hill.
Chafidz, A., Kerme, E.D., Wazeer, I., Khalid, Y., Ajbar, A., Al-Zahrani, S.M., 2016. Design and fabrication of a portable and hybrid solar-powered membrane distillation system. J. Clean. Prod., 133, 631-647.
Chandrashekara, M., Yadav, A., 2017. Water desalination system using solar heat: a review. *Renew. and Sust. Energ. Rev.,* 67, 1308-1330.
Chen, Z., Peng, J., Chen, G., Hou, L., Yu, T., Yao, Y., Zheng, H., 2017. Analysis of heat and mass transferring mechanism of multi-stage stacked-tray solar seawater desalination still and experimental research on its performance. *Sol. Energy*, 142, 278-287.
Chinyama, A., Ochieng, G.M., Snyman, J., Nhapi, I., 2016. Occurrence of cyanobacteria genera in the Vaal Dam: implications for potable water production. *Water SA*, 42 (3), 415.
City of Cape Town. 2017. Level 4 water restrictions frequently asked questions. [Online] Available from: http://gpokcid.co.za/wp-content/uploads/2017/06/Water-restrictions-FAQs.pdf[19 January 2021].
Coetzee, K., 2011. Climate Change and Trade: The Challenges for Southern Africa. SA J. of Int. Affairs., 18 (1), 136.
Crouse, A., 1986. The protection of water sources in developing countries. Doctoral dissertation, Cape Technikon, Cape Town.
Diaf, A., Cherfa, A., Karadaniz, L., Tigrine, Z., 2016. A technical–economical study of solar desalination. *Desalination*, 377, 123-127.
Delyannis, E., 2003. Historic background of desalination and renewable energies. *Sol. energy,* 75 (5), 358-359.
Diez, F.J., Martínez-Rodríguez, A., Navas-Gracia, L.M., Chico-Santamarta, L., Correa-Guimaraes, A. and Andara, R., 2021. Estimation of the hourly global solar irradiation on the tilted and oriented plane of photovoltaic solar panels applied to greenhouse production. *Agronomy*, *11* (3), 495.
Duffie, J.A. and Beckman, W.A., 2013. *Solar engineering of thermal processes*. John Wiley & Sons.
Elango, C., Gunasekaran, N., Sampathkumar, K., 2015. Thermal models of solar still-a comprehensive review. *Renew. and Sust. Energ. Rev*., 47, 856-911.
Elango, T., Murugavel, K.K., 2015. The effect of the water depth on the productivity for single and double basin double slope glass solar stills. *Desalination*, 359, 82-91.

El-Bahi, A., Inan, D., 1999. A solar still with minimum inclination, coupled to an outside condenser. *Desalination*, 123 (1), 79-83.
El-Bialy, E., Shalaby, S.M., Kabeel, A.E., Fathy, A.M., 2016. Cost analysis for several solar desalination systems. *Desalination*, 384, 12-30.
El-Sebaii, A.A., 2011. On effect of wind speed on passive solar still performance based on inner/outer surface temperatures of the glass cover. *Energy*, 36 (8), 4943-4949.
Eltawil, M.A., Zhengming, Z., Yuan, L., 2009. A review of renewable energy technologies integrated with desalination systems. *Renew. and Sust. Energ. Rev*., 13 (9), 2245-2262.
Estahbanati, M.K., Feilizadeh, M., Jafarpur, K., Feilizadeh, M., Rahimpour, M.R., 2015. Experimental investigation of a multi-effect active solar still: the effect of the number of stages. *Appl. Energy*, 137, 46-55.
Faegh, M., Shafii, M.B., 2017. Experimental investigation of a solar still equipped with an external heat storage system using phase change materials and heat pipes. *Desalination*, 409, 128-135.
Fant, C., Schlosser, C.A., Strzepek, K., 2016. The impact of climate change on wind and solar resources in southern Africa. *Appl. Energy*, 161, 556-564.
Fath, H.E., 1998. Solar distillation: a promising alternative for water provision with free energy, simple technology and a clean environment. *Desalination,* 116 (1), 45-56.
Fath, H., Jayswal, N. and Qadir, A., 2013. Novel multiple effect direct solar distillation system of integrated solar still and HDH system. *Desalination and water treatment*, *51*(4-6), 1319-1326.
Fath, H.E., El-Samanoudy, M., Fahmy, K., Hassabou, A., 2003. Thermal-economic analysis and comparison between pyramid-shaped and single-slope solar still configurations. *Desalination*, 159 (1), 69-79.
Feilizadeh, M., Estahbanati, M.K., Ardekani, A.S., Zakeri, S.M.E., Jafarpur, K., 2015. Effects of amount and mode of input energy on the performance of a multi-stage solar still: an experimental study. *Desalination*, 375, 108-115.
Firozuddin, S., Ahmad, M.A.N., 2014. Single Basin Solar Still Performance with Evacuated Tubes Solar Collector. *IOSR Journal of Mechanical and Civil Engineering (IOSR-JMCE*), 2278-1684.
Franco, J., Saravia, L., 1994. A new design for a passive atmospheric multistage still. *Renew. Energy,* 4 (1), 119-122.
Furter, L., 2004. Solar distillation solves rural water problems: consulting. IMIESA, *Energy Convers. and Manag.,* 29 (10), 59.
Gadgil, A., 1991. Drinking water in developing countries. *Annu. Rev. Energy Environ*. 23, 275.
Garcia-Rodriguez, L., 2002. Seawater desalination driven by renewable energies: a review. *Desalination,* 143 (2), 103-113.
Garg, H.P., Mann, H.S., 1976. Effect of climatic, operational, and design parameters on the year-round performance of single-sloped and double-sloped solar still under Indian arid zone conditions. *Sol. Energy*, 18 (2).
Gaur, M.K., Tiwari, G.N., 2010. Optimization of number of collectors for integrated PV/T hybrid active solar still. *Appl. Energy,* 87 (5), 1763-1772.
Ghaffour, N., Bundschuh, J., Mahmoudi, H., Goosen, M.F., 2015. Renewable energy-driven desalination technologies: A comprehensive review on challenges and potential applications of integrated systems. *Desalination*, 356, 94-114.
Ghaffour, N., Lattemann, S., Missimer, T., Ng, K.C., Sinha, S., Amy, G., 2014. Renewable energy-driven innovative energy-efficient desalination technologies. *Appl. Energy*, 136, 1155-1165.
Gnanaraj, S.J.P., Ramachandran, S., Christopher, D.S., 2017. Enhancing the design to optimize the performance of double basin solar still. *Desalination*, 411, 112-123.
Goldie, I., Sanderson, R.D., Seconna, J.D., Delcarme, B.A., Daries, L.M., Lodewyk, L.A., 2004. A guidebook on household water supply for rural areas with saline groundwater. WRC Report no. TT 221/04, pp. 36-42; 52-54. Water Research Commission, Pretoria, South Africa. [Online] Available from: http://www.wrc.org.za/wp-content/uploads/mdocs/TT-221-04.pdf [Accessed 20 January 2021].
Haddad, Z., Chaker, A., Rahmani, A., 2017. Improving the basin type solar still performances using a vertical rotating wick. *Desalination*, 418, 71-78.
Hamadou, O.A., Abdellatif, K., 2014. Modeling an active solar still for sea water desalination process optimization. *Desalination,* 354,1-8.
Hartwig, G.R., 2013. Grey water reclamation utilising solar thermal energy (Doctoral dissertation, Stellenbosch: Stellenbosch University).
Hassan, H., Abo-Elfadl, S., 2017. Effect of the condenser type and the medium of the saline water on the performance of the solar still in hot climate conditions. *Desalination*, 417, 60-68.

Hou, J., Yang, J., Chang, Z., Zheng, H., Su, Y., 2018. Effect of different carrier gases on productivity enhancement of a novel multi-effect vertical concentric tubular solar brackish water desalination device. *Desalination*, 432, 72-80.
Ibrahim, A.G., Elshamarka, S.E., 2015. Performance study of a modified basin type solar still. *Sol. Energy,* 118, 397-409.
Iqbal, M., 1983. *An introduction to solar radiation*. Academic press INC. New York.
Jadhav, A.S., Chembe, D.K., Strauss, J.M., Van Niekerk, J.L., 2017. Status of solar technology implementation in the Southern African Developing Community (SADC) region. *Renew. and Sust. Energ. Rev.,* 73, 626-627.
Jamil, B., Akhtar, N., 2017. Effect of specific height on the performance of a single slope solar still: An experimental study. *Desalination*, 414, 73-88.
Joubert, E.C., Hess, S. and Van Niekerk, J.L., 2016. Large-scale solar water heating in South Africa: Status, barriers, and recommendations. *Renew. Energy*, 97, 811.
Jubran, B.A., Ahmed, M.I., Ismail, A.F., Abakar, Y.A., 2000. Numerical modelling of a multi-stage solar still. *Energy Convers. and Manag.,* 41 (11), 1107-1121.
Kabeel, A.E., Arunkumar, T., Denkenberger, D.C., Sathyamurthy, R., 2017. Performance enhancement of solar still through efficient heat exchange mechanism–a review. Appl. *Therm. Eng.,* 114, 815-836.
Kabeel, A.E., El-Agouz, S.A., 2011. Review of researches and developments on solar stills. *Desalination*, 276 (1-3), 1-12.
Kabeel, A.E., Hamed, A.M., El-Agouz, S.A., 2010. Cost analysis of different solar still configurations. *Energy,* 35 (7), 2901-2908.
Kabeel, A.E., Omara, Z.M., Essa, F.A., 2017. Numerical investigation of modified solar still using nanofluids and external condenser. *J. Taiwan Inst. Chem. Eng*., 75, 77-86.
Kabeel, A.E., Omara, Z.M., Essa, F.A., 2014. Enhancement of modified solar still integrated with external condenser using nanofluids: an experimental approach. *Energy Convers. and Manag*., 78, 493-498.
Kabeel, A.E., Sathyamurthy, R., Sharshir, S.W., Muthumanokar, A., Panchal, H., Prakash, N., Prasad, C., Nandakumar, S., El Kady, M.S., 2019. Effect of water depth on a novel absorber plate of pyramid solar still coated with TiO2 nano black paint. *J. Clean. Prod.,* 213, 185-191.
Kabeel, A.E., Teamah, M.A., Abdelgaied, M., Aziz, G.B.A., 2017. Modified pyramid solar still with v-corrugated absorber plate and PCM as a thermal storage medium. *J. of Clean. Prod*., 161, 881-887.
Kamal, B. 2017. Water shortages put the region at severe risk. The Middle East online [Online] Available from: http://www.themiddleeastmagazine.com/?p=8935[19 January 2021].
Kanjere, M., Thaba, K., Lekoana, M., 2014. Water shortage management at Letaba water catchment area in Limpopo province, of South Africa. *Mediterr. J. Soc. Sci*. 5 (27), 1357.
Kaushal, A.K., Mittal, M.K., Gangacharyulu, D., 2016. Development and experimental study of an improved basin type vertical single distillation cell solar still. *Desalination*, 398, 121-132.
Khalifa, A.J.N., Hamood, A.M., 2009a. On the verification of the effect of water depth on the performance of basin type solar stills. *Sol. Energy*, 83 (8), 1312-1321.
Khalifa, A.J.N., Hamood, A.M., 2009b. Effect of insulation thickness on the productivity of basin type solar stills: An experimental verification under local climate. *Energy Convers. and Manag*., 50 (9), 2457-2461.
Khayet, M., 2013. Solar desalination by membrane distillation: Dispersion in energy consumption analysis and water production costs (a review). *Desalination,* 308, 89-101.
Khoshrou, I., Nasr, M.J., Bakhtari, K., 2017. New opportunities in mass and energy consumption of the Multi-Stage Flash Distillation type of brackish water desalination process. *Sol. Energy*, 153, 115-125.
Kumar, S., Dubey, A., Tiwari, G.N., 2014. A solar still augmented with an evacuated tube collector in forced mode. *Desalination*, 347, 15-24.
Kumar, S., Dwivedi, V.K., 2015. Experimental study on modified single slope single basin active solar still. *Desalination*, 367, 69-75.
Kumar, S., Tiwari, G.N., 2009. Life cycle cost analysis of single slope hybrid (PV/T) active solar still. *Appl. Energy*, 86 (10), 1995-2004.
Kumar, S., Tiwari, G.N., Singh, H.N., 2000. Annual performance of an active solar distillation system. *Desalination*, 127 (1), 79-88.
Kumar, S., Tiwari, A., 2010. Design, fabrication and performance of a hybrid photovoltaic/thermal (PV/T) active solar still. *Energy Convers. and Manag*., 51 (6), 1219-1229.
Kwatra, H.S., 1996. Performance of a solar still: predicted effect of enhanced evaporation area on yield and evaporation temperature. *Sol. Energy*, 56 (3), 261-266.

Lal, R.K., Mishra, S., Dwivedi, J.P., Dwivedi, H., 2017. A comprehensive study of the different parameters of solar still. *Materials Today: Proceedings,* 4 (2), 3572-3580.
Li, M., 2011. Reducing specific energy consumption in Reverse Osmosis (RO) water desalination: An analysis from first principles. *Desalination*, 276 (1-3), 128-135.
Li, S.F., Liu, Z.H., Shao, Z.X., Xiao, H.S. and Xia, N., 2018. Performance study on a passive solar seawater desalination system using multi-effect heat recovery. *Applied Energy*, *213*, 343-352.
Light, T.S., Licht, S., Bevilacqua, A.C. and Morash, K.R., 2004. The fundamental conductivity and resistivity of water. *Electrochemical and solid state letters*, *8*(1), E16-E19.
Liu, Z.H., Hu, R.L., Chen, X.J., 2014. A novel integrated solar desalination system with multi-stage evaporation/heat recovery processes. *Renew. Energ*., 64, 26-33.
Lumsden, T.G., Schulze, R.E., Hewitson, B.C., 2009. Evaluation of potential changes in hydrologically relevant statistics of rainfall in Southern Africa under conditions of climate change. *Water SA*, 35 (5), 654.
Mahian, O., Kianifar, A., Heris, S.Z., Wen, D., Sahin, A.Z., Wongwises, S., 2017. Nanofluids effects on the evaporation rate in a solar still equipped with a heat exchanger. *Nano Energ.,* 36, 134-155.
Malan, G.J., 1987. *Water consumption and possible water savings in apartment buildings*. p. 23. Division of Building Technology, CSIR.
Maleki, S.A.M., Hizam, H. and Gomes, C., 2017. Estimation of hourly, daily and monthly global solar radiation on inclined surfaces: Models re-visited. *Energies*, 10(1), 134.
Manokar, A.M., Winston, D.P., Mondol, J.D., Sathyamurthy, R., Kabeel, A.E., Panchal, H., 2018. Comparative study of an inclined solar panel basin solar still in passive and active mode. *Sol. Energy,* 169, 206-216.
Matchaya, G., Nhamo, L., Nhlengethwa, S., Nhemachena, C., 2019. An Overview of Water Markets in Southern Africa: An option for water management in times of scarcity. *Water*, 11 (5), 1006.
Mbadinga, P.J.K, 2015. A solar water purification system for rural areas. (Doctoral dissertation, Cape Peninsula University of Technology). Pp. 49-51.
Meigh, J.R., McKenzie, A.A., Sene, K.J., 1999. A grid-based approach to water scarcity estimates for eastern and southern Africa. *Water Resour. Manag*., 13 (2), 112.
Mkhize, M.M. and Msomi, V., 2020. Feasibility of a Multistage Solar Still in Southern Africa. In *2020 9th International Conference on Renewable Energy Research and Application (ICRERA)* (pp. 48-54). IEEE.
Mkhize, M.M. and Msomi, V., 2021. Challenges and progress made toward the improvement of a multistage solar still desalination system. *Desalination and water treatment*, (222), 23-35.
Mohamad, M.A., Soliman, S.H., Abdel-Salam, M.S. and Hussein, H.M.S., 1995. Experimental and financial investigation of asymmetrical solar stills with different insulation. *Appl. Energy*, 52(2-3), pp.265-271.
Monowe, P., Masale, M., Nijegorodov, N., Vasilenko, V., 2011. A portable single-basin solar still with an external reflecting booster and an outside condenser. *Desalination*, 280 (1-3), 332-338.
Morad, M.M., El-Maghawry, H.A., Wasfy, K.I., 2015. Improving the double slope solar still performance by using flat-plate solar collector and cooling glass cover. *Desalination*, 373, 1-9.
Morad, M.M., El-Maghawry, H.A., Wasfy, K.I., 2017. A developed solar-powered desalination system for enhancing freshwater productivity. *Sol. Energy,* 146, 20-29.
Mowla, D., Karimi, G., 1995. Mathematical modelling of solar stills in Iran. *Sol. Energ*., 55 (5), 389-393.
Muneer, T., Hawas, M.M. and Sahili, K., 1984. Correlation between hourly diffuse and global radiation for New Delhi. *Energy Conversion and Management*, *24*(4), 265-267.
Muftah, A.F., Alghoul, M.A., Fudholi, A., Abdul-Majeed, M.M., Sopian, K., 2014. Factors affecting basin type solar still productivity: A detailed review. *Renew. and Sust. Energ. Rev.,* 32, 430-447.
Muftah, A.F., Sopian, K., Alghoul, M.A., 2018. Performance of basin type stepped solar still enhanced with superior design concepts. *Desalination*, 435, 198-209.
Mukheibir, P., Sparks, D., 2003. Water resource management and climate change in South Africa: Visions, driving factors and sustainable development indicators. Report for Phase I of the Sustainable Development and Climate Change project. Energy and Development Research Centre (EDRC), University of Cape Town, p.6. [Online] Available from: https://idprc.org/wp-content/uploads/2015/08/Water_resource_management-in-Southern-Africa.pdf [Accessed 18 January 2021].
Nafey, A.S., Abdelkader, M., Abdelmotalip, A., Mabrouk, A.A., 2000. Parameters affecting solar still productivity. *Energy convers. and Manag.,* 41 (16), 1797-1809.

Nagarajan, P.K., El-Agouz, S.A., DG, H.S., Edwin, M., Madhu, B., Sathyamurthy, R., Bharathwaaj, R., 2017. Analysis of an inclined solar still with baffles for improving the yield of fresh water. *Process Safety and Environmental Protection,* 105, 326-337.
Nishikawa, H., Tsuchiya, T., Narasaki, Y., Kamiya, I. and Sato, H., 1998. Triple effect evacuated solar still system for getting fresh water from seawater. *Applied thermal engineering*, *18*(11), 1067-1075.
Omara, Z.M., Kabeel, A.E., Abdullah, A.S., 2017. A review of solar still performance with reflectors. *Renew. and Sust. Energy Rev*., 68, 638-649.
Omara, Z.M., Kabeel, A.E., Abdullah, A.S., Essa, F.A., 2016. Experimental investigation of corrugated absorber solar still with wick and reflectors. *Desalination*, 381, 111-116.
Omara, Z.M., Kabeel, A.E., Essa, F.A., 2015. Effect of using nanofluids and providing vacuum on the yield of corrugated wick solar still. *Energy Convers. and Manag.,* 103, 965-972.
Osuri, S.O., Ngoma, J.L., Chowdhury, S.P., 2015. Cost-effective renewable energy technologies in universities of south Africa: A case study. [Online] Available from: http://tutvital.tut.ac.za:8080/vital/access/services/Download/tut:2874/SOURCE1?view=true [Accessed 20 January 2021].
Panchal, H.N., Patel, S., 2017. An extensive review on different design and climatic parameters to increase distillate output of solar still. *Renew. and Sust. Energ. Rev*., 69, 750-752.
Peñate, B., García-Rodríguez, L., 2012. Current trends and future prospects in the design of seawater reverse osmosis desalination technology. *Desalination,* 284, 1-8.
Phadatare, M.K., Verma, S.K., 2007. Influence of water depth on internal heat and mass transfer in a plastic solar still. *Desalination*, 217 (1-3), 267-275.
Prakash, P., Velmurugan, V., 2015. Parameters influencing the productivity of solar stills–A review. *Renew. and Sust. Energ. Rev*., 49, 585-609.
Pugsley, A., Zacharopoulos, A., Mondol, J.D., Smyth, M., 2016. Global applicability of solar desalination. *Renew. Energy,* 88, 202; 205-206;208.
Rabhi, K., Nciri, R., Nasri, F., Ali, C., Bacha, H.B., 2017. Experimental performance analysis of a modified single-basin single-slope solar still with pin fins absorber and condenser. *Desalination*, 416, 86-93.
Rahmani, A., Boutriaa, A., 2017. Numerical and experimental study of a passive solar still integrated with an external condenser. *Int. J. of Hydr. Energy*, 42 (48), 29047-29055.
Raj, S.V., Manokar, A.M., 2017. Design and analysis of solar still. *Materials Today: Proceedings*, 4 (8), 9179-9185.
Rajamanickam, M.R., Ragupathy, A., 2012. Influence of water depth on internal heat and mass transfer in a double slope solar still. *Energy Procedia*, 14, 1701-1708.
Rajaseenivasan, T., Prakash, R., Vijayakumar, K., Srithar, K., 2017. Mathematical and experimental investigation on the influence of basin height variation and stirring of water by solar PV panels in solar still. *Desalination*, 415, 67-75.
Rajaseenivasan, T., Raja, P.N., Srithar, K., 2014. An experimental investigation on a solar still with an integrated flat plate collector. *Desalination*, 347, 131-137.
Raju, V.R. and Narayana, R.L., 2018. Effect of flat plate collectors in series on performance of active solar still for Indian coastal climatic condition. *Journal of king Saud university-engineering sciences,* 30 (1), 78-85.
Ranjan, K.R., Kaushik, S.C., 2013. Energy, exergy, and thermo-economic analysis of solar distillation systems: A review. *Renew. and Sust. Energ. Rev.,* 27, 711.
Rashidi, S., Esfahani, J.A., Rahbar, N., 2017. Partitioning of solar still for performance recovery: experimental and numerical investigations with cost analysis. *Sol. Energy*, 153, 41-50.
Reddy, K.S., Kumar, K.R., O'Donovan, T.S., Mallick, T.K., 2012. Performance analysis of an evacuated multi-stage solar water desalination system. *Desalination*, 288, 80-92.
Redelinghuys, N., Pelser, A.J., 2013. Challenges to cooperation on water utilisation in the Southern Africa region. *Water policy,* 15 (4), 554-569.
Reif, J.H. and Alhalabi, W., 2015. Solar-thermal powered desalination: Its significant challenges and potential. *Renew. and Sust. Energ. Rev*., 48, 153-154.
Roberts, D.A., Johnston, E.L., Knott, N.A., 2010. Impacts of desalination plant discharges on the marine environment: A critical review of published studies. Water res., 44 (18), 5117-5128.
Saeedi, F., Sarhaddi, F., Behzadmehr, A., 2015. Optimization of a PV/T (photovoltaic/thermal) active solar still. *Energy*, 87, 142-152.
Salem, M.G., 2013. Solar Desalination as an Adaptation tool for Climate Change impacts on the Water Resources of Egypt. *United states: United Nations Education, Scientific and Cultural Organization.*

Sampathkumar, K., Arjunan, T.V., Pitchandi, P., Senthilkumar, P., 2010. Active solar distillation—A detailed review. *Renew. and Sust. Energ. Rev.,* 14 (6), 1503-1526.
Samuel, D.H., Nagarajan, P.K., Sathyamurthy, R., El-Agouz, S.A., Kannan, E., 2016. Improving the yield of fresh water in conventional solar still using low-cost energy storage material. *Energy Convers. and Manag.,* 112, 125-134.
Santos, N.I., 2011. Modeling passive solar distillation production in Las Vegas. (Bachelor of Science in Engineering, University of Nevada, Las Vegas).
Schreiner, B.G., Mungatana, E.D. and Baleta, H., 2018. Impacts of Drought Induced Water Shortages in South Africa: Sector Policy Briefs, pp.21-23. [Online] Available from:http://www.wrc.org.za/wp-content/uploads/mdocs/2604%20Vol%202.pdf[Accessed 19 January 2021].
Schwarzer, K., da Silva, E.V., Hoffschmidt, B., Schwarzer, T., 2009. A new solar desalination system with heat recovery for decentralised drinking water production. *Desalination*, 248 (1-3), 204-211.
Schwarzer, K., Vieira, M.E., Faber, C. and Müller, C., 2001. Solar thermal desalination system with heat recovery. *Desalination,* 137(1-3), 24.
Seago, C.J., 2016. A comparison of the South African approach to water resources management and planning with four international countries. Research Report: a comparison of the South African approach to water resources management and planning with four international countries, p.66. [Online] Available from:http://www.wrc.org.za/wp-content/uploads/mdocs/KV%20341-15.pdf [Accessed 19 January 2021].
Selvaraj, K., Natarajan, A., 2018. Factors influencing the performance and productivity of solar stills-A review. *Desalination*, 435, 181-187.
Shafii, M.B., Mamouri, S.J., Lotfi, M.M. and Mosleh, H.J., 2016. A modified solar desalination system using evacuated tube collector. *Desalination*, *396*, 30-38.
Shalaby, S.M., El-Bialy, E. and El-Sebaii, A.A., 2016. An experimental investigation of a v-corrugated absorber single-basin solar still using PCM. *Desalination*, *398*, 247-255.
Sharshir, S.W., Peng, G., Wu, L., Yang, N., Essa, F.A., Elsheikh, A.H., Mohamed, S.I., Kabeel, A.E., 2017. Enhancing the solar still performance using nanofluids and glass cover cooling: experimental study. *Appl. Therm. Eng.,* 113, 684-693.
Sharshir, S.W., Peng, G., Yang, N., Eltawil, M.A., Ali, M.K.A., Kabeel, A.E., 2016. A hybrid desalination system using humidification-dehumidification and solar stills integrated with evacuated solar water heater. Energ. Convers. and Manag., 124, 287-296.
Sharshir, S.W., Yang, N., Peng, G., Kabeel, A.E., 2016. Factors affecting solar stills productivity and improvement techniques: a detailed review. *Appl. Therm. Eng.,* 100, 267-284.
Shatat, M.I., Mahkamov, K., 2010. Determination of rational design parameters of a multi-stage solar water desalination still using transient mathematical modelling. *Renew. energy*, 35 (1), 52-61.
Shemer, H., Semiat, R., 2017. Sustainable RO desalination–Energy demand and environmental impact. *Desalination*, 424, 13-14.
Simonis, J.J. and Nweze, A., 2016. A novel approach for providing potable water in rural Sodwana Bay, northern Kwazulu-Natal, South Africa. Journal of Water, Sanitation and Hygiene for Development, 6(3), 425-434.
Singh, D.B., Yadav, J.K., Dwivedi, V.K., Kumar, S., Tiwari, G.N., Al-Helal, I.M., 2016. Experimental studies of active solar still integrated with two hybrid PVT collectors. *Sol. Energy*, 130, 207-223.
Singh, G., Kumar, S., Tiwari, G.N., 2011. Design, fabrication and performance evaluation of a hybrid photovoltaic thermal (PVT) double slope active solar still. *Desalination,* 277 (1-3), 399-406.
Singh, P., Singh, P., Singh, J., Singh, R.I., Kundu, K., 2012, March. Performance Evaluation of Low Inertia Multi-Stage Solar Still. In Proceedings of the International Multi Conference of Engineers and Computer Scientists (pp. 14-16).
Singh, R.V., Kumar, S., Hasan, M.M., Khan, M.E., Tiwari, G.N., 2013. Performance of a solar still integrated with evacuated tube collector in natural mode. *Desalination*, 318, 25-33.
Sivakumar, V., Sundaram, E.G., 2013. Improvement techniques of solar still efficiency: A review. *Renew. and Sust. Energ. Rev*., 28, 246-264.
Smith, J.A., Green, J.M., 2005. Water service delivery in Pietermaritzburg: A community perspective. *Water SA*, 31 (4), 436.
SolarGIS. Solar resource map, direct normal irradiation, SA. [Online] Available from: https://solargis.com/maps-and-gis-data/download/south-africa [16 June 2020].
Soni, A., Stagner, J.A., Ting, D.S.K., 2017. Adaptable wind/solar powered hybrid system for household wastewater treatment. *Sustain. Energy Technol. and Assess.,* 24, 8-18.
South Africa. DME. 1998. White paper on the energy policy of the Republic of South Africa, p.79. [Online] Available from: http://www.energy.gov.za/files/policies/whitepaper_energypolicy_1998.pdf [Accessed 20 January 2021].

South Africa. DoE. 2019. Media statement, Minister of Energy, Mr Jeff Radebe, announces adjustment of fuel prices effective from the 3rd of April 2019. [Online] Available from: http://www.energy.gov.za/files/media/pr/2019/MediaStatement-fuel-prices-for-April-2019.pdf [02 May 2019].
South Africa. DoE. 2019. Media statement, Minister of Energy, Mr Jeff Radebe, announces adjustment of fuel prices effective from the 1st of May 2019. [Online] Available from: http://www.energy.gov.za/files/media/pr/2019/MediaStatement-fuel-prices-for-May-2019.pdf [02 May 2019].
South Africa. DoE. 2010. South African energy synopsis 2010. [Online] Available from: http://www.energy.gov.za/files/media/explained/2010/South_African_Energy_Synopsis_2010.pdf [Accessed 21 January 2021].
South Africa. DoE. 2018a. South African energy sector report 2018. [Online] Available from: http://www.energy.gov.za/files/media/explained/2018-South-African-Energy-Sector-Report.pdf [Accessed 21 January 2021].
South Africa. DoE. 2018b. State of renewable energy in SA, P.37. [Online] Available from: http://www.energy.gov.za/files/media/Pub/2017-State-of-Renewable-Energy-in-South-Africa.pdf [Accessed 21 January 2021].
South Africa. DWAF. 1994. White paper on water supply and sanitation policy. Cape Town: Dept. of water and forestry, pp.3-5;30. [Online] Available from: https://www.gov.za/sites/default/files/gcis_document/201409/wssp.pdf [Accessed 18 January 2021].
South Africa. DWS. 2018. National water and Sanitation Master plan, volume 1, p.2. [Online] Available from:https://www.dws.gov.za/National%20Water%20and%20Sanitation%20Master%20Plan/Documents/NWSMP(Master%20Plan)%20Call%20to%20Action%20v10.1.pdf[Accessed 18 January 2021].
South Africa. DWAF. 2012. Proposed National Water Resource Strategy 2 (NWRS 2): Summary, p.70. [Online] Available from:https://static.pmg.org.za/docs/120911proposed_0.pdf[Accessed 18 January 2021].
South Africa. DWAF. 2004. National water resource strategy, 1st ed, pp. 83-90. [Online] Available from: https://cer.org.za/wp-content/uploads/2017/10/NWRS-2004.pdf[19 January 2021].
South Africa. DWAF. 1999. Establishment of a pricing strategy for water use charges in terms of section 56 (1) of the national water act, 1998. Notice 1353 of 1999. *Government Gazette*, (20615): 1-38, November 12.
South Africa. DWAF. 1996. South African water quality guidelines volume 1, 2nd ed. Pp.23-25 [Online] Available from: https://www.iwa-network.org/filemanager-uploads/WQ_Compendium/Database/Selected_guidelines/041.pdf [Accessed 20 January 2021].
South Africa. DWS. 2015. Water service tariffs, p.15. [Online] Available from: http://www.dwa.gov.za/downloads/WS/P_I/Adhoc/AWensley/Water%20&%20Sanitation%20Tariffs_20152016%20portrait.pdf[02 May 2019].
South Africa. 2010. National climate change response green paper 2010. Notice 1083 of 2010. *Government Gazette*, (33801): 6, November 25.
South Africa. Statistics South Africa. 2014. Mid-year population estimates. [Online] Available from: https://www.statssa.gov.za/publications/P0302/P03022014.pdf[02 May 2019].
South Africa. Statistics South Africa. 2018. Mid-year population estimates. [Online] Available from: https://www.statssa.gov.za/publications/P0302/P03022018.pdf[02 May 2019].
Srivastava, P.K., Agrawal, S.K., 2013. Winter and summer performance of single sloped basin type solar still integrated with extended porous fins. *Desalination*, 319, 73-78.
Swartz, C.D., Du Plessis, J.A., Burger, A.J., Offringa, G., 2006. A desalination guide for South African municipal engineers. *Water SA*, 32 (5), 641.
Taghvaei, H., Taghvaei, H., Jafarpur, K., Feilizadeh, M., Estahbanati, M.K., 2015. Experimental investigation of the effect of solar collecting area on the performance of active solar stills with different brine depths. *Desalination*, 358, 76-83.
Taghvaei, H., Taghvaei, H., Jafarpur, K., Estahbanati, M.K., Feilizadeh, M., Feilizadeh, M., Ardekani, A.S., 2014. A thorough investigation of the effects of water depth on the performance of active solar stills. *Desalination*, 347, 77-85.
Tanaka, H., 2011. A theoretical analysis of basin type solar still with flat plate external bottom reflector. *Desalination,* 279 (1-3), 243-251.
Tapela, B.N., 2012. Social water scarcity and water use. WRC Research Report, Research Report, Pretoria, Water Research Commission, p.7. [online] Available from: http://www.wrc.org.za/wp-content/uploads/mdocs/1940-1-121.pdf[18 January 2021].

Tarawneh, M.S.K., 2007. Effect of water depth on the performance evaluation of solar still. *JJMIE*, 1(1).
Thirugnanasambandam, M., Iniyan, S., Goic, R., 2010. A review of solar thermal technologies. *Renew. and Sust. Energ. Rev.,* 14 (1), 312-322.
Tiwari, A.K., Tiwari, G.N., 2007. Annual performance analysis and thermal modelling of passive solar still for different inclinations of condensing cover. *Int. J. of Energy Res.,* 31 (14), 1358-1382.
Tiwari, G.N., Sahota, L., 2017. Review on the energy and economic efficiencies of passive and active solar distillation systems. *Desalination,* 401, 151-179.
Tiwari, G.N., Thomas, J.M., Khan, E., 1994. Optimisation of glass cover inclination for maximum yield in a solar still. *Heat Recovery Systems and CHP*, 14 (4), 447-455.
Trieb, F., Müller-Steinhagen, H., 2008. Concentrating solar power for seawater desalination in the Middle East and North Africa. *Desalination*, 220 (1-3), 166.
Van Steenderen, R.A., 1977. Studies on the Efficiency of a Solar Distillation Still for supplementing Drinking Water Supplies in South. *Water SA,* 3 (1).
Verm Verma, S.K., Tiwari, A.K., 2015. Progress of nanofluid application in solar collectors: a review. *Energy Convers. and Manag.,* 100, 324-346.
WHO. 2007.pH in Drinking-water: Revised background document for development of WHO guidelines for drinking-water quality. [Online] Available from: https://www.who.int/water_sanitation_health/dwq/chemicals/ph_revised_2007_clean_version.pdf [Accessed 06 May 2021].
WHO. 2019. Safer water, better health. [Online] Available from: https://apps.who.int/iris/bitstream/handle/10665/329905/9789241516891-eng.pdf?sequence=1&isAllowed=y [15 July 2020].
Yadav, S. and Sudhakar, K., 2015. Different domestic designs of solar stills: A review. *Renew. and Sust. Energ. Rev,* 47, 718-731.
Yadav, Y.P., Yadav, S.K., 2004. Parametric studies on the transient performance of a high-temperature solar distillation system. *Desalination,* 170 (3), 251-262.
Yilmaz, İ.H., Söylemez, M.S., 2012. Design and computer simulation on multi-effect evaporation seawater desalination system using hybrid renewable energy sources in Turkey. *Desalination,* 291, 23-40.
Zambolin, E., Del Col, D., 2010. Experimental analysis of thermal performance of flat plate and evacuated tube solar collectors in stationary standard and daily conditions. *Sol. Energy*, 84 (8), 1382-1396.
Zurigat, Y.H., Abu-Arabi, M.K., 2004. Modelling and performance analysis of a regenerative solar desalination unit. *Appl. Therm. Eng.,* 24 (7), 1061-1072.

APPENDICES

Appendix A

A-1: BTM-4208SD temperature data logger

2-1 General Specifications

Circuit	Custom one-chip of microprocessor LSI circuit.	
Display	LCD size : 82 mm x 61 mm. ** with green color backlight.*	
Channels	12 channels : T1, T2, T3, T4, T5, T6, T7, T8, T9, T10, T11 and T12.	
Sensor type	Type K thermocouple probe. Type J/T/E/R/S thermocouple probe.	
Resolution	0.1℃/1℃, 0.1℉/1 ℉.	
Datalogger Sampling Time Setting range	Auto	1 second to 3600 seconds *@ Sampling time can set to 1 second, but memory data may loss.*
	Manual	Push the data logger button once will save data one time. *@ Set the sampling time to 0 second.*
Data error no.	0.1% of total saved data max.	
Loop Datalogger	The record time can set for the duration every day. *For example the user intend set the record time from the 2:00 to 8:15 every day or record time 8:15 to 14:15.*	
Memory Card	SD memory card. 1 GB to 16 GB.	
Advanced setting	* Set clock time (Year/Month/Date, Hour/Minute/ Second) * Set loop time of recorder * Decimal point of SD card setting * Auto power OFF management * Set beep Sound ON/OFF * Set temperature unit to ℃ or ℉ * Set sampling time * SD memory card Format	

Temperature Compensation	Automatic temp. compensation for the type K/J/T/E/R/S thermometer.
Linear Compensation	Linear Compensation for the full range.
Offset Adjustment	To adjust the zero temperature deviation value.
Probe Input Socket	2 pin thermocouple socket. 12 sockets for T1 to T12.
Over Indication	Show " - - - - ".
Data Hold	Freeze the display reading.
Memory Recall	Maximum & Minimum value.
Sampling Time of Display	Approx. 1 second.
Data Output	RS 232/USB PC computer interface. * *Connect the optional RS232 cable UPCB-02 will get the RS232 plug.* * *Connect the optional USB cable USB-01 will get the USB plug.*
Power off	Auto shut off saves battery life or manual off by push button, it can select in the inner function.
Operating Temperature	0 to 50 ℃.
Operating Humidity	Less than 85% R.H.
Power Supply	* .Alkaline or heavy duty DC 1.5 V battery (UM3, AA) x 8 PCs, or equivalent.
	* .DC 9V adapter input. (AC/DC power adapter is optional).

Power Current	Normal operation (w/o SD card save data and LCD Backlight is OFF) : *Approx. DC 7.5 mA.*
	When SD card save the data but and LCD Backlight is OFF) : *Approx. DC 25 mA.*
	** .If LCD backlight on, the power consumption will increase approx. 11 mA.*
Weight	Meter : 944 g/2.1 LB.
Dimension	225 X 125 X 64 mm (8.86 X 4.92 X 2.52 inch)
Accessories Included	* Instruction manual.....1 PC * Type K Temp. probe, TP-01.....2 PC * Hard carrying case, CA-08..... 1 PC * SD memory card (2 GB)..... 1 PC
Optional Accessories	* Type K thermocouple probe. TP-01, TP-02A. TP-03, TP-04 * USB cable, USB-01. * RS232 cable, UPCB-02. * Data Acquisition software, SW-U801-WIN. * AC to DC 9V adapter.

2-2 Electrical Specifications (23± 5 ℃)

Sensor Type	Resolution	Range	Accuracy
Type K	0.1 ℃	-50.1 to -100.0 ℃	± (0.4 % + 1 ℃)
		-50.0 to 999.9 ℃	± (0.4 % + 0.5 ℃)
	1 ℃	1000 to 1300 ℃	± (0.4 % + 1 ℃)
	0.1 ℉	-58.1 to -148.0 ℉	± (0.4 % + 1.8 ℉)
		-58.0 to 999.9 ℉	± (0.4 % + 1 ℉)
	1 ℉	1000 to 2372 ℉	± (0.4 % + 2 ℉)
Type J	0.1 ℃	-50.1 to -100.0 ℃	± (0.4 % + 1 ℃)
		-50.0 to 999.9 ℃	± (0.4 % + 0.5 ℃)
	1 ℃	1000 to 1150 ℃	± (0.4 % + 1 ℃)
	0.1 ℉	-58.1 to -148.0 ℉	± (0.4 % + 1.8 ℉)
		-58.0 to 999.9 ℉	± (0.4 % + 1 ℉)
	1 ℉	1000 to 2102 ℉	± (0.4 % + 2 ℉)
Type T	0.1 ℃	-50.1 to -100.0 ℃	± (0.4 % + 1 ℃)
		-50.0 to 400.0 ℃	± (0.4 % + 0.5 ℃)
	0.1 ℉	-58.1 to -148.0 ℉	± (0.4 % + 1.8 ℉)
		-58.0 to 752.0 ℉	± (0.4 % + 1 ℉)
Type E	0.1 ℃	-50.1 to -100.0 ℃	± (0.4 % + 1 ℃)
		-50.0 to 900.0 ℃	± (0.4 % + 0.5 ℃)
	0.1 ℉	-58.1 to -148.0 ℉	± (0.4 % + 1.8 ℉)
		-58.0 to 999.9 ℉	± (0.4 % + 1 ℉)
	1 ℉	1000 to 1652 ℉	± (0.4 % + 2 ℉)
Type R	1 ℃	0 to 600 ℃	± (0.5 % + 1 ℃)
		601 to 1700 ℃	
	1 ℉	32 to 1112 ℉	± (0.5 % + 2 ℉)
		1113 to 3092 ℉	
Type S	1 ℃	0 to 600 ℃	± (0.5 % + 1 ℃)
		601 to 1500 ℃	
	1 ℉	32 to 1112 ℉	± (0.5 % + 2 ℉)
		1113 to 2732 ℉	

Remark :

a. Accuracy value is specified for the meter only.

b. Accuracy is tested under the meter's environment temperature within 23 ± 5℃.

c. Linearity Correction :
Memorize the thermocouple's curve into the intelligent CPU circuit,

@ Above specification tests under the environment RF Field Strength less than 3 V/M & frequency less than 30 MHz only.

A-2: Professional wireless internet weather station

Specifications

Outdoor data

Transmission distance in open field	:	100m(330 feet)
Frequency	:	433 MHz / 868 MHz / 915 MHz (option)
Temperature range	:	-30˚C--65˚C (-22℉ to +149℉)
Accuracy	:	+ / - 1 ˚C
Resolution	:	0.1˚C
Measuring range rel. humidity	:	1%～99%
Accuracy	:	+/- 5%
Rain volume display	:	0 – 9999mm (show --- if outside range)
Accuracy	:	+ / - 10%
Resolution	:	0.3mm (if rain volume < 1000mm) 1mm (if rain volume > 1000mm)
Wind speed	:	0-50m/s (0~100mph) (show --- if outside range)
Accuracy:		+/- 1m/s (wind speed< 5m/s) +/-10% (wind speed > 5m/s)
Light	:	0-400k Lux
Accuracy	:	+/-15%
Measuring interval outdoor sensor:		16 sec
Measuring interval indoor sensor	:	64 sec

Indoor data

Indoor temperature range	:	-10˚C--60˚C (14℉ to + 140℉) (show --- if outside range)
Resolution	:	0.1˚C
Measuring range rel. humidity	:	1%～99%
Resolution	:	1%
Measuring range air pressure	:	300-1100hPa (8.85-32.5inHg)
Accuracy	:	+/-3hpa under 700-1100hPa
Resolution	:	0.1hPa (0.01inHg)
Alarm duration	:	120 sec

A-3: Solar irradiance sample calculations

Date: 29 May 2021

Number of day in a year (n) = 149

Time: 10h00 am

Latitude = φ = -33.93°

Longitude = 18.46°

Solar panel inclination from the horizontal (β)= 56°

Standard meridian for local zone = 30°

Hourly solar irradiance on a horizontal surface recorded by the weather station between 09h00 am and 10h00 am = 216.723 W/m^2

Solar constant (I_{sc}) $= 1367\ W/m^2$

Ground reflectance = 0.2

A-3-1 Solar irradiance on a horizontal surface

$E_o = 1 + 0.033cos\left(\frac{2\pi n}{365}\right)$ (Eq. 4.4)

$= 1 + 0.033cos\left(\frac{2 \times \pi \times 149)}{365}\right)$

$= 0.972$

$B = \frac{360(n-81)}{365}$ (Eq. 4.7)

$= \frac{360(149-81)}{365}$

$= 67.07$

$ET = 9.87sin2B - 7.53cosB - 1.5sinB$ (Eq. 4.8)

$= 9.87\sin(2 \times 67.07) - 7.53\cos(67.07) - 1.5\sin(67.07)$

$= 2.768$ minutes

Solar time at 10h00 am and 11h00 am, respectively is:

$ST = 4(L_{st} - L_{loc}) + ET + LT$ (Eq. 4.9)

$= 4(30 - 18.46) + (2.768) + (10 \times 60)$

$= 648.928\ minutes = 10.815h$

$ST = 4(L_{st} - L_{loc}) + ET + LT$

$= 4(30 - 18.46) + (2.768) + (11 \times 60)$

$= 708.928\ minutes = 11.815h$

$S_c = 0.1645sin2B - 0.1255cosB - 0.025sinB$ (Eq. 4.10)

$= 0.1645\sin(2 \times 67.07) - 0.1255\cos(67.07) - 0.025\sin(67.07)$

$= 0.0461$

$\omega = \frac{\pi}{12}[(t + 0.06667(L_s - L_L) + S_c) - 12]$ (Eq. 4.11)

$= \frac{\pi}{12}\left\{\left[\left(\frac{10.815 + 11.815}{2}\right) + 0.06667(330 - 341.56) + 0.0461\right] - 12\right\}$

$= -0.369$

$= -21.144°$

$\omega_1 = \omega - \left[\frac{(\pi \times t_1)}{24}\right]$ (Eq. 4.5)

$= -0.369 - \left[\frac{(\pi \times 1)}{24}\right]$

$= -0.499 \approx 0.5$

$= -28.642°$

$\omega_2 = \omega + \left[\frac{(\pi \times t_1)}{24}\right]$ (Eq. 4.6)

$= -0.369 + \left[\frac{(\pi \times 1)}{24}\right]$

$= -0.238$

$= -13.642°$

$\delta = 0.409sin\left[\left(\frac{2\pi n}{365}\right) - 1.39\right]$ (Eq. 4.12)

$= 0.409sin\left[\left(\frac{2 \times \pi \times 149}{365}\right) - 1.39\right]$

$= 0.3774$

$= 21.622°$

$I_o = I_{sc}E_o[(\omega_2 - \omega_1)sin\varphi sin\delta + cos\varphi cos\delta(sin\omega_2 - sin\omega_1)]$ (Eq. 4.3)

$= 1367 \times 0.972\{(-0.238 + 0.499) \times \sin(-33.93) \times \sin(21.622)$

$+ \cos(-33.93) \times \cos(21.622) \times [\sin(-13.642) - \sin(-28.642)]\}$

$= 178.062\ W/m^2$

$M_t = \frac{I_H}{I_o}$ (Eq. 4.2)

$= \frac{216.723}{178.062}$

$\underline{= 1.217}$

Based on equations 4.13 through to equation 4.15 the diffuse fraction $(k_d = 0.18)$ on a horizontal surface, since $M_t = 1.217$. The diffuse fraction was also computed for equations 4.13 and 4.14.

$M_t > 0.76 k_d = 0.18$ (Eq. 4.15)

Therefore, the diffuse radiation at 10h00 am was

$I_d = k_d \times I_H$ (Eq. 4.16)

$= 0.18 \times 216.723$

$\underline{= 39.010\ W/m^2}$

Then the beam radiation on a horizontal surface becomes:

$I_b = I_H - I_d$ (Eq. 4.1)

$= 216.723 - 39.010$

$\underline{= 177.713\ W/m^2}$

A-3-2 Solar irradiance on an inclined surface

$f_{Hay} = \frac{I_b}{I_o} = \frac{I_H - I_d}{I_o}$ (Eq. 4.18)

$= \frac{177.713}{178.062}$

$\underline{= 0.998}$

$cos\theta_z = cos\delta cos\varphi cos\omega + sin\varphi sin\delta$ (Eq. 4.22)

$= \cos(21.622)\cos(-33.93)\cos(-21.144) + \sin(-33.93)\sin(21.622)$

$= 0.7194 + (-0.2057)$

$= 0.514$

$\underline{\theta_z = 59.07°}$

$cos\theta = \cos(\varphi + \beta) cos\delta cos\omega + sin(\varphi + \beta) sin\delta$ (Eq. 4.23)

$= \cos[(-33.93) + (56)]\cos(21.622)\cos(-21.144) + sin[(-33.93) + (56)]sin21.622$

$= 0.80352+0.1385$

$= 0.942$

$\underline{\theta = 19.61°}$

$I_{d\beta} = I_d \left[f_{Hay} \left(\frac{cos\theta}{cos\theta_z} \right) + \left(\frac{1+cos\beta}{2} \right) (1 - f_{Hay}) \right]$ (Eq. 4.19)

$= 39.010 \left[0.998 \left(\frac{0.942}{0.514} \right) + \left(\frac{1 + cos56}{2} \right) (1 - 0.998) \right]$

$\underline{= 71.593\ W/m^2}$

$I_{b\beta} = I_b R_b$ (Eq. 4.20)

$R_b = \frac{cos\theta}{cos\theta_z}$ (Eq. 4.21)

Then,

$I_{b\beta} = I_b R_b$

$= 177.713 \times \frac{0.942}{0.514}$

$\underline{= 325.692\ W/m^2}$

$I_r = I_H \rho_g \left(\frac{1-cos\beta}{2} \right)$ (Eq. 4.24)

$= 216.723 \times 0.2 \times \left(\frac{1 - cos56}{2} \right)$

$\underline{= 9.553\ W/m^2}$

$I_\beta = I_{b\beta} + I_{d\beta} + I_r$ (Eq. 4.17)

$= 325.692 + 71.593 + 9.553$

$\underline{= 406.838\ \mathrm{W}/m^2}$

Figure A-3 show the solar irradiance components on the horizontal and sloped surfaces.

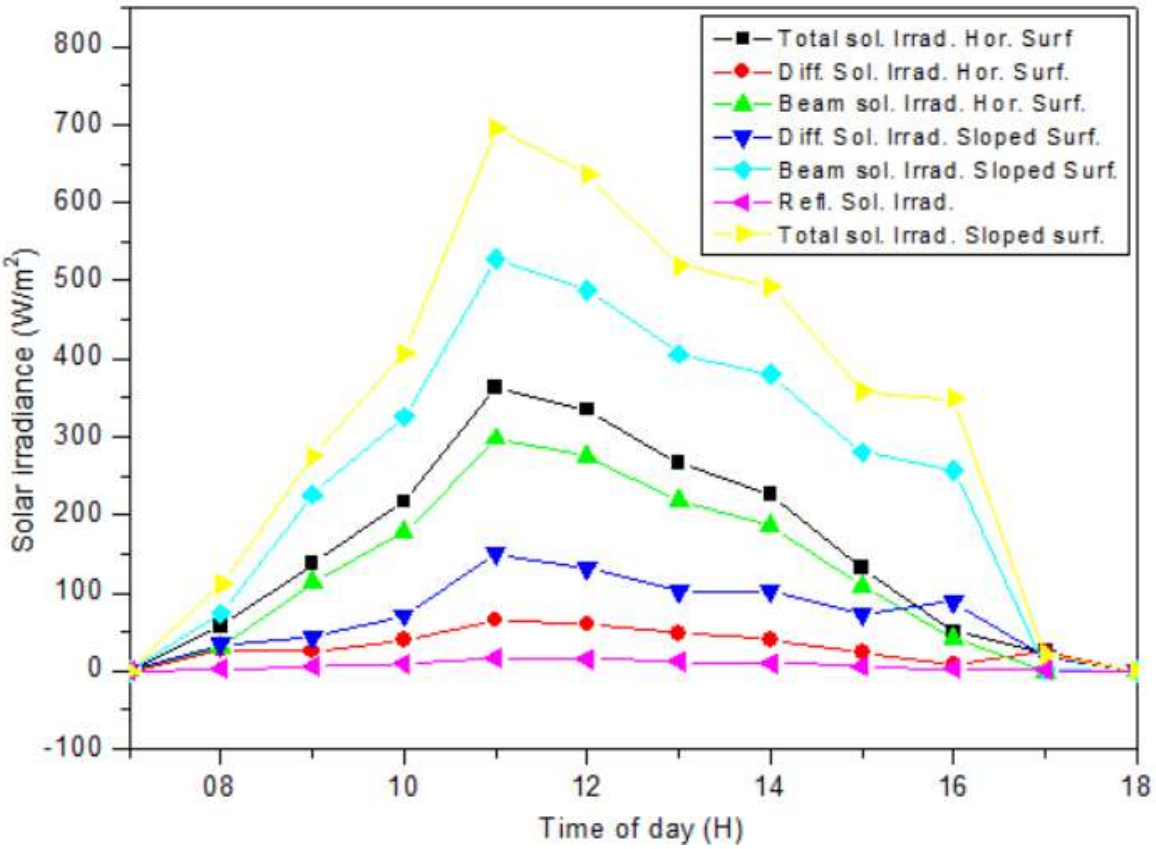

Figure A-3: Solar irradiance vs time of day

A-4: Performance and the distillate yield sample calculations for the vapour-based MSS-SS.

The estimated solar irradiance curve on a tilted surface is shown on figure A-4-1. The figure represents the data for the day of the 29th of May 2021.

Surface tilt (β)= 56°

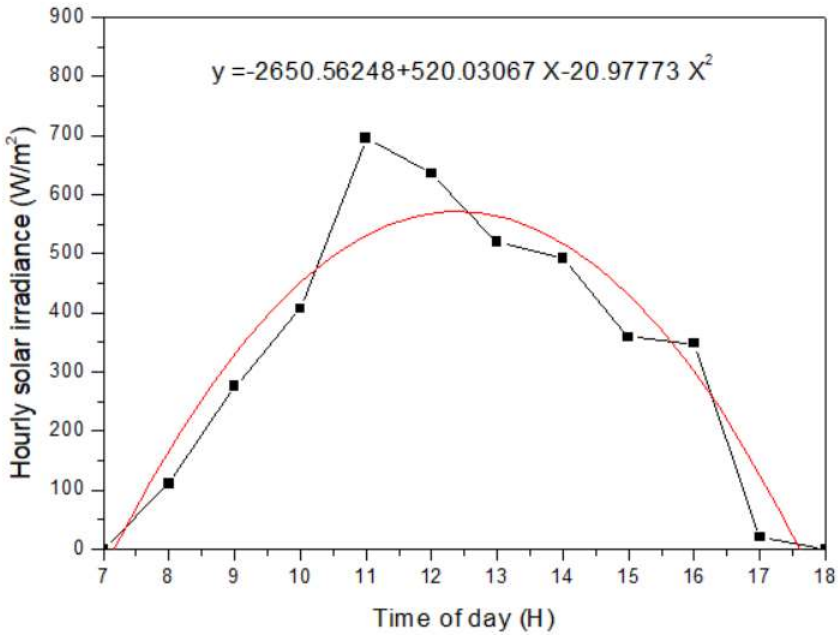

Figure A-4-1: Thermal energy received by the inclined surface

$$y = -2650.564 + 520.031t - 20.978t^2$$

$$I_\beta = \int_7^{18} -2650.564 + 520.031t - 20.978t^2$$

$$= \left\{[-2650.564t] + \left[\frac{1}{2}(520.031t^2)\right] - \left[\frac{1}{3}(20.978t^3)\right]\right\}_7^{18}$$

$$\underline{= 3965.323\ Wh/m^2}$$

The result log for the hourly total solar irradiance on an inclined surface are shown in the figure below. The quadratic function representing the area under the curve over-estimated the solar irradiance curve. Hence, the errors shown in the figure below.

Results Log

B1	520.03067	60.71814	
B2	-20.97773	2.41079	

R-Square(COD)	SD	N	P
0.89421	88.07368	12	<0.0001

[19/07/2021 13:49 "/Graph1" (2459414)]
Polynomial Regression for Data1_B:
Y = A + B1*X + B2*X^2

Parameter	Value	Error
A	-2650.56248	360.82771
B1	520.03067	60.71814
B2	-20.97773	2.41079

R-Square(COD)	SD	N	P
0.89421	88.07368	12	<0.0001

Figure A-4-2: Errors in the thermal energy received by the inclined surface

Total distillate yield from the stacked stages only = 1110 ml. The data used is tabulated in table A-4-1. The sample calculations are performed for 10h00 am and the ETSCs thermal energy efficiency and the energy absorbed is:

$$\eta = \left[0{,}803 - 2{,}01\left(\frac{T_m - T_a}{I_\beta}\right) - 0{,}0034\left(\frac{T_m - T_a}{I_\beta}\right)^2\right] \times 100\% \qquad \text{(Eq. 2.26)}$$

$$= \left[0{,}803 - 2{,}01\left(\frac{15.86 - 15.54}{406.93}\right) - 0{,}0034\left(\frac{15.86 - 15.54}{406.93}\right)^2\right] \times 100\%$$

$\underline{= 80.14\%}$

$$Q_{ETSC} = I_\beta \times \eta \qquad \text{(Eq. 4.25)}$$

$$= 406.93 \times 0.8014$$

$\underline{= 326.122\ W/m^2}$

Given the total ETSC aperture area of 1.8 m^2, the total estimated energy received by the SW at 10h00 am is:

$326.122 \times 1.8 = 587.0196\ W$

Table A-4-1: ETSCs performance

Time	Hourly Av. Ambient temp. **(°C)**	Hourly Av. SW Temp. **(°C)**	Hourly solar irradiance (I_β) **(W/m^2)**	ETSC hourly efficiency (Π) **(%)**	Energy input (Q_{ETSC}) **(W/m^2)**	Energy input (Q_{ETSC}) **(W)**
8	14.29	16.61	110.88	76.08	84.36	151.848
9	14.75	16.06	275.37	79.34	218.48	393.264
10	15.54	15.86	406.93	80.14	326.12	587.019
11	16.09	20.06	695.02	79.15	550.13	990.234
12	17.85	80.67	635.80	60.44	384.25	691.65
13	17.54	85.83	519.93	53.89	280.21	504.378
14	18.67	92.60	492.73	50.13	247.02	444.636
15	18.79	84.74	358.91	43.35	155.60	280.08
16	18.15	64.01	348.23	53.82	187.43	337.374
17	17.38	55.36	20.97	-284.81 (error)	-59.74 (error)	N/A

Figure A-4-1 merely show the hourly energy received by an inclined surface per metre squared without considering the absorptivity and transmittivity efficiencies of the surface of the ETSC. Assuming negligible heat losses between the ETSCs and the evaporator, the total energy absorbed by the SW through the day in Watts is calculated using figure A-4-3.

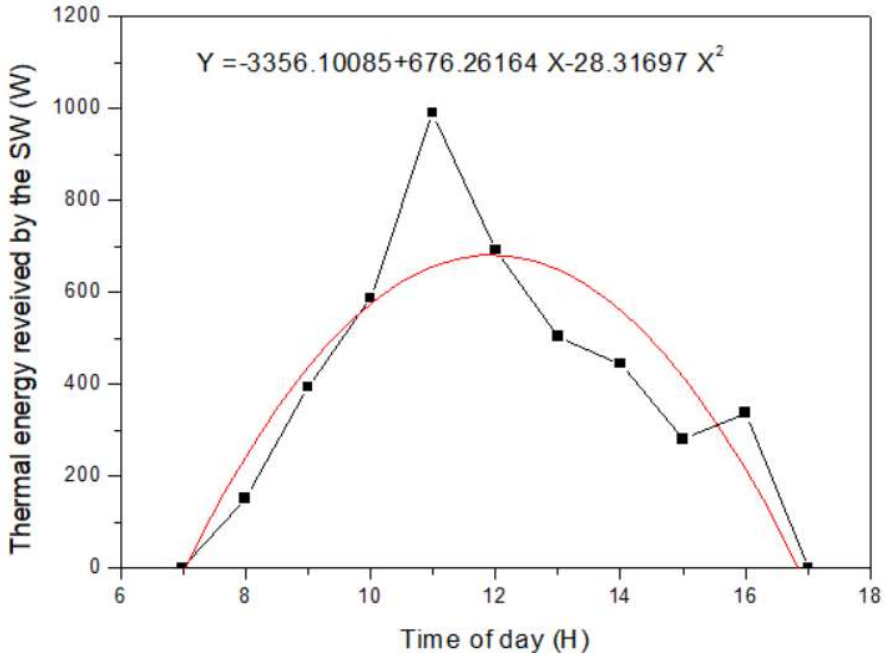

Figure A-4-3: Thermal energy received by the SW in Watts

$$y = -3356.101 + 676.262t - 28.317t^2$$

$$Q_{ETSC} = \int_7^{18} -3356.101 + 676.262t - 28.317t^2$$

$$= \left\{[-3356.101t] + \left[\frac{1}{2}(676.262t^2)\right] - \left[\frac{1}{3}(28.317t^3)\right]\right\}_7^{17}$$

$$\underline{= 4454.099\ Wh}$$

$$\underline{= 16034.755\ kJ}$$

This 16034.755 kJ is the total energy received by the SW throughout the day. Using table, A-4-1, with the temperature of 15.86°C at 10h00 am. The evaporative energy (hfg_{evap}) for SW temperature (T_{SW}) below 70°C is:

$$hfg_{evap} = 2.4935 \times 10^6\left[(1 - 9.4779 \times 10^{-4}T_{sw}) + \left(1.3132 \times 10^{-7}{T_{sw}}^2\right) - \left(4.7979 \times 10^{-9}{T_{sw}}^3\right)\right] \quad \text{(Eq. 4.41)}$$

$$= 2.4935 \times 10^6[(1 - 9.4779 \times 10^{-4} \times 15.86) + (1.3132 \times 10^{-7} \times 15.86^2) - (4.7979 \times 10^{-9} \times 15.86^3)]$$

$$\underline{= 2456.0525\ kJ/kg}$$

Noting that,

$$T_{sw} = T_v \quad \text{(Eq. 4.40)}$$

For temperatures above 70°C, equation 4.39 was used to calculate the evaporative energy in the evaporator. Averaging all the hourly evaporative energy calculated for the day gives:

$$\underline{hfg_{evap} = 2633.22\ kJ/kg}$$

The volume of the distillate produced which was 1110 ml (1.11 litres) was assumed to be equal to the evaporated SW in the evaporator and reached the stages. In addition, 1 litre of water was assumed to be equal to 1 kg of water.

The total evaporative energy in kilo-Joules is:

$$m_e hfg_{evap} = 2633.22\ kJ/kg\ \times 1.11\ kg$$

$$\underline{= 2922.874\ kJ}$$

$$Q_{ETSC} = \left[m_{sw} cp \frac{dT}{dt} + m_e hf_g\right]_{evap} \quad \text{(Eq. 4.27)}$$

$$m_{sw} cp \frac{dT}{dt} = Q_{ETSC} - m_e hfg_{evap}$$

$$= 16034.755\ kJ - (1.11kg \times 2633.22kJ/kg)$$

$= 13111.881\ kJ$

The 13111.881 kJ of energy was responsible heating and increasing the SW temperature in the evaporator. It not only accounted for the heat absorbed by the SW but the heat losses in the evaporator and vapour make-up tubes due to pre-mature condensation. Therefore, the overall thermal efficiency of the desalination system is:

$$\eta = \frac{\dot{m}_e\, hfg_{evap}}{A_{cc} \int I_\beta dt} \times 100\% \qquad (4.38)$$

$$= \frac{2922.874}{16034.755} \times 100\%$$

$= 18.23\%$

The distillate yield from each stage was 560, 100, 170, 30 and 250 ml for stages 1 to 5, respectively.

$\dot{m}_e hfg_{evap} = \dot{m}_{e1} hfg_1 + \dot{m}_{e2} hfg_2 + \dot{m}_{e3} hfg_3 + \dot{m}_{e4} hfg_4 + \dot{m}_{e5} hfg_5$ (Eq. 4.30)

Since,

$\dot{m}_1 = \dot{m}_{dist1} = \dot{m}_{e1}$ (Eq. 4.32)

The total evaporative energy in stage 1 was 0.56 of the total evaporative energy from the evaporator. That is,

$m_{e1} hfg_1 = 0.56 \times 2633.22 = 1474.603\ kJ$

$m_{e2} hfg_2 = 0.1 \times 2633.22 = 263.322\ kJ$

$m_{e3} hfg_3 = 0.17 \times 2633.22 = 447.647\ kJ$

$m_{e4} hfg_4 = 0.03 \times 2633.22 = 78.997\ kJ$

$m_{e5} hfg_5 = 0.25 \times 2633.22 = 658.305\ kJ$

These stage's evaporative energies were responsible for pre-heating the SW in the zigzagged SW tube in addition to the BSS. Some of this evaporative energy was lost through the stage walls and stage trays of the condensing tower.

Therefore,

$m_e hfg_{evap} = \sum (m_e hfg)_{1-5}$

$2922.874 = 1474.603 + 263.322 + 447.647 + 78.997 + 658.305$

$2922.874\ kJ = 2922.874\ kJ$

Moreover, equations 4.31 and 4.33 to 4.37 accounts for the heat losses in each stages. However, the evaporative energy of 2922.874 kJ was responsible for the total volume of distillate produced.

A-5: Economic analysis sample calculations

Date: 13 Jan. 2021

Annual interest rate (i) = 15%

No. of operational years (n) = 12

Present capital cost (P) = R40 000 (SA Rands)

No. of operational days per year = 260

Dist. Yield/day from the MSS-SS stages = 6.73 (litres), annual yield = 6.73 x 260 = 1749.8 (Litres).

Dist. Yield/day from the MSS-SS + BSS = 7.79 (litres), annual yield = 7.79 x 260 = 2025.4 (Litres).

$$CRF = \frac{i(1+i)^n}{[(1+i)^n-1]} \quad \text{(Eq. 4.43)}$$

$$= \frac{0.15(1+0.15)^{12}}{[(1+0.15)^{12}-1]}$$

$$\underline{= 0.1845}$$

$$FAC = P \times CRF \quad \text{(Eq. 4.44)}$$

$$= 40000 \times 0.1845$$

$$\underline{= R\ 7379.23}$$

$$SFF = \frac{i}{[(1+i)^n-1]} \quad \text{(Eq. 4.45)}$$

$$= \frac{0.15}{[(1+0.15)^{12}-1]}$$

$$\underline{= 0.0345}$$

$$S = 0.2P \quad \text{(Eq. 4.46)}$$

$$= 0.2 \times 40000$$

$$\underline{= \text{R } 8000.00}$$

$$ASV = SFF \times S \quad \text{(Eq. 4.47)}$$

$$= 0.0345 \times 8000$$

$$\underline{= \text{R } 276.00}$$

$$AMC = 0.15 \times FAC \quad \text{(Eq. 4.48)}$$

$$= 0.15 \times 7379.23$$

$$= R\ 1106.88$$

$$AC = FAC + AMC - ASV \quad \text{(Eq. 4.49)}$$

$$= 7379.23 + 1106.88 - 276$$

$$= \text{R } 8210.11$$

$$CPL = \frac{AC}{M} \quad \text{(Eq. 4.50)}$$

Capital cost of the MSS-SS stage based on annual yield of 1749.8 litres is:

$$CPL_{MSS-S} = \frac{8210.11}{1749.8} = R\ 4.69/litre$$

Capital cost of the MSS-SS + BSS based on annual yield of 2025.4 litres is:

$$CPL_{MSS-SS+BSS} = \frac{8210.11}{2025.4} = R\ 4.05/litre$$

Appendix B

B-1: Tabulated experimental results data

Dates	Average Solar irradiance (I_H)	Average ambient temp.	Average velocity	Stacked stages dist. Yield	BSS dist. Yield	Solar Incidence duration per day	Condensing tower thermal insulation
	(W/m²)	**(°C)**	**(m/s)**	**(ml)**	**(ml)**	**(00h00minutes)**	
20 Sept. 2020	201.8	14.9	3.1	N/A	N/A	11h45	Yes
21 Sept. 2020	388.9	15.6	3.8	N/A	N/A	12h05	Yes
22 Sept. 2020	424.2	18.2	1.9	5180	560	12h10	Yes
23 Sept. 2020	420.9	17.9	2	N/A	N/A	12h10	Yes
24 Sept. 2020	418.9	19.3	1.5	4820	360	12h00	Yes
25 Sept. 2020	145.1	14.1	4	NM	NM	11h50	Yes
26 Sept. 2020	253.7	12.5	1.7	4750	340	12h10	Yes
27 Sept. 2020	368.7	14.2	1.3	N/A	N/A	12h15	Yes
28 Sept. 2020	371.6	14.2	1.8	N/A	N/A	12h15	Yes
29 Sept. 2020	385.7	15.5	3.2	4980	480	12h20	Yes
30 Sept. 2020	412.2	15.4	2.4	5080	510	12h20	Yes
01 Oct. 2020	337.2	15.2	9.1	5170	400	12h20	Yes
02 Oct. 2020	410.8	17.3	5.4	5100	330	12h05	Yes
03 Oct. 2020	424.8	21	1.7	5220	490	12h05	Yes
04 Oct. 2020	469.9	21.7	0.9	5150	720	12h35	No
05 Oct. 2020	426.0	18.3	1.7	5730	610	12h30	No
06 Oct. 2020	446.9	19.3	3.1	5770	740	12h40	No
07 Oct. 2020	373.0	17.8	4.2	N/A	N/A	12h25	No
08 Oct. 2020	268.8	18.6	1.2	4870	460	12h30	No
09 Oct. 2020	291.2	15.2	4.3	N/A	N/A	12h45	No
10 Oct. 2020	449.7	17.8	5.3	5890	780	12h45	No
11 Oct. 2020	496.9	19.1	1.5	5740	800	12h50	No
12 Oct. 2020	483.3	21.5	2.3	5610	720	12h55	No
13 Oct. 2020	452.2	16.6	4.8	5960	650	12h40	No
14 Oct. 2020	358.1	20.7	1.4	5430	540	12h58	No
15 Oct. 2020	405.5	18.3	5	5690	490	12h45	No
16 Oct. 2020	498.7	24.6	1.4	5980	990	13h00	No
17 Oct. 2020	422.8	19.7	2.2	5330	740	12h50	No
18 Oct. 2020	318.0	14.4	2.1	N/A	N/A	12h55	No
19 Oct. 2020	314.4	18	1.8	N/A	N/A	13h05	No
20 Oct. 2020	407.6	17.9	1.9	5270	730	13h05	No
21 Oct. 2020	472.2	17.2	3.2	5850	960	13h10	No
22 Oct. 2020	495.0	20.1	3.2	5880	970	13h10	No
23 Oct. 2020	488.5	21.5	1.6	5820	840	13h05	No
24 Oct. 2020	247.5	18.9	1.7	4820	490	13h05	No
25 Oct. 2020	394.8	19	4	5050	790	13h03	No
26 Oct. 2020	512.2	22.8	1.9	N/A	N/A	13h15	No
27 Oct. 2020	512.2	22.8	1.9	6020	940	13h15	No
28 Oct. 2020	396.0	19	3.3	5000	660	13h05	No
29 Oct. 2020	378.9	18.2	4.1	4250	490	12h55	No
30 Oct. 2020	489.3	16.4	4.5	N/A	N/A	13h30	No
31 Oct. 2020	506.8	20	4.4	N/A	N/A	13h30	No
01 Nov. 2020	540.1	23.5	2.7	N/A	N/A	13h30	No
02 Nov. 2020	546.8	25.3	2	N/A	N/A	13h30	No
03 Nov. 2020	479.2	23.0	2.5	4890	920	13h40	No
04 Nov. 2020	514.1	24.8	2.9	5700	750	13h35	No
05 Nov. 2020	320.3	19.9	3.7	4970	640	13h15	No
06 Nov. 2020	125.6	15.3	3.3	NM	NM	13h20	No
07 N0v. 2020	443.4	18.1	7.1	5370	810	13h40	No
08 Nov. 2020	390.7	16.6	3.9	5110	640	13h20	No
09 Nov. 2020	467.2	16.2	2.7	5030	610	13h50	No
10 Nov. 2020	521.9	18.3	4.6	6020	890	13h50	No

11 Nov. 2020	560.3	22.4	2	6390	930	13h50	No
12 Nov. 2020	581.8	28.0	1.5	6730	770	13h50	No
13 Nov. 2020	528.5	20.7	3.4	5480	690	13h50	No
15 N0v. 2020	506.6	18	5.1	5830	730	14h00	No
16 Nov. 2020	510	19.7	3.7	5100	550	13h55	No
17 Nov. 2020	537.3	21.7	3.6	5390	590	13h55	No
18 Nov. 2020	520.6	21.2	5.6	N/A	N/A	14h05	No
19 Nov. 2020	549.4	23.7	3.4	6040	760	14h05	No
20 Nov. 2020	572.6	26.4	1.7	6380	1000	14h05	No
21 Nov. 2020	479.3	21.9	2.3	5650	650	13h55	No
22 Nov. 2020	452.8	19.5	3.3	5190	700	14h00	No
23 Nov. 2020	411	18.5	2.9	5110	630	13h55	No
24 Nov. 2020	244.0	16.7	3.6	N/A	N/A	13h55	No
25 Nov. 2020	357.5	17.4	1.7	N/A	N/A	14h00	No
26 Nov. 2020	463.5	18.7	4.3	N/A	N/A	14h00	No
27 Nov. 2020	548.0	23.5	2.7	6290	860	14h05	No
28 Nov. 2020	536.6	21	6.1	6200	800	14h20	No
29 Nov. 2020	535.1	19.8	4.9	6180	990	14h10	No
30 Nov. 2020	434.9	19.6	2.4	5430	670	14h10	No
01 Dec. 2020	324.2	18.6	3	4970	580	14h05	No
02 Dec. 2020	532.5	19.8	5.5	6120	920	14h10	No
03 Dec. 2020	531.4	20.2	6.4	5770	900	14h20	No
04 Dec. 2020	569.1	24.6	3.1	6320	1010	14h20	No
05 Dec. 2020	566.4	25.5	2.6	6360	1020	14h20	No
06 Dec. 2020	562.9	24.7	2.3	6260	1000	14h15	No
07 Dec. 2020	424.4	21.2	2.9	N/A	N/A	14h20	No
08 Dec. 2020	369.8	20	3	N/A	N/A	13h45	No
09 Dec. 2020	484.7	22	3.2	5740	780	14h15	No
10 Dec. 2020	407.3	21.5	2	N/A	N/A	14h20	No
11 Dec. 2020	291.9	19.1	2.6	4490	410	14h15	No
12 Dec. 2020	516.4	20	4.2	5740	730	14h25	No
13 Dec. 2020	579.2	22.6	2.5	6130	970	14h25	No
14 Dec. 2020	482.7	20.1	3	5850	880	14h20	No
15 Dec. 2020	546.1	20.9	5.8	6270	860	14h30	No
16 Dec. 2020	554.5	21	4.7	6310	830	14h25	No
17 Dec. 2020	436.6	22.6	5.2	5100	730	14h25	No
13 Jan. 2021	585	29.3	3.1	6730	1060	14h20	No
14 Jan. 2021	580.6	27.4	2	6440	1140	14h25	No
17 Jan. 2021	434.4	21.9	2.6	5360	590	13h50	No
18 Jan. 2021	551.3	24.2	3.7	6360	820	13h50	No
19 Jan. 2021	525.6	20.9	2.7	6020	660	13h40	No
21 Jan. 2021	478.4	23.1	3.4	6560	720	14h00	No
22 Jan. 2021	548.3	24.4	2.9	6200	610	14h05	No
23 Jan. 2021	392.0	23.4	2.3	5750	500	13h45	No
24 Jan. 2021	512.9	21.9	5.6	5920	630	14h05	No
25 Jan. 2021	567.3	25.7	2.4	7680	1110	14h00	No
26 Jan. 2021	519.3	22.2	7	6360	980	14h00	No
27 Jan. 2021	464.9	22.1	5.6	5790	750	13h55	No
28 Jan. 2021	515.6	21.6	4	6210	910	14h00	No
29 Jan. 2021	502.1	22.6	3.2	6040	790	13h55	No
30 Jan. 2021	404.2	24.3	2	5980	710	13h45	No
31 Jan. 2021	316.9	21.8	3.8	5520	570	13h15	No
01 Feb. 2021	425.8	23.4	4.1	5710	590	13h35	No
02 Feb. 2021	569.7	27.7	1.9	6160	960	13h45	No
03 Feb. 2021	514.3	22.3	5.7	5910	880	13h45	No
04 Feb. 2021	518.7	23.1	4.9	6190	580	13h45	No
05 Feb. 2021	519.9	23.2	4.4	6150	620	13h45	No
06 Feb. 2021	547.5	24.2	4.7	5960	910	13h40	No
07 Feb. 2021	455.1	22	6.2	N/A	N/A	13h35	No
08 Feb. 2021	492.2	23.5	6	6020	560	13h30	No
09 Feb. 2021	501.2	23.6	6	N/A	N/A	13h35	No
10 Feb. 2021	504.9	23.9	4.2	5710	840	13h35	No
11 Feb 2021	510.5	24.6	3.7	5870	790	13h30	No
12 Feb. 2021	414.1	23.7	5.2	5080	480	13h25	No

13 Feb. 2021	509.3	24.4	3.3	5460	610	13h30	No
14 Feb. 2021	426.6	22.2	3	5540	340	13h05	No
15 Feb. 2021	472.9	20.9	4	5300	490	13h15	No
16 Feb. 2021	525.1	24.8	3.2	6040	560	13h20	No
17 Feb. 2021	516.9	24	3.1	5950	630	13h15	No
18 Feb. 2021	323.7	20.8	2.5	5830	510	13h10	No
19 Feb. 2021	485.1	21.9	4.2	5150	450	13h10	No
20 Feb. 2021	401.2	21.8	2.2	5040	430	13h05	No
21 Feb. 2021	417.7	20.6	3.4	5480	520	13h10	No
22 Feb. 2021	479.2	21.2	2.6	5610	530	13h05	No
23 Feb. 2021	466.8	22.3	2.7	5360	570	13h05	No
24 Feb. 2021	452.9	22.4	5.9	5430	440	13h00	No
25 Feb. 2021	459.8	22.7	6.5	N/A	N/A	13h15	No
26 Feb 2021	440.2	25.7	3.6	5160	560	12h50	No
27 Feb. 2021	439.9	27.3	2.5	5190	620	12h50	No
28 Feb. 2021	474.9	28.9	2.3	5460	530	12h55	No
01 Mar. 2021	311.5	25.7	2.7	N/A	N/A	13h00	No
02 Mar. 2021	424.3	23.2	3.2	N/A	N/A	13h00	No
03 Mar. 2021	416.4	23.5	2.3	N/A	N/A	12h50	No
04 Mar. 2021	377.9	21	4.3	4680	270	12h25	No
05 Mar. 2021	466.7	27.7	2.3	5290	670	12h45	No
08 Mar. 2021	338.8	19.6	3.3	2250	360	12h15	No
11 Mar. 2021	425.4	22.3	1.5	3080	340	12h25	No
13 Mar. 2021	401.4	22.8	3.7	3390	440	12h25	Yes
15 Mar. 2021	209.5	18.3	4.3	950	170	11h10	Yes
16 Mar. 2021	491	21.7	4.9	5620	750	11h45	Yes
17 Mar. 2021	301.8	24.1	1.6	5690	820	12h10	Yes
18 Mar. 2021	436.4	22.1	2.8	4830	600	12h14	Yes
20 Mar. 2021	442.7	20.9	4.4	3600	340	12h56	Yes
21 Mar. 2021	404.6	20.3	5.7	5880	700	12h10	Yes
22 Mar. 2021	444.2	23.8	2.9	5270	650	12h10	Yes
23 Mar. 2021	435.5	24.9	2.4	5760	860	12h10	Yes
24 Mar. 2021	442.0	27.2	1.9	4780	700	12h05	Yes
25 Mar. 2021	439.2	27.5	1.3	5370	670	12h00	Yes
26 Mar. 2021	301.4	21.7	4.4	1980	210	11h40	Yes
27 Mar. 2021	396.0	18.9	3.7	5020	530	11h55	Yes
28 Mar. 2021	418.9	23.1	1.3	3370	500	11h45	Yes
29 Mar. 2021	435.6	26.6	1.3	4990	660	11h50	Yes
30 Mar. 2021	383.1	20.6	3	4730	470	11h45	Yes
31 Mar. 2021	155.5	18.1	1.7	220	150	11h25	Yes
01 Apr. 2021	411.1	19.7	4.6	3870	520	11h40	Yes
02 Apr. 2021	262.4	20.2	1.4	1590	230	11h30	Yes
03 Apr. 2021	411.7	23.1	1.9	3750	600	11h40	Yes
05 Apr. 2021	395.0	20.1	5.1	4540	540	11h40	Yes
06 Apr. 2021	415.6	22.3	1.5	5160	980	11h35	Yes
07 Apr. 2021	400.2	20.5	2.6	3850	660	11h30	Yes
08 Apr. 2021	388.0	19.5	3.5	4530	440	11h30	Yes
09 Apr. 2021	388.7	21.2	4.1	4050	380	11h30	Yes
10 Apr. 2021	403.5	21.4	1.9	3040	300	11h15	Yes
11 Apr. 2021	400.5	20.4	3.9	3970	560	11h15	Yes
12 Apr. 2021	357.2	21.8	1.3	3440	280	11h20	Yes
13 Apr. 2021	393.4	23.3	1.2	3560	440	11h15	Yes
14 Apr. 2021	385	21.4	1.9	3590	460	11h20	Yes
15 Apr. 2021	329.9	22.3	3.8	2200	210	11h10	Yes
16 Apr. 2021	386.6	24.4	1.6	4530	720	11h15	Yes
17 Apr. 2021	378.2	24.2	0.7	4020	650	11h15	Yes
18 Apr. 2021	392.1	29.2	2.6	4450	620	11h05	Yes
19 Apr. 2021	328.0	22.6	4.5	2810	290	11h05	Yes
20 Apr. 2021	367.0	22.5	1.4	4040	480	11h05	Yes
21 Apr. 2021	354.1	22.1	1.5	3550	500	10h55	Yes
22 Apr. 2021	358.4	20.4	1.1	4140	580	11h05	Yes
23 Apr. 2021	299.4	19.5	2.7	3240	380	10h55	Yes
27 Apr. 2021	262.2	19.0	1.5	960	540	10h35	Yes
28 Apr. 2021	361.7	17.1	4.6	2330	340	10h50	Yes

29 Apr. 2021	258.7	17.3	3.9	1890	170	10h45	Yes
30 Apr. 2021	340.2	17.6	4.7	2640	380	10h50	Yes
01 May 2021	338.8	18.8	1	3250	430	10h45	Yes
02 May 2021	361.8	23.6	1.1	4260	620	10h45	Yes
03 May 2021	332.1	26.3	1.5	1990	770	10h35	Yes
04 May 2021	273.0	19.8	2.1	2030	340	10h30	Yes
08 May 2021	268.5	18.2	1.4	1950	590	10h30	Yes
09 May 2021	290.5	18.2	1.2	2600	380	10h25	Yes
10 May 2021	219.9	18.1	1.3	1690	290	10h30	Yes
11 May 2021	288.4	17.4	1.8	2810	380	10h30	Yes
12 May 2021	305.4	18.7	1.4	2930	470	10h25	Yes
13 May 2021	229.4	17.6	1.8	1180	180	10h30	Yes
14 May 2021	269.6	18.9	3.8	1420	310	10h10	Yes
16 May 2021	283.6	16.1	1.1	1890	310	10h20	Yes
18 May 2021	281.1	16.6	0.9	2190	350	10h25	Yes
20 May 2021	105.2	14.2	3.5	NM	NM	09h55	Yes
21 May 2021	187.4	14.7	1.6	920	140	10h05	Yes
22 May 2021	281.7	15.1	0.7	2530	330	10h10	Yes
23 May 2021	278.7	22.0	1.3	2870	390	10h15	Yes
24 May 2021	195.0	19.1	2.5	290	100	10h00	Yes
25 May 2021	114.7	17.0	2	NM	NM	09h45	Yes
26 May 2021	208.3	17.4	2.2	870	90	09h50	Yes
27 May 2021	164.4	16.0	3.9	290	140	10h00	Yes
28 May 2021	179.2	17.2	4.2	210	100	09h35	Yes
29 May 2021	179.5	16.9	2.1	1110	80	09h55	Yes
30 May 2021	234.6	16.9	0.7	1680	140	10h00	Yes
31 May 2021	197.6	14.7	1.6	580	130	09h50	Yes
01 Jun. 2021	209.9	14.5	1.2	1020	140	09h15	Yes
02 Jun. 2021	246.1	15.8	2.1	1720	220	09h20	Yes
03 Jun. 2021	287.8	15.3	0.6	2290	310	10h36	Yes
04 June 2021	258.0	16.1	0.9	2300	320	10h15	Yes
05 June 2021	241.5	16.2	0.2	2510	490	10h00	Yes
06 June 2021	265.2	22.3	3.9	1980	250	10h10	Yes
07 June 2021	259.5	23.7	2.8	1620	190	09h50	Yes
08 June 2021	239.5	18.7	1.4	790	110	09h50	Yes
09 June 2021	176.1	16.5	0.4	1270	110	09h55	Yes
10 June 2021	218.3	14.9	1.2	780	150	10h05	Yes
11 June 2021	228.7	18.6	1.1	1970	200	09h55	Yes
12 June 2021	240.8	16.9	0.7	2070	230	09h45	Yes
13 June 2021	173.6	14.6	1.9	720	130	09h45	Yes
14 June 2021	207.4	13.9	0.9	1290	220	09h45	Yes
15 June 2021	204.7	15.9	1.5	660	120	09h40	Yes
16 June 2021	139.1	15.9	2.4	NM	NM	09h50	Yes
17 June 2021	122.7	14.9	1.3	NM	NM	09h50	Yes
18 June 2021	242.2	15.2	1.2	1490	290	09h55	Yes
19 June 2021	253.7	20.6	0.9	2450	340	09h55	Yes
20 June 2021	220.1	22.5	1.3	1490	200	09h55	Yes
21 June 2021	250.1	20.4	3.8	1190	210	09h45	Yes
22 June 2021	129.3	16.2	4.9	NM	NM	09h50	Yes
23 June 2021	160.2	16.7	0.9	NM	NM	09h20	Yes
24 June 2021	228.9	13.0	0.6	1850	340	09h50	Yes
25 June 2021	120.2	14.0	5.3	NM	NM	09h45	Yes
26 June 2021	209.8	15.0	2.5	340	170	09h40	Yes
27 June 2021	268.6	14.9	4.1	1200	190	09h50	Yes
28 June 2021	48.0	11.0	0.7	NM	NM	08h55	Yes
29 June 2021	70.5	11.2	2.4	NM	NM	08h40	Yes
30 June 2021	157.3	14.1	6.5	NM	NM	08h35	Yes
01 July 2021	164.2	15.2	3.3	190	110	08h40	Yes
02 July 2021	142.0	15.2	4.4	NM	NM	08h50	Yes
03 July 2021	130.2	14.4	2.7	NM	NM	09h35	Yes
04 July 2021	168.2	12.9	1.3	220	140	09h40	Yes
05 July 2021	240.1	14.1	0.7	1170	180	09h55	Yes
06 July 2021	226.7	12.5	1.8	980	160	10h00	Yes

B-2: Economic analysis results

Date	Dist. Yield MSS-SS (litres)	Dist. Yield MSS-SS + BSS (litres)	Annual yield (M) MSS-SS	Annual yield (M) MSS-SS +BSS	Cost per litre (CPL) MSS-SS	Cost per litre (CPL) MSS-SS +BSS
	(Litres)				(Rands)	
19-Sep-20	4.21	4.46	1094.6	1159.6	R 7.50	R 7.08
22-Sep-20	5.18	5.74	1346.8	1492.4	R 6.10	R 5.50
24-Sep-20	4.82	5.18	1253.2	1346.8	R 6.55	R 6.10
26-Sep-20	4.75	5.09	1235	1323.4	R 6.65	R 6.20
29-Sep-20	4.98	5.46	1294.8	1419.6	R 6.34	R 5.78
30-Sep-20	5.08	5.59	1320.8	1453.4	R 6.22	R 5.65
01-Oct-20	5.17	5.57	1344.2	1448.2	R 6.11	R 5.67
02-Oct-20	5.1	5.43	1326	1411.8	R 6.19	R 5.82
03-Oct-20	5.22	5.71	1357.2	1484.6	R 6.05	R 5.53
04-Oct-20	5.15	5.87	1339	1526.2	R 6.13	R 5.38
05-Oct-20	5.73	6.34	1489.8	1648.4	R 5.51	R 4.98
06-Oct-20	5.77	6.51	1500.2	1692.6	R 5.47	R 4.85
08-Oct-20	4.87	5.33	1266.2	1385.8	R 6.48	R 5.92
10-Oct-20	5.89	6.67	1531.4	1734.2	R 5.36	R 4.73
11-Oct-20	5.74	6.54	1492.4	1700.4	R 5.50	R 4.83
12-Oct-20	5.61	6.33	1458.6	1645.8	R 5.63	R 4.99
13-Oct-20	5.96	6.61	1549.6	1718.6	R 5.30	R 4.78
14-Oct-20	5.43	5.97	1411.8	1552.2	R 5.82	R 5.29
15-Oct-20	5.69	6.18	1479.4	1606.8	R 5.55	R 5.11
16-Oct-20	5.98	6.97	1554.8	1812.2	R 5.28	R 4.53
17-Oct-20	5.33	6.07	1385.8	1578.2	R 5.92	R 5.20
20-Oct-20	5.27	6	1370.2	1560	R 5.99	R 5.26
21-Oct-20	5.85	6.81	1521	1770.6	R 5.40	R 4.64
22-Oct-20	5.88	6.85	1528.8	1781	R 5.37	R 4.61
23-Oct-20	5.82	6.66	1513.2	1731.6	R 5.43	R 4.74
24-Oct-20	4.82	5.31	1253.2	1380.6	R 6.55	R 5.95
25-Oct-20	5.05	5.84	1313	1518.4	R 6.25	R 5.41
27-Oct-20	6.02	6.96	1565.2	1809.6	R 5.25	R 4.54
28-Oct-20	5	5.66	1300	1471.6	R 6.32	R 5.58
29-Oct-20	4.25	4.74	1105	1232.4	R 7.43	R 6.66
03-Nov-20	5.89	6.81	1531.4	1770.6	R 5.36	R 4.64
04-Nov-20	5.7	6.45	1482	1677	R 5.54	R 4.90
05-Nov-20	4.97	5.61	1292.2	1458.6	R 6.35	R 5.63
07-Nov-20	5.37	6.18	1396.2	1606.8	R 5.88	R 5.11
08-Nov-20	5.11	5.75	1328.6	1495	R 6.18	R 5.49
09-Nov-20	5.03	5.64	1307.8	1466.4	R 6.28	R 5.60
10-Nov-20	6.02	6.91	1565.2	1796.6	R 5.25	R 4.57
11-Nov-20	6.39	7.32	1661.4	1903.2	R 4.94	R 4.31
12-Nov-20	6.73	7.5	1749.8	1950	R 4.69	R 4.21
13-Nov-20	5.48	6.17	1424.8	1604.2	R 5.76	R 5.12
15-Nov-20	5.83	6.56	1515.8	1705.6	R 5.42	R 4.81
16-Nov-20	5.1	5.65	1326	1469	R 6.19	R 5.59
17-Nov-20	5.39	5.98	1401.4	1554.8	R 5.86	R 5.28
19-Nov-20	6.04	6.8	1570.4	1768	R 5.23	R 4.64
20-Nov-20	6.38	7.38	1658.8	1918.8	R 4.95	R 4.28
21-Nov-20	5.65	6.3	1469	1638	R 5.59	R 5.01
22-Nov-20	5.19	5.89	1349.4	1531.4	R 6.08	R 5.36
23-Nov-20	5.11	5.74	1328.6	1492.4	R 6.18	R 5.50
27-Nov-20	6.29	7.15	1635.4	1859	R 5.02	R 4.42
28-Nov-20	6.2	7	1612	1820	R 5.09	R 4.51
29-Nov-20	6.13	7.12	1593.8	1851.2	R 5.15	R 4.44
30-Nov-20	5.43	6.1	1411.8	1586	R 5.82	R 5.18
01-Dec-20	4.97	5.55	1292.2	1443	R 6.35	R 5.69
02-Dec-20	6.12	7.04	1591.2	1830.4	R 5.16	R 4.49
03-Dec-20	5.77	6.67	1500.2	1734.2	R 5.47	R 4.73
04-Dec-20	6.32	7.33	1643.2	1905.8	R 5.00	R 4.31
05-Dec-20	6.36	7.38	1653.6	1918.8	R 4.97	R 4.28

06-Dec-20	6.26	7.26	1627.6	1887.6	R 5.04	R 4.35
09-Dec-20	5.74	6.52	1492.4	1695.2	R 5.50	R 4.84
11-Dec-20	4.49	4.9	1167.4	1274	R 7.03	R 6.44
12-Dec-20	5.74	6.47	1492.4	1682.2	R 5.50	R 4.88
13-Dec-20	6.13	7.1	1593.8	1846	R 5.15	R 4.45
14-Dec-20	5.85	6.73	1521	1749.8	R 5.40	R 4.69
15-Dec-20	6.27	7.13	1630.2	1853.8	R 5.04	R 4.43
16-Dec-20	6.31	7.14	1640.6	1856.4	R 5.00	R 4.42
17-Dec-20	5.1	5.83	1326	1515.8	R 6.19	R 5.42
18-Dec-20	6.72	7.7	1747.2	2002	R 4.70	R 4.10
13-Jan-21	6.73	7.79	1749.8	2025.4	R 4.69	R 4.05
14-Jan-21	6.44	7.58	1674.4	1970.8	R 4.90	R 4.17
15-Jan-21	6.43	7.22	1671.8	1877.2	R 4.91	R 4.37
16-Jan-21	6.76	7.7	1757.6	2002	R 4.67	R 4.10
17-Jan-21	5.36	5.95	1393.6	1547	R 5.89	R 5.31
18-Jan-21	6.36	7.18	1653.6	1866.8	R 4.97	R 4.40
19-Jan-21	6.02	6.68	1565.2	1736.8	R 5.25	R 4.73
21-Jan-21	6.56	7.28	1705.6	1892.8	R 4.81	R 4.34
22-Jan-21	6.2	6.81	1612	1770.6	R 5.09	R 4.64
23-Jan-21	5.75	6.25	1495	1625	R 5.49	R 5.05
24-Jan-21	5.92	6.92	1539.2	1799.2	R 5.33	R 4.56
25-Jan-21	6.36	7.47	1653.6	1942.2	R 4.97	R 4.23
26-Jan-21	6.59	7.57	1713.4	1968.2	R 4.79	R 4.17
27-Jan-21	5.79	6.54	1505.4	1700.4	R 5.45	R 4.83
28-Jan-21	6.21	7.12	1614.6	1851.2	R 5.09	R 4.44
29-Jan-21	6.04	6.83	1570.4	1775.8	R 5.23	R 4.62
30-Jan-21	5.98	6.69	1554.8	1739.4	R 5.28	R 4.72
31-Jan-21	5.52	6.09	1435.2	1583.4	R 5.72	R 5.19
01-Feb-21	5.71	6.3	1484.6	1638	R 5.53	R 5.01
02-Feb-21	6.16	7.12	1601.6	1851.2	R 5.13	R 4.44
03-Feb-21	5.91	6.79	1536.6	1765.4	R 5.34	R 4.65
04-Feb-21	6.19	6.77	1609.4	1760.2	R 5.10	R 4.66
05-Feb-21	6.15	6.77	1599	1760.2	R 5.13	R 4.66
06-Feb-21	5.96	6.87	1549.6	1786.2	R 5.30	R 4.60
08-Feb-21	6.02	6.58	1565.2	1710.8	R 5.25	R 4.80
10-Feb-21	5.71	6.45	1484.6	1677	R 5.53	R 4.90
11-Feb-21	5.87	6.66	1526.2	1731.6	R 5.38	R 4.74
12-Feb-21	5.08	5.56	1320.8	1445.6	R 6.22	R 5.68
13-Feb-21	5.46	6.07	1419.6	1578.2	R 5.78	R 5.20
14-Feb-21	5.54	5.88	1440.4	1528.8	R 5.70	R 5.37
15-Feb-21	5.3	5.79	1378	1505.4	R 5.96	R 5.45
16-Feb-21	6.04	6.6	1570.4	1716	R 5.23	R 4.78
17-Feb-21	5.95	6.58	1547	1710.8	R 5.31	R 4.80
18-Feb-21	5.83	6.34	1515.8	1648.4	R 5.42	R 4.98
19-Feb-21	5.15	5.6	1339	1456	R 6.13	R 5.64
20-Feb-21	5.04	5.47	1310.4	1422.2	R 6.27	R 5.77
21-Feb-21	5.48	6	1424.8	1560	R 5.76	R 5.26
22-Feb-21	5.61	6.14	1458.6	1596.4	R 5.63	R 5.14
23-Feb-21	5.36	5.93	1393.6	1541.8	R 5.89	R 5.33
24-Feb-21	5.43	5.87	1411.8	1526.2	R 5.82	R 5.38
26-Feb-21	5.16	5.72	1341.6	1487.2	R 6.12	R 5.52
27-Feb-21	5.19	5.81	1349.4	1510.6	R 6.08	R 5.44
28-Feb-21	5.46	5.99	1419.6	1557.4	R 5.78	R 5.27
04-Mar-21	4.68	4.95	1216.8	1287	R 6.75	R 6.38
05-Mar-21	5.29	5.96	1375.4	1549.6	R 5.97	R 5.30
07-Mar-21	4.27	4.95	1110.2	1287	R 7.40	R 6.38
08-Mar-21	3.66	4.02	951.6	1045.2	R 8.63	R 7.86
11-Mar-21	3.08	3.42	800.8	889.2	R 10.25	R 9.23
13-Mar-21	3.39	3.83	881.4	995.8	R 9.32	R 8.24
15-Mar-21	0.95	1.12	247	291.2	R 33.24	R 28.19
16-Mar-21	5.62	6.37	1461.2	1656.2	R 5.62	R 4.96
17-Mar-21	5.69	6.54	1479.4	1700.4	R 5.55	R 4.83
18-Mar-21	4.83	5.43	1255.8	1411.8	R 6.54	R 5.82
19-Mar-21	4.82	5.51	1253.2	1432.6	R 6.55	R 5.73

20-Mar-21	3.6	3.94	936	1024.4	R 8.77	R 8.01
21-Mar-21	5.88	6.58	1528.8	1710.8	R 5.37	R 4.80
22-Mar-21	5.27	5.92	1370.2	1539.2	R 5.99	R 5.33
23-Mar-21	5.76	6.62	1497.6	1721.2	R 5.48	R 4.77
24-Mar-21	4.78	5.48	1242.8	1424.8	R 6.61	R 5.76
25-Mar-21	5.37	6.04	1396.2	1570.4	R 5.88	R 5.23
26-Mar-21	1.98	2.19	514.8	569.4	R 15.95	R 14.42
27-Mar-21	4.02	4.55	1045.2	1183	R 7.86	R 6.94
28-Mar-21	3.37	3.87	876.2	1006.2	R 9.37	R 8.16
29-Mar-21	4.99	5.65	1297.4	1469	R 6.33	R 5.59
30-Mar-21	4.73	5.2	1229.8	1352	R 6.68	R 6.07
31-Mar-21	0.22	0.37	57.2	96.2	R 143.54	R 85.35
01-Apr-21	3.87	4.39	1006.2	1141.4	R 8.16	R 7.19
02-Apr-21	1.59	1.82	413.4	473.2	R 19.86	R 17.35
03-Apr-21	3.75	4.35	975	1131	R 8.42	R 7.26
05-Apr-21	4.54	5.08	1180.4	1320.8	R 6.96	R 6.22
06-Apr-21	5.16	6.14	1341.6	1596.4	R 6.12	R 5.14
07-Apr-21	3.85	4.51	1001	1172.6	R 8.20	R 7.00
08-Apr-21	4.53	4.97	1177.8	1292.2	R 6.97	R 6.35
09-Apr-21	4.05	4.43	1053	1151.8	R 7.80	R 7.13
10-Apr-21	3.04	3.34	790.4	868.4	R 10.39	R 9.45
11-Apr-21	3.97	4.53	1032.2	1177.8	R 7.95	R 6.97
12-Apr-21	3.44	3.72	894.4	967.2	R 9.18	R 8.49
13-Apr-21	3.56	4	925.6	1040	R 8.87	R 7.89
14-Apr-21	3.59	4.05	933.4	1053	R 8.80	R 7.80
15-Apr-21	2.2	2.41	572	626.6	R 14.35	R 13.10
16-Apr-21	4.53	5.25	1177.8	1365	R 6.97	R 6.01
17-Apr-21	4.02	4.67	1045.2	1214.2	R 7.86	R 6.76
18-Apr-21	4.45	5.07	1157	1318.2	R 7.10	R 6.23
19-Apr-21	2.81	3.1	730.6	806	R 11.24	R 10.19
20-Apr-21	4.04	4.52	1050.4	1175.2	R 7.82	R 6.99
21-Apr-21	3.55	4.05	923	1053	R 8.90	R 7.80
22-Apr-21	4.14	4.72	1076.4	1227.2	R 7.63	R 6.69
23-Apr-21	3.24	3.62	842.4	941.2	R 9.75	R 8.72
27-Apr-21	0.96	1.5	249.6	390	R 32.89	R 21.05
28-Apr-21	2.33	2.67	605.8	694.2	R 13.55	R 11.83
29-Apr-21	1.89	2.06	491.4	535.6	R 16.71	R 15.33
30-Apr-21	2.64	3.02	686.4	785.2	R 11.96	R 10.46
01-May-21	3.25	3.68	845	956.8	R 9.72	R 8.58
02-May-21	4.26	4.88	1107.6	1268.8	R 7.41	R 6.47
03-May-21	1.99	2.76	517.4	717.6	R 15.87	R 11.44
04-May-21	2.03	2.37	527.8	616.2	R 15.56	R 13.32
08-May-21	1.95	2.54	507	660.4	R 16.19	R 12.43
09-May-21	2.6	2.98	676	774.8	R 12.15	R 10.60
10-May-21	1.69	1.98	439.4	514.8	R 18.69	R 15.95
11-May-21	2.81	3.19	730.6	829.4	R 11.24	R 9.90
12-May-21	2.93	3.4	761.8	884	R 10.78	R 9.29
13-May-21	1.18	1.36	306.8	353.6	R 26.76	R 23.22
14-May-21	1.42	1.73	369.2	449.8	R 22.24	R 18.25
16-May-21	1.89	2.2	491.4	572	R 16.71	R 14.35
17-May-21	2.8	3.35	728	871	R 11.28	R 9.43
18-May-21	2.19	2.54	569.4	660.4	R 14.42	R 12.43
19-May-21	0.98	1.1	254.8	286	R 32.22	R 28.71
21-May-21	0.92	1.06	239.2	275.6	R 34.32	R 29.79
22-May-21	2.53	2.86	657.8	743.6	R 12.48	R 11.04
23-May-21	2.87	3.26	746.2	847.6	R 11.00	R 9.69
24-May-21	0.24	0.36	62.4	93.6	R 131.57	R 87.72
26-May-21	0.87	0.96	226.2	249.6	R 36.30	R 32.89
27-May-21	0.29	0.43	75.4	111.8	R 108.89	R 73.44
28-May-21	0.21	0.31	54.6	80.6	R 150.37	R 101.86
29-May-21	1.11	1.19	288.6	309.4	R 28.45	R 26.54
30-May-21	1.68	1.82	436.8	473.2	R 18.80	R 17.35
31-May-21	0.45	0.58	117	150.8	R 70.17	R 54.44
01-Jun-21	1.02	1.16	265.2	301.6	R 30.96	R 27.22

02-Jun-21	1.5	1.72	390	447.2	R 21.05	R 18.36
03-Jun-21	2.29	2.6	595.4	676	R 13.79	R 12.15
04-Jun-21	2.3	2.62	598	681.2	R 13.73	R 12.05
05-Jun-21	2.51	3	652.6	780	R 12.58	R 10.53
06-Jun-21	1.98	2.23	514.8	579.8	R 15.95	R 14.16
07-Jun-21	1.62	1.81	421.2	470.6	R 19.49	R 17.45
08-Jun-21	0.79	0.9	205.4	234	R 39.97	R 35.09
09-Jun-21	1.27	1.38	330.2	358.8	R 24.86	R 22.88
10-Jun-21	0.78	0.93	202.8	241.8	R 40.48	R 33.95
11-Jun-21	1.97	2.17	512.2	564.2	R 16.03	R 14.55
12-Jun-21	2.07	2.3	538.2	598	R 15.26	R 13.73
13-Jun-21	0.72	0.85	187.2	221	R 43.86	R 37.15
14-Jun-21	1.29	1.51	335.4	392.6	R 24.48	R 20.91
15-Jun-21	0.66	0.78	171.6	202.8	R 47.85	R 40.48
18-Jun-21	1.49	1.78	387.4	462.8	R 21.19	R 17.74
19-Jun-21	2.45	2.79	637	725.4	R 12.89	R 11.32
20-Jun-21	1.49	1.69	387.4	439.4	R 21.19	R 18.69
21-Jun-21	1.19	1.4	309.4	364	R 26.54	R 22.56
24-Jun-21	1.85	2.19	481	569.4	R 17.07	R 14.42
26-Jun-21	0.34	0.51	88.4	132.6	R 92.88	R 61.92
27-Jun-21	1.2	1.39	312	361.4	R 26.31	R 22.72
01-Jul-21	0.19	0.3	49.4	78	R 166.20	R 105.26
04-Jul-21	0.22	0.36	57.2	93.6	R 143.54	R 87.72
05-Jul-21	1.17	1.35	304.2	351	R 26.99	R 23.39
06-Jul-21	0.98	1.14	254.8	296.4	R 32.22	R 27.70

B-3: Distillate yield trends of the stages

Date	Stage 1	Stage 2	Stage 3	Stage 4	Stage 5	Basin still	MSS-SS + BSS	MSS-SS
	(ml)							
19-Sep-20	850	990	940	690	740	250	4460	4210
22-Sep-20	960	1110	1150	690	1270	560	5740	5180
24-Sep-20	760	990	1030	570	1470	360	5180	4820
25-Sep-20	NM	NM	NM	NM	NM	NM	NM	NM
26-Sep-20	980	1120	1070	680	900	340	5090	4750
29-Sep-20	1020	1040	1050	590	1280	480	5460	4980
30-Sep-20	880	1120	1180	640	1260	510	5590	5080
01-Oct-20	1050	1180	1130	610	1200	400	5570	5170
02-Oct-20	890	1100	1120	690	1300	330	5430	5100
03-Oct-20	1080	1140	1090	800	1110	490	5710	5220
04-Oct-20	930	1010	1120	750	1340	720	5870	5150
05-Oct-20	970	1250	1220	850	1440	610	6340	5730
06-Oct-20	920	1240	1330	660	1620	740	6510	5770
08-Oct-20	990	1190	1100	650	940	460	5330	4870
10-Oct-20	930	1250	1360	680	1670	780	6670	5890
11-Oct-20	1020	1290	1160	840	1430	800	6540	5740
12-Oct-20	1000	1260	1050	910	1390	720	6330	5610
13-Oct-20	900	1470	1250	1010	1330	650	6610	5960
14-Oct-20	1130	1210	1120	810	1160	540	5970	5430
15-Oct-20	990	1200	860	1090	1550	490	6180	5690
16-Oct-20	860	1150	1330	840	1800	990	6970	5980
17-Oct-20	850	1120	950	1110	1300	740	6070	5330
20-Oct-20	1050	1230	1120	860	1010	730	6000	5270
21-Oct-20	810	1250	1390	820	1580	960	6810	5850
22-Oct-20	800	1230	1370	790	1690	970	6850	5880
23-Oct-20	900	1370	1190	840	1520	840	6660	5820
24-Oct-20	930	1110	1060	560	1160	490	5310	4820
25-Oct-20	900	1090	1260	680	1120	790	5840	5050
27-Oct-20	780	1290	1420	760	1770	940	6960	6020
28-Oct-20	900	1100	1130	820	1050	660	5660	5000
29-Oct-20	850	830	970	510	1090	490	4740	4250
03-Nov-20	1200	1150	1210	990	1340	920	6810	5890
04-Nov-20	1030	1190	1240	920	1320	750	6450	5700
05-Nov-20	1070	1060	1170	590	1080	640	5610	4970
06-Nov-20	NM	NM	NM	NM	NM	NM	NM	NM
07-Nov-20	1040	1140	1050	520	1620	810	6180	5370
08-Nov-20	1030	1150	1080	830	1020	640	5750	5110
09-Nov-20	1090	1130	960	740	1110	610	5640	5030
10-Nov-20	740	1170	1390	1000	1720	890	6910	6020
11-Nov-20	860	1310	1460	980	1780	930	7320	6390
12-Nov-20	880	1550	1360	1380	1560	770	7500	6730
13-Nov-20	890	1110	1050	970	1460	690	6170	5480
15-Nov-20	1040	1290	1240	890	1370	730	6560	5830
16-Nov-20	840	1010	1100	960	1190	550	5650	5100
17-Nov-20	750	1300	1290	1050	1000	590	5980	5390
19-Nov-20	980	1200	1330	880	1650	760	6800	6040
20-Nov-20	980	1210	1420	1050	1720	1000	7380	6380
21-Nov-20	1070	1310	1290	700	1280	650	6300	5650
22-Nov-20	860	1230	1150	1120	830	700	5890	5190
23-Nov-20	1020	1050	1130	690	1220	630	5740	5110
27-Nov-20	1190	1200	1360	860	1680	860	7150	6290
28-Nov-20	1060	1280	1400	940	1520	800	7000	6200
29-Nov-20	1100	1310	1360	860	1500	990	7120	6130
30-Nov-20	1020	1150	1160	720	1380	670	6100	5430
01-Dec-20	1090	1160	1020	670	1030	580	5550	4970
02-Dec-20	980	1330	1420	780	1610	920	7040	6120
03-Dec-20	1000	1140	1230	960	1440	900	6670	5770
04-Dec-20	970	1240	1430	1000	1680	1010	7330	6320

05-Dec-20	890	1260	1480	1050	1680	1020	7380	6360
06-Dec-20	750	1360	1460	930	1760	1000	7260	6260
09-Dec-20	990	1210	1230	650	1660	780	6520	5740
11-Dec-20	1060	880	790	650	1110	410	4900	4490
12-Dec-20	1040	1210	1280	870	1340	730	6470	5740
13-Dec-20	830	1350	1510	740	1700	970	7100	6130
14-Dec-20	920	1310	1290	850	1480	880	6730	5850
15-Dec-20	890	1360	1520	820	1680	860	7130	6270
16-Dec-20	820	1340	1590	780	1780	830	7140	6310
17-Dec-20	1130	980	1100	890	1000	730	5830	5100
18-Dec-20	1160	1450	1470	1330	1310	980	7700	6720
13-Jan-21	760	1550	1630	910	1880	1060	7790	6730
14-Jan-21	970	1210	1360	820	2080	1140	7580	6440
15-Jan-21	1030	1420	1370	630	1980	790	7220	6430
16-Jan-21	1140	1490	1410	890	1830	940	7700	6760
17-Jan-21	1110	1120	1230	610	1290	590	5950	5360
18-Jan-21	1040	1440	1480	790	1610	820	7180	6360
19-Jan-21	1010	1330	1320	820	1540	660	6680	6020
21-Jan-21	1220	1470	1400	1040	1430	720	7280	6560
22-Jan-21	860	1360	1460	910	1610	610	6810	6200
23-Jan-21	1030	1330	1360	590	1440	500	6250	5750
24-Jan-21	890	1360	1480	660	1530	1000	6920	5920
25-Jan-21	970	1420	1390	1010	1570	1110	7470	6360
26-Jan-21	1050	1660	1590	770	1520	980	7570	6590
27-Jan-21	1090	1230	1330	800	1340	750	6540	5790
28-Jan-21	1140	1300	1360	790	1620	910	7120	6210
29-Jan-21	1110	1270	1220	840	1600	790	6830	6040
30-Jan-21	990	1280	1390	800	1520	710	6690	5980
31-Jan-21	980	1320	1200	580	1440	570	6090	5520
01-Feb-21	1120	1200	1190	780	1420	590	6300	5710
02-Feb-21	930	1310	1380	740	1800	960	7120	6160
03-Feb-21	1110	1280	1290	800	1430	880	6790	5910
04-Feb-21	840	1320	1380	920	1730	580	6770	6190
05-Feb-21	790	1340	1400	910	1710	620	6770	6150
06-Feb-21	670	1290	1370	880	1750	910	6870	5960
08-Feb-21	1120	1370	1440	740	1350	560	6580	6020
10-Feb-21	960	1250	1230	810	1460	740	6450	5710
11-Feb-21	830	1360	1470	690	1520	790	6660	5870
12-Feb-21	840	1150	1320	670	1100	480	5560	5080
13-Feb-21	930	1130	1220	610	1570	610	6070	5460
14-Feb-21	1100	1060	1440	810	1130	340	5880	5540
15-Feb-21	990	1020	1100	740	1450	490	5790	5300
16-Feb-21	1110	1280	1300	830	1520	560	6600	6040
17-Feb-21	950	1210	1330	860	1600	630	6580	5950
18-Feb-21	1090	1180	1190	840	1530	510	6340	5830
19-Feb-21	1080	1340	950	610	1170	450	5600	5150
20-Feb-21	1020	1280	960	660	1120	430	5470	5040
21-Feb-21	1050	1390	1100	850	1090	520	6000	5480
22-Feb-21	990	1210	1240	780	1390	530	6140	5610
23-Feb-21	840	1180	1200	810	1330	570	5930	5360
24-Feb-21	860	1260	1120	910	1280	440	5870	5430
26-Feb-21	840	1150	1170	690	1310	560	5720	5160
27-Feb-21	930	1210	1130	620	1300	620	5810	5190
28-Feb-21	1120	1150	1130	770	1290	530	5990	5460
04-Mar-21	1010	1090	1100	670	810	270	4950	4680
05-Mar-21	860	1140	1220	550	1520	670	5960	5290
07-Mar-21	880	1020	1010	560	800	680	4950	4270
08-Mar-21	670	950	870	480	690	360	4020	3660
11-Mar-21	440	780	720	300	840	340	3420	3080
13-Mar-21	840	600	530	310	1110	440	3830	3390
15-Mar-21	220	280	240	130	80	170	1120	950
16-Mar-21	1050	1380	1330	660	1200	750	6370	5620
17-Mar-21	750	1270	1780	860	1030	850	6540	5690
18-Mar-21	660	1210	1220	660	1080	600	5430	4830

19-Mar-21	810	1190	1160	570	1090	690	5510	4820
20-Mar-21	600	1020	1060	440	480	340	3940	3600
21-Mar-21	670	1440	1740	1030	1000	700	6580	5880
22-Mar-21	610	1280	1440	1150	790	650	5920	5270
23-Mar-21	590	1380	1420	1200	1170	860	6620	5760
24-Mar-21	830	980	960	670	1340	700	5480	4780
25-Mar-21	740	1180	1300	1170	980	670	6040	5370
26-Mar-21	850	230	310	190	400	210	2190	1980
27-Mar-21	760	850	1000	820	590	530	4550	4020
28-Mar-21	190	800	1170	720	490	500	3870	3370
29-Mar-21	680	1120	1380	900	910	660	5650	4990
30-Mar-21	820	1390	1060	1010	450	470	5200	4730
31-Mar-21	80	50	30	10	50	150	370	220
01-Apr-21	140	1020	1170	950	590	520	4390	3870
02-Apr-21	110	400	430	250	400	230	1820	1590
03-Apr-21	150	920	1160	930	590	600	4350	3750
05-Apr-21	620	1330	1280	860	450	540	5080	4540
06-Apr-21	800	1350	1150	850	1010	980	6140	5160
07-Apr-21	920	780	940	640	570	660	4510	3850
08-Apr-21	690	1210	1170	640	820	440	4970	4530
09-Apr-21	530	1210	1130	560	620	380	4430	4050
10-Apr-21	690	700	740	580	330	300	3340	3040
11-Apr-21	570	1160	980	570	690	560	4530	3970
12-Apr-21	1190	630	790	460	370	280	3720	3440
13-Apr-21	820	700	900	650	490	440	4000	3560
14-Apr-21	530	950	860	640	610	460	4050	3590
15-Apr-21	540	530	520	320	290	210	2410	2200
16-Apr-21	930	910	1100	770	820	720	5250	4530
17-Apr-21	850	750	1080	640	700	650	4670	4020
18-Apr-21	700	1030	1100	790	830	620	5070	4450
19-Apr-21	310	700	750	540	510	290	3100	2810
20-Apr-21	590	1030	1020	730	670	480	4520	4040
21-Apr-21	590	880	900	650	530	500	4050	3550
22-Apr-21	860	960	930	750	640	580	4720	4140
23-Apr-21	580	870	780	560	450	380	3620	3240
27-Apr-21	220	190	240	60	250	540	1500	960
28-Apr-21	420	460	530	330	590	340	2670	2330
29-Apr-21	290	370	440	240	550	170	2060	1890
30-Apr-21	160	590	720	440	730	380	3020	2640
01-May-21	250	860	910	550	680	430	3680	3250
02-May-21	510	1070	1120	860	700	620	4880	4260
03-May-21	330	430	440	300	490	770	2760	1990
04-May-21	370	350	430	80	800	340	2370	2030
08-May-21	610	240	350	110	640	590	2540	1950
09-May-21	440	500	590	390	680	380	2980	2600
10-May-21	510	290	330	130	430	290	1980	1690
11-May-21	370	790	730	520	400	380	3190	2810
12-May-21	250	810	780	490	600	470	3400	2930
13-May-21	390	140	180	30	440	180	1360	1180
14-May-21	200	170	290	120	640	310	1730	1420
16-May-21	520	220	340	110	700	310	2200	1890
17-May-21	570	600	550	290	790	550	3350	2800
18-May-21	260	520	520	230	660	350	2540	2190
19-May-21	450	110	160	20	240	120	1100	980
20-May-21	NM	NM	NM	NM	NM	NM	NM	NM
21-May-21	280	230	190	130	90	140	1060	920
22-May-21	360	670	610	330	560	330	2860	2530
23-May-21	290	860	740	420	560	390	3260	2870
24-May-21	110	30	50	NM	50	120	360	240
25-May-21	NM	NM	NM	NM	NM	NM	NM	NM
26-May-21	350	160	150	20	190	90	960	870
27-May-21	20	40	80	NM	150	140	430	290
28-May-21	70	50	40	NM	50	100	310	210
29-May-21	560	100	170	30	250	80	1190	1110

30-May-21	700	230	340	80	330	140	1820	1680
31-May-21	250	30	120	20	30	130	580	450
01-Jun-21	50	150	210	140	470	140	1160	1020
02-Jun-21	160	390	510	60	380	220	1720	1500
03-Jun-21	310	630	600	400	350	310	2600	2290
04-Jun-21	390	530	540	330	510	320	2620	2300
05-Jun-21	280	750	700	430	350	490	3000	2510
06-Jun-21	400	520	530	310	220	250	2230	1980
07-Jun-21	260	390	440	290	240	190	1810	1620
08-Jun-21	340	120	190	50	90	110	900	790
09-Jun-21	240	330	330	180	190	110	1380	1270
10-Jun-21	320	140	130	60	130	150	930	780
11-Jun-21	380	500	590	300	200	200	2170	1970
12-Jun-21	370	600	590	360	150	230	2300	2070
13-Jun-21	200	80	190	20	230	130	850	720
14-Jun-21	220	180	310	70	510	220	1510	1290
15-Jun-21	290	80	180	10	100	120	780	660
16-Jun-21	NM	NM	NM	NM	NM	NM	NM	NM
17-Jun-21	NM	NM	NM	NM	NM	NM	NM	NM
18-Jun-21	230	220	280	140	620	290	1780	1490
19-Jun-21	290	680	640	470	370	340	2790	2450
20-Jun-21	310	200	330	160	490	200	1690	1490
21-Jun-21	200	300	300	190	200	210	1400	1190
22-Jun-21	NM	NM	NM	NM	NM	NM	NM	NM
23-Jun-21	NM	NM	NM	NM	NM	NM	NM	NM
24-Jun-21	530	240	370	230	480	340	2190	1850
25-Jun-21	NM	NM	NM	NM	NM	NM	NM	NM
26-Jun-21	180	30	50	20	60	170	510	340
27-Jun-21	190	210	250	130	420	190	1390	1200
28-Jun-21	NM	NM	NM	NM	NM	NM	NM	NM
29-Jun-21	NM	NM	NM	NM	NM	NM	NM	NM
30-Jun-21	NM	NM	NM	NM	NM	NM	NM	NM
01-Jul-21	80	60	20	NM	30	110	300	190
02-Jul-21	NM	NM	NM	NM	NM	NM	NM	NM
03-Jul-21	NM	NM	NM	NM	NM	NM	NM	NM
04-Jul-21	90	60	30	NM	40	140	360	220
05-Jul-21	260	410	280	50	170	180	1350	1170
06-Jul-21	310	140	230	100	200	160	1140	980

B-4: Electrical resistance of the distillate results

Date	ST1	ST 2	ST 3	ST 4	ST 5	BSS
	Ohms (Ω) (x10^3)					
04-Mar-21	36. 1	45.4	91.7	392	57.4	56.6
05-Mar-21	44.2	35.5	49.5	66.9	54.8	47. 4
07-Mar-21	56.4	43.4	74.2	397	86.4	66.4
08-Mar-21	35.	32.7	126.5	189	63.2	89.5
11-Mar-21	43.7	46.4	86.6	144.3	54.3	60.6
13-Mar-21	87.7	50.9	186.3	375	72.1	126.4
16-Mar-21	37.5	64.7	90.5	461	75.6	80.5
17-Mar-21	34.1	60.6	139.3	406	81.6	74.41
18-Mar-21	56.8	77.5	404	577	934	115.9
19-Mar-21	55.7	124.9	855	851	112.5	178.5
20-Mar-21	35.9	63.5	465	570	82.4	199.8
21-Mar-21	65.3	72.3	434	705	74.6	132.9
22-Mar-21	43.6	64.5	67.7	449	74.1	139.3
23-Mar-21	34.9	61.1	139.2	512	78.5	122.1
24-Mar-21	73.9	66.7	47.3	171.6	54.5	129.4
25-Mar-21	65.1	81.8	152.3	498	79.8	116.4
26-Mar-21	33.8	65.5	132.7	469	81.2	111.9
27-Mar-21	34.7	66.4	175.7	517	84.6	457
28-Mar-21	47.6	74.2	548	674	91.6	576
29-Mar-21	66.3	79.5	182.9	601	73.2	76.3
30-Mar-21	45.6	66.6	122.1	630	88.8	157.7
01-Apr-21	76.6	88.6	191.3	587	94.9	151.2
02-Apr-21	83.7	156.4	667	698	119.6	616
03-Apr-21	47.8	150.6	100.1	59.7	85.6	56.7
05-Apr-21	36.1	86.1	730	56.8	71.1	528
06-Apr-21	44.4	56.7	138.5	143.2	78.6	71.3
07-Apr-21	38.9	70.7	106.7	701	83.1	66.8
08-Apr-21	66.8	69.1	497	762	95.6	132.
09-Apr-21	70.6	73.7	504	626	80.8	168.6
10-Apr-21	55.1	17.8	58.1	156.8	63.4	136.3
11-Apr-21	78.8	71.6	590	942	90.2	562
12-Apr-21	65.6	70.4	187.0	676	89.4	114.8
13-Apr-21	45.4	51.2	117.3	151.2	75.4	148.5
14-Apr-21	86.6	44.8	173.5	553	73.0	80.7
15-Apr-21	64.1	91.7	538	652	57.2	143.2
16-Apr-21	76.1	73.0	109.7	472	71.2	69.5
17-Apr-21	55.5	53.0	138.5	195.6	83.7	76.6
18-Apr-21	76.5	65.1	523	738	112.3	173.9
19-Apr-21	62.5	71.2	520	726	108.7	142.3
20-Apr-21	62.2	82.6	497	742	145.3	586
21-Apr-21	49.3	71.0	577	860	110.8	676
22-Apr-21	60.4	70.1	482	792	102.4	88.6
23-Apr-21	65.3	65.2	649	835	105.4	583
27-Apr-21	65.9	75.1	168.6	515	105.8	104.7
28-Apr-21	81.8	141.4	738	942	131.6	163.7
29-Apr-21	80.2	167.3	905	817	120.6	170
30-Apr-21	99.8	178.1	982	1160	139.3	838
01-May-21	80.3	688	186.1	950	106.1	687
02-May-21	85.7	137.5	693	969	132.8	840
03-May-21	80.1	180.7	988	1042	132.8	85.5
04-May-21	94.9	112.7	537	594	147.4	525
08-May-21	74.8	87.7	526	459	118.3	102.3
09-May-21	51.8	114.1	753	952	150.4	157.9
10-May-21	80.6	110.7	805	875	130.4	126.6
11-May-21	78.8	178.8	708	986	136.7	892
12-May-21	87.9	641	1074	1067	160.4	1070
13-May-21	80.9	147.7	761	809	151.8	984
14-May-21	98.6	154.8	847	969	173.2	908
16-May-21	83.4	118.4	711	772	168.5	914
17-May-21	85.8	121.7	845	864	164.3	117.2

18-May-21	102.6	706	993	1106	153.8	514
19-May-21	78.3	108.8	109.5	505	102.5	122.8
26-May-21	18.68	82.9	649	194.3	64.3	115.5

B-5: Solar irradiance results

Table B-5-1: Data for day 149-29 May 2021

Time	Hourly Irrad. (I_H) (W/m^2)	B **(Radians)**	Equation of time **(ET) (Minutes)**	Solar time **(ST)**	Hour angle **(ω)** Radians	Seasonal correction for solar time **(S_c)**	Hour angle 1 **(ω_1)**	Hour angle 2 **(ω_2)**	Declination angle **(δ) (Radians)**	Eccentricity factor **(E_o)**	Solar constant **(W/m^2)**	**Zenith cosθ$_z$**	Extra-terrestrial **(I_o)** (W/m^2)	Hourly Clearness index **(M_t)**	Hourly diffuse fraction **(k_d)**	Hourly diffuse Irrad. On horizontal **(I_d)**	Hourly beam Irrad. on Horizontal **(I_b)**	$f_{Hay\text{ - index}}$	**cosθ**	Hourly diffuse Irrad. on sloped **(I_dß)**	Hourly beam Irrad. on sloped **(I_bß)**	Hourly reflected Irrad. **(I_r)**	Total hourly Irrad. on sloped surface **($I_ß$)**
7	0.0	1.2	2.8	7.8	-1.2	0.05	-1.3	-1.0	0.4	1.0	1367	0.1	36.6	0.0	1.0	0.0	0.0	0.0	0.5	0.0	0.0	0.0	0.0
8	56.7	1.2	2.8	8.8	-0.9	0.05	-1.0	-0.8	0.4	1.0	1367	0.3	96.3	0.6	0.5	26.4	30.3	0.3	0.7	34.4	74.0	2.5	110.9
9	138.0	1.2	2.8	9.8	-0.6	0.05	-0.8	-0.5	0.4	1.0	1367	0.4	144.6	1.0	0.2	24.8	113.1	0.8	0.8	43.1	226.2	6.1	275.4
10	216.7	1.2	2.8	10.8	-0.4	0.05	-0.5	-0.2	0.4	1.0	1367	0.5	178.0	1.2	0.2	39.0	177.7	1.0	0.9	71.5	325.9	9.6	406.9
11	363.4	1.2	2.8	11.8	-0.1	0.05	-0.2	0.0	0.4	1.0	1367	0.6	194.5	1.9	0.2	65.4	298.0	1.5	1.0	150.6	528.4	16.0	695.0
12	334.8	1.2	2.8	12.8	0.2	0.05	0.0	0.3	0.4	1.0	1367	0.6	192.9	1.7	0.2	60.3	274.5	1.4	1.0	132.7	488.3	14.8	635.8
13	266.8	1.2	2.8	13.8	0.4	0.05	0.3	0.5	0.4	1.0	1367	0.5	173.2	1.5	0.2	48.0	218.7	1.3	0.9	102.6	405.6	11.8	519.9
14	226.5	1.2	2.8	14.8	0.7	0.05	0.5	0.8	0.4	1.0	1367	0.4	136.8	1.7	0.2	40.8	185.7	1.4	0.8	102.1	380.7	10.0	492.7
15	131.8	1.2	2.8	15.8	0.9	0.05	0.8	1.1	0.4	1.0	1367	0.2	86.2	1.5	0.2	23.7	108.1	1.3	0.6	72.5	280.6	5.8	358.9
16	50.4	1.2	2.8	16.8	1.2	0.05	1.1	1.3	0.4	1.0	1367	0.1	24.9	2.0	0.2	9.1	41.4	1.7	0.4	89.1	256.9	2.2	348.2
17	24.2	1.2	2.8	17.8	1.5	0.05	1.3	1.6	0.4	1.0	1367	-0.1	-43.0	-0.6	1.0	25.1	-1.0	0.0	0.2	18.1	1.8	1.1	21.0
18	0.0	1.2	2.8	18.8	-0.9	0.05	-1.0	-0.7	0.4	1.0	1367	0.3	101.4	0.0	0.0	0.0	0.0	0.0	0.7	0.0	0.0	0.0	0.0

Table B-5-2: Data for day 151-01 June 2021

Time	Hourly Irrad. (I_H) **(W/m^2)**	B **(Radians)**	Equation of time **(ET) (Minutes)**	Solar time **(ST)**	Hour angle **(ω)** Radians	Seasonal correction for solar time **(S_c)**	Hour angle 1 **(ω_1)**	Hour angle 2 **(ω_2)**	Declination angle **(δ) (Radians)**	Eccentricity factor **(E_o)**	Solar constant **(W/m^2)**	**Zenith $\cos\theta_z$**	Extra-terrestrial (I_o) **(W/m^2)**	Hourly Clearness index **(M_t)**	Hourly diffuse fraction **(k_d)**	Hourly diffuse Irrad. On horizontal **(I_d)**	Hourly beam Irrad. on Horizontal **(I_b)**	$f_{Hay\text{ - index}}$	**cosθ**	Hourly diffuse Irrad. on sloped **($I_d\beta$)**	Hourly beam Irrad. on sloped **($I_b\beta$)**	Hourly reflected Irrad. **(I_r)**	Total hourly Irrad. on sloped surface **(I_β)**
7	0	1.2	2.5	7.8	-1.2	0.042	-1.3	-1.0	0.38	1.0	1367	0.10	34.9	0	1.00	0	0	0	0.5	0	0	0	0
8	70.3	1.2	2.5	8.8	-0.9	0.042	-1.0	-0.8	0.38	1.0	1367	0.27	94.5	0.7	0.20	14.1	56.2	0.6	0.7	25.3	139.6	3.1	168.1
9	162.4	1.2	2.5	9.8	-0.6	0.042	-0.8	-0.5	0.38	1.0	1367	0.41	142.7	1.1	0.18	29.2	133.2	0.9	0.8	56.7	269.3	7.2	333.1
10	387.1	1.2	2.5	10.8	-0.4	0.042	-0.5	-0.2	0.38	1.0	1367	0.51	176.3	2.2	0.18	69.7	317.4	1.8	0.9	188.7	587.3	17.1	793.1
11	482.3	1.2	2.5	11.8	-0.1	0.042	-0.2	0.0	0.38	1.0	1367	0.56	192.8	2.5	0.18	86.8	395.5	2.1	1.0	247.0	706.8	21.3	975.1
12	406.5	1.2	2.5	12.8	0.2	0.042	0.0	0.3	0.38	1.0	1367	0.55	191.4	2.1	0.18	73.2	333.3	1.7	1.0	186.1	597.4	17.9	801.4
13	281.9	1.2	2.5	13.8	0.4	0.042	0.3	0.5	0.38	1.0	1367	0.50	171.9	1.6	0.18	50.7	231.2	1.3	0.9	113.9	432.1	12.4	558.4
14	134.8	1.2	2.5	14.8	0.7	0.042	0.5	0.8	0.38	1.0	1367	0.39	135.7	1.0	0.18	24.3	110.6	0.8	0.8	44.4	228.7	5.9	279.1
15	96.4	1.2	2.5	15.8	0.9	0.042	0.8	1.1	0.38	1.0	1367	0.25	85.4	1.1	0.18	17.3	79.0	0.9	0.6	43.2	207.7	4.2	255.2
16	73.1	1.2	2.5	16.8	1.2	0.042	1.1	1.3	0.38	1.0	1367	0.07	24.3	3.0	0.18	13.2	60.0	2.5	0.5	192.5	383.4	3.2	579.1
17	24.9	1.2	2.5	17.8	1.5	0.042	1.3	1.6	0.38	1.0	1367	-0.12	-43.4	-0.6	1.04	26.0	-1.0	0.0	0.2	18.6	1.9	1.1	21.6

Table B-5-3: Data for day 172-21 June 2021

Time	Hourly Irrad. (I_H) **(W/m²)**	B **(Radians)**	Equation of time **(ET) (Minutes)**	Solar time **(ST)**	Hour angle **(ω)** Radians	Seasonal correction for solar time **(S_c)**	Hour angle 1 **(ω_1)**	Hour angle 2 **(ω_2)**	Declination angle **(δ) (Radians)**	Eccentricity factor **(E_O)**	Solar constant **(W/m²)**	**Zenith cosθz**	Extra-terrestrial **(I_O) (W/m²)**	Hourly Clearness index **(M_t)**	Hourly diffuse fraction **(k_d)**	Hourly diffuse Irrad. **(I_d)**	Hourly beam Horizontal **(I_b)**	$f_{Hay\text{ - index}}$	**cosθ**	Hourly diffuse Irrad. on sloped **($I_d\beta$)**	Hourly beam Irrad. on sloped **($I_b\beta$)**	Hourly reflected Irrad. **(I_r)**	Total hourly Irrad. on sloped surface **(I_β)**
7	0.0	1.6	-1.4	7.8	-1.2	-0.024	-1.3	-1.0	0.4	1.0	1367	0.1	23.6	0.0	1.0	0.0	0.0	0.0	0.5	0.0	0.0	0.0	0.0
8	81.3	1.6	-1.4	8.8	-0.9	-0.024	-1.0	-0.8	0.4	1.0	1367	0.2	83.0	1.0	0.2	14.6	66.7	0.8	0.7	34.7	184.3	3.6	222.7
9	264.6	1.6	-1.4	9.8	-0.7	-0.024	-0.8	-0.5	0.4	1.0	1367	0.4	131.6	2.0	0.2	47.6	216.9	1.6	0.8	145.4	468.2	11.7	625.2
10	391.2	1.6	-1.4	10.8	-0.4	-0.024	-0.5	-0.3	0.4	1.0	1367	0.5	165.9	2.4	0.2	70.4	320.8	1.9	0.9	213.3	623.3	17.2	853.8
11	456.7	1.6	-1.4	11.8	-0.1	-0.024	-0.3	0.0	0.4	1.0	1367	0.5	183.7	2.5	0.2	82.2	374.5	2.0	1.0	245.6	697.7	20.1	963.4
12	493.5	1.6	-1.4	12.8	0.1	-0.024	0.0	0.3	0.4	1.0	1367	0.5	183.8	2.7	0.2	88.8	404.6	2.2	1.0	281.1	753.8	21.8	1056.7
13	376.5	1.6	-1.4	13.8	0.4	-0.024	0.3	0.5	0.4	1.0	1367	0.5	166.0	2.3	0.2	67.8	308.7	1.9	0.9	199.4	599.7	16.6	815.7
14	182.2	1.6	-1.4	14.8	0.7	-0.024	0.5	0.8	0.4	1.0	1367	0.4	131.7	1.4	0.2	32.8	149.4	1.1	0.8	76.8	322.4	8.0	407.3
15	117.5	1.6	-1.4	15.8	0.9	-0.024	0.8	1.0	0.4	1.0	1367	0.2	83.2	1.4	0.2	21.1	96.3	1.2	0.7	65.0	266.1	5.2	336.3
16	68.4	1.6	-1.4	16.8	1.2	-0.024	1.0	1.3	0.4	1.0	1367	0.1	23.8	2.9	0.2	12.3	56.1	2.4	0.5	185.7	383.6	3.0	572.3
17	20.3	1.6	-1.4	17.8	1.4	-0.024	1.3	1.6	0.4	1.0	1367	-0.1	-42.5	-0.5	1.0	21.0	-0.7	0.0	0.3	15.4	1.5	0.9	17.8
18	0.0	1.6	-1.4	18.8	-0.9	-0.024	-1.0	-0.8	0.4	1.0	1367	0.3	88.6	0.0	0.7	0.0	0.0	0.0	0.7	0.0	0.0	0.0	0.0

Table B-5-4: Data for day 269-26 September 2020

Time	Hourly Irrad. (I_H) **(W/m²)**	B **(Radians)**	Equation of time **(ET) (Minutes)**	Solar time **(ST)**	Hour angle **(ω)** Radians	Seasonal correction for solar time **(S_c)**	Hour angle 1 **(ω_1)**	Hour angle 2 **(ω_2)**	Declination angle **(δ) (Radians)**	Eccentricity factor **(E_o)**	Solar constant **(W/m²)**	**Zenith cosθ$_Z$**	Extra-terrestrial **(I_o) (W/m²)**	Hourly Clearness index **(M_t)**	Hourly diffuse fraction **(k_d)**	Hourly diffuse Irrad. **(I_d)**	Hourly beam Horizontal **(I_b)**	$f_{Hay\text{ - index}}$	**cosθ**	Hourly diffuse Irrad. on sloped **($I_d\beta$)**	Hourly beam Irrad. on sloped **($I_b\beta$)**	Hourly reflected Irrad. **(I_r)**	Total hourly Irrad. on sloped surface **(I_β)**
6	0.0	3.2	9.5	6.9	-1.4	0.2	-1.5	-1.2	-0.041	1.0	1367	0.2	70.6	0.0	1.00	0.0	0.0	0.0	0.2	0.0	0.0	0.0	0.0
7	72.4	3.2	9.5	7.9	-1.1	0.2	-1.2	-1.0	-0.041	1.0	1367	0.4	143.1	0.5	0.62	45.1	27.3	0.2	0.4	37.2	27.8	3.2	68.1
8	215.8	3.2	9.5	8.9	-0.8	0.2	-1.0	-0.7	-0.041	1.0	1367	0.6	206.4	1.0	0.18	38.9	177.0	0.9	0.6	39.2	185.3	9.5	234.0
9	428.5	3.2	9.5	9.9	-0.6	0.2	-0.7	-0.4	-0.041	1.0	1367	0.7	256.2	1.7	0.18	77.1	351.3	1.4	0.8	89.8	372.6	18.9	481.3
10	305.6	3.2	9.5	10.9	-0.3	0.2	-0.4	-0.2	-0.041	1.0	1367	0.8	289.1	1.1	0.18	55.0	250.6	0.9	0.9	56.6	267.4	13.5	337.4
11	442.1	3.2	9.5	11.9	0.0	0.2	-0.2	0.1	-0.041	1.0	1367	0.9	302.8	1.5	0.18	79.6	362.5	1.2	0.9	89.6	387.6	19.5	496.7
12	292.5	3.2	9.5	12.9	0.2	0.2	0.1	0.3	-0.041	1.0	1367	0.8	296.5	1.0	0.18	52.6	239.8	0.8	0.9	53.3	256.2	12.9	322.4
13	283.9	3.2	9.5	13.9	0.5	0.2	0.3	0.6	-0.041	1.0	1367	0.8	270.5	1.0	0.18	51.1	232.8	0.9	0.8	52.3	247.6	12.5	312.5
14	442.4	3.2	9.5	14.9	0.7	0.2	0.6	0.9	-0.041	1.0	1367	0.6	226.6	2.0	0.18	79.6	362.8	1.6	0.7	97.0	382.0	19.5	498.5
15	297.5	3.2	9.5	15.9	1.0	0.2	0.9	1.1	-0.041	1.0	1367	0.5	167.8	1.8	0.18	53.5	243.9	1.5	0.5	61.3	251.4	13.1	325.8
16	171.0	3.2	9.5	16.9	1.3	0.2	1.1	1.4	-0.041	1.0	1367	0.3	98.1	1.7	0.18	30.8	140.2	1.4	0.3	32.3	135.9	7.5	175.8
17	108.8	3.2	9.5	17.9	1.5	0.2	1.4	1.7	-0.041	1.0	1367	0.1	22.3	4.9	0.18	19.6	89.2	4.0	0.0	-9.2	41.7	4.8	37.3
18	51.5	3.2	9.5	18.9	1.8	0.2	1.7	1.9	-0.041	1.0	1367	-0.2	-54.6	-0.9	1.07	55.2	-3.7	0.1	-0.2	45.2	-5.1	2.3	42.4
19	0.0	3.2	9.5	19.9	-0.7	0.2	-0.8	-0.6	-0.041	1.0	1367	0.7	235.5	0.0	1.00	0.0	0.0	0.0	0.7	0.0	0.0	0.0	0.0

Table B-5-5: Data for day 315-11 November 2020

Time	Hourly Irrad. (I_H) **(W/m²)**	B **(Radians)**	Equation of time **(ET) (Minutes)**	Solar time **(ST)**	Hour angle **(ω)** Radians	Seasonal correction for solar time **(S_c)**	Hour angle 1 **(ω_1)**	Hour angle 2 **(ω_2)**	Declination angle **(δ) (Radians)**	Eccentricity factor **(E_o)**	Solar constant **(W/m²)**	**Zenith cosθ_Z**	Extra-terrestrial **(I_o) (W/m²)**	Hourly Clearness index **(M_t)**	Hourly diffuse fraction **(k_d)**	Hourly diffuse Irrad. **(I_d)**	Hourly beam Horizontal **(I_b)**	$f_{Hay\ -\ index}$	**cosθ**	Hourly diffuse Irrad. on sloped **($I_d\beta$)**	Hourly beam Irrad. on sloped **($I_b\theta$)**	Hourly reflected Irrad. **(I_r)**	Total hourly Irrad. on sloped surface **(I_θ)**
5	0	4.03	15.6	6.03	-1.2	0.26	-1.29	-1.03	-0.32	1.02	1367	0.49	177.8	0	1.0	0	0	0	0.2	0	0	0.0	0
6	149.4	4.03	15.6	7.03	-0.9	0.26	-1.03	-0.77	-0.32	1.02	1367	0.66	242.2	0.62	0.4	61.7	87.6	0.4	0.4	53.1	56.6	0.5	110.3
7	475.5	4.03	15.6	8.03	-0.6	0.26	-0.77	-0.51	-0.32	1.02	1367	0.81	294.4	1.61	0.2	85.6	389.9	1.3	0.6	55.4	284.4	1.6	341.4
8	653.5	4.03	15.6	9.03	-0.4	0.26	-0.51	-0.25	-0.32	1.02	1367	0.91	330.9	1.97	0.2	117.6	535.9	1.6	0.7	75.5	413.8	2.2	491.6
9	758.4	4.03	15.6	10.03	-0.1	0.26	-0.25	0.02	-0.32	1.02	1367	0.96	349.2	2.17	0.2	136.5	621.9	1.8	0.8	87.4	491.5	2.6	581.5
10	843.7	4.03	15.6	11.03	0.1	0.26	0.02	0.28	-0.32	1.02	1367	0.95	348.1	2.42	0.2	151.9	691.8	2.0	0.8	90.8	546.1	2.9	639.8
11	879.3	4.03	15.6	12.03	0.4	0.26	0.28	0.54	-0.32	1.02	1367	0.90	327.6	2.68	0.2	158.3	721.0	2.2	0.7	81.0	554.3	3.0	638.2
12	866.0	4.03	15.6	13.03	0.7	0.26	0.54	0.80	-0.32	1.02	1367	0.79	289.1	3.00	0.2	155.9	710.1	2.5	0.6	53.4	513.0	3.0	569.3
13	814.1	4.03	15.6	14.03	0.9	0.26	0.80	1.06	-0.32	1.02	1367	0.64	235.2	3.46	0.2	146.5	667.5	2.8	0.4	-1.9	421.9	2.8	422.7
14	725.8	4.03	15.6	15.03	1.2	0.26	1.06	1.32	-0.32	1.02	1367	0.46	169.7	4.28	0.2	130.6	595.2	3.5	0.2	-118.3	264.6	2.5	148.7
15	643.5	4.03	15.6	16.03	1.5	0.26	1.32	1.59	-0.32	1.02	1367	0.27	97.0	6.64	0.2	115.8	527.7	5.4	0.0	-544.1	-32.2	2.2	-574.1
16	484.9	4.03	15.6	17.03	1.7	0.26	1.59	1.85	-0.32	1.02	1367	0.06	22.0	22.08	0.2	87.3	397.7	18.1	-0.2	-7975.8	-1637.3	1.7	-9611.5
17	297.5	4.03	15.6	18.03	2.0	0.26	1.85	2.11	-0.32	1.02	1367	-0.14	-50.2	-5.93	1.5	438.8	-141.3	2.8	-0.5	3394.2	-477.8	1.0	2917.5
18	149.0	4.03	15.6	19.03	2.2	0.26	2.11	2.37	-0.32	1.02	1367	-0.31	-114.6	-1.30	1.1	163.9	-14.9	0.1	-0.7	185.2	-31.5	0.5	154.2
19	60.8	4.03	15.6	20.03	2.5	0.26	2.37	2.63	-0.32	1.02	1367	-0.46	-166.8	-0.36	1.0	62.3	-1.5	0.0	-0.8	61.6	-2.7	0.2	59.2
20	0	4.03	15.6	21.0	-0.2	0	0	0	0	0	0	0	0	0	0	0	0	0	0	0	0	0	0